DESIGNING MOLYBDENUM DISULFIDE NANOCOMPOSITE ELECTRODES FOR POST-LITHIUM-ION BATTERIES

Jalal Rahmatinejad

A thesis
in
The Department
of
Chemical and Materials Engineering

Presented in Partial Fulfillment of the Requirements
For the Degree of Doctor of Philosophy
Concordia University
Montréal, Québec, Canada

April 2025

Concordia University
School of Graduate Studies

This is to certify that the thesis prepared

By: **Mr. Jalal Rahmatinejad**

Entitled: **Designing Molybdenum Disulfide Nanocomposite Electrodes for Post-Lithium-Ion Batteries**

and submitted in partial fulfillment of the requirements for the degree of

Doctor of Philosophy (Ph.D.)

complies with the regulations of this University and meets the accepted standards with respect to originality and quality.

Signed by the final examining commitee:

_____ Chair
Dr. Mehdi Hojjati

_____ External Examiner
Dr. Yuning Li

_____ Arm's Length Examiner
Dr. Marc-Antoni Goulet

_____ Examiner
Dr. Xia Li

_____ Examiner
Dr. Jung Kwon (John) Oh

_____ Supervisor
Dr. Zhibin Ye

Approved by _____
Dr. Alex De Visscher, Chair
Department of Chemical and Materials Engineering

_____ April 2025 _____ _____
Dr. Mourad Debbabi, Dean
Gina Cody School of Engineering and Computer Science

Abstract

Designing Molybdenum Disulfide Nanocomposite Electrodes for Post-Lithium-Ion Batteries

Jalal Rahmatinejad,
Concordia University, 2025

Expanding electrical energy storage beyond lithium-ion batteries (LIBs) is crucial due to their limitations in material availability, cost, and performance. LIBs rely on lithium, which has a limited supply, uneven global distribution, and increasing demand, leading to concerns about long-term sustainability and price volatility. Additionally, LIBs face intrinsic challenges such as safety risks from thermal runaway, capacity fading over extended cycles, and performance limitations at extreme temperatures. These constraints drive the search for alternative battery chemistries, such as sodium-ion, potassium-ion, magnesium-ion, zinc-ion, and aluminum-ion batteries. However, these alternatives introduce new challenges due to differences in ionic size, charge density, and electrochemical behavior, necessitating the development of advanced electrode materials. Molybdenum disulfide (MoS_2), a 2D nanomaterial with larger interlayer spacing than graphene, shows promise for storing such ions but faces challenges from its semiconducting nature and side reactions.

This thesis begins with a comprehensive review of recent literature on strategies for modifying the structure of MoS_2 and its nanocomposites to enhance ion storage capabilities for Na^+, K^+, Mg^{2+}, Zn^{2+}, and Al^{3+}. Next, four novel composites were designed and synthesized, with their potential as active materials for post-LIBs comprehensively investigated. A range of material characterization techniques, including Brunauer-Emmett-Teller (BET) surface area analysis, thermogravimetric analysis (TGA), X-ray diffraction (XRD), transmission electron microscopy (TEM), and X-ray photoelectron spectroscopy (XPS), were employed to study their structural and chemical properties. To evaluate their electrochemical performance as active battery materials, various methods such as cyclic voltammetry (CV), galvanostatic charge-discharge (GCD), and electrochemical impedance spectroscopy (EIS) were utilized.

Two anode composites for sodium-ion batteries (SIBs), MoS_2@HPC (crystalline MoS_2 in hierarchically porous carbon) and a-MoS_x@HPC (amorphous MoS_x in HPC), were designed

and evaluated. The hybridization with HPC was found to enhance Na^+ storage by improving capacity and cycling stability. At 0.5 A g^{-1}, capacities of 550 mAh g^{-1} and 301 mAh g^{-1} were achieved by a-MoS_x@HPC and MoS_2@HPC, respectively, both outperforming pure MoS_2, which delivered 253 mAh g^{-1}. After 100 cycles, capacity retentions of 75% and 89% were maintained by a-MoS_x@HPC and MoS_2@HPC, respectively, in contrast to the 53% retention observed for pure MoS_2.

Following this, a 1T/2H mixed-phase MoS_2 (MP-MoS_2) modified with a polyethylene ionomer (I@MP-MoS_2) was investigated for Mg^{2+} storage in magnesium-ion batteries (MIBs) and Mg^{2+}/Li^+ storage in dual-salt magnesium-lithium-ion batteries (MLIBs). With 53% of metallic 1T phase, increased interlayer spacing (1.11 nm vs. 0.62 nm in MoS_2), and enhanced electrolyte interaction, I@MP-MoS_2 achieved 144 mAh g^{-1} at 20 mA g^{-1} in MIBs and 270 mAh g^{-1} in MLIBs, with 87% of capacity retention after 200 cycles.

Finally, a novel cathode design was investigated for MLIBs using a 2D/2D nanocomposite of 1T/2H-MoS_2 and delaminated $Ti_3C_2T_x$ MXene (1T/2H-MoS_2@MXene). This structure improves Mg^{2+} kinetics, structural integrity, and reversible Mg^{2+}/Li^+ co-intercalation, achieving 253 mAh g^{-1} at 50 mA g^{-1} and retaining 36% of capacity at 1,000 mA g^{-1}.

Overall, this thesis presents innovative MoS_2-based materials for post-LIBs, addressing ion storage, conductivity, and stability challenges, contributing to next-generation energy storage solutions.

Acknowledgments

I would like to express my deepest gratitude to my supervisor, Professor Zhibin Ye, for his unwavering support, guidance, and trust throughout my research journey. His insights and encouragement have been invaluable, helping me grow both professionally and personally.

I am also deeply grateful to Dr. Xudong Liu, whose collaboration and technical expertise have greatly enhanced this work. His mentorship, particularly in teaching me key technical skills, was fundamental to my development.

My heartfelt thanks go to my colleagues Zaana Chevinli, Bahareh Raisi, Ximeng Zhang, Liuqing Yang, Xinling Wang, and Peishuai Dai for their continuous support and collaboration. Working alongside them has enriched my experience and fostered a strong sense of teamwork.

I would also like to extend my appreciation to Harriet Laryea, the Technical Supervisor of the CME department, and Kerri Warbanski, the Chemical Laboratory Technician, for their technical assistance and unwavering support in ensuring smooth lab operations.

Lastly, I wish to thank Concordia University and the Department of Chemical and Materials Engineering for providing me with the resources and environment to carry out this research.

Contribution of Authors

Throughout this thesis, Jalal Rahmatinejad was responsible for conceptualization (with Professor Ye as the primary contributor), conducting experiments or data collection, designing research methods and strategies, computational work, results validation and analysis, statistical or mathematical analysis, data curation, writing original drafts, and visualization.

Professor Zhibin Ye was responsible for supervision, conceptualization, project administration, designing research methods and strategies, ensuring the accuracy and reliability of results, reviewing and revising manuscripts and the thesis, and funding acquisition.

Chapter 2: This chapter is adapted from an article titled *Advanced MoS_2 nanocomposites for post-lithium-ion batteries* published in the *Chemical Engineering Journal*, Elsevier. It was a collaborative work between Jalal Rahmatinejad and Professor Zhibin Ye.

Chapters 3 to 5 saw contributions from various colleagues:

Chapter 3: This chapter is adapted from an article titled *Embedding Amorphous MoS_x Within Hierarchical Porous Carbon by Facile One-Pot Synthesis for Superior Sodium Ion Storage* published in the *Journal of Energy Chemistry*, Elsevier. In this article, Xudong Liu contributed to designing research methods and strategies, formal analysis, and data validation. Bahareh Raisi and Ximeng Zhang were involved in data validation.

Chapter 4: This chapter is adapted from an article titled *1T-2H Mixed-Phase MoS_2 Stabilized with a Hyperbranched Polyethylene Ionomer for Mg^{2+}/Li^+ Co-Intercalation Toward High-Capacity Dual-Salt Batteries* published in *Small*, Wiley-VCH. In this article, Xudong Liu contributed to designing research methods and strategies, formal analysis, and data validation. Bahareh Raisi contributed to some experiments and data collection. Ximeng Zhang, Ahmad Sadeghi Chevinli, and Liuqing Yang engaged in result discussion and data interpretation, providing critical feedback that shaped the theoretical framework and final conclusions.

Chapter 5: This chapter is adapted from an article titled *Synergistic Cathode Design for High-Performance Dual-Salt Magnesium/Lithium-Ion Batteries Using 2D/2D 1T/2H-MoS_2@$Ti_3C_2T_x$ MXene Nanocomposite* published in *Small*, Wiley-VCH. In this article,

Xudong Liu contributed to designing research methods and strategies, formal analysis, and data validation. Bahareh Raisi and Ximeng Zhang participated in result discussion and data interpretation, offering essential feedback that shaped the theoretical framework and final conclusions.

Contents

List of Figures

List of Tables

List of Abbreviations

2D Two-Dimensional. ix, 2–4, 9–11, 15, 32, 38, 67, 72, 74, 87, 88, 94, 107, 108, 110–114, 119, 122, 124, 126, 131

3D Three-Dimensional. xiii, xiv, 21, 34, 35, 37, 38, 40, 42, 43, 45–47, 55, 59

a-MoS$_x$ Amorphous Molybdenum Sulfide. 4, 71, 73–76, 78, 81, 84

AIB Aluminum-Ion Battery. xxi, 2, 8, 9, 58, 59

APC All-Phenyl Complex. 51, 96, 99, 106, 128

AZIB Aqueous Zinc-Ion Battery. xv, xxi, 19, 23, 27, 36, 53–58, 61, 62, 120

BET Brunauer-Emmett-Teller. iii, 70, 75, 128

CI-NEB Climbing-Image Nudged Elastic Band. 31

CNF Carbon Nanofiber. xiv, 47–49

CTAB Cetyltrimethylammonium Bromide. 57

CV Cyclic Voltammetry. iii, xv–xviii, 14, 55, 56, 60, 61, 70, 76, 77, 81–83, 95–99, 101, 103, 106, 118–121, 124, 125, 129

CVD Chemical Vapor Deposition. 12

DFT Density Functional Theory. xv, 19, 20, 22, 23, 26, 33, 61, 62

Diglyme Diethylene Glycol Dimethyl Ether. 69, 70

DLS Dynamic Light Scattering. 105

EDX Energy Dispersive X-Ray. xv, xvii, 72, 112, 113

EIS Electrochemical Impedance Spectroscopy. iii, 46, 70, 76, 78, 106, 124, 125, 129

FEC Fluoroethylene Carbonate. 28

GCD Galvanostatic Charge-Discharge. iii, xiii, xvi, 39, 76–79, 96, 97, 99, 100, 106, 121, 122, 129

GITT Galvanostatic Intermittent Titration Technique. xiv, xv, xvii, 51, 56, 95, 96, 106

HCS Hollow Carbon Spheres. xiv, 44–46

HRTEM High-Resolution Transmission Electron Microscopy. xiii, xv, xvii, 14, 24, 30, 31, 56, 57, 71, 72, 93, 95, 112, 113, 128

HsGDY hydrogen-Substituted Graphdiyne. 52

LDCFF Liquid-Driven Coaxial Flow Focusing. 35

LIB Lithium-Ion Battery. xvii, 1–3, 15, 16, 21, 22, 63, 87, 98, 99, 109, 130, 133

LMB lithium-Metal Battery. 2, 7, 48

MIB Magnesium-Ion Battery. iv, xv, xvii, xviii, xxi, 2–4, 8, 9, 27, 35, 48, 49, 51, 60, 61, 86–88, 92, 95–100, 102, 104, 106, 108–110, 118–121, 126, 128, 131, 134

MLIB Magnesium/Lithium-Ion Battery. iv, xv, xvii, xviii, xxi, 3, 4, 27, 60, 61, 86, 87, 89, 98–103, 106, 108–111, 118–126, 129, 131

NMP N-Methyl-2-Pyrrolidone. 68, 70, 104, 105, 127, 128

OAm Oleylamine. 44

PEO Polyethylene Oxide. xii, xiv, 23–25, 49–51, 88

PhMgCl Phenylmagnesium Chloride. 104, 106, 127, 129

PIB Potassium-Ion Battery. xxi, 1, 7, 8, 13, 14, 36–39, 41, 47–49, 63

PVDF Poly(vinylidene fluoride). 68, 70, 104, 105, 127, 128

PVP Polyvinylpyrrolidone. xiv, 23, 42, 43, 45–47, 49, 50

R_{ct} Charge-Transfer Resistance. 36, 79, 103, 124, 125

rGO Reduced Graphene Oxide. xiii, xiv, 11, 12, 17, 30, 31, 34, 37, 38, 44–46, 56, 57, 59

SAED Selected-Area Electron Diffraction. 72

SEI Solid Electrolyte Interphase. 28, 76, 78, 79, 97, 99

SHE Standard Hydrogen Electrode. 1, 2, 7, 48, 53, 67, 87

SIB Sodium-Ion Battery. iii, xiii, xiv, xxi, 1, 3, 7, 8, 13, 14, 20, 28–32, 34, 36–45, 47–49, 63, 67, 68, 76, 78, 84, 131

STEM Scanning Transmission Electron Microscopy. xi, 17, 18, 128

TEM Transmission Electron Microscopy. iii, xii–xv, xvii, 25, 34, 41–47, 53, 70–72, 93, 95, 96, 105, 112, 113, 128

TGA Thermogravimetric Analysis. iii, xvi, 70, 74, 75, 90, 91, 105, 113, 128

THF Tetrahydrofuran. xvi, 4, 51, 86, 88–92, 96, 99, 103–106, 127, 129

TMD Transition Metal Dichalcogenide. xi, 6, 9–11, 133

XPS X-Ray Photoelectron Spectroscopy. iii, xi, xiii, xvi, xviii, 17–19, 29, 30, 33, 70, 72–75, 80, 92–94, 97, 105, 115–117, 128

XRD X-Ray Diffraction. iii, xii, xvi, xviii, 14, 24, 25, 33, 69, 73–76, 92, 94–96, 102, 105, 112, 114–116, 123, 128, 133

ZIB Zinc-Ion Battery. 2, 8, 9, 36, 53, 62

Chapter 1

Introduction

Conventional lithium-ion batteries (LIBs) are approaching their theoritical energy density ceiling of 350 Wh kg^{-1}, falling short of the high energy density demands of emerging technologies.[1,2] Additionally, a major concern with lithium-based batteries is the limited availability of lithium and other essential elements used in their manufacture. Lithium is relatively scarce in the Earth's crust and unevenly distributed globally. To overcome these challenges, extensive research is focused on developing new battery materials and designing innovative alternative energy storage systems.[3]

Elements like sodium and potassium are much more abundant and globally accessible compared to lithium. Moreover, zinc, magnesium, and aluminum are found in significantly greater quantities than lithium, with magnesium and aluminum being particularly plentiful. Their abundance suggests that batteries based on these elements could potentially lower material costs. As a result, shifting towards more abundant elements can reduce costs and broaden the application of energy storage technologies.[3]

Recently, sodium-ion batteries (SIBs) and potassium-ion batteries (PIBs) have gained significant interest due to their lower costs and favorable standard reduction potentials (Na: -2.71 V and K: -2.93 V vs. standard hydrogen electrode [SHE]). This makes them promising candidates for next-generation energy storage solutions, offering a viable alternative to LIBs for efficient electrical energy storage.[4–7] However, SIBs and PIBs face challenges in practical use, particularly due to the larger size of Na^+ and K^+ ions compared to Li^+ (1.02 Åand 1.38 Å, respectively, versus 0.76 Å). This size difference can lead to significant volume expansion and the breakdown of active materials during ion insertion and extraction processes. Therefore, there is a critical need to develop robust anode materials that can effectively store ions and maintain stability through repeated charge and discharge cycles for these types of

batteries.[8,9]

Alongside the exploration of alternatives to LIBs, there is a concerted effort to improve the capacity of lithium batteries through the development of lithium-metal batteries (LMBs), which utilize lithium metal as the anode. LMBs are considered promising contenders against traditional LIBs due to the exceptionally high theoretical specific capacity of the lithium metal anode (3,860 mAh g^{-1}) and its low redox potential (-3.040 V vs. SHE). However, the use of lithium metal anodes is accompanied with significant safety risks. These risks stem from the formation of dendrites on the surface of lithium metal during the electro-adsorption process of Li^+ ions, which can lead to severe battery failure and shorted circuits.[10,11] To mitigate these issues, alternatives to lithium metal anodes are being explored, including magnesium, zinc, and aluminum. These elements are more chemically stable and more abundant than lithium, making them attractive for use in magnesium-ion batteries (MIBs), zinc-ion batteries (ZIBs), and aluminum-ion batteries (AIBs), respectively.[12,13] For example, magnesium anodes exhibit limited dendrite formation, potentially offering a safer option compared to lithium metal anodes. Furthermore, multivalent metal anodes such as magnesium, zinc, and aluminum provide higher volumetric energy densities than lithium metal anodes, despite their lower gravimetric energy densities. Nonetheless, multivalent ion batteries face challenges related to the high polarization of multivalent ions, which result in strong interactions with the cathode material. These interactions lead to slow solid-state diffusion kinetics, ultimately reducing the reversible storage capacity and compromising the rate performance of the batteries. Therefore, a key challenge for multivalent ion batteries is the identification of suitable cathode materials that can effectively manage these interactions while delivering adequate electrochemical performance.[14–17]

Molybdenum disulfide (MoS_2), a layered material and 2-dimensional (2D) material known for its promising electrochemical properties and larger interlayer spacing compared to graphite, has emerged as a potential anode material for accommodating large ions like Na^+ and K^+. Despite its advantages, MoS_2 faces significant obstacles in electrochemical applications, including substantial volume changes that can cause pulverization, and its inherently low electronic conductivity.[18–21] Conversely, MoS_2 also shows potential as a cathode material for MIBs, ZIBs, and AIBs batteries. However, it encounters substantial challenges in these roles as well, primarily due to the sluggish kinetics associated with the storage of multivalent ions. Also, semiconducting nature of MoS_2, leading to low electrical conductivity, is another obstacle for its application as active material for batteries.[16,22–24]

This thesis overviews the structure and characteristics of MoS_2, followed by a thorough

discussion of its challenges as an active material in post-LIBs. Various strategies from the literature for improving MoS_2-based materials for use in post-LIBs have been summerized. To enhance the performance of MoS_2 nanocomposites as active materials in post-LIBs, several research projects have been undertaken in this thesis.

The objectives of these projects are as follows:

- Synthesis of MoS_2 embedded in a carbonaceous matrix to form a nanocomposite with enhanced electrical conductivity, mechanical robustness, and increased electrolyte-electrode interface area. The goal is to develop a high-capacity, stable anode for SIBs.
- Synthesis of amorphous MoS_x ($x > 2$) embedded in a carbon matrix to explore the electrochemical properties of this composite as a SIB anode and compare its performance with its crystalline counterpart containing crystalline MoS_2 nanosheets
- Enhancing Mg^{2+} storage in MoS_2 by synthesizing MoS_2 modified with a hyperbranched polyethylene ionomer containing quaternary ammonium ions, using a top-down approach. This modification is aimed at developing a magnesium battery cathode.
- Fabrication of dual-salt magnesium/lithium-ion batteries (MLIBs) using ionomer-modified MoS_2 as the cathode, and investigating the electrochemical properties of these dual-salt batteries.
- Bottom-up synthesis of a nanocomposite of MoS_2 and MXene to achieve a 2D/2D nanocomposite with enhanced conductivity and a unique structure. This composite will be used as a cathode for MLIBs.

In these projects, sodium-ion batteries serve as prototypes for batteries containing ions larger than lithium, while Mg^{2+} in MIBs and MLIBs represents multivalent ions. Therefore, the methods developed in this thesis can be potentially adapted for the storage of other ions, such as K^+, Zn^{2+}, and Al^{3+}.

The outline of this thesis is as follows:

Chapter 1 introduces post-LIBs, explaining their necessity, development challenges, and obstacles. It highlights MoS_2 as a promising active material for ion storage in post-LIBs, discusses the challenges associated with MoS_2-based battery materials, and outlines the objectives of this thesis.

Chapter 2 reviews the synthesis and design strategies for MoS_2-based electrode materials discussed in the literature for post-LIBs, which overcome the challenges posed by

large Na^+ and K^+ ions, as well as multivalent Zn^{2+}, Mg^{2+}, and Al^{3+} ions in rechargeable batteries. The strategies include interlayer engineering, defect engineering, crystal phase (1T/2H) engineering, heteroatom doping, hybridization, and morphology design. By analyzing previous theoretical and experimental studies, it summarizes how these strategies enhance the electrochemical performance of MoS_2-based materials, including their capacity, kinetics, reversibility, and stability in post-lithium-ion energy storage.

Chapter 3 reports a straightforward, cost-effective, and scalable method developed for the synthesis of nanocomposites, including both amorphous molybdenum sulfide (a-MoS_x) and crystalline MoS_2, each combined with hierarchical porous carbon, along with their performance in sodium ion storage.

Chapter 4 reports the synthesis of a 1T/2H mixed-phase MoS_2 (MP-MoS_2), modified with a hyperbranched polyethylene ionomer (I@MP-MoS_2) for high-performance Mg^{2+} storage. The synthesis method enhances conductivity, widens van der Waals gaps, and improves interactions with Tetrahydrofuran (THF)-based electrolytes. I@MP-MoS_2 shows significantly enhanced Mg^{2+} storage capability as a cathode in MIBs, compared to its unmodified form. Additionally, the chapter also explores the performance of I@MP-MoS_2 as a cathode for dual-salt MLIBs, highlighting impressive specific capacities achieved through a Mg^{2+}/Li^+ co-intercalation mechanism, along with excellent cycling stability.

Chapter 5 reports a novel cathode configuration for MLIBs, utilizing a 2D/2D nanocomposite of 1T/2H mixed-phase MoS_2 and delaminated $Ti_3C_2T_x$ MXene (1T/2H-MoS_2@MXene) to address the challenges associated with slow Mg^{2+} kinetics during cathode interactions. This cathode design leverages the high electrical conductivity of $Ti_3C_2T_x$ MXene and the expanded interlayer spacing, along with the enhanced conductivity of the 1T metallic phase in 1T/2H mixed-phase MoS_2. The nanocomposite has been systematically characterized and investigated for its electrochemical performance.

Chapter 6 discusses the significance of the research conducted in this thesis, highlighting the key contributions to the existing body of knowledge in the field. It provides an overview of the novel insights, methodologies, and findings generated throughout the study. Additionally, the chapter explores the thesis's potential to influence and shape future research directions within the field.

Chapter 2

Literature Review

Adapted from article:

Advanced MoS_2 Nanocomposites for Post-Lithium-Ion Batteries

Jalal Rahmatinejad, Zhibin Ye

Published in: ***Chemical Engineering Journal***

https://doi.org/10.1016/j.cej.2024.156872

Abstract The pursuit of advanced energy storage systems beyond lithium-ion batteries has intensified, driving the exploration of alternative electrode materials. Molybdenum disulfide (MoS_2) and its nanocomposites have emerged as promising active material candidates due to their unique structural characteristics and electrochemical properties. In this review, we provide a comprehensive overview of synthesis and design strategies of MoS_2-based electrode materials tailored to address the challenges posed on rechargeable batteries by large Na^+ and K^+ ions, as well as the multivalent nature of Zn^{2+}, Mg^{2+}, and Al^{3+} ions. We review various structural design/modification strategies, such as interlayer engineering, defect engineering, crystal phase (1T/2H) engineering, heteroatom doping, hybridization, and morphology design. Through an examination of previous theoretical and experimental research, we summarize their impacts on enhancing the electrochemical performance of MoS_2-based active materials, aiming to improve their capacity, kinetics, reversibility, and stability in post-lithium-ion storage. By compiling numerous research findings, this review offers insights into the rational design principles that guide the development of high-performance layered active materials for next-generation energy storage devices. With MoS_2 as a prototype transition metal dichalcogenide (TMD), these principles are applicable to other layered battery materials, contributing to the advancement of sustainable and efficient electrochemical energy storage technologies.

2.1 Introduction

Lithium-ion batteries (LIBs) with graphite anode (with theoretical gravimetric and volumetric capacity of 372 mAh g^{-1} and 735 mAh cm^{-3}, respectively) are approaching their theoretical specific energy density limit of 350 Wh kg^{-1}, yet they still fall short of delivering the elevated energy density necessary for deployment in emerging technologies.[1,2] Another pivotal concern about lithium-based batteries revolves around the abundance of elements required for battery components. As illustrated in Figure 2.1, lithium abundance in the Earth's crust is notably low (Figure 2.1), with resources unevenly distributed worldwide.[3] These limitations (both in terms of energy density and material scarcity) have prompted a growing interest in exploring alternative energy storage systems. Researchers are actively seeking solutions that not only enhance performance metrics such as cost-efficiency, energy density, and safety but also utilize more abundant and widely distributed elements. This shift has brought attention to SIBs and PIBs as promising alternatives. Sodium and potassium, unlike lithium, are among the most abundant elements on Earth, and their widespread availability is a significant factor in reducing material costs (Figure 2.1).[3] In addition, sodium and potassium possess favorable standard reduction potential [Na: -2.71 V and K: -2.93 V vs. SHE]. This transition toward more readily available elements shows potential for reducing expenses and expanding the reach of energy storage technologies. This positions SIBs and PIBs as promising contenders for next-generation energy storage devices. Consequently, they are regarded as feasible substitutes for LIBs, capable of meeting the growing need for effective electrical energy storage systems in emerging technologies.[4–7] Despite the numerous advantages of SIBs and PIBs, their practical implementation, nevertheless, still encounters challenges. The larger size of Na^+ and K^+ ions compared to Li^+ ions (Figure 2.1; 1.02 Å and 1.38 Å vs. 0.76 Å, respectively) often causes drastic volume expansion and the pulverization of active materials during the ion insertion/extraction process.[8,9] Therefore, there is a pressing need for designing and synthesizing durable anode materials for these batteries that can efficiently store ions and maintain stability throughout continuous charge/discharge cycles.

In addition to research focused on alternative batteries to LIBs, parallel efforts are underway to enhance the capacity of lithium batteries through the development of LMBs benefiting from lithium metal as their anode.[1] LMBs are widely acknowledged as ta promising contender among alternative of LIBs due to the high theoretical specific capacity (3,860 mAh g^{-1} and 2060 mAh cm^{-3}) and very low redox potential (-3.040 V vs. SHE) of their lithium metal anode. But, utilizing lithium metal anode presents significant safety concerns.[30,31]

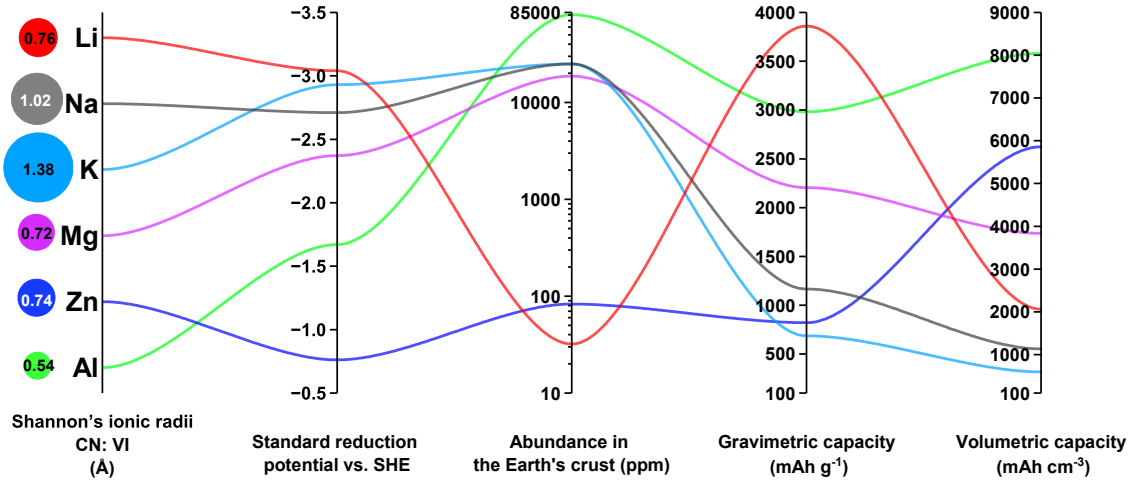

Figure 2.1: Shannon's ionic radii,[25] standard reduction potential,[4–7,26–29] abundance in the Earth's crust,[3] and gravimetric and volumetric capacities of Li, Na, K, Mg, Zn, and Al.[12,27–32]

These concerns arise from the formation of dendrites on the lithium metal surface during the reduction of Li^+ via the electro-adsorption process, which can result in catastrophic battery failure, short-circuiting, and even fires.[10,11] Potential alternatives to lithium metal anodes, such as magnesium, zinc, and aluminum, are being investigated due to their chemical stability and greater abundance compared to lithium, for MIBs, zinc-ion ZIBs, and AIBs, respectively. Some of these alternatives, like Mg anodes, show restricted dendrite formation, potentially enhancing safety compared to lithium metal anodes. Meanwhile, what is particularly noteworthy is the higher volumetric energy densities offered by multivalent metal anodes compared to lithium metal anode, despite somewhat lower gravimetric energy densities due to the higher atomic weights of multivalent metals (Figure 2.1).[12,13] However, the small size and highly polarizing characteristics of multivalent ions create strong interactions with the cathode material, which results in slow solid-state diffusion kinetics. This issue ultimately reduces the reversible storage capacity and hinders rate performance.[14] Consequently, multivalent ion batteries face ongoing challenges in identifying appropriate cathode materials that can alleviate these interactions while maintaining acceptable electrochemical performance.[15–17]

MoS_2, a layered material with favorable electrochemical performance and a larger interlayer distance compared to graphite. Unlike graphite, which struggles with the accommodation of larger ions like Na^+ and K^+ due to the smaller interlayer spacing, MoS_2's structure, bound by weak van der Waals forces, provides more sufficient space for ion transport, making it particularly suitable for SIBs and PIBs. Additionally, MoS_2 offers a higher theoretical

capacity for ion storage, particularly 670 mAh g^{-1} for Na^+ and K^+, compared to graphite's much lower capacity, positioning MoS_2 as a stronger candidate for batteries that require high energy density. However, in such electrochemical systems, it faces challenges such as significant volume changes leading to pulverization, as well as its inherently low electronic conductivity.[18–21] MoS_2 has also shown promise as a cathode material for multivalent-ion batteries (MIBs, ZIBs, and AIBs), demonstrating potential for storing Mg^{2+}, Zn^{2+}, and Al^{2+}. Its layered structure provides accessible sites for ion intercalation, and its tunable chemical properties make it adaptable for enhancing ion transport. However, MoS_2 faces significant challenges related to sluggish kinetics during the storage of multivalent ions. The sluggishness primarily arises from the strong interactions between these multivalent ions and the MoS_2 lattice, which create higher energy barriers for ion diffusion. Additionally, the larger charge density of multivalent ions leads to more pronounced electrostatic interactions, which can further hinder the smooth insertion and extraction of ions during cycling, resulting in slow reaction kinetics and lower rate performance. Overcoming these kinetic barriers is crucial for optimizing MoS_2 as an efficient electrode material for multivalent-ion batteries.[16,22–24]

In this comprehensive review, we delve to summarize recent advancements in the synthesis of MoS_2 and its nanocomposites as electrode materials in rechargeable batteries, with a particular focus on addressing the challenges associated with ion storage in post-LIBs. By thorough examining a wide range of recent articles, we aim to shed light on innovative strategies that enhance the electrical conductivity, kinetics, reversibility of ion storage, and cyclic stability of MoS_2-based materials. Additionally, we also overview theoretical research efforts that elucidate the underlying mechanisms driving these improvements. Through this holistic approach, we strive to offer valuable insights that can pave the way for the design and development of cutting-edge 2D materials tailored for next-generation electrical energy storage technologies.

2.2 MoS_2: Structure, Polymorphism, and Synthesis Methods

MoS_2 belongs to an inorganic material family called transition metal dichalcogenides (TMDs). The general formula for TMDs is MX_2, where M signifies a transition metal, and X denotes a chalcogen (elements in group 16 of the periodic table). TMDs featuring

transition metals from groups 4 to 7 predominantly adopt a layered structure, whereas certain TMDs containing elements from groups 8 to 10 exhibit a non-layered configuration.[33] MoS_2 is a 2D compound composed of molybdenum and sulfur atoms. Each layer of it consists of a metal plane (molybdenum) sandwiched between two planes of chalcogen atoms (sulfur). Each metal center forms covalent bonds with six chalcogens, and the layers are stacked to each other through weak van der Waals forces. The interlayer distance in bulk MoS_2 is approximately 0.62 nm (Figure 2.2a).[33] With its unique properties, MoS_2 finds applications in diverse areas such as energy storage, electrocatalysis, photocatalysis, lubrication, solar cells, electronics, heavy metal adsorption, as well as sensors.[34,35] The characteristics of MoS_2 are heavily influenced by the number of layers and crystal phase. Consequently, these factors play a crucial role in defining the appropriateness of this material for various applications.

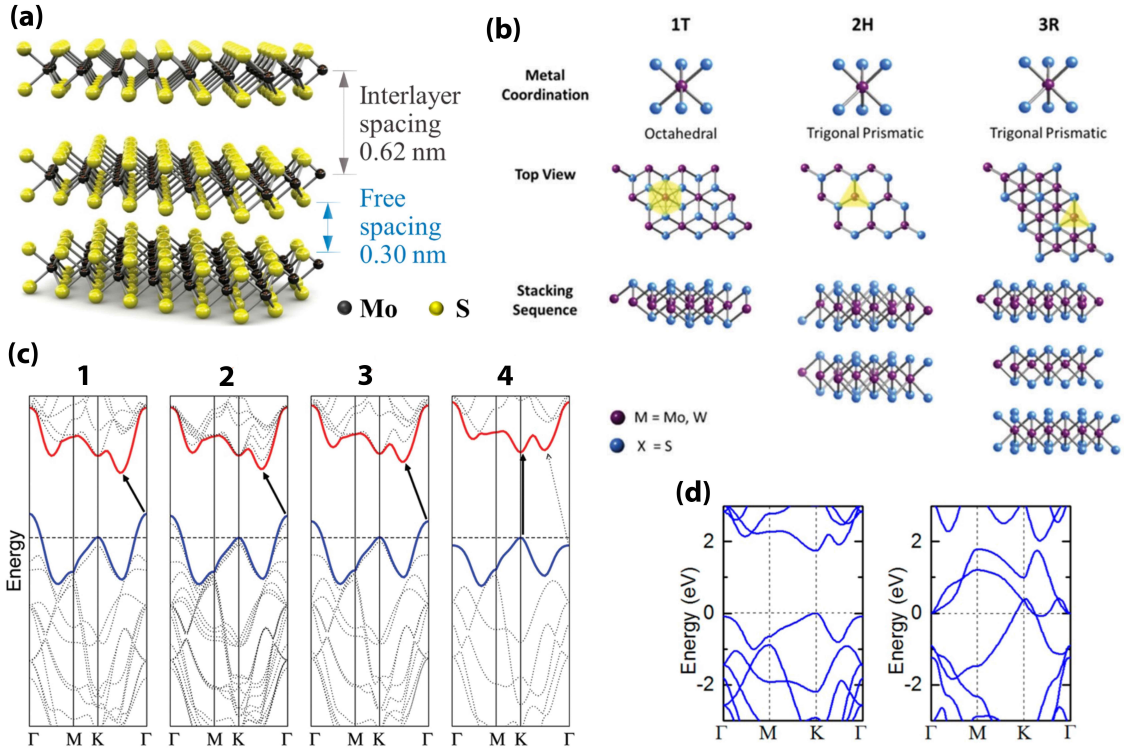

Figure 2.2: (a) Schematic illustration of the layered structure of MoS_2.[35] (b) Different metal coordinations and stacking sequences in TMDs.[36] (c) Computed band diagrams for (1) bulk, (2) quadrilayer, (3) bilayer, and (4) monolayer MoS_2, where the red and blue lines represent the conduction and valence band edges, respectively, and the solid arrows highlight transitions associated with the lowest energy levels.[37] (d) Comparison of 2H (left) and 1T (right) MoS_2 band structures.[38]

2.2.1 MoS_2 Polymorphism

The coordination of metals in TMDs can manifest in either trigonal prismatic or octahedral (also known as trigonal-antiprismatic) configurations. These materials, influenced by the occupation of the metal's d orbital, typically demonstrate three phases of 1T, 2H, and 3R, which are known as polymorphism (Figure 2.2b). Here, 'T', 'H', and 'R' correspond to trigonal, hexagonal, and rhombohedral symmetries, respectively. The numerical indicators 1, 2, and 3 represent the number of layers per crystallographic unit cell. In the 2H and 3R phases, the metal coordination adopts a trigonal prismatic configuration, while takes on an octahedral arrangement in the 1T phase.[36,39] Natural MoS_2 primarily exists in the 2H phase, which is the most thermodynamically stable form. In contrast, synthetic MoS_2, influenced by its formation history, may encompass 3R and 1T phases.[33] Mono- or few-layered 2D TMDs offer distinct characteristics compared to their bulk counterparts. For example, the bulk 2H-MoS_2 exhibits semiconductor properties with an indirect bandgap of 1.29 eV. However, as the number of layers decreases, the bandgap increases. In the case of its monolayer form, the bandgap becomes direct and measures 1.9 eV (refer to Figure 2.2c).[34,37,40] Particularly, 1T-MoS_2 exhibits metallic characteristics (Figure 2.2d), and its monolayer demonstrates electrical conductivity that is 10^7 times greater than that of monolayers of 2H-MoS_2. This notable electrical conductivity, ranging from 10 to 100 S cm^{-1}, approaches the conductivity levels observed in the most conductive reduced graphene oxide (RGO) nanosheets (100 S cm^{-1}).[41]

2.2.2 Synthesis Methods of MoS_2 Nanostructures

Layered TMDs like MoS_2 can be synthesized using either top-down or bottom-up techniques. In the top-down approach, mono- or few-layered TMDs are obtained by exfoliating them from their parent bulk materials. Mechanical exfoliation, such as the Scotch tape technique, and liquid-phase exfoliation via ultrasonication or ion intercalation, are common top-down approaches.[42] The Scotch tape method yields high-quality monolayers, ideal for electronic applications or fundamental experiments. However, the Scotch tape method is less suitable for large-scale production.[33] Liquid-phase exfoliation allows the large-scale production of few-layered TMDs. Coleman et al. presented a straightforward method for preparing few-layer 2D materials, creating a dispersion in common solvents through ultrasonication, and subsequently using centrifugation to separate unexfoliated materials.[43] This technique is applicable to a diverse range of 2D materials, including TMDs like MoS_2 and WS_2, and

facilitates the production of free-standing films through further vacuum filtration. Additionally, exfoliated layers via sonication can be stabilized against aggregation by adding polymers to the solvent, which induces steric repulsion.[44] Sonication-assisted exfoliation extends to water-based methods, where nanosheets are stabilized by electrostatic repulsions of surfactants like sodium cholate.[45] An alternative liquid-phase exfoliation method involves alkali ion intercalation followed by the subsequent hydration of ion-intercalated nanosheets. For instance, bulk materials can undergo treatment with lithium-containing substances and subsequent exposure to water. During the lithiation process, lithium ions insert into interlayer spaces. Subsequently, through the reaction between water and lithium, the generation of hydrogen gas occurs, effectively pushing the layers apart.[41,46] This method induces the phase transition (from 2H to 1T) and enables the production of 1T-rich MoS_2 due to the electron-donating nature of alkali metals, facilitating electron transfer to the d orbital of the metal center.[47]

In the bottom-up approach, nanostructures are crafted from atoms or molecular building blocks through chemical reactions.[42] Various bottom-up approaches, including hydrothermal/solvothermal,[48–50] chemical vapor deposition (CVD),[51] electrodeposition,[52] etc., have been utilized to prepare MoS_2. The solvothermal/hydrothermal methods stand out as the most efficient approach for large-scale MoS_2 synthesis. These methods, dependent on the chosen precursors and synthesis conditions, yield diverse nanostructures with varying morphologies. The solvothermal/hydrothermal methods provide a versatile route, especially when hybridization of MoS_2 with other materials is essential. For example, when product conductivity is a crucial criterion, the methods enable the fabrication of vertically aligned MoS_2 on a highly conductive substrate, such as RGO.[53] Ammonium heptamolybdate ($(NH_4)_6Mo_7O_{24}$), sodium molybdate (Na_2MoO_4), and molybdenum trioxide (MoO_3) are the most commonly used sources of Mo, while thiourea (NH_2CSNH_2), thioacetamide (C_2H_5NS), and L-cysteine ($C_3H_7NO_2S$) are commonly utilized as sources of sulfur in hydrothermal and solvothermal synthesis of MoS_2. Ammonium thiomolybdate ($(NH_4)_2MoS_4$) is another widely used compound that serves as a source of both Mo and S, capable of decomposing into MoS_2 during hydrothermal and solvothermal reactions.[34]

2.3 Challenges of MoS_2-Based Electrode Materials

Bulk MoS_2 suffers from poor electronic conductivity and sluggish ion diffusion kinetics, leading to limited rate capability and poor cycling stability. During the insertion/extraction

of ions, the low conductivity of MoS_2 may result in high charge-transfer resistance, compromising the battery's performance.[18,54] The kinetic challenges associated with MoS_2 in ion storage become even more significant for multivalent ion storage due to their inherently polarizing characteristics. These characteristics foster strong interactions between the multivalent ions and the negatively charged host lattice, hindering ion movement within the cathode material. Moreover, the intense Coulombic forces between ions further worsen this sluggishness, leading to elevated energy barriers for intercalation and diminished diffusion coefficients.[15,16,22,23]

MoS_2 also experiences significant volume changes upon ion insertion/extraction. This mechanical stress can lead to pulverization, loss of electrical contact, and eventual structural collapse and capacity degradation.[18–21,55,56] Wang et al. conducted a comprehensive investigation into the structural alterations of MoS_2 induced by the storage of alkali ions, including Li^+, Na^+, and K^+, employing various experimental and theoretical methodologies. Their findings reveal distinct stages in the storage process, where the maximum volume expansion is approximately 4%, 27%, and 37% for Li-, Na-, and K-intercalated MoS_2, respectively (Figure 2.3). These results underscore the significant impact of volume expansion, particularly concerning the storage of Na^+ and K^+ in MoS_2, emphasizing the necessity to address its adverse effects.[57] Addressing this issue requires structural design strategies, such as the incorporation of buffer layers, to accommodate the volume changes.

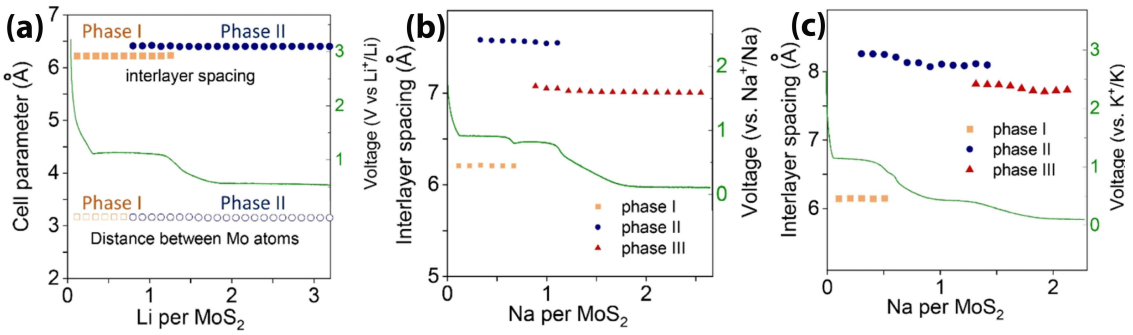

Figure 2.3: Interlayer spacing during insertion of (a) Li^+, (b) Na^+, and (c) K^+ into the MoS_2 at different stages.[57]

Another contributing factor to the diminished cycling stability of MoS_2 anodes in SIBs and PIBs stems from the conversion reactions.[58,59] The alkali ion storage mechanism in MoS_2 involves two main steps: intercalation ($MoS_2 + nI^+ + ne^- \longrightarrow I_nMoS_2$) and conversion reactions ($I_nMoS_2 + (4-n)I^+ + (4-n)e^- \longrightarrow Mo + 2I_2S$), resulting in the generation of Mo nanograins and alkali ion sulfide.[54,60,61] Conversion reactions have been observed to occur below ≈0.80 V vs. Li/Li^+ in LIBs,[60] below ≈0.40 V vs. Na/Na^+ in SIBs,[62] and

below ≈0.55 V vs. K/K^+ in PIBs.[54] In voltage ranges higher than these thresholds, visible peaks in cyclic voltammetry (CV) curves are attributed to the intercalation/deintercalation of ions into MoS_2, as well as phase transformations from 2H to 1T induced by the interaction between ions and MoS_2. Taking Li^+ storage in MoS_2 as an illustration, based on the aforementioned mechanisms, the theoretical capacity of MoS_2 is calculated to be 669.6 mAh g^{-1} ($4Li + MoS_2 \longrightarrow 2Li_2S + Mo$). Some studies propose that conversion reactions are irreversible. Following these conversion reactions, the mechanism of Li^+ storage resembles that of lithium-sulfur (Li-S) batteries ($Li_2S \longleftrightarrow S + 2Li^+ + 2e^-$).[63] According to this proposition, these subsequent reactions are believed to be the reason why numerous experimental studies have reported capacity of MoS_2 in LIBs higher than its theoretical capacity (in some cases two times higher). Accordingly, the oxidation of Li_2S to S and Li^+ is responsible for the limited conversion of Mo/Li_2S back to MoS_2 during Li^+ extraction.[64] As a result, although the conversion reaction plays a vital role in achieving substantial storage capacity, questions persist regarding its reversibility. Even under the assumption of complete reversibility of the conversion reactions, the process itself can compromise the integrity of the active material, potentially leading to instability. It is widely recognized that the conversion reaction substantially contributes to instability during the battery's cycling due to the substantial volume changes experienced upon charging and discharging. These changes lead to microstructure collapse and active material pulverization, ultimately hindering the capacity and cycling stability of the electrode materials.[65] For Na^+ storage in MoS_2, similar disagreements have arisen, but robust research has demonstrated the reversibility of the conversion reaction and the regeneration of MoS_2. Evidence supporting this includes high-resolution transmission electron microscopy (HRTEM), X-ray diffraction (XRD), and first-principles calculated formation energy.[61,66,67] These studies provide compelling evidence for the reversible nature of the conversion reaction and the ability to regenerate MoS_2, as evidenced by the discharge products ($Mo + Na_2S$) being oxidized back to MoS_2. However, even though the conversion reactions in such systems are reversible, the shuttling of conversion reaction products, in the absence of a matrix to trap them and improve the dynamics of reversible reactions, leads to active material loss and reduced stability.[68,69] This is supported by experimental research comparing the cycling of SIB half cells with MoS_2-based anodes at two different potential windows, approximately 0.01-3 V and 0.4-3 V (the region where conversion reactions do not occur), demonstrates significantly improved cycling stability with the latter potential window. This finding underscores the adverse impact of conversion reactions

on cycling stability and highlights the importance of the selection of proper operating potential window to minimize such reactions.[62,70] In such studies, high cycling stability has been reported, but often accompanied with sacrificed capacity.[71] One crucial aspect to consider in the design of MoS_2-based active material for Na^+/K^+ ion batteries is the incorporation of a substance that can enhance the integrity of the composites, mitigate volume changes during ion insertion/extraction, and prevent collapse during conversion reactions.

To address these challenges, numerous strategies have been developed in the literature to improve the electrochemical performances of MoS_2 as an active electrode material for post-LIBs. These strategies are outlined in the following sections.

2.4 Performance Enhancement Strategies

2.4.1 Electronic Conductivity Enhancement

The semiconducting nature of MoS_2 poses a significant challenge for its application in energy storage. This limitation leads to increased resistance and slower electron/ion mobility, which can impede the performance of energy storage devices such as batteries and capacitors. Overcoming these challenges requires innovative strategies to enhance the conductivity and optimize the electronic properties of MoS_2-based materials for improved energy storage performance.

Hybridizing with Conductive Agents

Hybridizing MoS_2 materials with carbonaceous counterparts presents an efficient solution to enhance electrical conductivity, structural integrity, and ion diffusion kinetics. A significant body of research on MoS_2 active material for post-LIBs focuses on its nanocomposites with various carbonaceous materials such as graphene,[72–75] carbon nanotubes,[56] graphdiyne,[76,77] and amorphous carbon.[67,78] The hybridization process can involve nanoscale mixing, such as the exfoliation of graphene and MoS_2 followed by thorough blending.[18] Alternatively, by synthesizing MoS_2 nanosheets (mostly by hydrothermal/solvothermal method) in the presence of carbonaceous materials diverse morphologies, like MoS_2/graphene 2D/2D heterointerface, vertically aligned MoS_2 on graphene,[53] or few-layer MoS_2 embedded in amorphous carbon matrices[68] can be obtained. Carbon content can be directly added into the synthesis reactor, such as hydrothermal synthesis of MoS_2 in the presence of graphene/graphene oxide,[73] carbon nanotubes,[79] carbon paper,[80] carbon cloth,[81] etc.

Alternative carbon sources, like dopamine hydrochloride,[82] surfactants,[83] polymers,[84,85] carbohydrates,[78] etc., can also be utilized, which can be carbonized during synthesis and subsequent annealing processes.

As an example demonstrating the effect of the carbon materials on conductivity of MoS_2, Figure 2.4 illustrates the band structure of MoS_2 monolayers and two different MoS_2/graphene heterointerface configurations of MC (Mo on top of C atoms, Figure 2.4a) and SC (S on top of C atoms, Figure 2.4a) calculated by Xie et al.[73] The pristine monolayer MoS_2 exhibits a direct band gap of ≈1.8 eV at the K-point (Figure 2.4b). Notably, both configurations of the MoS_2/graphene heterointerface display a near-zero band gap and exhibit conductive behavior akin to pristine graphene at the Dirac K-point (Figure 2.4c,d).

In addition to carbon-based materials, various other conductivity enhancers have been utilized in hybridizing with MoS_2 to enhance its performance in post-LIBs. These include different types of MXene[86–88] as well as conductive polymers such as polyaniline[89,90] and polypyrrole[91,92] among others. These hybrid materials have demonstrated improved conductivity, leading to enhanced battery performance.

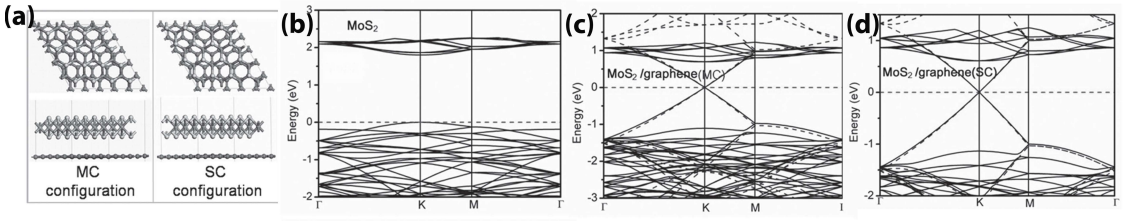

Figure 2.4: (a) Two possible configurations MoS_2/graphene and the band structures of (b) monolayer MoS_2, (c) MC-MoS_2/graphene, and (d) SC-MoS_2/graphene.[73]

Crystal Phase Engineering

In recent years, extensive research has been undertaken to synthesize products based on MoS_2 containing 1T phase, aiming to leverage electronic conductivity for storing electrical energy in diverse devices such as supercapacitors and batteries. However, the synthesis methods employed to produce these 1T phase-containing products often induce structural changes in MoS_2, such as alterations in crystallinity or interlayer distances. This makes it challenging to understand the exclusive impact of the 1T phase alone. For example, Acerce et al.[41] utilized alkali metal intercalation method (using n-butyllithium) to exfoliate bulk MoS_2 into monolayer nanosheets of MoS_2 with 70% of 1T phase. This resulted in a substantial enhancement of almost 20 times higher specific gravimetric capacitance compared

to its bulk counterpart. Nevertheless, it is crucial to acknowledge that the organolithium chemistry used for the exfoliation of bulk MoS_2 induces structural changes, suggesting that the observed improvement cannot be solely attributed to the presence of the 1T phase. In bottom-up approaches, where 1T-MoS_2 is synthesized, the process often involves the incorporation of other materials such as RGO or various types of carbon,[93,94] leading to the formation of unique structures with improved ion transport kinetics. Many studies highlighted the significant performance of these 1T-MoS_2 nanocomposites in storing challenging ions. However, given the multifaceted nature of such materials where performance is influenced by a number of factors (like enlarged interlayer spacing) it becomes challenging in experimental research to definitively attribute the efficacy solely to the presence of the 1T phase. Despite this, the elevated conductivity of the 1T phase compared to the semiconducting 2H phase (10^7 times higher conductivity[41]) is widely recognized, offering significantly improved conditions for this material as an active component in electrical energy storage devices. The enhanced ion storage performance of 1T phase compared to 2H phase has also been proved through theoretical research.[95–98]

Given the critical role of the crystal phase of MoS_2 in its performance in electrochemical systems, researchers in this field need to characterize and quantify the proportions of its crystalline phases. Various methods exist for discerning the 1T and 2H phases of MoS_2, with Raman spectroscopy, scanning transmission electron microscopy (STEM) image processing, and X-ray photoelectron spectroscopy (XPS) as the most convenient and commonly employed techniques. The Raman spectrum of 2H-MoS_2 shows two characteristic peaks of the in-plane ${E_{2g}}^1$ mode (results from the opposite vibration of two S atoms with respect to the Mo atom) at around 383 cm^{-1} and out-of-plane mode of around A_{1g} (associated with the out-of-plane vibration of only S atoms in opposite directions) at around 408 cm^{-1} (Figure 2.5a). It should be noted that the frequency of the pair of peaks depends on the number of the layers and wavelength of the laser used.[99] The Raman spectrum of 1T-MoS_2 is notably different from that of 2H-MoS_2. Its spectrum displays extra peaks of J_1, J_2, and J_3 associated with the superlattice structure of 1T-MoS_2 nanosheets. The E_{1g} band observed between 284 and 307 cm^{-1}, alongside a faint ${E_{2g}}^1$ band, verifies the predominant octahedral coordination of molybdenum in the 1T-MoS_2 (Figure 2.5c). By inducing a phase transition from 1T to 2H (via heat treatment, infrared laser, etc.), the Raman peaks corresponding to the 1T phase completely disappear, leaving only the 2H characteristic peaks of ${E_{2g}}^1$ and A_{1g} observable (Figure 2.5d).[100,101]

STEM can be used to identify the 1T and 2H phases of MoS_2 by examining their distinct

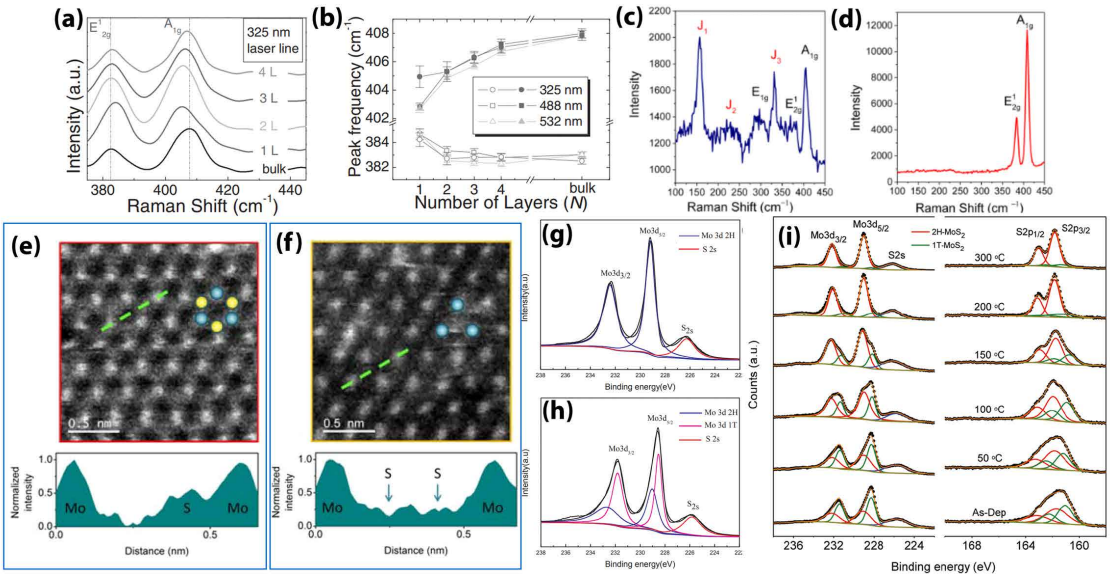

Figure 2.5: (a) Raman spectra of 2H-MoS_2 with different numbers of layers measured with a 325 nm wavelength laser. (b) The frequency of the 2H-MoS_2 Raman characteristic peaks vs. the number of layers measured by lasers with different wavelengths.[99] (c) Raman spectrum of 1T-MoS_2 obtained by the chemical exfoliation method and (d) its corresponding Raman spectrum after complete phase transition from 1T to 2H.[100] High-resolution STEM images and intensity profiles along the green lines of (e) 2H-MoS_2 and (f) 1T-MoS_2.[102] Mo 3d XPS spectra of (g) 2H-MoS_2 and (h) 1T-MoS_2.[103] (i) Mo 3d and S 2p XPS spectra of as-synthesized 1T/2H-MoS_2 and the changes in the spectra through 1T to 2H phase transition induced by heat treatment.[104]

atomic arrangements. STEM provides high-resolution images that reveal these structural differences enabling precise phase identification. In these images, a honeycomb lattice with minor intensity variation between two adjacent sites is characteristic of a single layer of 2H-MoS_2 (Figure 2.5e). In contrast, a hexagonal lattice pattern is indicative of 1T-MoS_2 (Figure 2.5f).[102] By comparing the intensity profiles of 2H-MoS_2 and 1T-MoS_2 in STEM images, one can distinguish the two phases based on the sulfur atom intensity. In the case of 2H-MoS_2, the signal from sulfur sites is intensified due to the alignment of two S atoms along the direction of the electron beam, resulting in contrast nearly equivalent to that of Mo (Figure 2.5e). Conversely, in a single layer of 1T-MoS_2, sulfur atoms are evenly distributed around the Mo sites, creating a pronounced contrast between the Mo and S sites (Figure 2.5f).[102,105]

While Raman spectroscopy and STEM are valuable for the qualitative analysis of 1T/2H phases in MoS_2, XPS stands out as a powerful tool for both qualitative and quantitative examination of the phase structure. Mo 3d spectrum for the 2H-MoS2 phase displays a single

doublet at around 229.5 and 232.5 eV, which correspond to Mo^{+4} $3d_{5/2}$ and Mo^{+4} $3d_{3/2}$, respectively (Figure 2.5g).[41] In contrast, mixed-phase 1T/2H-MoS_2 generally shows two doublets, with the second doublet arising from the 1T phase at lower binding energies (around 228.5 and 231.5 eV for Mo^{+4} $3d_{5/2}$ and Mo^{+4} $3d_{3/2}$, respectively), in addition to the doublet from the 2H phase (Figure 2.5h).[103,106,107] Similarly, in the S $2p$ XPS spectrum, another doublet also emerges for the mixed-phase 1T/2H MoS_2 at lower binding energies (Figure 2.5i). By peak deconvolution and calculations of the area under the curves corresponding to 2H and 1T phases, it is possible to measure the content of each phase. Accordingly, XPS is a reliable technique for confirming the presence of the 1T phase in a sample and provides an easy method to monitor its content over time and under various conditions. For instance, Figure 2.5i shows the gradual changes in the Mo $3d$ and S $2p$ spectra of 1T/2H-MoS_2 samples annealed at different temperatures, illustrating that the conversion from the 2H to the 1T phase increases at higher temperatures.[104] This quantitative analysis of the crystal phases of MoS_2 is highly valuable for research into its applications in energy storage.

2.4.2 Kinetics Enhancement

In general, enhancing electronic conductivity can augment ion diffusion in MoS_2 and elevate its performance in ion storage applications. Sun et al. employed density functional theory (DFT) to compute the diffusion barriers associated with Na atom mobility in MoS_2, utilizing the climbing image nudged elastic band method.[95] Focusing on both 2H and 1T-MoS_2 structures, their analysis primarily concentrated on the movement of a Na atom along the interlayer region between two adjacent MoS_2 layers. Figure 2.6a illustrates the diffusion pathway between neighboring low-energy octahedral sites and the corresponding energy barrier. They discovered that the diffusion barrier for 1T-MoS_2 is 0.23 eV, significantly lower than that of 2H-MoS_2, which is 0.98 eV, indicating greater Na mobility in the former. Accordingly, they found that the Na diffusion barrier in 1T-MoS_2 is comparable to that in cathode materials like layered $NaCoO_2$ (0.3 eV) and $NaMPO_4F$ (M = Fe, Mn, $Fe_{0.5}Mn_{0.5}$) (0.375 eV), and even smaller than the diffusion barrier of lithium atoms in graphite (0.4 eV).

Previous research findings[95–97,108,109] suggest that 1T-MoS_2 exhibits a lower multivalent ion diffusion energy barrier compared to semiconducting 2H-MoS_2. Liu et al. conducted a series of experimental and DFT studies, which uncovered that MoS_2 nanosheets with a substantial 1T phase content (≈70%) possess remarkable characteristics in rechargeable aqueous zinc-ion batteries (AZIBs), delivering a capacity of 168 mAh g^{-1} at 0.1 A g^{-1} and 98% of capacity retention over 400 cycles at 1 A g^{-1}.[96] According to their DFT studies, the diffusion

energy barrier of Zn^{2+} decreases as the interlayer spacing increases in both 1T- and 2H-MoS_2 (Figure 2.6b). At a given interlayer distance, the 1T phase MoS_2 displays a notably lower Zn^{2+} ion diffusion energy barrier compared to the 2H phase. Additionally, an increase in the interlayer spacing leads to more significant decrease in the diffusion energy barrier within the 1T phase than within the 2H phase. Yang et al. conducted a theoretical and experimental study aimed at enhancing magnesium storage in MoS_2.[97] Their findings revealed that, the introduction of the 1T phase and interlayer expansion improve conductivity, enrich active sites for Mg^{2+} storage, and enhance the diffusion kinetics of Mg^{2+}. Using DFT, they computed the adsorption energies of a single Mg^{2+} within the octahedral and tetrahedral sites of both 2H- and 1T-MoS_2 structures. The results, depicted in Figure 2.6c, indicate that the absorption of Mg^{2+} within the interlayer of 2H-MoS_2 is thermodynamically unfeasible due to the positive absorbed energy. However, the energies associated with Mg absorption within the octahedral and tetrahedral sites of 1T-MoS_2 were calculated as -3.077 eV and -4.926 eV, respectively, suggesting a thermodynamically favorable process and stable adsorption of Mg^{2+}. These computational findings indicate that, in terms of thermodynamics, 1T-MoS_2 is more suited as an electrode material for magnesium storage compared to 2H-MoS_2.

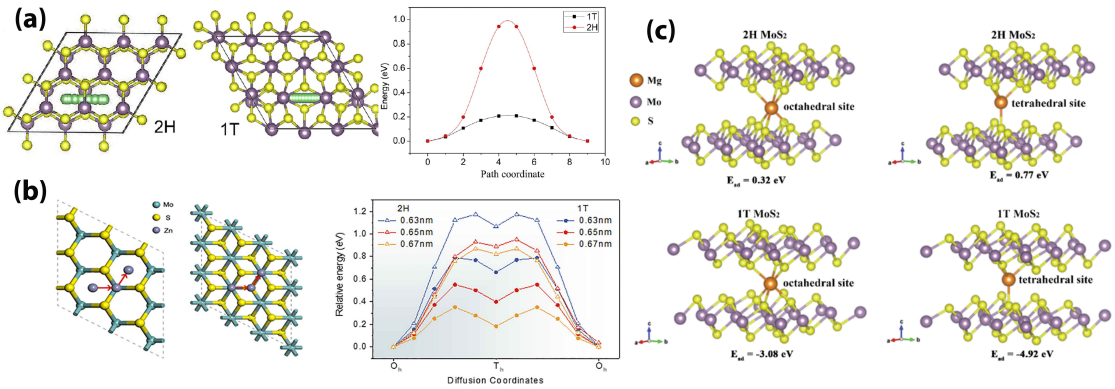

Figure 2.6: (a) The Na migration path and diffusion barrier in 2H- and 1T-MoS_2.[95] (b) energy profiles of Zn diffusion in 2H and 1T-MoS_2 with different interlayer distances.[96] (c) Optimized structures of Mg^{2+} in octahedral and tetrahedral sites of 2H- and 1T-MoS_2.[97]

Hybridizing with conductive agents such as carbon-based materials not only enhances conductivity but also yields unique structures that facilitate ion transport kinetics. Wu et al. synthesized a nanocomposite of MoS_2 and dopamine-derived carbon microsphere using a hydrothermal method followed by annealing at 700 °C. They investigated the diffusion kinetics through first-principles calculations and experimental studies, focusing on its performance as an anode for SIBs.[82] As illustrated in Figure 2.7a, the energy barrier for Na atom diffusion along the Mo–Mo pathway (Figure 2.7b) within the MoS_2/C composite was determined

to be 0.21 eV, which is roughly 40% less than the barrier of 0.34 eV computed for diffusion between two neighboring octahedral sites (Oh–Oh) within the MoS_2/MoS_2 bilayer (Figure 2.7b). This decrease in barrier energy correlated well with their experimental findings, showcasing a significant enhancement in rate performance (300 vs. 143 mAh g^{-1} at 5,000 mA g^{-1}). The distinctive three-dimensional (3D) architecture and improved conductivity account for the observed enhancement in Na^+ storage capability. Wu et al. investigated the diffusion kinetics of divalent Mg^{2+} in both bilayer MoS_2 and MoS_2/graphene heterostructure (MoS_2/GR).[110] As demonstrated in the corresponding energy profiles and diffusion pathways of Mg^{2+} (Figure 2.7c,d), the diffusion barrier for Mg^{2+} within the MoS_2/GR heterostructure (0.4 eV) is significantly lower than that within the bilayer MoS_2 (1.1 eV).

Accordingly, the modification aimed at enhancing the electronic conductivity of MoS_2 can also significantly improve ion diffusion kinetics. This enhancement stems from elevated electronic conductivity and structural alterations achieved during the modification process. However, the key approaches crucial for improving ion diffusion kinetics in MoS_2 in post-LIBS are alterations in interlayer spacing and defect engineering of MoS_2.

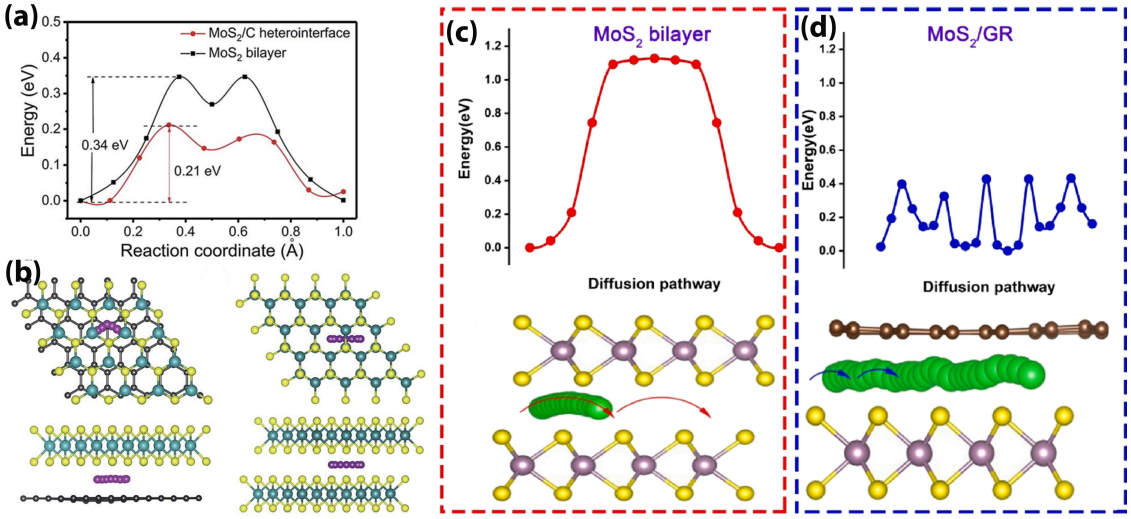

Figure 2.7: (a) Energy profiles of Na^+ along the diffusion path illustrated in (b) within MoS_2/C and MoS_2 bilayer.[82] Energy profiles of Mg^{2+} diffusion within (c) bilayer MoS_2 and (d) MoS_2-GR heterostructure.[110]

Interlayer Engineering

The engineering of interlayer spacing has been demonstrated to be an efficient strategy to improve the ion storage performance of MoS_2 for both large monovalent or multivalent ions. While the interlayer spacing (≈6.2 Å) of MoS_2 suits Li^+ well, it has been proven inadequate

for larger ions like Na^+ and K^+. Additionally, the storage of multivalent ions, characterized by high charge density, within MoS_2 entails robust Columbic interactions between ions and the host material leading to sluggish solid state kinetics. To achieve optimal storage, the intercalation energy barrier must be mitigated by increasing interlayer distances.

Shuai et al. conducted a DFT investigation into the intercalation of Li, Na, and Mg atoms in 2H-MoS_2 possessing various interlayer spacings.[111] Figure 2.8a illustrates the diffusion barrier curves plotted against the lattice constant c for Li, Na, and Mg atoms. These findings suggest that the heightened polarization strength exhibited by divalent Mg^{2+} ions mitigate their size advantage when compared to the larger, monovalent Na^+ ions. The polarization strengths of Li^+, Mg^{2+}, and Na^+, calculated as $P = q.r^{-2}$ where q represents the charge number and r denotes the ion radius, are 2.16 $\times$ 10^{-4}, 4.73 $\times$ 10^{-4}, and 1.11 $\times$ 10^{-4} pm^{-2}, respectively.[16] Figure 2.8a also reveals that at a lattice constant of approximately 17 Å (equivalent to an interlayer distance of 8.5 Å), the diffusion barriers for Li, Na, and Mg atoms are nearly identical, ranging from 0.28 to 0.30 eV. Notably, the diffusion barrier for Li in graphene mirrors this value at 0.277 eV, implying that 2H-MoS_2 with expanded interlayer spacing holds promise as a prospective candidate for post-LIBs active materials.[111]

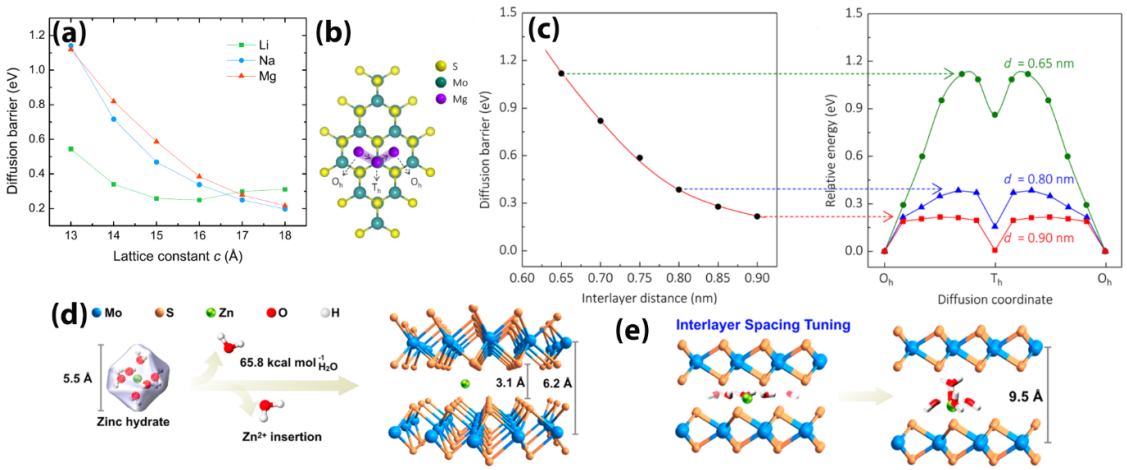

Figure 2.8: (a) Diffusion barrier vs. lattice constant c of 2H-MoS_2 for Li, Na, and Mg atoms,[111] (b) calculated Mg diffusion path in MoS_2, and (c) energy barrier for Mg^{2+} diffusion vs. interlayer distance and potential energy diagram for Mg^{2+} migration at interlayer spacings of 0.65, 0.80, and 0.90 nm.[16] Schematic illustration of hydrated Zn^{2+} intercalation in (d) pristine and (e) interlayer expanded MoS_2.[112]

Liang et al. conducted a comprehensive investigation into the diffusion behavior of Mg^{2+} within MoS_2 with varying interlayer spacing using DFT, yielding valuable insights into the impact of interlayer spacing on the storage of multivalent ions (Figure 2.8c).[16] According to their findings, the diffusion energy barrier experiences a notable decrease as the interlayer

spacing expands from 0.65 to 0.9 nm, dropping from 1.12 to 0.22 eV (equivalent to 10^{15} times faster Mg^{2+} diffusion). Their research underscores the critical importance of interlayer spacing expansion, particularly for divalent ions like Mg^{2+}, compared to monovalent counterparts such as Li^+ and Na^+, which exhibit substantially lower polarizing strengths. Their study reveals that to achieve a Mg^{2+} diffusion energy barrier equivalent to that of Li^+ in bulk MoS_2 (with an interlayer spacing of 6.2 Å), the interlayer distance of MoS_2 should be expanded to 7.72 Å.

Liang et al. explored the intercalation behavior of Zn^{2+} in MoS_2 within an AZIBs using DFT calculations.[112] Their findings revealed that for the intercalation of hydrated zinc ions (with dimensions of 0.55 nm) between MoS_2 layers (with distances between sulfur atoms from one layer to the sulfurs atoms of the adjacent layer of 0.31 nm), the $Zn^{2+}-OH_2$ bonds must first be disrupted, which requires approximately 66 kcal mol^{-1} per Zn−O coordination (Figure 2.8d). Consequently, this process demands high energy input and leads to sluggish kinetics. They have investigated the correlation between the interlayer distance and the highest number of maintained $Zn^{2+}-OH_2$ bonds. According to their study, an increase of 3 Å in interlayer spacing is sufficient to accommodate Zn^{2+} accompanying five water molecules (the solvation shell). Therefore, breakage of only one out of six $Zn^{2+}-OH_2$ bond is enough for the intercalation process (Figure 2.8e).

The impact of interlayer expansion in MoS_2 on the storage of various large or multivalent ions has been extensively demonstrated through both theoretical and experimental research. Enlarged interlayers in MoS_2 can be achieved through different approaches. One method is the top-down approach, which involves initial exfoliation using techniques such as sonication-assisted or n-butyllithium-assisted methods, followed by the incorporation of a guest molecule between the layers. This guest molecule prevents full restacking of the nanosheets, providing a means to adjust the interlayer distance of the exfoliated MoS_2. Guest substances reported to be effective intercalants in this synthesis method include polyethylene oxide (PEO),[113] polyvinylpyrrolidone (PVP),[114] hyperbranched polyethylene ionomer,[26] graphene,[115] along with various other organic and inorganic compounds.[116–118] Each of these intercalants, besides expanding the interlayers, can confer other desirable characteristics to the nanocomposite. These may include enhanced electron/ion conductivity[113] and improved wetting behavior of the nanocomposite with electrolytes,[26] thereby further augmenting the performance in energy storage applications. In bottom-up synthesis approaches like hydrothermal/solvothermal synthesis, it is feasible to achieve interlayer-expanded MoS_2 depending on reaction parameters or additives. For instance, through in-situ intercalation

of NH_3/NH_4^+, which are generated through the decomposition of $(NH_4)_6Mo_7O_{24}.4H_2O$ and CH_4N_2S (Mo and S sources, respectively) during the synthesis process, an enlarged interlayer distance of 9.8 Å can be attained.[106,119] Another viable method to expand the interlayer spacing of MoS_2 is to dope it with oxygen or nitrogen. In these cases, the bond length between Mo and the heteroatom is generally shorter than that between Mo and S, leading to a weakening of the van der Waals interactions between neighboring layers. Consequently, this weakening facilitates an expansion in the interlayer spacing. Previous research has shown that O-MoS_2 and N-MoS_2 exhibit interlayer spacings of approximately 9.5 and 6.25 Å, respectively.[112,120]

Measuring the interlayer spacing of MoS_2 is crucial in experimental research for developing its applications in post-lithium-ion batteries. HRTEM and XRD are the most commonly used to measure its interlayer distance. HRTEM images provide direct visualization of the atomic structure of MoS_2, offering high spatial resolution and enabling researchers to observe and quantify the spacing between MoS_2 layers with good accuracy. For example, as shown in Figures 2.9a-c, the interlayer distances in bulk MoS_2 and PEO-intercalated MoS_2 samples with varying amounts of PEO have been measured using HRTEM images to be 6.2 Å, 11 Å, and 14 Å respectively.[113]

Similarly, XRD analysis, particularly the (002) peak, is utilized to determine the interlayer distance of MoS_2. The position of the (002) peak in the XRD pattern corresponds to the d-spacing between the layers. By analyzing the shift of this peak, researchers can deduce changes in the interlayer distance. For instance, as shown in Figure 2.9d, the interlayer distance of MoS_2 varies depending on the intercalant. This variation is reflected in the (002) XRD peak, where larger interlayer distances result in shifts towards lower 2θ values. Together, HRTEM and XRD provide complementary insights into the structural characteristics of MoS_2, enabling a comprehensive understanding of its interlayer spacing, which is crucial for its applications in energy storage field.

Defect Engineering

Structural defects can disrupt the regular crystal pattern, leading to changes in the chemical and electronic properties of nanomaterials.[121,122] Defects and impurities are naturally found in crystalline materials like MoS_2. Engineering these defects can be advantageous for material design, as they cause the crystal lattice to fracture, increasing the material's surface area.[123] Defects in MoS_2 can be formed through the creation of sulfur vacancies[124] and molybdenum vacancies.[125] Adding defects to MoS_2 electrode material makes the sites more

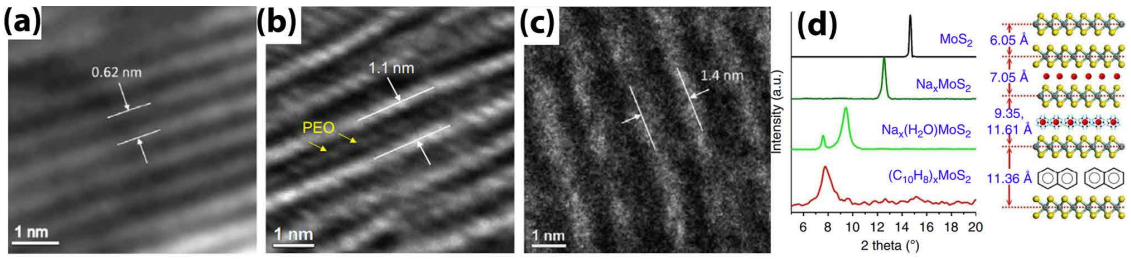

Figure 2.9: TEM images employed to assess the interlayer distance of (a) commercially available MoS_2, and (b, c) MoS_2 intercalated with varying amounts of PEO.[113] (d) XRD spectra showing the (002) peak positions for bulk MoS_2 and MoS_2 intercalated with different atoms/molecules.[46]

accessible for the ions and shortens the paths for ion transport. These defects aid in the movement of guest ions between layers, reducing stress and electrostatic repulsion between neighboring layers. This directly overcomes barriers to migration and diffusion, facilitating the movement of ions and the transfer of charges during electrochemical reactions.[126] Figure 2.10a schematically illustrates how defects, along with interlayer expansion, collaborate to make all sites accessible for K^+. The micro-channels serve as intercalation sites for K^+, shortening the diffusion distance and exposing edge sites, thereby enhancing kinetics.[127]

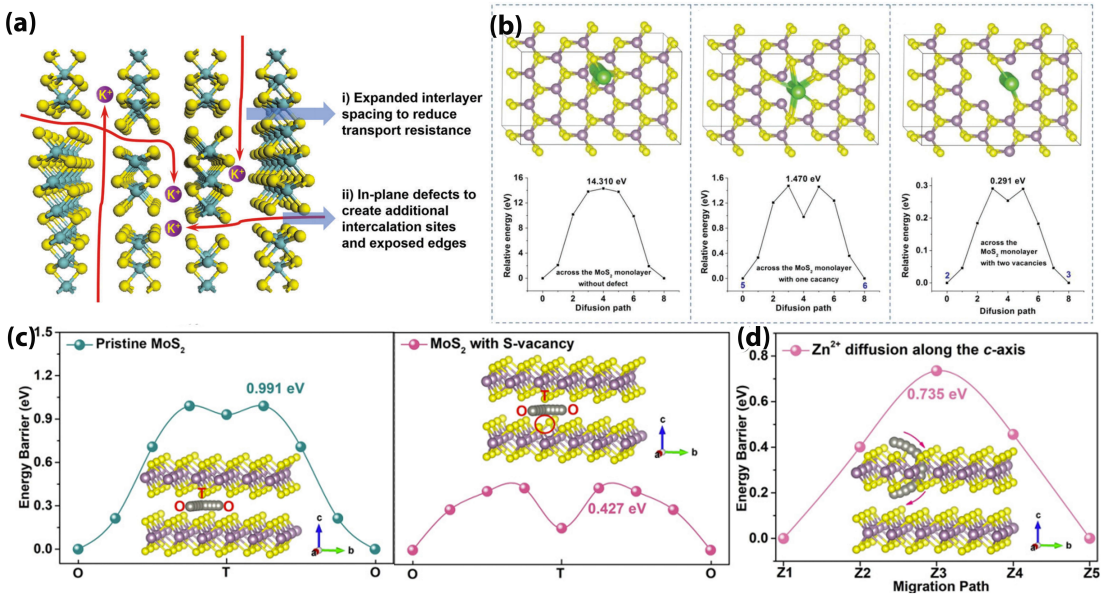

Figure 2.10: Schematic illustration of MoS_2 defects and interlayer engineering in movement of K^+ in the electrode (a).[127] The pathways of Na^+ diffusion with (b, left) in non-defective MoS_2, (b, middle) MoS_2 with one vacancy and (b, right) with two vacancies and their corresponding potential energy curves.[128] Zn^{2+} migration path and energy profile along the ab plane in pristine MoS_2 and MoS_2 with S-vacancy (c) and through the along the *c*-axis (d).[129]

Yao et al. performed a DFT study, simulating the diffusion barrier of Na^+ in MoS_2.[128] Their findings reveal that Na^+ diffusion across the non-defective MoS_2 plane faces an exceedingly high activation energy barrier of 14.310 eV, rendering it impossible (Figure 2.10b). However, for defective MoS_2 with a single vacancy, the activation energy barrier for Na^+ diffusion decreases significantly (1.470 eV) compared to the nondefective MoS_2 monolayer, indicating a higher likelihood of Na^+ diffusion across the plane (Figure 2.10b). In the case of MoS_2 with two vacancies, the activation energy barriers range from 0.291 to 0.661 eV, substantially smaller than those observed in the single vacancy case (Figure 2.10b). This suggests that larger vacancy holes correspond to lower activation energy barriers for Na^+ diffusion across the defective MoS_2 plane. Consequently, Na^+ is capable of achieving three-dimensional diffusion within defective MoS_2 structures, while its diffusion within nondefective MoS_2 materials occurs predominantly in a two-dimensional manner.

According to DFT investigations conducted by Li et al., the computed migration barriers for Zn^{2+} at S-vacancy sites (0.427 eV, Figure 2.10c) is notably lower compared to that within pristine MoS_2 (0.991 eV, Figure 2.10c).[129] The vacancies effectively diminish the resistance encountered by Zn^{2+} during migration, thereby reducing the overall energy barrier. Additionally, simulation results demonstrate a relatively modest migration barrier of 0.735 eV for Zn^{2+} diffusion along the *c*-axis, indicating the plausible diffusion of Zn^{2+} through structural defects present on the basal plane of MoS_2 (Figure 2.10d).

Charge Screening

The kinetic hurdles of MoS_2 in ion storage are more pronounced in multivalent ion storage, owing to their intrinsically polarizing feature promoting robust interactions between them and the host lattice, impeding their mobility within the cathode material.[15,16,22,23] One approach to bypass this problem is to introduce an intercalant with the charge shielding effect that can effectively weaken the interaction between the multivalent ion and the host material. For example, structural water molecules have been proven to be very effective to mitigate the interactions of the interaction of Mg^{2+} and MoS_2. Wu et al. synthesized oxygen-doped MoS_2 (O-MoS_2) via a hydrothermal reaction and subsequently introduced hydration through an electrochemically assisted method.[116] Their resulting product had enlarged interlayer distances and benefited from the charge shielding effect of crystalline H_2O. This effect weakened the electrostatic interaction between Mg^{2+} ions and the host frameworks, thereby enhancing the mobility of Mg^{2+} ions. Consequently, the hydrous MoS_2 (H-MoS_2) exhibited a Mg^{2+} diffusion rate three times faster than that of MoS_2 prior to

hydration.

Such a charge screening effect has also been reported in MIBs utilizing MoS_2-based cathode material and magnesium salt in DME solvent as the electrolyte. In these batteries, the capacity has been observed to gradually increase over cycling tests.[76,130] This gradual capacity augmentation, termed electro-activation, is a common occurrence resulting from the continuous intercalation/deintercalation of ions and consequently, the expansion of the active surface area.[131,132] Regarding MoS_2, the intercalation of Mg^{2+} into its layered structures can induce a degree of distortion, leading to a phase transition from the semi-conductive 2H to the metallic 1T phase. With repeated cycling, the proportion of the 1T phase and the available active surface area increase. Consequently, more favorable conditions for Mg^{2+} accommodation are attained throughout cycling. Furthermore, following each charge/discharge cycle, some DME molecules and a small amount of Mg^{2+} remain between the 2H-MoS_2 layers. These residual DME molecules aid in enhancing kinetics by acting as a shielding layer, thereby attenuating interactions between Mg^{2+} and the host material.[76,130]

The insertion of cations such as Li^+, Na^+, and K^+ between the layers of MoS_2 can expand the interlayer spacing, creating additional active sites accessible to multivalent ions. Simultaneously, this process diminishes the intense electrostatic interactions between multivalent ions and the host material. Such ions can be incorporated into MoS_2 structure during the synthesis method like what Li et al. showed.[117] They synthesized a nanocomposite of K^+ intercalated MoS_2 with carbon name as K-MoS_2@C and utilized it as cathode for AZIB cathode. Therein, $K_2S_2O_8$ was added in the hydrothermal reaction of conventional Mo and S sources during the synthesis. K-MoS_2@C outperformed its counterparts without intercalant in terms of capacity and rate performance.

Harnessing the shielding effect of monovalent ions to mitigate the strong interactions of multivalent ions with the host material can be achieved through dual-salt batteries featuring a co-intercalation mechanism. These batteries utilize an electrolyte composed of salts containing both monovalent and multivalent ions. For instance, in dual-salt MLIBs, Li^+ diffuse into MoS_2 structure, establishing a shielding effect that enhances the diffusion of Mg^{2+}.[133–135]

2.4.3 Stability Enhancement

Dealing with Volume Changes

Creating nanostructured MoS_2 with increased interlayer spacing is a promising approach that has been thoroughly investigated due to its ability to facilitate effective strain relief. However, integrating MoS_2 with carbon-based substances can have dual effects; enhancing the electronic conductivity and mitigating volume changes during the process of the ions insertion/extraction with bolstered structural stability.[136] Various carbon-based substrates such as graphene,[53,137] carbon nanotubes,[66] and amorphous carbon[21,136] have been employed for this purpose. Carbon-based materials also contribute to the overall structural stability of the composite electrodes. They provide a scaffold-like support structure that helps maintain the integrity of the MoS_2 active material. By anchoring the MoS_2 particles within the electrode matrix, carbon materials prevent agglomeration and detachment of active material particles, which could otherwise lead to capacity loss and electrode degradation over repeated cycling. Carbon materials can be engineered to have a porous structure with a high surface area. These pores act as reservoirs to accommodate the volume expansion and contraction of the MoS_2 particles as ions are intercalated and deintercalated during cycling. By providing space for MoS_2 to expand into, the pores help mitigate mechanical stresses that could otherwise lead to loss of electrode materials.[56,138]

In addition to the structural modifications, there have been significant adjustments related to battery fabrication, such as incorporating fluoroethylene carbonate (FEC) into the electrolyte. This addition fosters the creation of a highly stable solid electrolyte interphase (SEI), capable of accommodating volume changes effectively,[67]. Furthermore the superiority of sodium alginate over conventional polyvinylidene fluoride (PVDF) binder for stabilizing the MoS_2-based anode of SIB has been demonstrated. This superiority stems from its rigid backbone in both dry and wet states, along with its robust interaction with active materials. As a result, it significantly enhances both mechanical stability and electrochemical performance.[53]

Dealing with Conversion Reactions

In cases of alkali ion storage in MoS_2, when narrowing down the potential window is not desired while still achieving acceptable cyclic stability, several solutions have been proposed, with most of them being based on combination with carbon materials. In general, the goal of these strategies is to have the product of conversion reactions trapped in the structure

and their shuttling preserved, while also improving the dynamics of reverse reactions.

Confinement Effects:

Zhu et al. embedded single-layered ultra-small nanoplates of MoS_2 (Figure 2.11a: thickness 0.4 nm, lateral dimension 4.0 nm) within an amorphous carbon matrix.[68] They discussed that when MoS_2 is confined within such a matrix at a small scale, the resulting products formed during a discharge process may exhibit distinct behavior compared to the bulk material. This phenomenon is attributed to the confinement effect, wherein the movement of atoms or molecules is constrained within the matrix. Consequently, the confined material may deviate from the typical processes of phase separation, which leads to the formation of distinct metal and sulfide phases. Moreover, due to the limited amount of material involved in the reaction within the confined space, the resulting products may remain within the confines of the matrix. This confinement effect ultimately contributes to higher reversibility of the conversion reactions.[68,69]

Coupling Effects:

Li et al. proposed a method to enhance the reversibility of intercalation and conversion reactions with Na^+ storage within MoS_2 by synergistically coupling few-layered MoS_2 and graphene sheets through covalently doped S atoms.[65] They synthesized this composite through a hydrothermal reaction involving Mo and S sources, along with GO and S powder. This concept is grounded in the distinctive composite structure, wherein few-layered MoS_2 is tightly bound to the sulfur doped graphene (SG) nanosheets through a potent synergistic coupling effect facilitated by S dopants in the SG component. Comparing the XPS S $2p$ spectrum of pure MoS_2 with that of MoS_2/SG reveals a slight shift towards lower energy, indicating a reduced degree of S element oxidation in MoS_2 (Figure 2.11b). This observation is consistent with the Mo $3p$ curves of MoS_2/SG (Figure 2.11c). Consequently, there is a discernible increase in electron density around MoS_2 in the MoS_2/SG composites. It is worth mentioning that the introduction of heteroatoms like N, S, and P facilitates the electron enrichment of graphene localized at the doping sites. In these nanocomposites, the electron cloud exhibits a bias from SG to MoS_2, thereby forming a robust electronic coupling between the two components (see Figure 2.11d). Cycling the SIBs with MoS_2/SG within two distinct potential windows (0.005-3 V and 0.4-3 V) for 1,000 cycles at 1.0 A g^{-1} resulted in

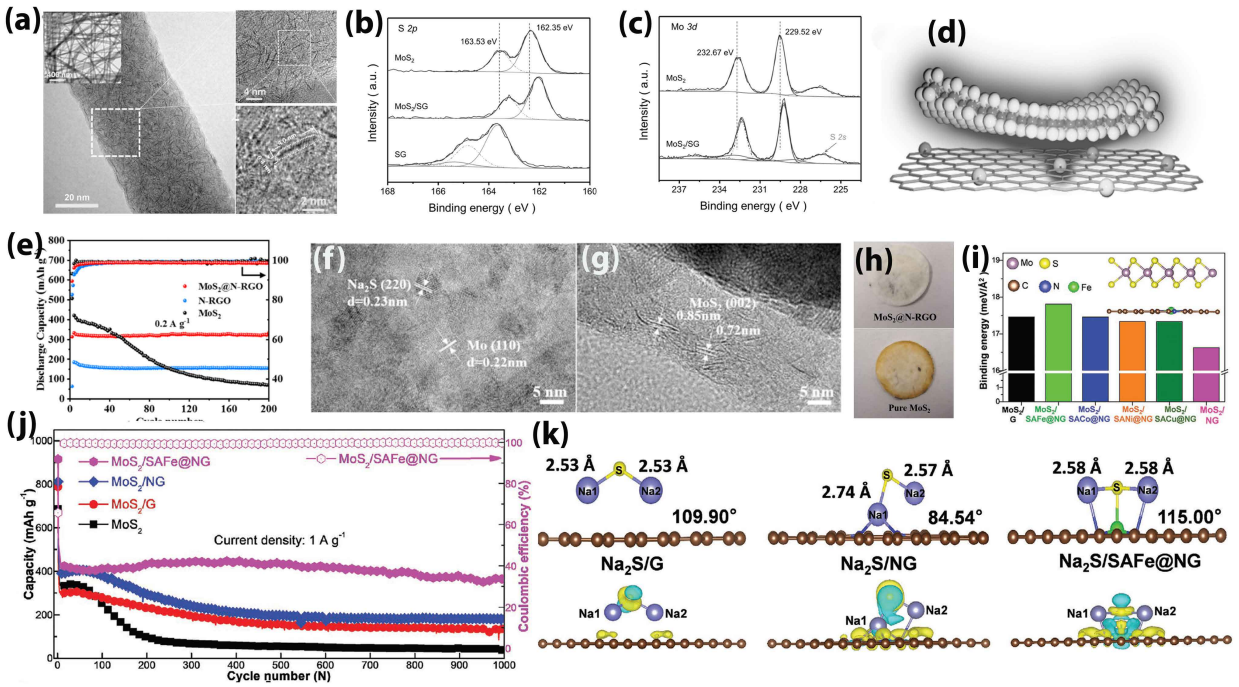

Figure 2.11: (a) HRTEM images of MoS_2 nanodots embedded in the carbon nanofiber.[68] (b) XPS S $2p$ spectra of MoS_2, MoS_2/SG and SG, (c) XPS Mo $3d$ spectra of MoS_2 and MoS_2/SG, (d) schematic illustration of the electron cloud bias from SG to MoS_2.[65] (e) cycling performance of pure MoS_2, N-RGO, and MoS_2@N-RGO at 0.2 A g^{-1}, HRTEM images of MoS_2@N-RGO at (f) full discharge (0.005 V) state and (g) full charge (3.0 V) state, (h) the separator of SIB with pure MoS_2 (bottom) and MoS_2@N-RGO after (top) electrodes after cyclic tests.[139] (i) Adsorption energies of MoS_2 on graphene, NG, SAFe@NG, SACo@NG, SANi@NG, and SACu@NG, (j) cycling performance of MoS_2, MoS_2/G, MoS_2/NG, and MoS_2/SAFe@NG at 1 A g^{-1}; (k) bond length, bond angle and charge density difference of Na_2S adsorption on graphene, NG, and SAFe@NG. The blue and yellow zones show the electron loss and accumulation, respectively.[140]

a high stability of ≈85%, which was consistent across both windows. These findings suggest that the composite not only maintains high stability during intercalation/deintercalation reactions but also withstands conversion reactions without the loss of its original structure or collapse under deep charge/discharge processes.

Zhan et al. also investigated the coupling effect in MoS_2 nanosheets modified by porous nitrogen-doped graphene (MoS_2@N-RGO).[139] Unlike pure MoS_2, the S $2p$ and Mo $3d$ peaks in the composite shift towards higher energy levels, indicating an electron cloud bias from MoS_2 to N-RGO, thus establishing a robust coupling effect between them. Their findings

demonstrate that the strong synergistic coupling between MoS_2 and N-RGO effectively mitigates the excessive volume variation of MoS_2 nanosheets during Na^+ intercalation and deintercalation. When utilized as anodes for SIBs, MoS_2@N-RGO exhibits significantly enhanced stability throughout cycling tests compared to pure MoS_2 (Figure 2.11e). HRTEM images revealed that upon over-discharge to 0.005 V, only Mo and Na_2S nanoparticles were observed (Figure 2.11f). However, after charging to 3.0 V, Mo and Na_2S could not be detected, indicating the reformation of the layered structure of MoS_2 nanosheets (Figure 2.11g). Consequently, the reconstructed layered structure of MoS_2 suggests the reversible conversion of MoS_2@N-RGO during sodium storage processes. Furthermore, a comparison of the color of separators used in SIBs with pure MoS_2 and MoS_2@N-RGO indicated that the shuttle effect of the reaction intermediate could be effectively suppressed in the electrolyte (Figure 2.11h). This inhibition of the shuttle effect helps prevent the loss of active materials, ensuring the high reversibility of the conversion reaction.

Single Atom Catalysts:

Recently, there has been a surge in research exploring transition metal single atoms on nitrogen-doped graphene (SAM'@NG, M' = Fe, Co, Ni, or Cu) as potential electrocatalysts for Li/Na–S batteries, aiming to facilitate the formation and decomposition processes of Li_2S/Na_2S.[141,142] Chen et al. have conducted investigations indicating that SAM'@NG nanosheets exhibit potential for enhancing the dynamic properties of Mo/Na_2S, which could potentially result in more efficient reversible conversion during the cycling of SIBs.[140] Initially, they conducted theoretical simulations to evaluate the adsorption energies and identify the most promising transition metal single atom in SAM'@NG (Figure 2.11i). Among these, SAFe@NG was found to have the highest interfacial binding energy to MoS_2 (17.84 meV $Å^{-2}$) and significantly enhance the electrical conductivity of MoS_2, thereby expediting the reaction kinetics of $MoS_2 \longrightarrow NaMoS_2 \longrightarrow Mo/Na_2S$ during SIB discharge. As anticipated, SAFe@NG in MoS_2/SAFe@NG nanocomposite demonstrated significant catalytic activity in the decomposition of Na_2S and $NaMoS_2$ during the charging process, resulting in an efficient reversible conversion reaction of $Mo/Na_2S \longrightarrow NaMoS_2 \longrightarrow MoS_2$ with a favorable formation energy barrier. Benefiting from this efficient conversion reaction throughout the complete cycle, MoS_2/SAFe@NG exhibited impressive long-term cycling performance (Figure 2.11j) compared to pristine MoS_2, and its nanocomposites with graphene (MoS_2/G) and nitrogen-doped graphene (MoS_2/NG). They further analyzed the energy barriers of reaction pathways using the climbing-image nudged elastic band (CI-NEB) method and concluded

that the reversible conversion reaction likely proceeds in two steps of Mo + $2Na_2S$ $\longrightarrow$ $NaMoS_2 + Na^+ + e^-$ and $NaMoS_2$ $\longrightarrow$ $MoS_2 + Na^+ + e^-$ rather than a one-step reaction of Mo + $2Na_2S$ $\longrightarrow$ $MoS_2 + 4Na^+ + 4e^-$. Additionally, they conducted theoretical simulations to investigate the catalytic mechanism of SAFe@NG on the first step of the reversible conversion reaction of Mo/Na_2S. Their findings highlight stark differences in adsorption energies: while graphene exhibits minimal affinity for Na_2S (0.52 eV), NG demonstrates significantly higher adsorption energy (2.25 eV), with SAFe@NG falling in between at 1.6 eV. This trend is similarly reflected in the adsorption energies towards Mo. Consequently, NG and SAFe@NG can effectively anchor Mo/Na_2S, facilitating their interaction during the charge process.

Regarding the decomposition of Na_2S in the reaction (Mo + $2Na_2S \rightarrow NaMoS_2 + Na^+ + e^-$), they investigated the bond strength of Na−S to assess the catalytic activity of SAFe@NG, NG, and G (Figure 2.11k). The interaction between the Na_2S molecule and NG primarily occurs through the Na_1−N bond, as confirmed by its strong electronic transformation. The highest adsorption energy of Na_2S on NG (2.25 eV) implies that the strong Na_1−N bond strength makes it challenging to detach the Na1 atom from the NG catalyst, thereby inhibiting the catalyst's activity and blocking subsequent reactions. However, for the Na_2S/SAFe@NG system, electron migration predominantly accumulates on the Fe−S bond, weakening the Na_1−S and Na_2−S bond strengths simultaneously. This sulfur affinity mechanism results in a moderate adsorption energy (1.60 eV) for Na_2S on SAFe@NG, which is beneficial for the reversible adsorption and decomposition of Na_2S, contributing to the durability of the SAFe@NG catalyst.

Xie et al. recently investigated a 2D heterostructure comprising Co-doped MoS_2 and N-doped graphene (Co-MoS_2/NG) as an SIB anode featured with enhanced stability.[143] Their combined theoretical and experimental analyses unveiled that this heterostructure exhibits superior electrical conductivity and Na^+ adsorption capacity during discharge, surpassing both Co-MoS_2/G and MoS_2/NG configurations. In discharge process similar to Mo nanoclusters generated from MoS_2, the doped Co undergoes transformation into Co nanoclusters due to the analogous properties between Co and Mo. Theoretical investigations revealed that the N doping sites in NG exhibit higher adsorption energy toward Mo and Co compared to Na_2S. On the other hand, Mo and Co nanoclusters adsorbed on G and NG substrates display stronger adsorption ability toward Na_2S than the primary G and NG substrates. Consequently, the initial anchoring of Mo and Co is followed by the adsorption of Na_2S, resulting in close contact and uniform distribution of transformed metal nanoclusters

and Na_2S. The uncovered Na_2S-Mo(Co)/NG interface significantly enhances the dispersion, adsorption, and decomposition of Na_2S, thereby facilitating stable and reversible conversion reactions.

Trapping Sulfur Species by 1T Phase:

Sun et al. synthesized a 1T-MoS_2 utilizing a thermal-driven ion intercalation assisted exfoliation of bulk MoS_2.[95] Their study and comparison of 1T and 2H-MoS_2 for sodium ion storage indicated that 1T phase can significantly suppress the release and dissolution of polysulfide generated due to the conversion reaction. Trapping the sulfur species by 1T phase is the main reason for more stable cycling results of 1T-MoS_2 compared to 2H-MoS_2. Their study is supported by evidence from in-situ XRD, ex-situ Raman spectroscopy, XPS, and DFT calculation.

2.4.4 Other Modifications

Morphology Engineering

The synthesis of various morphologies of MoS_2 or its nanocomposites has been attempted in numerous research studies. These special morphologies aim to enhance electrolyte permeation from the outer to the inner regions, reduce ion diffusion distances, increase accessibility to active sites, and improve durability amid volume changes resulting from ion insertion/extraction processes.[144] Various morphologies of pure MoS_2 can be achieved through hydro/-solvothermal synthesis methods by employing specific reaction media or using precursors with tailored compositions. For instance, the introduction of ethanol to water as the solvent during hydrothermal/solvothermal reaction facilitates the synthesis of flower-like MoS_2 spheres with a diameter of approximately 700 nm (Figure 2.12a).[145] Conversely, in the absence of ethanol (pure hydrothermal reaction), the reaction typically yields heavily agglomerated products. This phenomenon can be explained by the thermodynamic principle; the presence of alcohol reduces the solvation power of the solvent due to its lower permittivity compared to distilled water. Consequently, this reduces the solubility of the product and increases the supersaturation of the solvent, favoring the formation of dispersed MoS_2 spheres. Such a flower-like structure possesses a higher surface area compared to MoS_2 synthesized in the absence of alcohol (23.34 $m^2\ g^{-1}$ vs. 12.86 $m^2\ g^{-1}$), facilitating active site accessibility for ions. Therefore, it can deliver higher capacity for alkali ions like Li^+.[145] Additionally, MoS_2

nanoflowers have been shown to exhibit enhanced kinetics and low energy barrier for the intercalation of Na^+ ions compared to bulk MoS_2.[62] Therefore, as a anode for SIBs, it can deliver 200 mAh g^{-1} vs. approximately 120 mAh g^{-1} with bulk materials at 1 mA g^{-1}.

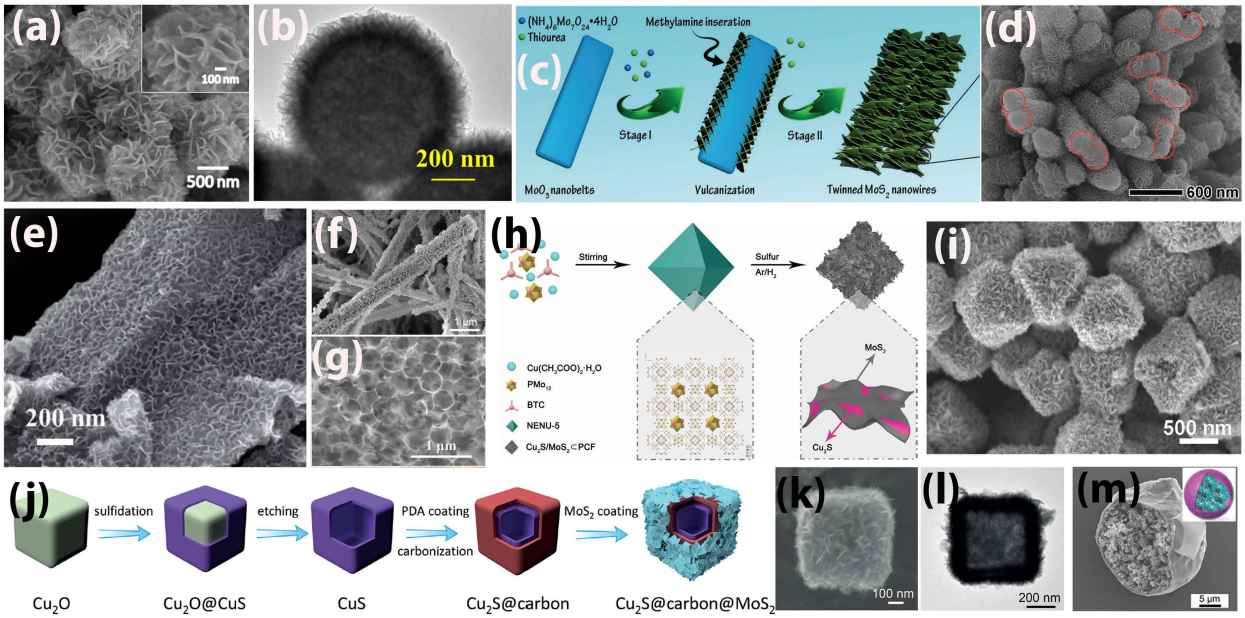

Figure 2.12: (a) SEM image of MoS_2 nanoflowers.[145] (b) TEM image of hollow MoS_2 sphere.[146] (c) schematic illustration of synthesis and (d) FESEM image of MoS_2 twinned nanowires.[147] (e) SEM image of vertically aligned MoS_2 on RGO.[53] (f) SEM image of MoS_2-coupled carbon nanosheets encapsulated on sodium titanate nanowires.[148] (g) SEM image of 3D ordered porous MoS_2/Carbon.[149] (h) Synthesis steps and (i) FESEM image of hierarchical octahedra constructed by Cu_2S/MoS_2@Carbon framework.[150] (j) synthesis steps, (k) SEM image, and (l) TEM image of three-layered Cu_2S@Carbon@MoS_2 hierarchical nanoboxes.[151] (m) MoS_2-infilled carbon microcapsules.[152]

A self-template approach was reported for the synthesis of molybdenum-based solid sphere templates through hydro/solvothermal treatment of molybdyl acetoacetate ($C_{10}H_{14}MoO_6$) in a mixture of isopropanol and water.[146] Subsequent sulfidation (hydrothermal/solvothermal in a water/ethanol mixture) results in the formation of MoS_2 hollow nanospheres with a diameter of around 940 nm (Figure 2.12b). The synthesized hollow structure facilitates swift and consistent movement of Na^+ ions without relying on conductive agents, enabling it to serve as an anode for SIBs with a notable capacity of 527 mAh g^{-1} at a current density of 100 mA g^{-1}. Another study by Ye et al. utilized MoO_3 nanobelts as sacrificial templates to produce MoS_2 twinned nanowires (Figure 2.12c,d).[147] In both cases, the final morphology of the MoS_2 product inherits the shape of its precursor (Mo source), leading to the formation of distinct morphologies.

Hybridizing MoS_2 with carbon-based materials, metal oxides, metal sulfides, etc. not only enhances ion storage capabilities through synergistic effects but also allows for the attainment of diverse architectures during synthesis process. These alterations can yield a wide array of structures, including vertically aligned structures (on graphene (Figure 2.12e)[53] and carbon paper,[80]) nanowires (Figure 2.12f),[148] 3D network porous structures (Figure 2.12g),[138,149] hierarchical octahedra (Figure 2.12h,i),[150], penne-like,[153] hollow spheres,[154] hollow rhomboids,[155] hollow nanobox (Figure 2.12j-l)[151] and more. Furthermore, it is possible to fabricate highly unique architectures such as carbonaceous capsules infilled with MoS_2 of various morphologies (Figure 2.12m).[76,152] For instance, when comparing the performance of pure MoS_2 nanosheets with MoS_2-infilled carbonaceous microcapsules synthesized by Lin et al. via liquid-driven coaxial flow focusing (LDCFF) approach (Figure 2.12m) as cathodes for MIBs, it is evident that the latter exhibits superior stability and capacity.[152] Specifically, the MoS_2-infilled microcapsules demonstrate approximately 161 mAh g^{-1} and 65 mAh g^{-1}, compared to approximately 70 mAh g^{-1} and 30 mAh g^{-1} for pure MoS_2 nanosheets without the shell, at current densities of 0.05 A g^{-1} and 0.3 A g^{-1}, respectively.

Each of the structures mentioned can offer benefits for ion storage purposes, but hollow structures stand out as particularly advantageous. They provide pronounced active sites, facilitate short ion transport paths, and mitigate volume expansion and lattice stress, thereby enhancing cycling stability and rate capability.[144] In addition, the hollow structure act as a dynamic electrolyte reservoir upon volumetric variation.[156] Hollow structures can be achieved through various approaches including template-free methods, self templating, soft templating, hard templating, and sacrificial templating.[144]

Heteroatom Doping

Heteroatom doping of MoS_2 can modify its properties and offer several benefits for battery applications, such as enhanced electrical conductivity and increased stability, among other advantages.[157–160] Sn doping in MoS_2 has been proved to make a phase transition from 2H to 1T by acting as a electron donor, leading to the enhanced conductivity and better performance for Na^+ storage.[161] In a study conducted by Li et al., it has been demonstrated that Co-doping plays a critical role in preserving the structural integrity of MoS_2 during continuous Na^+ insertion/extraction cycles, as confirmed by first-principles calculations. In comparison with pristine MoS_2, Co-doped MoS_2 exhibits a significant reduction in volume deformation, with a notable decrease of 52% during cycling. Thus, Co-doping emerges as a pivotal factor in enhancing the cycle stability of MoS_2, effectively addressing one of the most

challenging aspects of Na^+ storage in MoS_2, which arises from drastic volume changes.[162] In a study conducted by Zhuo et al. on Mg^{2+} storage in Cu-doped MoS_2@hydrogen-substituted graphdiyne, it was observed that doping with Cu heteroatoms leads to a significant increase in the Mg^{2+} diffusion coefficient for Cu-MoS_2 compared to pure MoS_2, by a factor of 1.76. This enhancement directly implicates the role of the Cu-Mo-S phase in facilitating Mg^{2+} diffusion. Additionally, the charge transfer resistance (R_{ct}) value decreases notably from 111.70 to 57.76 Ω upon doping MoS_2 with Cu, indicating a substantial improvement in charge transfer facilitated by the introduction of transition metal heteroatoms into MoS_2.

Heteroatom doping also can lead to the interlayer expansion of MoS_2. Liang et al. conducted a hydrothermal reaction at 180 °C to synthesize oxygen-incorporated MoS_2 (MoS_2−O).[112] At this lower reaction temperature, the molybdate precursor (source of molybdenum) may not fully decompose, leaving some Mo−O bonds that can react with thiourea (the source of sulfur) to yield oxygen-incorporated MoS_2 (MoS_2−O). The smaller size of O atoms (48 pm compared to 88 pm for S atoms) and the shorter Mo−O bonds (1.86 Å vs. 2.42 Å for Mo−S bonds) weaken the van der Waals interactions between adjacent S layers, resulting in a slightly expanded interlayer spacing (9.5 Å). In their study, oxygen doping offers an additional benefit of enhancing hydrophilicity, a crucial factor contributing to improved performance in an AZIB.

Nitrogen doping not only leads to interlayer expansion of MoS_2 but also introduces sulfur vacancies, thereby enhancing the kinetics of Zn^{2+} storage.[163] Furthermore, studies have demonstrated that nitrogen doping enhances the electronic conductivity of MoS_2, as evidenced by density functional theory investigations of N-MoS_2 monolayers.[120,164] Yang et al. synthesized Mn-doped MoS_2 on MXene as active materials for ZIBs.[165] They employed a hydrothermal/solvothermal reaction and utilized $MnCl_2$ as the Mn source. Their investigation revealed that Mn forms covalent bonds with two sulfur atoms from adjacent MoS_2 layers, thereby enlarging the interlayer spacing to 8.8 Å. Additionally, the S-Mn-S bonds function as "electron bridges", facilitating electron transfer and ultimately enhancing the performance of the nanocomposite for AZIBs.

2.5 Ion Storage in MoS_2 Nanostructures

2.5.1 Na^+/K^+ Storage

Among the various active anode materials investigated thus far for SIBs and PIBs, MoS_2 with its unique structural properties and high theoretical capacity of 670 mAh g^{-1}, stands out as

promising contenders.[21,128,166] In recent years, there has been a significant surge in research focusing on the design of MoS_2 nanocomposites as anode materials for SIBs and PIBs. Table 2.1 and Table 2.2 present the characteristics of distinctive MoS_2-based nanocomposite anode materials reported for SIBs and PIBs, respectively.

Table 2.1: Key structural features and performance characteristics of MoS_2-based electrode active materials for SIBs.

Material	Key features	Capacity (mAh g^{-1})	Cycling stability (cycles @ current density)	Ref.
Defect-rich MoS_2	Large vacancies bundled by MoO_3	411 @ 0.1 A g^{-1} 262 @ 5 A g^{-1}	≈97% (1,000 @ 5 A g^{-1})	[128]
1T MoS_2	Metallic conductivity Few-layered structure	450 @ 0.05 A g^{-1} 253 @ 2 A g^{-1}	≈98% (150 @ 0.1 A g^{-1}) 94% (200 @ 1 A g^{-1})	[95]
MoS_2 hollow microcubes	3D hierarchical hollow architecture Mo-defect-rich ultrathin structure	412 @ 0.1 A g^{-1} 226 @ 5 A g^{-1}	88% (100 @ 0.1 A g^{-1}) ≈94% (125 @ 1 A g^{-1})	[125]
Porous MoS_2/C	3D ordered porous structure Vast macro/mesoporous structure. Enhanced conductivity	446 @ 0.5 A g^{-1} 196 @ 50 A g^{-1}	85% (500 @ 2 A g^{-1})	[149]
Co-doped MoS_2@N,O-carbon	Enlarged interlayer spacing High conductivity by Co doping Agglomeration resistant Enabled spin-polarized capacitance	≈860 @ 0.1 A g^{-1} ≈450 @ 20 A g^{-1}	>100% (100 @ 0.1 A g^{-1}) ≈86% (3,000 @ 5 A g^{-1})	[167]
Nitrogen-doped MoS_2/C foam	Enhanced conductivity Large pore volume	557 @ 0.05 A g^{-1} 432 @ 1 A g^{-1} 324 @ 5 A g^{-1}	≈88% (150 @ 0.2 A g^{-1}) ≈91% (150 @ 0.5 A g^{-1})	[120]
MoS_2/amorphous carbon	Enhanced conductivity Highly reversible conversion reactions Tabular structure alleviating the volume changes	≈656 @ 0.2 A g^{-1} ≈401 @ 10 A g^{-1}	≈100% (100 @ 0.2 A g^{-1}) ≈100% (500 @ 1 A g^{-1})	[136]
MoS_2-RGO/carbon spheres	3D porous structure Enhanced conductivity Hollow structure accommodating the volume changes few-layered MoS_2	≈646 @ 0.1 A g^{-1} 364 @ 5 A g^{-1}	86% (100 @ 0.1 A g^{-1})	[138]
MoS_2/C-MWCNT	Few-layered and defect-rich MoS_2 Enlarged interlaye spacing (6.4 Å) Enhanced interparticle and intraparticle conductivity, High structural stability	415 @ 1 A g^{-1} 324 @ 20 A g^{-1}	≈96% (1000 @ 2 A g^{-1})	[56]
A. niger-derived carbon/MoS_2	Hollow biconcave structure Abundant doping of N and P Enlarged interlayer spacing (6.7 Å)	625 @ 0.5 A g^{-1} 409 @ 5 A g^{-1}	≈95% (1,000 @ 1 A g^{-1})	[168]
Graphene@MoS_2-C	Few-layered structure Enhanced conductivity	≈654 @ 0.1 A g^{-1} 201 @ 20 A g^{-1}	76% (400 @ 1 A g^{-1}) ≈55% (4,500 @ 3 A g^{-1})	[169]
MoS_2@SnO_2@C	Restacking resistance Stable with carbon cover	595 @ 0.05 A g^{-1} 168 @ 2 A g^{-1}	≈75% (150 @ 0.1 A g^{-1})	[170]
Nb_2CT_x@MoS_2@C	3D cross-linked structure Carbon-reinforced structure Enhanced conductivity High volume elasticity	572 @ 0.1 A g^{-1} 454 @ 5 A g^{-1}	≈87% (200 @ 0.1 A g^{-1}) ≈80% (2,000 @ 1 A g^{-1})	[171]
N-MoS_2/C@silicon oxycarbide	Core-shell heterostructure Enhanced conductivity (N-doped) Enlarged interlayer spacing (6.6 Å) Structure-reinforcing of SiOC shell	≈506 @ 0.05 A g^{-1} ≈277 @ 10 A g^{-1}	>100% (200 @ 0.1 A g^{-1})	[172]
MoS_2/SAFe@NG	Enhanced conductivity	531 @ 0.1 A g^{-1}	≈186% (1,000 @ 1 A g^{-1})	[140]

Continued on next page

Table 2.1 – continued from previous page

Material	Key features	Capacity (mAh g^{-1})	Cycling stability (cycles @ current density)	Ref.
	Highly reversible conversion reactions	380 @ 2 A g^{-1}		
Fe_9S_{10}@MoS_2@C	Improving the electronic conductivity Heterogeneous interfaces with a strong electric field Highly reversible conversion reactions Fast charging capability Reinforcing geometry architecture	≈520 @ 0.2 A g^{-1} 132 @ 50 A g^{-1}	≈100% (100 @ 0.2 A g^{-1}) ≈93% (1000 @ 2 A g^{-1})	[173]
Cu_2S@Carbon@MoS_2 nanoboxes	N-doped carbon Hollow structure accommodating the volume changes Enhanced conductivity	430 @ 0.05 A g^{-1} 316 @ 2 A g^{-1}	≈80% (200 @ 0.3 A g^{-1})	[151]
Nb_2O_5@MoS_2@ C CNFs	3D flexible fiber paper structure Highly stable structure	245 @ 0.2 A g^{-1} 97 @ 20 A g^{-1}	≈95% (1,000 @ 1 A g^{-1}) ≈82% (20,000 @ 5 A g^{-1})	[85]
Sodium titanate/MoS_2-C	Enhanced conductivity Very stable sodium titanate core	≈425 @ 0.2 A g^{-1} ≈279 @ 4 A g^{-1}	≈81% (16,000 @ 8 A g^{-1})	[148]

Table 2.2: Key structural features and performance characteristics of MoS_2-based electrode active materials for PIBs.

Material	Key features	Capacity (mAh g^{-1})	Cycling stability (cycles @ current density)	Ref.
MoS_2 nanoflowers	Enlarged interlayer spacing (9.1 Å) Defective structure	90 @ 0.1 A g^{-1} 48 @ 0.8 A g^{-1}	≈80% (100 @ 0.05 A g^{-1})	[127]
MoS_2/RGO	Enlarged interlayer spacing Conductive carbonacious skeleton Thin and uniform rose-like structure	353 @ 0.1 A g^{-1} 178 @ 0.5 A g^{-1}	>100% (100 @ 0.1 A g^{-1})	[54]
Densified 1T-MoS_2/Graphene	Metallic conductivity Compact structure	511 @ 0.1 A g^{-1} 327 @ 1 A g^{-1}	≈75% (800 @ 1 A g^{-1})	[74]
MoS_2/carbon nanotubes	Enlarged interlayer spacing (9.8 Å) Unique fiber-like morphology	520 @ 0.2 A g^{-1} 310 @ 1 A g^{-1}	≈96% (100 @ 0.2 A g^{-1}) 84% (100 @ 1 A g^{-1})	[174]
MoS_2/N-Doped-C hollow tubes	Enlarged interlayer spacing (10.0 Å) High structural integrity Enhanced conductivity	258 @ 0.1 A g^{-1} 131 @ 2 A g^{-1}	≈95% (70 @ 0.1 A g^{-1}) ≈74% (1,000 @ 1 A g^{-1})	[21]
$Ti_3C_2T_x$ MXene/MoS_2	Enhanced conductivity Hierarchical 2D structure	≈290 @ 0.05 A g^{-1} ≈206 @ 0.5 A g^{-1}	≈76% (100 @ 0.05 A g^{-1})	[86]

As shown in Tables 2.1 and 2.2, only a minority of research has utilized pure MoS_2 as the anode materials for SIBs and PIBs. This is due to its low stability when used without any supporting matrices.[95,127,175] The focal point of the investigations on pure MoS_2 lies in the design of specific nanostructures, characterized by 1T phases, structural defect points, and thin-layered structures with expanded interlayer distances. However, most of studies concerning pure MoS_2 in SIBs and PIBs have adjusted the potential window to minimize conversion reactions and to delve into the intercalation/deintercalation processes rather than conversion reactions. Consequently, the reported capacities have not reached significant highs. For instance, Xu et al. altered the stoichiometric ratio of Mo source to S source during hydrothermal synthesis, resulting in two variations of MoS_2 nanoflowers: one without defects (stoichiometric ratio; MoS_2 NFs) and another with defects (utilizing

additional sulfur source; D-MoS_2 NFs).[127] They evaluated their performance as the anode material in PIBs. Interestingly, the defective structure exhibited a higher diffusion coefficient and capacities compared to the non-defective counterpart (Figure 2.13a,b). D-MoS_2 NFs displayed relatively robust cyclic stability when charged and discharged within a potential window of 0.5-2.5 V due to absence of the conversion reactions (see the cycling test results and galvanostatic charge-discharge (GCD) curves in Figure 2.13c and Figure 2.13d, respectively).

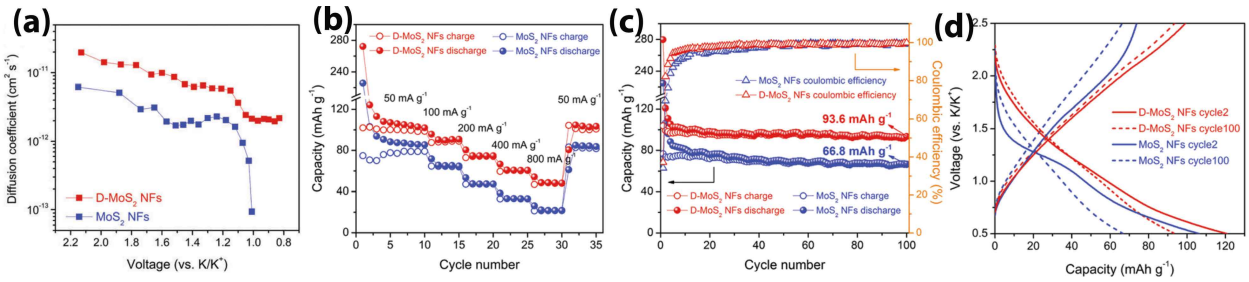

Figure 2.13: Comparison of D-MoS_2 NFs and MoS_2 NFs in terms of (a) K^+ diffusion coefficient, (b) rate performance, (c) cycling stability, and (d) 2_{nd} and 100_{th} GCD curves at 50 mA g^{-1}.[127]

Some other studies concerning pure MoS_2, explored the synthesis of mixed crystal phases comprising of both 1T and 2H phases. In two separate studies, Wu et al.[107] and Ye et al.,[147] demonstrated that mixed-phase 1T/2H-MoS_2 exhibited enhanced capacity and kinetics for Na^+ storage compared to its semiconducting 2H phase. However, these investigations employed a voltage window of 0.4-3 V, leading to decent cycle stability at the expense of somewhat limited capacity (below 350 mAh g^{-1} at a current of 100 mA g^{-1}).

Ding et al. achieved the synthesis of MoS_2 with a 100% 1T phase using a hydrothermal method under the influence of a magnetic field (magneto-hydrothermal processing).[175] They demonstrated that, in the absence of a magnetic field, their synthesized sample (MoS_2-0T) contained approximately 25% 1T phase. However, upon application of a 9 T magnetic field, the synthesized sample (MoS_2-9T) transitioned to 100% 1T phase composition (Figure 2.14a). Their work showcased the superiority of MoS_2-9T over the MoS_2-0T as anodes for SIBs. They observed enhanced ion diffusion coefficient (Figure 2.14b), rate performance (Figure 2.14c; 224 mAh g^{-1} vs. $\approx$120 mAh g^{-1} at 8 A g^{-1}), and stability (Figure 2.14d). Nevertheless, their study limited the potential window to the range of 0.3-3 V, effectively reducing the likelihood of the conversion reactions.

A notable study on pure MoS_2 for Na^+ storage with voltages close to zero is the work by Sun et al.[95] They compared MoS_2 having a high percentage of the 1T phase, synthesized

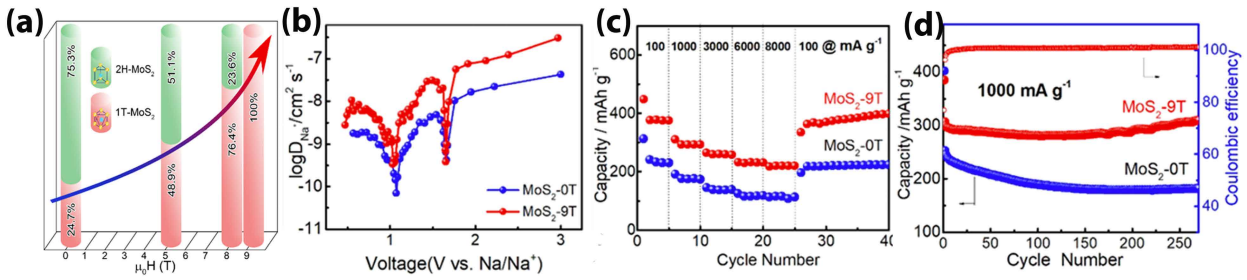

Figure 2.14: (a) 1T/2H percentage in the MoS_2 synthesized under different magnetic fields and comparison of (b) Na^+ diffusion coefficient, (c) rate performance, and (d) cycling stability (at 1,000 mA g^{-1}) of MoS_2-0T and MoS_2-9T.[175]

via the thermal-driven ion intercalation assisted exfoliation, against bulk 2H-MoS_2 as anodes for SIBs. By employing a potential window of 0.01-2.7 volts, the 1T phase containing sample delivered a relatively robust capacity of 450 mAh g^{-1} at 50 mA g^{-1}, maintaining an impressive stability of approximately 98% after 150 cycles at 100 mA g^{-1}. This notable stability is attributed to the ability of 1T phase to capture sulfur species generated during conversion reactions, as previously discussed. In another investigation on the use of 1T MoS_2 in Li-S batteries, findings indicated that a substrate based on mixed 1T/2H-phase MoS_2 effectively trapped sulfur species, resulting in remarkable long-term stability (≈79% over 300 cycles at 0.5 C) during cycling of the Li-S battery.[176] However, such high stabilities are rare in most of reports related to pure MoS_2, specifically those synthesized by top-down approaches, for alkali ion storage.

A slight oxidation of pure MoS_2 has been proven effective in enhancing its cycling stability in SIBs. Yao et al. were inspired by the steel quenching process, a common surface treatment technique for metallic materials, to develop a method involving heating MoS_2 nanosheets to 350 °C at a rate of 5 °C min^{-1} in an air atmosphere, followed by rapidly quenching them in deionized water at room temperature to produce MoS_2 with large vacancies bundled by ultrathin MoO_3 (BD-MoS_2, Figure 2.15a).[128] During the oxidation process, some Mo^{4+} ions depart from their positions and are oxidized to Mo^{6+}, resulting in vacancy defects. The material was then rapidly cooled to maintain its instantaneous state. As an SIB anode, BD-MoS_2 facilitated Na^+ insertion into the material and diffusion between the layers through the vacancies, rather than solely along the MoS_2 layers, enabling 3D Na^+ diffusion for faster kinetics, as demonstrated in rate performance tests compared to non-defective MoS_2 (Figure 2.15b; 262 mAh g^{-1} vs. ≈10 mAh g^{-1} at 5 A g^{-1}). Additionally, the bundled architecture maintained the structural integrity of the electrode (see cycling stability comparison of BD-MoS_2 with non-defective MoS_2 in Figure 2.15c). The high stability observed

within a potential window of 0.01-3 V was attributed to the bundling architecture, which effectively reduced the stacking of MoS_2. To validate this, they removed the MoO_3 content with a NaOH solution and conducted cycling tests on the resulting product, revealing drastic capacity decay within the first 100 cycles (see Figure 2.15d).

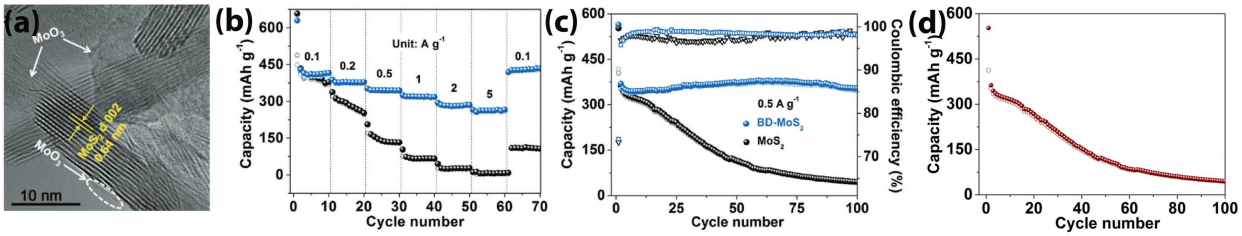

Figure 2.15: (a) TEM image of BD-MoS_2 illustrating the MoS_2 structure bundled by ultrathin MoO_3 and comparison of its (b) rate performance and (c) cycling stability (at 500 mA g^{-1}) with as-prepared MoS_2; (d) cycling stability of MoS_2 sample obtained by washing off the MoO_3 content of BD-MoS_2.[128]

Based on these examples, phase engineering and structural modifications, such as interlayer expansion and defect introduction, can significantly enhance the electrochemical performance of MoS_2 in SIBs and PIBs by improving conductivity and ion diffusion kinetics, and can also slightly enhance cycling stability. However, as summarized in Tables 2.1 and 2.2, these strategies often requires compositing MoS_2 with other materials, particularly conductive carbon-based ones, to achieve a synergistic effect. These nanocomposite materials not only boost conductivity and ion diffusion but also provide additional advantages like structural reinforcement. As explained earlier, compounding MoS_2 with common carbon materials like graphene and carbon nanotubes enhances cycling stability. Aside from traditional crystalline carbon materials, the combination of MoS_2 with amorphous carbon materials, sometimes by template-assisted synthesis methods, enables the creation of composites with diverse structures, including three-dimensional, hierarchical, hollow configurations, etc. These structures offer more than just electrical conductivity and cycling stability; they also enhance the interaction between the electrode and the electrolyte, thereby improving overall battery performance. For example, Li et al. synthesized a hollow microcube framework constructed by defect-rich MoS_2 nanosheets (HMF-MoS_2) through a zeolite-like-framework-engaged strategy (Figure 2.16a).[125] They utilized a synthesis method involving a Zn, Mo-based hybrid zeolitic imidazolate framework (HZIF-Zn/Mo). Initially, HZIF-Zn/Mo was dispersed in an ethanol solution, followed by the addition of thioacetamide (sulfur source). This mixture was then refluxed at high temperature, resulting in the formation of HMF-MoO_x/ZnS through sulfidation. Afterward, the mixture was subjected to calcination treatment in the presence

of sulfur, which converted the Mo component to the MoS_2 phase while enhancing the crystallinity of the ZnS shell, leading to the creation of HMF-MoS_2/ZnS. Finally, the desired HMF-MoS_2 phase was obtained by selective removal of the ZnS phase using hydrochloric acid (HCL) solution (see Figure 2.16b for its TEM image). HMF-MoS_2 possessed a large quantity of Mo vacancies and slightly expanded interlayer distance (0.66 nm), facilitating the ion diffusion kinetics. Based on thermogravimetric analysis, they found an 8 wt% of carbon residue in HMF-MoS_2, improving its conductivity. The robust hierarchical hollow architecture with more exposed electrochemical active species endowed HMF-MoS_2 high specific capacity and large electrolyte/electrode contact area. Moreover, the directional alignment of the ultrathin MoS_2 nanosheets facilitated Na^+ transfer and diffusion. The comparison of rate performance (Figure 2.16c) and charge/discharge cycling tests (Figure 2.16d) between HMF-MoS_2 and pristine MoS_2 distinctly underscored the enhancements resulting from the unique characteristics of HMF-MoS_2.

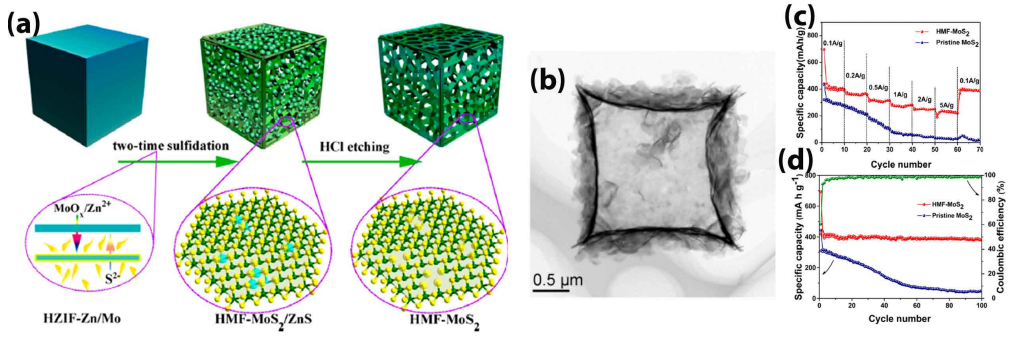

Figure 2.16: (a) Synthesis steps and (b) TEM image of HMF-MoS_2, along with a comparison of (c) its rate performance and (d) charge/discharge cycling with pristine MoS_2 as anodes for SIBs.[125]

Wang et al. developed a 3D ordered porous MoS_2/C material using a straightforward template-assisted nanocasting technique.[149] Their approach involved the use of $(NH_4)_2MoS_4$, PVP, and SiO_2 nanospheres as the precursors for MoS_2, carbon, and the hard template, respectively (Figure 2.17a). Upon the elimination of the SiO_2 (by HF washing) templates, they successfully obtained a 3D ordered porous structure comprising of interconnected hollow MoS_2/C spheres with expanded interlayer distances of 9.8 Å(see the TEM image in Figure 2.17a). This unique macro/mesoporous architecture endowed the synthesized MoS_2/C material with pseudocapacitive behavior, showcasing remarkably high sodium storage capacity. Figure 2.17b-d present a comparison of the nanocomposites (with two different MoS_2/C compositions) with pure MoS_2 as anodes for SIBs, highlighting the significant impact of the distinct structure by reducing charge transfer resistance, improving solid-state

ion diffusion, enhancing rate performance, and ensuring cycling stability.

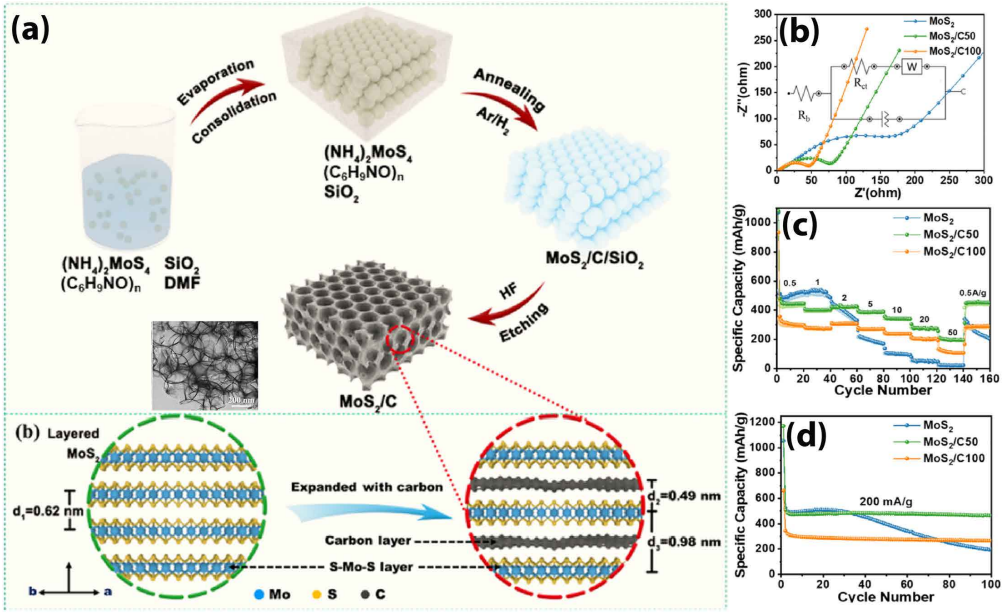

Figure 2.17: (a) Synthesis scheme and TEM image of 3D ordered porous MoS_2/C material, with comparisons of (b) Nyquist plots, (c) rate performance, and (d) charge/discharge cycling stability of MoS_2/C50 (50 mg PVP utilized in the synthesis) and MoS_2/C100 (100 mg PVP utilized in the synthesis) with pure MoS_2 as anodes for SIBs.[149]

Kim and colleagues developed a composite material consisting of MoS_2 and carbon with cubic nanorooms, MoS_2/C-NR, by employing NaCl as a washable template (Figure 2.18a).[177] This approach, serving as a versatile synthesis method, was applied to create various metal sulfides enclosed within a carbon shell featuring cubic nanorooms (MeS_x/C-NR). Initially, a heat treatment at 700 °C was applied to a mixture containing metal salt ($(NH_4)_6Mo_7O_{24}.4H_2O$), dextrin, and NaCl to yield MoO_x/C-NR, followed by NaCl removal through water washing. Subsequently, sulfurization using thiourea (CH_4N_2S) at 400 °C led to the formation of MoS_2/C-NR. Additionally, a nanocomposite without nanorooms (MoS_2/C) was also synthesized using the same method but without NaCl. A comparison of the cycling stability and rate performance between the two products as anodes for SIBs revealed that, although the carbon content contributed to the overall cycling stability (Figure 2.18b), the presence of nanorooms in MoS_2/C-NR substantially enhanced both capacity and rate performance (Figure 2.18c). This enhancement was attributed to the rational design, which significantly increased the contact area with the electrolyte, thereby facilitating electrochemical reactions without compromising structural integrity.

Jia et al synthesized a bamboo-like hollow tubes nanocomposites of MoS_2 and nitrogen

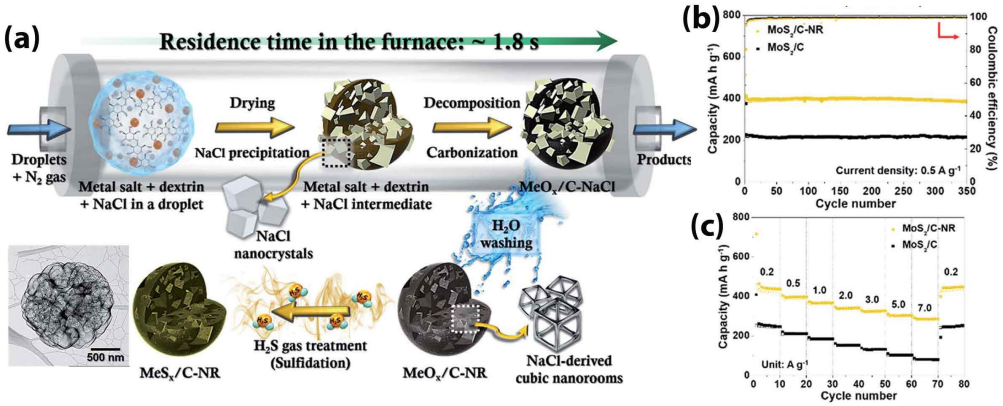

Figure 2.18: (a) Schematic illustration of the synthesis method of MeS_x/C-NR and TEM image of MoS_2/C-NR, accompanied by comparisons of the (b) charge/discharge cycling and (c) rate performance of MoS_2/C-NR with MoS_2/C (the composite without nanorooms) as anodes for SIBs.[177]

doped amorphous carbon.[21] with MoS_2/N-doped carbon interfaces (Figure 2.19a). To do so, they firstly synthesized MoS_2/oleylamine (OAm) tubes by a solvothermal method using MoO_3 as the Mo source, S powder as the sulfur source, OAm as the additive, and ethanol-water solution as the mixed solvent. By annealing this product, they obtained the tubes with MoS_2/N-doped carbon interfaces (MoS_2/N-doped-C tubes). The structure resembling bamboo features gaps along its axis, coupled with an inner cylindrical hollow space (see SEM and TEM images of the MoS_2/N-doped-C tubes in Figure 2.19b and Figure 2.19c, respectively), which helps alleviate strains in both radial and vertical directions, thereby ensuring robust structural integrity for prolonged cycling stability. Furthermore, the nitrogen-doped carbon layers, constituting part of the layered structure, create a framework that encapsulates potassiation products (like polysulfide and Mo nanoparticles) and also effectively impedes the continuous expansion of the solid electrolyte interphase within the particles. All these feature along with interlayer distance of 10.3 Å led to the enhanced ion kinetics (Figure 2.19d), and superior rate performance and cycling stability compared to pure MoS_2 as depicted in Figure 2.19e,f.

Some other studies have ventured into synthesizing complex structures to further enhance the performance of MoS_2-based for big alkali ion storage. Particularly, such complex structures with multifunctional features can be synthesized by employing both crystalline and amorphous carbon contents (Table 2.1 and Table 2.2). For instance, Hu et al. developed a few-layered MoS_2 nanosheets on RGO crosslinked hollow carbon spheres (MoS_2-RGO/HCS).[138] In the synthesis, hollow carbon spheres (HCS) were first prepared via self-assembly using a carbon resin and a silicate source (Figure 2.20a). Subsequently, the silica

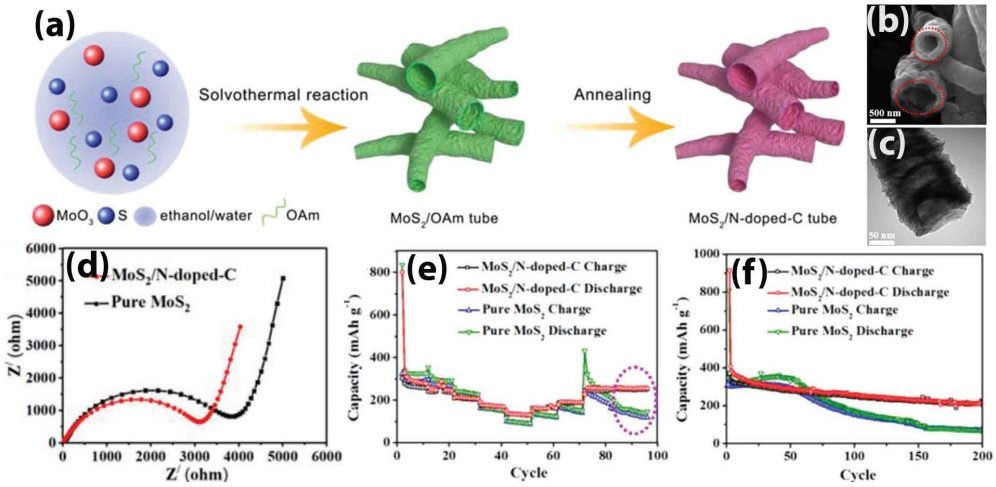

Figure 2.19: (a) Schematic illustration of MoS_2/N-doped-C hollow tube and its (b) SEM and (C) TEM images; comparison of (d) Nyquist plots, (e) rate performance, and (f) cycling stability of MoS_2/N-doped-C and pure MoS_2.[21]

cores were eliminated through acid washing (Figure 2.20a). Next, amino-functionalized HCS was obtained by treating the hollow carbon spheres with a solution of poly(allylamine hydrochloride). MoS_2-RGO/HCS was then synthesized through a solvothermal reaction incorporating MoS_2 precursor, RGO, and the amino-functionalized HCS, followed by annealing at 800 °C (see TEM image of MoS_2-RGO/HCS at Figure 2.20b). Finally, the synthesis involved a solvothermal reaction incorporating MoS_2 precursor, RGO, and the amino-functionalized HCS, followed by annealing at 800 °C to produce the desired nanocomposite material (see TEM image of MoS_2-RGO/HCS at Figure 2.20b). This nanocomposite was characterized by a hierarchical porous structure spanning micro-, meso-, and macro-scales pore size. This hierarchical porous nature, in conjunction with 3D architectures, served as a reservoir for ions and electrolytes, minimizing diffusion paths and providing ample buffer space to mitigate volume changes throughout charge/discharge cycles. As an anode for SIBs, this structure exhibited lower charge transfer kinetics (Figure 2.20c) and superior rate performance (Figure 2.20d) compared to pure MoS_2 or its composites with RGO or HCS. Additionally, it demonstrated enhanced cyclic stability, outperforming these counterparts (Figure 2.20e).

Another instance of integrating porous MoS_2 composite with both crystalline and amorphous carbon is exemplified by the creation of porous MoS_2/carbon spheres anchored on 3D interconnected multiwall carbon nanotube networks (MoS_2/C-MWCNT), synthesized by Chen et al.[56] Their synthesis aimed to produce MoS_2/C-MWCNT for use as an anode in SIBs. In the initial phase of synthesis, they employed an emulsion comprising of CS_2-PVP-Na_2MoO_4 (Figure 2.21a). Within this emulsion, nonpolar CS_2 oil droplets were

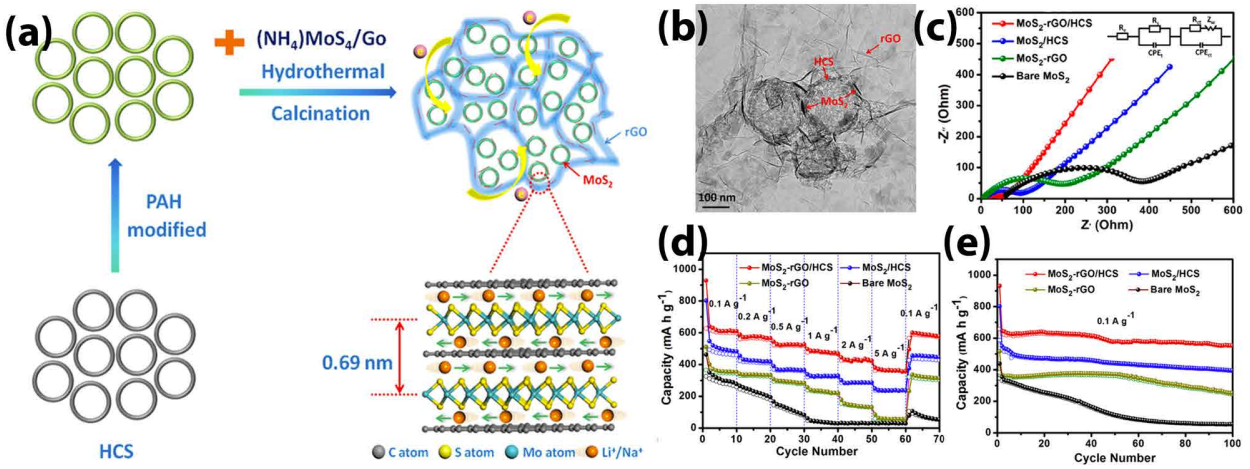

Figure 2.20: (a) Synthesis process and (b) TEM image of MoS_2 nanosheets on RGO crosslinked hollow carbon spheres (MoS_2-RGO/HCS); comparison of (c) Nyquist plots, (d) rate performance, and (e) cycling stability of MoS_2-RGO/HCS with MoS_2/HCS, MoS_2/RGO, and bare MoS_2.[138]

enveloped by PVP surfactants, arranged with their hydrophobic alkyl groups oriented inwards towards the CS_2 droplet and their hydrophilic amide groups facing the water, resulting in the self-assembly of spherical micelles and the creation of a stable microemulsion. The MoO_4^{2-} anions were adsorbed onto the functional groups of PVP. Upon the addition of carboxylated MWCNTs, they interacted with CS_2 micelles through C(O)−O−C(S)−S species, formed from the reaction of CS_2 with C(O)−OH under alkaline conditions. Throughout the hydrothermal process, the CS_2 soft template released sulfur to generate pores and reduced MoO_4^{2-} anions to MoS_2 on the surface of the PVP. Following calcination at 800 °C, the MoS_2 nanosheets were deposited onto the carbon surface, forming continuous porous spheres interconnected by the 3D MWCNT networks (see Figure 2.21b for the TEM image of MoS_2/C-MWCNT). As evidenced by rate performance testing, electrochemical impedance spectroscopy (EIS) analysis, and charge/discharge cycling (Figure 2.21c-e), MoS_2/C-24MWCNT (24 mg MWCNT used in its synthesis) exhibited markedly superior electronic, ionic, and structural characteristics compared to traditional MoS_2/C spheres (prepared without MWCNT). These advantages stem from its unique design at both the active microstructure and electrode microstructure levels. Firstly, the presence of few-layered, defect-rich MoS_2 nanosheets with expanded interlayers (6.4 Å) and ample mesopores/macropores facilitates Na^+ transport. Additionally, MoS_2 anchored on N-doped

carbon enhances electron transport and structural stability at the active material microstructure level. Secondly, at the electrode microstructure level, the incorporation of a 3D conductive MWCNT network establishes pathways for enhanced electron/ion transfer and reduces the diffusion path for electrons/ions at the inter-particle and intra-particle interfaces of the MoS_2/C spheres. Moreover, the porous MoS_2/C spheres anchored onto the 3D MWCNT networks via robust chemical bonding preserve the electrode's structural integrity during repeated discharge/charge cycles.

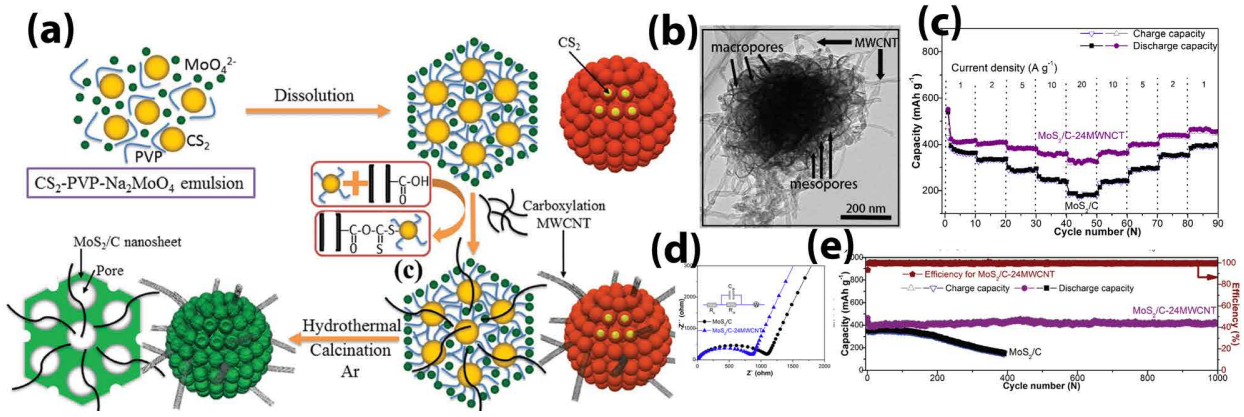

Figure 2.21: (a) Synthesis steps and (b) TEM image of MoS_2/carbon spheres anchored on 3D interconnected multiwall carbon nanotube networks (MoS_2/C-MWCNT) and comparison of (c) rate performance (d) Nyquist plots, and (e) cycling stability with MoS_2/C (synthesized without MWCNT).[56]

Accordingly, as summarized in Tables 2.1 and 2.2 the nanocomposites of MoS_2 and carbonaceous materials can provide decent stability, enhanced capacities ($>$ 600 mAh g^{-1} and $>$ 300 mAh g^{-1} at 0.1 A g^{-1} in SIBs[138,168,169] and PIBs[54,74,174], respectively) and remarkable rate capabilities ($>$ 400 mAh g^{-1} at 5 A g^{-1} in SIBs[136,138,168] and $>$ 300 mAh g^{-1} at 1 A g^{-1} in PIBs[74,174]). However, the hybridization of MoS_2 to enhance its potential for Na^+ and K^+ storage extends beyond carbon. Numerous studies explored its hybridization with metal sulfides,[150,151,173,178–180] metal oxides,[85,181–185] MXenes,[86,171,186–189] polymers,[91] and ternary composites of MoS_2 with these materials alongside carbon-based counterparts (Tables 2.1 and 2.2). The focus of some of these studies was on designing nanocomposites that provide ultrahigh cycling stability, at the cost of the capacity that is lower than that of pure MoS_2.[85,148] For example, Deng et al., synthesized a flexible fibre paper anode consisting of Nb_2O_5, MoS_2, soft carbon, and hard carbon (carbon nanofibers, CNFs). In the synthesis, they first fabricated $Nb(C_2H_5O)_5$@PAN nanofibers via electrospinning (Figure 2.22a). Then, they applied thermal treatment to convert them into black Nb_2O_5 CNFs. In the next step, with the aid of PVP, MoS_2 nanospheres were grown on the surface of Nb_2O_5 CNFs. To

enhance electronic conductivity, glucose-derived soft carbon layers were strongly attached to the surface of Nb_2O_5@MoS_2 CNFs in the final annealing step (see Figure 2.22b for SEM image of the product). The product named Nb_2O_5@MoS_2@C CNFs, when used as an anode for SIBs, showed relatively lower capacities compared to pure MoS_2 (Figure 2.22c,d) but demonstrated outstanding cycling stability, maintaining around 95% capacity over 1,000 charge/discharge cycles at 1 A g^{-1} and around 82% over 20,000 cycles at 5 A g^{-1}. As evidenced from the rate performance and cycling test results (Figure 2.22d,e), Nb_2O_5@MoS_2@C CNFs inherited the high stability of Nb_2O_5 and high capacity of MoS_2, and benefited from structural integrity and conductivity of CNFs and coated carbon layers.

Overall, as shown in Tables 2.1 and 2.2, MoS_2-based nanocomposites with enhanced conductivity (such as those rich in the 1T phase, hybridized with carbon or MXene), enlarged interlayer distances, and defect-rich structures exhibit improved capacities and rate capabilities due to enhanced ion kinetics. However, in SIBs and PIBs, the lack of cycling stability tends to be a more pressing concern compared to ion kinetics. While enhanced ion mobility can improve the rate capability, the structural degradation of the electrode materials over repeated cycles often leads to significant capacity loss. Hybridizing with crystalline and amorphous carbon can provide enhanced stability through the mechanisms explained in Section 2.4.3. Additionally, incorporating an ultra-stable core (such as Nb_2O_5 or sodium titanate) into the nanocomposite design can further elevate stability.

2.5.2 Mg^{2+} Storage

Magnesium metal anodes in MIBs exhibit a relatively low reduction potential of -2.37 V vs. SHE, and the divalent nature of Mg^{2+} contributes to the impressive volumetric capacity of 3833 mAh cm^{-3}, surpassing lithium metal's capacity by 86%.[26] Moreover, magnesium is abundantly and evenly distributed, making it cost-effective and helping mitigate concerns regarding the depletion of lithium resources. MIBs are more cost-effective and safer batteries compared to LMBs due to dendrite-free charge/discharge mechanism, coupled with magnesium's high melting point, non-toxicity and abundance.[190,191]

MoS_2 as a cathode for MIBs is no exception and faces challenges similar to other cathodes, primarily due to the sluggish solid-state kinetics caused by the strong Coulombic interactions between Mg^{2+} ions and the MoS_2 host, triggered by the divalent nature of Mg^{2+}.[16,192] Table 2.3 offers a comprehensive overview of MoS_2-based cathodes for MIBs, including their properties and electrochemical performances. In contrast to Na^+ and K^+ storage cases, conversion reactions do not occur within the potential windows typically applied in MIBs,

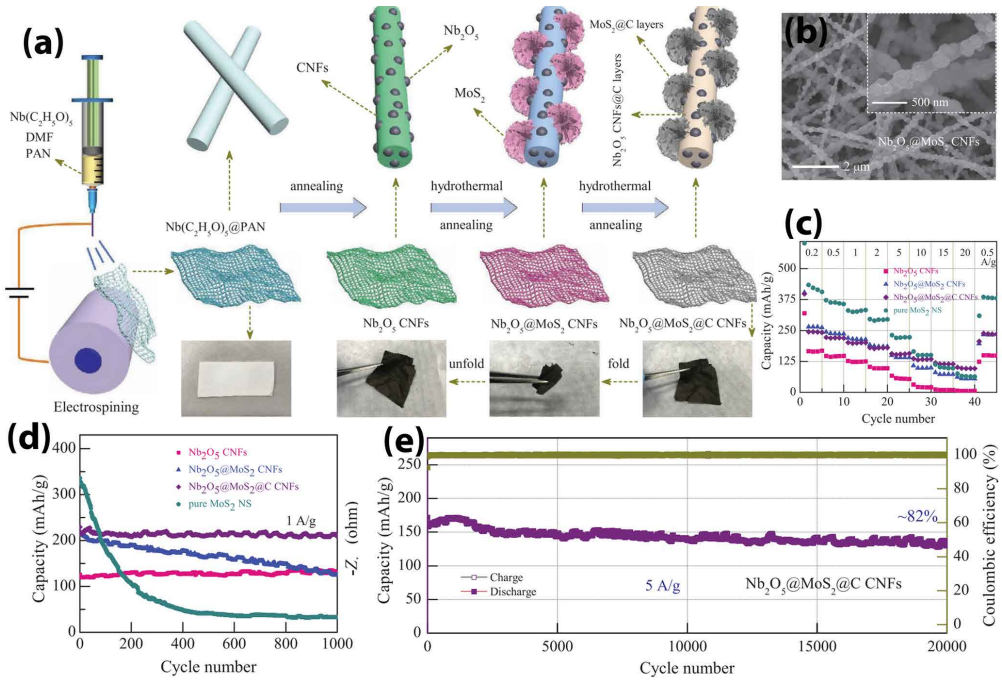

Figure 2.22: (a) The process of synthesis of Nb_2O_5@MoS_2@C CNFs and its (b) SEM image; comparison of (c) rate performance and (d) cycling stability of Nb_2O_5@MoS_2@C CNFs and its components; (e) cycling stability of Nb_2O_5@MoS_2@C CNFs over 20,000 cycles at 5 A g^{-1}.[85]

which are usually within 0.01 to 2 V vs. Mg/Mg^{2+}. Thus, while cycling stability issues persist, they are not as severe as those in SIBs and PIBs. The more significant challenges in MIBs relate to kinetics. Therefore, as shown in Table 2.3, numerous studies have reported the use of MoS_2 as a cathode for MIBs without hybridizing it with structural integrity enhancers, with the focus on kinetics improvement.[16,26,97,114,116]

Table 2.3: Key structural features and performance characteristics of MoS_2-based electrode active materials for MIBs.

Material	Key features	Capacity (mAh g^{-1})	Cycling stability (cycles @ current density)	Ref.
1T/2H-MoS_2	Enlarged interlayer spacing Metallic conductivity	130 @ 0.05 A g^{-1} 25 @ 1 A g^{-1}	90% (200 @ 0.05 A g^{-1})	[97]
MoS_2 with structural water	Enlarged interlayer spacing (9.4 Å) Weakened interaction with Mg^{2+}	≈140 @ 0.05 A g^{-1} ≈75 @ 0.5 A g^{-1}	≈91% (300 @ 0.02 A g^{-1})	[116]
PEO-intercalated MoS_2	Enlarged interlayer spacing (14.5 Å) High ionic conductivity	≈70 @ 0.005 A g^{-1} ≈25 @ 0.5 A g^{-1}	94% (30 @ 0.005 A g^{-1})	[16]
Ionomer@1T/2H-MoS_2	Enlarged interlayer spacing (11.1 Å) Metallic conductivity Compatible with low-polarity solvents	144 @ 0.02 A g^{-1} 32 @ 1 A g^{-1}	>100% (100 @ 0.05 A g^{-1})	[26]
PVP incorporated MoS_2	Enlarged interlayer spacing (9.7 Å)	≈143 @ 0.02 A g^{-1} 43 @ 0.2 A g^{-1}	≈86% (100 @ 0.02 A g^{-1})	[114]
Graphene-intercalated MoS_2	Enlarged interlayer spacing (9.8 Å)	116 @ 0.02 A g^{-1}	71% (50 @ 0.02 A g^{-1})	[115]

Continued on next page

Table 2.3 – continued from previous page

Material	Key features	Capacity (mAh g^{-1})	Cycling stability (cycles @ current density)	Ref.
	Enhanced conductivity			
MoS_2@carbon@polyaniline	Enhanced conductivity Carbon coated ternary structure	143 @ 0.1 A g^{-1} ≈40 @ 1 A g^{-1}	≈89% (100 @ 0.1 A g^{-1})	[193]
MoS_2/graphene heterostructure	Specific ionic diffusion path Reduced Mg-diffusion barrier	210 @ 0.02 A g^{-1} 90 @ 0.5 A g^{-1}	84% (300 @ 0.02 A g^{-1}) 83% (500 @ 0.5 A g^{-1})	[110]
Cu-Doped MoS_2@Graphdiyne	Extended π-conjugated structure Abundant active sites Buffering volume change	≈170 @ 0.01 A g^{-1} ≈91 @ 1 A g^{-1}	>100% (200 @ 0.05 A g^{-1}) >100% (300 @ 0.5 A g^{-1})	[76]
MoS_2-infilled microcapsule	Hollow structure Conductive carbon shell	≈161 @ 0.05 A g^{-1} ≈65 @ 0.3 A g^{-1}	≈62% (100 @ 0.05 A g^{-1})	[152]
MXene-supported layered MoS_2	Enhanced conductivity	165 @ 0.05 A g^{-1} 93 @ 0.2 A g^{-1}	≈65% (50 @ 0.05 A g^{-1})	[194]

MoS_2 interlayer expansion has been identified as the primary requisite for achieving sufficient Mg^{2+} storage. Various materials such as hyperbranched polyethylene ionomer,[26] PEO,[16] PVP,[114] structural water,[116] and graphene[115] have been used as the intercalants between the layers of exfoliated MoS_2, resulting in increased interlayer distances. Depending on their specific properties, these guest materials can impart additional advantageous characteristics to the composites alongside interlayer expansion.

A study by Liang et al. synthesized PEO-intercalated MoS_2 to adjust the interlayer spacing, highlighting the significance of interlayer expansion in enhancing the storage capacity of Mg^{2+}.[16] Following delamination of MoS_2 via the n-butyllithium exfoliation method, as depicted in Figure 2.23a, the layers undergo restacking in the absence of any intercalant, with some water molecules retained between them. Conversely, with the introduction of a polymer such as PEO, it becomes intercalated between the layers during the restacking process, leading to an expansion in the interlayer spacing of the resultant product. In the synthesis of MoS_2 intercalated with PEO, a control over the quantity of PEO utilized enabled a fine adjustment of the interlayer distance (1.19 Å and 14.5 Å for PEO_1-MoS_2 and PEO_2-MoS_2 with MoS_2/PEO ratios of 4:1 and 1:1, respectively). As the interlayer distance of MoS_2 increased from 6.15 Å (in bulk MoS_2) to 14.5 Å, specific capacity improved by 200% and Mg^{2+} mobility increased by 100 times. (see Mg^{2+} diffusivity and rate performance results comparison in Figure 2.23b and Figure 2.23c, respectively)

As an alternative top-down synthesis approach for obtaining interlayer-expanded MoS_2, Rahmatinejad et al. utilized a hyperbranched polyethylene ionomer containing quaternary ammonium cations to modify 1T/2H mixed-phase MoS_2 (MP-MoS_2).[26] Through this method, they achieved an ionomer modified MoS_2 (I@MP-MoS_2) with interlayer distance of 11.1 Å(Figure 2.24a). The choice of this ionomer was based on several factors, including the

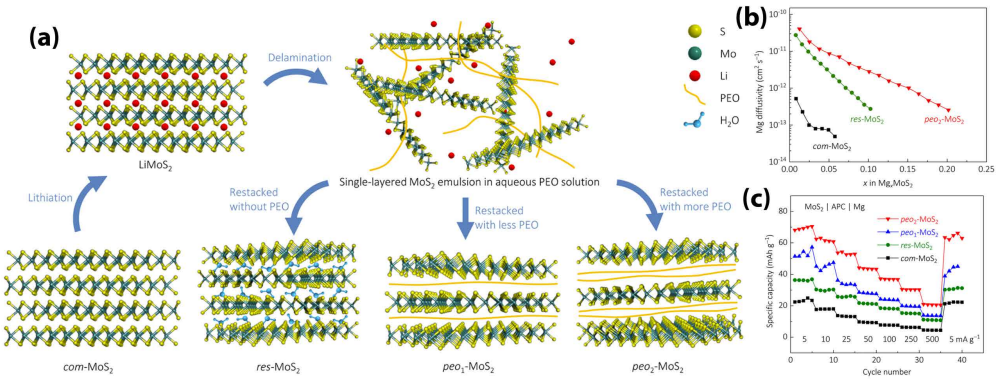

Figure 2.23: (a) Schematic illustration of the n-buthyllithium assisted exfoliation of MoS_2, res-MoS_2 and PEO-MoS_2 nanocomposites and comparison of (b) Mg^{2+} diffusivity in them vs. the concentration of intercalated Mg^{2+} obtained by galvanostatic intermittent titration technique (GITT), and (c) their rate performance.[16]

strong interaction of its positively charged quaternary ammonium ions with the negatively charged surface of the MoS_2 layers,[195,196] and its high dispersibility in nonpolar/low-polarity solvents like THF owing to its nonpolar hyperbranched polyethylene skeleton. All-phenyl complex (APC) in THF is widely recognized as a promising electrolyte for MIBs.[197] The excellent compatibility of I@MP-MoS_2 with THF contributes to its superior wetting properties and favorable electrode/electrolyte interactions when employed as an active electrode material for MIBs. The ability of the electrodes to be wetted by electrolyte is an essential factor that impacts the accessibility of electrolyte and the speed at which charge carriers diffuse within the electrodes.[198] The combination of a high content of the 1T phase (53%) with an expanded interlayer distance and improved electrode/electrolyte interface interactions, enabled I@MP-MoS_2 to achieve a remarkable capacity of 144 mAh g^{-1} at 20 mA g^{-1}, significantly outperforming its parent bulk material that showed negligible capacity under the same current conditions (Figure 2.24b).

Such modified MoS_2 cathodes with enlarged interlayer distances and enhanced conductivity from the 1T phase show significant improvement in Mg^{2+} storage compared to bulk MoS_2. However, hybridizing them with conductive agents can further enhance their performance, particularly in terms of rate capability. Thus, the synthesis of MoS_2-based cathode materials for MIBs extends beyond top-down methods. Bottom-up approaches (more facile route for hybridizing) have been employed to create its various nanocomposites incorporating carbon-based materials, MXene, and conductive polymers (Table 2.3).[76,110,152,183,193,194]

As an example of complex structures with multiple advantages, Zhuo et al. synthesized a hierarchical nanocapsule encapsulating Cu-doped MoS_2 (Cu-MoS_2) nanopetals within an

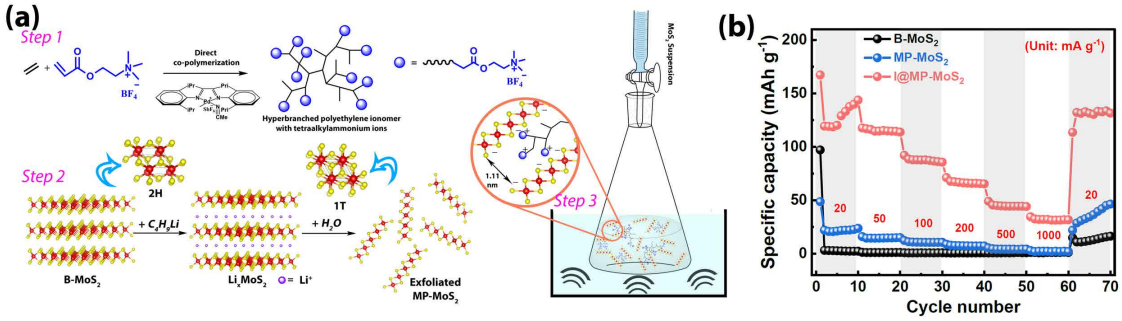

Figure 2.24: (a) The synthesis steps of ionomer intercalated mixed phase 1T/2H-MoS_2 and (b) comparison of its rate performance with mixed-phase 1T/2H-MoS_2 and bulk MoS_2.[26]

organic-carbon-rich nanotube made of hydrogen-substituted graphdiyne (HsGDY), termed Cu-MoS_2@HsGDY.[76] They used Cu^{2+} coordinated with L-cysteine as the sacrificial template. Next, they applied a thin layer of HsGDY onto the nanowires' surface through a cross-linking process using a Glaser coupling reaction involving 1,3,5-triethynylbenzene to obtain Cu-cysteine@HsGDY. Then, Cu-cysteine@HsGDY nanowires were subjected to a solvothermal reaction with $(NH_4)_2MoS_4$ in dimethylformamide solvent, rendering Cu-MoS_2@HsGDY after 15h at 210 °C (Figure 2.25a). HsGDY possesses a π-conjugated structure, rendering it conductive and suitable as an active material for batteries. Furthermore, Cu is incorporated into MoS_2, forming the Cu−Mo−S phase by substituting on Mo sites, leading to the formation of the 1T phase due to the mismatch in bond length between Cu and Mo atoms. Additionally, the unique structure of encapsulated Cu-MoS_2 nanoboxes provides a stress-release skeleton and accessible active sites for Mg^{2+} storage. Comparisons of the Nyquist plots and rate performance of pristine MoS_2, Cu-MoS_2, and Cu-MoS_2@HsGDY revealed the lowest charge transfer resistance and the best rate performance with Cu-MoS_2@HsGDY (Figure 2.25b,c).

Overall, research on magnesium ion storage in MoS_2 indicates that improving the ion transport kinetics is crucial to enhancing electrochemical performance. Specifically, strategies such as enlarging the interlayer spacing of MoS_2 to facilitate easier ion intercalation, improving its intrinsic electrical conductivity, and designing shorter ion transport pathways are essential to address the inherently sluggish diffusion of Mg^{2+}, which have higher charge density compared to alkali ions. Although some degree of stability issues may still arise, particularly due to the limited conversion reactions involved in Mg^{2+} storage, these are not as severe as those typically seen with alkali ion storage. As a result, efforts to enhance kinetics can be effectively implemented on pure MoS_2 without the structural reinforcement typically achieved through hybridization. However, incorporating hybrid materials, such as

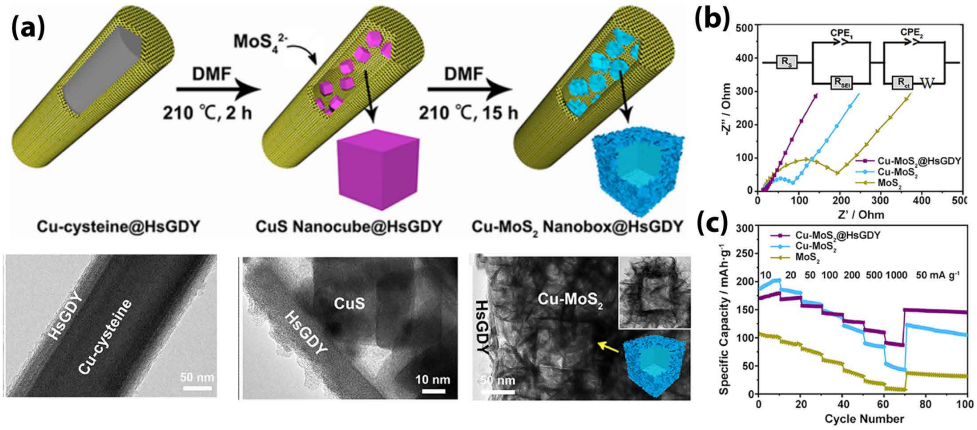

Figure 2.25: (a) Schematic illustration of the synthesis of hierarchical porous Cu-MoS_2@HsGDY nanocapsules and TEM images corresponding to each step and comparison of (b) the Nyquist plots and (c) the rate performance of Cu-MoS_2@HsGDY with Cu-MoS_2 and MoS_2.[76] Licensed under CC-BY 4.0, American Chemical Society

graphene, MXene, or other conductive nanomaterials, could introduce synergistic effects, further improving both the conductivity and mechanical integrity of the electrode, leading to even better overall performance.

2.5.3 Zn^{2+} Storage

ZIBs emerge as a promising alternative technology for large-scale energy storage, primarily due to the cost advantage of zinc over lithium. This affordability is further highlighted by the use of conventional aqueous electrolytes in these batteries, which not only mitigates flammability risks and provides high ionic conductivity but also contributes to a lower overall cost compared to traditional organic electrolytes. The direct utilization of zinc metal as an anode in these batteries is supported by its resistance to water coupled with its high theoretical capacity of 820 mAh g^{-1} and 5855 mAh cm^{-3}. Additionally, the low standard redox potential of zinc metal at -0.76 V vs. SHE further underscores its suitability for direct application as an anode in ZIBs.[27] Owing to its divalent nature, the storage of Zn^{2+} presents challenges like those encountered with Mg^{2+}. The electrostatic interactions arising from its bivalency hinder the effective diffusion of the ion into the solid state, resulting in sluggish kinetics. However, the sluggish kinetics of Zn^{2+} is less pronounced compared to Mg^{2+}, primarily due to its lower charge density.[17]

AZIBs are extensively explored and represent a significant area of research interest. The water molecule, with its small radius (2–3 Å) and pronounced polarity, can interact with Zn^{2+}

to generate larger hydrates. These hydrates serve to enhance ionic conductivity, enabling rapid diffusion at both the electrolyte and solid–liquid interfaces. In contrast to traditional organic electrolytes, aqueous electrolytes exhibit superior ionic conductivity (around 1–10 S cm^{-1}) and ion transference number. This is attributed to their high polarity and small ionic radius.[199] MoS_2 has emerged as a promising cathode material in AZIBs despite several challenges that impede its broader acceptance in AZIBs. Like the obstacles encountered in storing Mg^{2+}, MoS_2 confronts challenges in storing Zn^{2+} due to factors such as low intrinsic conductivity, small interlayer spacings, and substantial volume fluctuations.[200] Hydrated zinc ions exhibit relatively large dimensions, necessitating significant energy for intercalation into MoS_2. The bonds between the Zn^{2+} and water molecules must be broken prior to intercalation. Thus, bulk MoS_2 demonstrates a notably limited capability for storing zinc ions, registering below 25 mAh g^{-1}.[24] Therefore, tuning intercalation energy is necessary for MoS_2 as a cathode for AZIB, which can be achieved through interlayer expansion. However, it should be considered that, for these aqueous batteries, enhancing the hydrophilicity of MoS_2 is another crucial factor. Increasing hydrophilicity can significantly decrease the Zn^{2+} intercalation energy and facilitate its storage. Hence, many research efforts aim to modify MoS_2 to enhance its capability to sufficiently store Zn^{2+}, often by enhancing its hydrophilicity along with other types of modifications. Table 2.4 provides a summary of MoS_2-based cathode materials for AZIBs, highlighting their respective features as reported in the literature.

Table 2.4: Key structural features and performance characteristics of MoS_2-based electrode active materials for AZIBs.

Material	Key features	Capacity (mAh g^{-1})	Cycling stability (cycles @ current density)	Ref.
1T-MoS_2	Metallic conductivity Enhanced hydrophilicity	168 @ 0.1 A g^{-1} 104 @ 1 A g^{-1}	≈98% (400 @ 1 A g^{-1})	[96]
O-incorporated-MoS_2	Enlarged interlayer distance (9.5 Å) Enhanced hydrophilicity	≈228 @ 0.1 A g^{-1} 98 @ 1 A g^{-1}	≈68% (2,000 @ 1 A g^{-1})	[112]
Defect engineered MoS_{2-x}	Abundant sulfur vacancies Numerous edge sites	≈139 @ 0.1 A g^{-1} ≈81 @ 2 A g^{-1}	≈98% (600 @ 0.5 A g^{-1}) ≈88% (1,000 @ 1 A g^{-1})	[124]
Sandwich-Like MoS_2/Graphene	Enlarged interlayer spacing (11.6 Å) Enhanced hydrophilicity Flower-like architecture Enhanced conductivity	≈285 @ 0.05 A g^{-1} ≈142 @ 5 A g^{-1}	93% (100 @ 0.05 A g^{-1}) ≈88% (1,800 @ 1 A g^{-1})	[83]
N-doped 1T-MoS_2	Enlarged interlayer spacing (8.6 Å) Sulfur vacancies Enhanced conductivity	≈150 @ 0.1 A g^{-1} ≈110 @ 3 A g^{-1}	97% (600 @ 1 A g^{-1}) ≈89% (1,000 @ 3 A g^{-1})	[163]
Vanadium-ion-intercalated MoS_2	Enlarged interlayer spacing (10.2 Å) Decelerating volume expansion rate	385 @ 0.1 A g^{-1} 230 @ 0.8 A g^{-1}	88% (150 @ 0.1 A g^{-1})	[201]
Defective oxygen doped MoS_2	Enlarged interlayer spacing (9.6Å) Enhanced hydrophilicity High 1T phase content Defect rich structure	≈238 @ 0.1 A g^{-1} ≈102 @ 10 A g^{-1}	>100% (50 @ 0.1 A g^{-1}) ≈91% (1,000 @ 1 A g^{-1})	[129]

Continued on next page

Table 2.4 – continued from previous page

Material	Key features	Capacity (mAh g^{-1})	Cycling stability (cycles @ current density)	Ref.
	Enhanced conductivity			
Carbon motifs intercalated MoS_2	Enlarged interlayer spacing (9.6 Å) Abundant ion transfer channels Volume change resistant 3D conductive network	≈248 @ 0.1 A g^{-1} ≈ 101 @ 8 A g^{-1}	≈86% (3,200 @ 1 A g^{-1})	[202]
K^+-intercalated MoS_2@Carbon	Enlarged interlayer spacing (9.4 Å) Abundant 1T phase Enhanced hydrophilicity 3D conductive network Electrostatic shielding effect	292 @ 0.1 A g^{-1} ≈ 110 @ 5 A g^{-1}	≈93% (300 @ 1 A g^{-1}) ≈87% (3,000 @ 5 A g^{-1})	[117]
Hydrated MoS_2@carbon fiber	Enlarged interlayer spacing (6.8 Å) Enhanced hydrophilicity	182 @ 0.1 A g^{-1} ≈ 92 @ 4 A g^{-1}	≈100% (300 @ 0.1 A g^{-1}) ≈94% (1,500 @ 2 A g^{-1})	[203]
MoS_2-$C_{19}H_{42}N^+$(CTAB)	Enlarged interlayer spacing (10.0 Å) Volume self-regulation ability	≈182 @ 0.1 A g^{-1} ≈79 @ 10 A g^{-1}	≈79% (100 @ 1 A g^{-1}) ≈93% (2,100 @ 10 A g^{-1})	[118]
1T-MoS_2 on carbon cloth	Vertically aligned structure Free standing structure Metallic conductivity	198 @ 0.1 A g^{-1} 100 @ 2 A g^{-1}	≈97% (1,000 @ 2 A g^{-1}) ≈88% (2,000 @ 2 A g^{-1})	[204]
1T-MoS_2@MXene	Enhanced conductivity Free standing structure hierarchical layer structure	270 @ 0.1 A g^{-1} 120 @ 10 A g^{-1}	≈95% (2,500 @ 10 A g^{-1})	[205]
MoS_2/Ti_3C_2 MXene	layer-by structure Enlarged interlayer spacing (13.1 Å) Enhanced hydrophilicity Enhanced conductivity	318 @ 0.1 A g^{-1} 107 @ 20 A g^{-1}	≈96% (200 @ 0.2 A g^{-1}) ≈76% (7,000 @ 15 A g^{-1})	[206]
MoS_2@carbon nanoplates	Enhamced conductivity Enhanced hydrophilicity	602 @ 0.05 A g^{-1} 328 @ 1 A g^{-1}	≈84% (1,000 @ 0.1 A g^{-1}) ≈76% (7,000 @ 15 A g^{-1})	[207]
MoS_2/polyaniline	Enlarged interlayer spacing (10.3 Å) Enhanced stability	≈182 @ 0.1 A g^{-1} ≈83 @ 2 A g^{-1}	86% (1,000 @ 1 A g^{-1})	[90]
Mn^{2+}-Doped MoS_2/MXene	Enlarged interlayer spacing (9.1 Å) Ti-O-Mo bonds as electron bridges Metallic conductivity Enhanced hydrophilicity	≈197 @ 0.1 A g^{-1} ≈124 @ 2 A g^{-1}	≈80% (500 @ 1 A g^{-1})	[165]

Liang et al. reported a hydrothermal synthesis of oxygen-incorporated MoS_2 (MoS_2−O) featured with enhanced hydrophilicity (due to the oxygen incorporation) and expanded interlayer spacing of 9.5 Å (arising from weakened interlayer van der Waals interactions) at 180 °C (see Figure 2.26a,b for comparison of interlayer distances of pristine MoS_2 and MoS_2−O).[112] While faint redox peaks were observable in the CV of AZIB utilizing unmodified MoS_2 (with an interlayer spacing of 6.2 Å, Figure 2.26a), the achieved capacity did not surpass 21 mAh g^{-1} at 0.1 mA g^{-1} (Figure 2.26c). By employing a straightforward approach of interlayer spacing adjustment and hydrophilicity enhancement via oxygen incorporation, the diffusivity of Zn^{2+} ions experienced a significant boost by three orders of magnitude (Figure 2.26d). This enhancement effectively enabled the initially modestly active MoS_2 to achieve a high capacity of 232 mAh g^{-1} (at 100 mA g^{-1}), representing a tenfold increase over its pristine form. This improvement was well reflected in the rate performance test results as illustrated in Figure 2.26e.

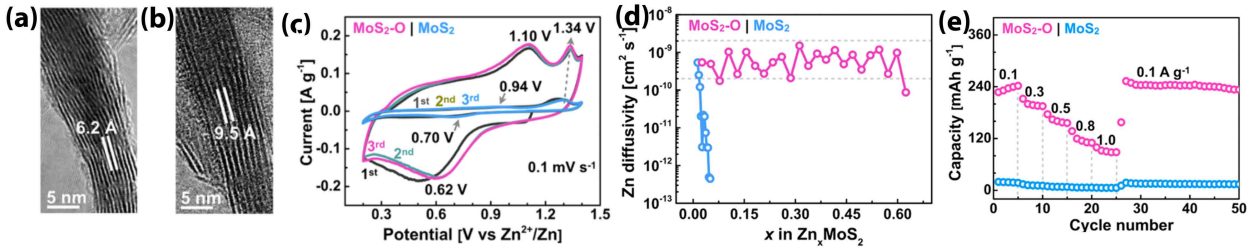

Figure 2.26: HRTEM images of (a) bulk MoS_2 and (b) MoS_2−O; comparison of (c) CV curves, (d) Zn^{2+} diffusivity within the cathode material as a function of the concentration of intercalated Zn^{2+} measured with GITT, and (e) rate performance of AZIBs with unmodified MoS_2 and MoS_2−O cathodes.[112]

As another approach, the crystal water molecules can act as supportive pillars, expanding the interlayer spacing of MoS_2 and enhancing hydrophilicity leading to enhanced Zn^{2+} diffusion (Figure 2.27a). In a study conducted by Liu et al., where hydrated MoS_2 was synthesized on carbon fiber as a cathode material for AZIBs, a comparison of the hydrated (h-MoS_2: obtained by hydrothermal synthesis) and dehydrated samples (d-MoS_2: obtained by annealing of h-MoS_2 at 400 °C) revealed significant differences in capacity (see their CV curves in Figure 2.27b) and rate performance (Figure 2.27c).[203] The hydrated sample exhibited a water contact angle of 25°, whereas the dehydrated sample displayed a contact angle of 83° (See the inset of Figure 2.27c).

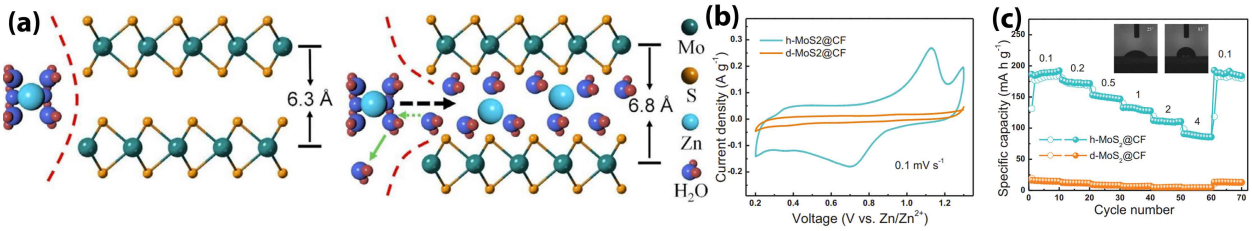

Figure 2.27: (a) Scheme depicting Zn^{2+} diffusion into both dehydrated MoS_2 (d-MoS_2, left) and hydrated MoS_2 (d-MoS_2, right); comparison of (b) CV and (d) rate performance, and water contact angle (inset figure) of d-MoS_2 and h-MoS_2.[203]

Alternative methods have been utilized to tackle the inherent low hydrophilicity of bulk MoS_2. Notably, the 1T phase of MoS_2 demonstrates significant hydrophilic properties, rendering it advantageous for enhanced overall hydrophilicity.[96] Additionally, hybridization with RGO with oxygen-containing functional groups can improve hydrophilicity. To harness both enhancements, Li et al. synthesized sandwich-like heterostructures of MoS_2/graphene.[83] This composite not only showed an enlarged interlayer distance (11.6 Å), but also exhibited enhanced conductivity and hydrophilicity due to the presence of 1T

phase MoS_2 and RGO with oxygen-containing functional groups. The synthesis involved a hydrothermal treatment of chemically exfoliated MoS_2 with cetyltrimethylammonium bromide (CTAB) surfactant and graphene oxide in the presence of thiourea (Figure 2.28a). With ultralarge interlayer distance (Figure 2.28b,c), enhanced conductivity, and improved hydrophilicity as its main characteristics, this composite demonstrated promising performance, delivering 285.4 mAh g^{-1} at 0.05 A g^{-1} and 141.6 mAh g^{-1} at 5 A g^{-1} (Figure 2.28d).[83]

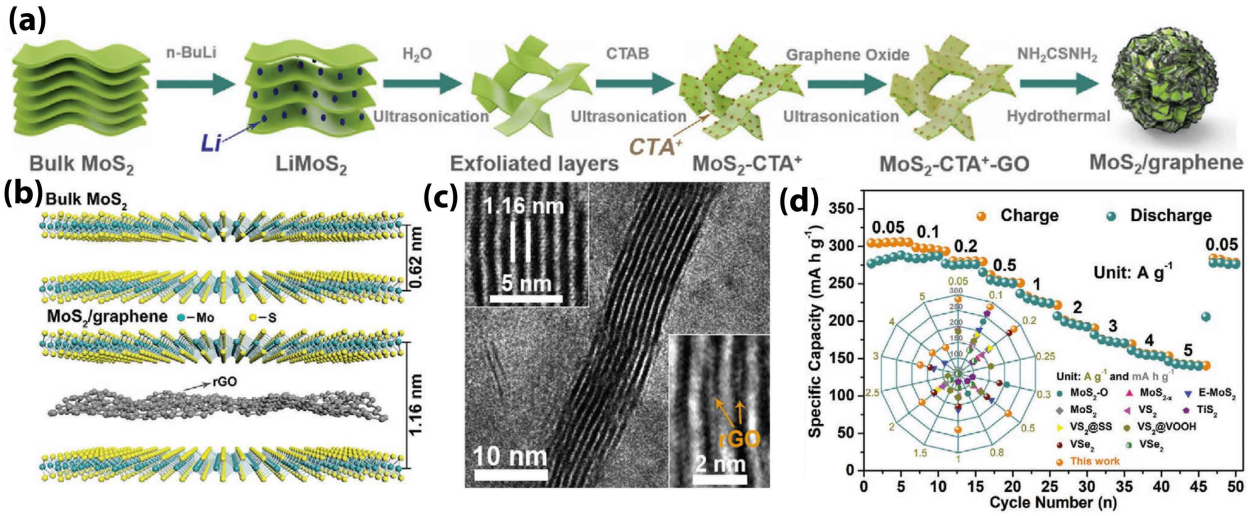

Figure 2.28: (a) Synthesis steps, (b) graphene intercalated structure and enlarged interlayer distance, (c) HRTEM image, and (d) rate performance of MoS_2/graphene nanocomposites.[83]

Furthermore, apart from carbonaceous materials with oxygen-containing functional groups, incorporating MoS_2 into hybrids with other hydrophilic matrices can also bolster the performance of MoS_2-based composites for AZIBs. For instance, blending MoS_2 with $Ti_3C_2T_x$ MXene (T_x: −OH, −O, and −F), known for its outstanding conductivity and pronounced hydrophilicity due to surface functional groups,[208] has demonstrated dual benefits as a conductivity and hydrophilicity enhancer.[165,206] Niu et al. synthesized nanocomposites of MoS_2 and Ti_3C_2 through two distinct methods.[206] Initially, they employed the HCL/LiF method to etch Ti_3AlC_2 MAX phase, followed by sonication to obtain few-layered Ti_3C_2 MXene. Subsequently, they conducted a hydrothermal reaction synthesis of MoS2 in the presence of few-layered MXene to fabricate a nanocomposite, denoted as C-MoS_2/Ti_3C_2. For their second nanocomposite, L-MoS_2/Ti_3C_2, they adopted a different approach (Figure 2.29a). Few-layered Ti_3C_2 and few-layered MoS_2 (achieved through n-buthyl lithium-assisted exfoliation and stabilized by CTAB surfactant) were mixed via sonication, followed

by hydrothermal treatment of the mixture. The resulting L-MoS_2/Ti_3C_2 nanocomposite exhibited an enlarged interlayer distance of 13.1 Å and improved hydrophilicity. Notably, it displayed outstanding performance as a cathode for AZIBs, surpassing bulk MoS_2 performance and C-MoS_2/Ti_3C_2 (Figure 2.29b,c). The superior performance of L-MoS_2/Ti_3C_2 over C-MoS_2/Ti_3C_2 was attributed to its layer-by-layer structure, which afforded an increased interlayer distance of 13.1 Å compared to the 9.2 Å interlayer distance observed in C-MoS_2/Ti_3C_2.

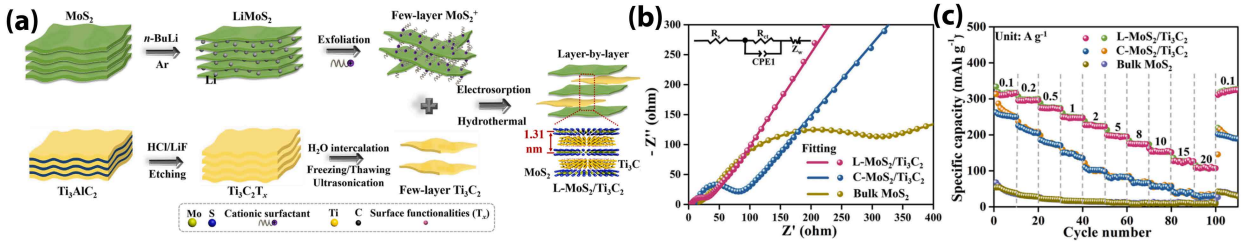

Figure 2.29: (a) Synthesis procedure of layer-by-layer L-MoS_2/Ti_3C_2 and comparison of its (b) nyquist plot and (c) rate performance with C-MoS_2/Ti_3C_2 and bulk MoS_2.Adapted with permission.[206]

Summarizing the discussion on Zn^{2+} storage in MoS_2, it becomes evident that this system shares several similarities with Mg^{2+} storage, particularly regarding the challenges of ion transport and conductivity. To address these issues, similar strategies, widening the interlayer spacing, enhancing conductivity, and creating shorter ion transport pathways, are required to improve performance. However, in AZIBs enhancing the hydrophilicity of MoS_2 can significantly improve its interaction with the aqueous electrolyte. This improvement facilitates faster ion diffusion and boosts overall electrochemical performance. Methods such as oxygen doping, phase engineering, and hybridizing with hydrophilic compound have proven to be effective strategies for increasing the water affinity of MoS_2.

2.5.4 Al^{3+} Storage

With a three-electron-transfer electrode reaction (Al^{3+} + $3e^-$ $\longleftrightarrow$ Al), aluminum (Al) demonstrates a gravimetric capacity (2980 mAh g^{-1}) comparable to lithium (Li) metal, and it boasts the highest volumetric capacity (8040 mAh cm^{-3}) among metals except for beryllium (Be). Al is abundant in nature and economical, exhibiting inert reactivity when exposed to air, thus ensuring safe handling. Consequently, researchers are exploring rechargeable AIBs as promising alternatives for energy storage solutions.[28,29,209] Nevertheless, AIBs

encounter numerous hurdles, particularly concerning the cathode and electrolyte. The utilization of MoS_2 as a cathode is relatively recent and requires substantial refinement. In a groundbreaking study, Li et al. pioneered the utilization of MoS_2 microspheres (hydrothermally synthesized) as a cathode for AIBs. They assembled an AIB with the mixture of $AlCl_3$ and 1-ethyl-3-methylimidazolium chloride ([EMIm]Cl) as the electrolyte and aluminum as the anode, resulting in a battery with a modest capacity of ≈67 mAh g^{-1} at 20 mA g^{-1}.[210] Incorporating conductive materials has been demonstrated to boost capacity. According to Yang et al., MoS_2 nanosheets embedded in carbon nanofibers achieved a capacity of 293.2 mAh g^{-1} at a current density of 100 mA g^{-1}.[84] However, after 200 cycles, the capacity decreased to 126.6 mAh g^{-1}. Additionally, Tan et al. revealed that hydrothermally synthesized MoS_2 on $Ti_3C_2T_x$ MXene resulted in enhanced conductivity and structural integrity, leading to a first-cycle capacity of 224 mAh g^{-1}. This cathode maintained a capacity of 166 mAh g^{-1} for nearly 60 cycles, representing a slight improvement over the stability of pure MoS_2.[87] Accordingly, the engineering of MoS_2 nanocomposites to render them suitable for Al^{3+} storage is grounded on the enhancement of conductivity and the shortening ion transport pathways. However, despite these efforts, cycling tests outlined in the literature reveal a primary challenge with the low cycling stability stemming from structural distortion within the MoS_2 matrix. Table 2.5 summarizes recent research endeavors aimed at bolstering the performance of MoS_2 cathode materials for AIBs. The nanocomposites featuring more desirable characteristics, such as interlayer-expanded MoS_2/N-doped carbon as proposed by Guo et al., exhibit promising advancements. These include enlarged interlayer spacing, improved accessibility to active sites, enhanced conductivity, and structural robustness. Notably, these enhancements have led to progress in MoS_2-based cathode materials, achieving 280 mAh g^{-1} at 0.3 A g^{-1} and retaining 191.2 mAh g^{-1} after 450 charge/discharge cycles at 0.5 A g^{-1}.[211] Nevertheless, the development of MoS_2-based cathode materials for AIBs still requires further scientific exploration and efforts to achieve improved performance.

Table 2.5: Key structural features and performance characteristics of MoS_2-based electrode active materials for AIBs.

Material	Key features	Capacity (mAh g^{-1})	Cycling stability (cycles @ current density)	Ref.
MoS_2 Microspheres	Hierarchical flower-Like structure	≈154 @ 0.5 A g^{-1}	≈73% (100 @ 0.5 A g^{-1})	[212]
MoS_2/Carbon Nanofibers	Enhanced conductivity Binder-free cathode	≈293 @ 0.1 A g^{-1}	≈43% (200 @ 0.1 A g^{-1})	[84]
MoS_2/RGO	Enhanced conductivity High structural integrity	≈278 @ 1 A g^{-1}	≈58% (100 @ 1 A g^{-1})	[75]
MoS_2/N-Doped Carbon	Enlarged interlayer spacing (8.2 Å) 3D hierarchical structure Enhanced conductivity	≈280 @ 0.3 A g^{-1} ≈62 @ 5 A g^{-1}	≈77% (450 @ 0.5 A g^{-1}) ≈95% (1,700 @ 1 A g^{-1})	[211]

Continued on next page

Table 2.5 – continued from previous page

Material	Key features	Capacity (mAh g^{-1})	Cycling stability (cycles @ current density)	Ref.
	Improved structural integrity			
$FeSe_2/MoS_2$ heterostructure	Built-in electric field in the interface Stable structure	222 @ 0.5 A g^{-1} 113 @ 1 A g^{-1}	60% (140 @ 1 A g^{-1})	[209]

2.5.5 Monovalent/Multivalent Ions Co-Intercalation

Dual-salt batteries, such as MLIBs, present a promising avenue for energy storage due to their unique mechanisms and advantageous properties. The inclusion of a monovalent ion like Li^+ can address the sluggish kinetics often associated with multivalent ion diffusion in the cathode. In MLIBs, the battery structure resembles that of MIBs, with a Mg plate serving as the anode, but with the magnesium salt electrolyte containing a lithium salt additive such as LiCl. These batteries benefit from the efficient insertion and extraction of swift Li^+ ions in the cathode, which enhances their performance. Moreover, since the anode primarily experiences magnesium deposition and dissolution due to its high redox potential, MLIBs retain the well-known advantages of a Mg metal anode, such as high safety.[213] Depending on various factors, predominantly linked to the properties of the cathode utilized, the mechanism of such batteries can manifest as either the Daniell-type or co-intercalation mechanism.[133] Figure 2.30a illustrates these two mechanisms schematically in dual-salt batteries with an Mg anode and Li^+ or Na^+ salt additives incorporated into the Mg salt electrolyte.[214] In the Daniell-type MLIB, Li^+ participates solely in the cathodic reactions, while Mg^{2+} is exclusively involved in the anodic reactions.

Bulk MoS_2, owing to its small interlayer spaces, cannot accommodate Mg^{2+} and typically exhibits the Daniell-type mechanism. Nevertheless, a comparison of the CV cycles of MIB and MLIB employing bulk MoS_2 (B-MoS_2) cathodes reveals a significant increase in the capacity of MLIBs (Figure 2.30b).[26] However, it is worth noting that batteries operating on the Daniell-type mechanism necessitate a considerable amount of electrolyte. This requirement contributes to their relatively low energy density.[?] Hence, cathode materials capable of facilitating a co-intercalation mechanism would be advantageous for enhancing the efficiency of dual-salt batteries. It is also noteworthy that the intercalated monovalent ion can accelerate multivalent ions diffusion due to the reduced activation energy following the intercalation of the former. For example, in case of MLIBs, the intercalated Li^+ ions interact with the host lattices, thereby leading to the weakened interactions between Mg^{2+} and the host material.[133–135] MoS_2, along with modified MoS_2 and their nanocomposites thereof with various materials like metal sulfides, polymers, carbon-based materials, and MXenes,

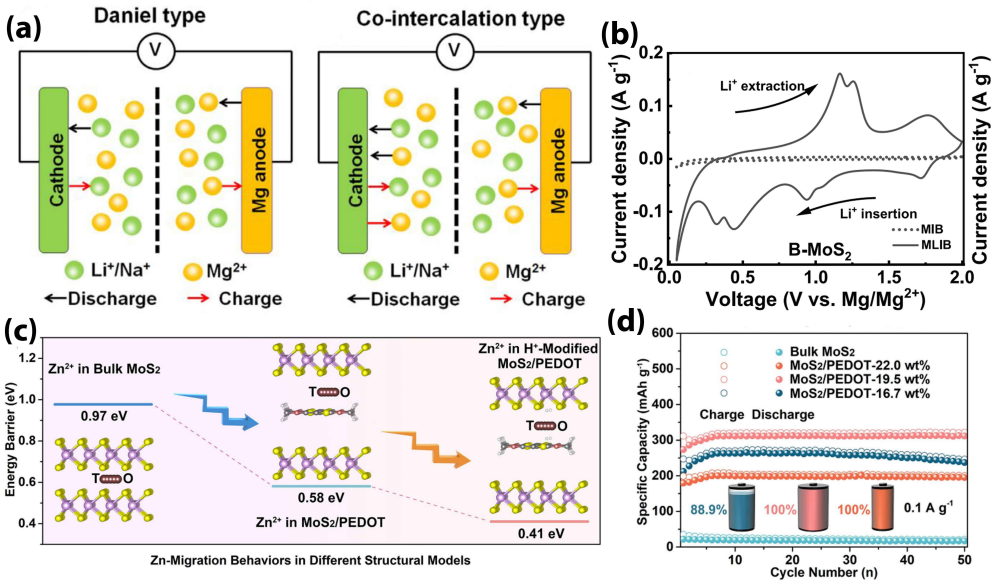

Figure 2.30: (a) Schematic illustration of the Daniel type and the co-intercalation type Mg hybrid batteries.[214] (b) CV curves of MIB and MLIB with bulk MoS_2 cathode.[26] (c) the energy profile of Zn^{2+} migration behaviors in bulk MoS_2, MoS_2/PEDOT, and H^+ modified MoS_2/PEDOT obtained by DFT computations; (d) comparison of the cycling test of AZIBs with bulk MoS_2 and MoS_2/PEDOT nanocomposites.[215]

can serve as viable cathode options for MLIBs. A summary of these cathodes and their respective properties is presented in Table 2.6. Notably, cathode materials such as ionomer-intercalated 1T/2H-MoS_2 and MoS_2 composites with highly electron-conducting compounds like graphene and carbon nanofibers exhibit the capability of co-intercalating both ions. This behavior stems from their high conductivity and large interlayer distances.[26,213,216]

Table 2.6: Key structural features and performance characteristics of MoS_2-based electrode active materials for MLIBs.

Material	Key features	Capacity (mAh g^{-1})	Cycling stability (cycles @ current density)	Ref.
MoS_2/graphene	Conductive carbon-based content Li^+-intercalation-induced 1T phase	225 @ 0.025 A g^{-1} 150 @ 1 A g^{-1}	90% (200 @ 0.1 A g^{-1})	[217]
MoS_2/Graphene	Free-standing structure Enlarged interlayer spacing Enhanced conductivity and stability	300 @ 0.02 A g^{-1} 186 @ 0.5 A g^{-1}	81% (200 @ 0.5 A g^{-1})	[218]
Ionomer@1T/2H-MoS_2	Enlarged interlayer spacing (11.1 Å) Metallic conductivity Compatible with low-polarity solvents	260 @ 0.05 A g^{-1} 107 @ 1 A g^{-1}	75% (2,000 @ 1 A g^{-1})	[26]
MoS_2@carbon nanofibres	Conductive N-doped carbon content Well-defined 1D structure	260 @ 0.02 A g^{-1} 69 @ 0.5 A g^{-1}	≈75% (120 @ 0.2 A g^{-1})	[219]
MoS_2-CuS-expanded graphite	Hollow nanoflower-like structure Enhanced conductivity	≈176 @ 0.1 A g^{-1} 147 @ 1 A g^{-1}	≈20% (200 @ 0.05 A g^{-1}) ≈92% (150 @ 0.5 A g^{-1})	[220]
MoS_2/N-doped carbon	Enlarged interlayer spacing Hollow structure	≈312 @ 0.02 A g^{-1} ≈145 @ 1 A g^{-1}	≈81% (150 @ 0.02 A g^{-1})	[216]

Continued on next page

Table 2.6 – continued from previous page

Material	Key features	Capacity (mAh g^{-1})	Cycling stability (cycles @ current density)	Ref.
	Oxygen-incorporated MoS_2			
MoS_2/graphene	Alternately stacking structure Unique ion channels Enhanced conductivity	≈280 @ 0.02 A g^{-1} ≈150 @ 1 A g^{-1}	≈75% (200 @ 0.02 A g^{-1})	[213]
MoS_2 nanoflowers@graphene	Enlarged interlayer spacing oxygen-incorporated MoS_2 Enhanced conductivity	≈295 @ 0.02 A g^{-1} ≈124 @ 1 A g^{-1}	≈80% (150 @ 0.02 A g^{-1})	[135]
1T/2H-MoS_2@MXene	Enlarged interlayer distance (9.3 Å) Metallic conductivity	253 @ 0.05 A g^{-1} 90 @ 1 A g^{-1}	65% (1,000 @ 0.5 A g^{-1})	[221]
VS_4/MoS_2	Abundant sulfur vacancies	≈643 @ 0.2 A g^{-1} ≈473 @ 1.5 A g^{-1}	≈99% (100 @ 0.5 A g^{-1})	[222]
Highly dispersed MoS_2	High surface area Enlarged interlayer spacing (6.5 Å)	≈321 @ 0.1 A g^{-1} ≈81 @ 10 A g^{-1}	≈60% (100 @ 0.1 A g^{-1})	[223]

Recent research has delved into a debated issue regarding the aqueous storage of multivalent ions, with a particular focus on understanding their unique mechanisms compared to non-aqueous systems. Contrary to previous assumptions, it suggests that, in certain cases, such as AZIBs with VPO_4F or $Na_3V_2(PO_4)_2F_3$ as cathode, water might not substantially improve the storage of multivalent ions. Instead, water functions as a source of H^+, with H^+ identified as the guest ion species rather than Zn^{2+}.[224–226] Therefore, while H^+ insertion/extraction has been overlooked in much of the research on MoS_2-based AZIBs, the prospect of an H^+/Zn^{2+} co-intercalation mechanism is plausible. Recently, Li et al. have introduced a novel strategy using a specific polymer hybridized with MoS_2, which facilitates H^+ insertion/extraction alongside Zn^{2+} in aqueous ZIB.[215] Their study successfully elucidated the proton insertion chemistry in aqueous Zn-MoS_2 system through deliberate design of the cathode material. They synthesized a MoS_2/poly(3,4-ethylenedioxythiophene) (MoS_2/PEDOT) hybrid via exfoliation and reflux processes, where the intercalated PEDOT endowed the MoS_2 with significantly enlarged interlayer space (12.9 Å), enhanced hydrophilicity, high electronic conductivity, and reinforced layered structure. Moreover, the MoS_2/PEDOT cathode exhibited a highly reversible H^+/Zn^{2+} co-intercalation mechanism. The co-inserted protons induced by PEDOT shield the electrostatic interactions between the MoS_2/PEDOT host and divalent Zn^{2+} ions, thus reducing the Zn^{2+} diffusion energy barrier, introducing a novel concept termed "proton lubricant" that enhances Zn-ion diffusion. Figure 2.30c presents the DFT simulations showcasing the Zn-migration pathways (from tetrahedral (T) sites to octahedral (O) sites) and the corresponding energy barriers across various MoS_2-based structural models.[215] The diffusion barrier for Zn^{2+} in H^+-modified MoS_2/PEDOT (0.41 eV) is notably lower compared to that in bulk MoS_2 (0.97 eV) and MoS_2/PEDOT (0.58 eV). This observation underscores the significant impact of enlarged

interlayers and inserted protons on facilitating the Zn^{2+} migration. This improvement has also been reflected in their experimental tests like Figure 2.30d illustrating the comparison of the cycling test for MoS_2 with MoS_2/PEDOT nanocomposites.

2.6 Conclusion

In this comprehensive review, we have delved into the realm of post-LIBs, focusing particularly on the potential of MoS_2 and its nanocomposites as active materials for such batteries. While MoS_2 has shown promise for storage of these ions, further improvements in electronic conductivity, kinetics, and stability are essential to fully realize its potential.

Our exploration indicated that in the case of storage of Na^+ and K^+ in MoS_2 in SIBs and PIBs, the main challenge is related to the drastic volume changes during the insertion/extraction and conversion reactions, as well as the shuttling of the products of the conversion reaction, which lead to low cycling stability. The larger size of Na^+ and K^+ makes structural instability during cycling more severe than what is seen in LIBs. Therefore, hybridizing MoS_2 with carbon-based materials, metal sulfides, metal oxides, etc., to enhance its structural integrity is a necessary part of electrode design for SIBs and PIBs. Furthermore, any modification that enhances the conductivity and ion transport rate of MoS_2-based SIB/PIB electrode materials can improve performance in terms of capacity and rate capability. On the other hand, in the case of storage of multivalent ions like Mg^{2+}, Zn^{2+}, and Al^{3+}, the highly interactive nature of these ions makes sluggish kinetics a more serious issue, necessitating kinetic enhancement methods such as interlayer expansion, defect creation, reduction of the number of layers, and conductivity enhancement through either hybridization or 1T phase creation. Without such modifications, the storage ability of MoS_2 for multivalent ion storage is negligible.

Despite significant progress in recent years, the use of MoS_2 as an active material for these types of batteries requires further advancements. Continued efforts should focus on solving challenges related to kinetics and stability to fully unlock MoS_2's potential in energy storage systems beyond LIBs. Future research in this area should prioritize exploring advanced hybrid materials that combine MoS_2 with materials possessing superior electronic conductivity and structural stability. Additionally, optimizing synthesis techniques will allow for better control over morphology and structural characteristics, improving ion transport pathways and increasing active sites. Furthermore, advanced characterization methods, including in situ and operando spectroscopy, should be employed to gain deeper insights into

structural changes and ion dynamics during cycling. Investigating interfacial interactions between MoS_2 and electrolytes can enhance electrode/electrolyte interfaces, improving cycling stability. Studies focusing on the long-term cycling performance of MoS_2, particularly for alkali-ion storage systems, are essential for understanding degradation mechanisms and enhancing stability. Lastly, computational modeling and machine learning techniques can aid in predicting performance based on structural properties, guiding the design of next-generation MoS_2-based energy storage devices. By addressing these research avenues, the understanding and application of MoS_2 in various battery technologies can be significantly advanced.

Chapter 3

Embedding Amorphous MoS_x Within Hierarchical Porous Carbon by Facile One-Pot Synthesis for Superior Sodium Ion Storage[†]

Adapted from article:

Embedding Amorphous MoS_x Within Hierarchical Porous Carbon by Facile One-Pot Synthesis for Superior Sodium Ion Storage

Jalal Rahmatinejad, Xudong Liu, Ximeng Zhang, Bahareh Raisi, Zhibin Ye

Published in: ***Journal of Energy Chemistry***

https://doi.org/10.1016/j.jechem.2022.08.008

[†] Supplementary Information available: See Appendix A

Abstract The design of anode materials with a high specific capacity, high cyclic stability, and superior rate performance is required for the practical applications of sodium-ion batteries (SIBs). In this regard, we introduce in this work a facile, low-cost and scalable method for the synthesis of nanocomposites of amorphous molybdenum sulfide (a-MoS_x) and hierarchical porous carbon and have systematically investigated their performance for sodium ion storage. In the synthesis, ammonium molybdate tetrahydrate and thioacetamide are used as molybdenum and sulfur sources, respectively, with abundant corn starch as the carbon source and KOH as an activation agent. A simple pyrolysis of their mixtures leads to the formation of nanocomposites with a-MoS_x embedded within a hierarchical porous carbon (MoS_x@HPC), which are featured with a high surface area of up to 518.4 m^2 g^{-1} and hierarchical pores ranging from micropores to macropores. It has also been shown that the annealing of MoS_x@HPC results in the formation of crystalline MoS_2 nanosheets anchored in the hierarchical porous carbon matrix (MoS_2@HPC). The as-prepared nanocomposite MoS_x@HPC1 at an optimum carbon content of 32 wt% delivers a high specific sodium storage capacity of 599 mAh g^{-1} at 0.2 A g^{-1} and a high-rate performance with a retained capacity of 289 mAh g^{-1} at 5 A g^{-1}. A comparison of the electrochemical performances of MoS_x@HPC and MoS_2@HPC demonstrates the superior specific capacity, rate performance, and charge transfer kinetics of the former, highlighting the unique advantageous role of amorphous MoS_x relative to crystalline MoS_2.

3.1 Introduction

Recently, SIBs have received a great deal of interest.[4–6] With the accelerating consumption of lithium resources, the abundance (the fourth most abundant element in earth crust), low cost, and appropriate electrochemical voltage (-2.71 V vs. SHE) of sodium make SIB promising as next-generation energy storage devices. Therefore, SIBs are viewed as a viable alternative to lithium-ion batteries that can meet the growing demand for efficient electrical energy storage systems in emerging technologies.[227,228] Despite all the benefits of SIBs, their practical use still faces challenges. From an electrochemical standpoint, the bigger size of Na^+ compared to Li^+ causes a sluggish electrochemical kinetic and pulverization of the active cathode/anode materials during the sodiation process.[8,62]

To realize SIBs with practical usability, it is imperative to discover/develop anode materials that provide high areal and gravimetric capacities, high rate performance, and high cycling stability. Among the various materials studied thus far as active anode materials for SIBs, molybdenum sulfides are regarded as promising candidates. MoS_2, as the most common form of molybdenum sulfides, possesses a crystalline 2D layered structure with weak interlayer van der Waals interactions, leading to a favorable alkali metal ions intercalation and a high theoretical capacity of 670 mAh g^{-1}.[128,166] Nevertheless, bulk MoS_2-based anodes have drawbacks, including low intrinsic electrical conductivity and sluggish kinetics of Na^+ diffusion. In addition, MoS_2 suffers from severe volume changes during sodiation/desodiation reactions, leading to the pulverization and, in turn, structural collapse and capacity fading.[18–20,55,56] On the other hand, amorphous MoS_x ($x > 2$), consisting of sulfide/disulfide ligands, has been recently revealed to exhibit desirable electrochemical performance in various electrical energy storage systems, despite its amorphous structure.[229–237] Previous research has shown that materials with amorphous structures can show fast diffusion kinetics and high tolerance against volume changes caused by the insertion/extraction of alkali metal ions.[231,238–240] Hybridizing such materials with carbonaceous materials is an efficient solution to further improve the electrical conductivity, structural strength and kinetics of ion diffusion.[138,149,241] Therefore, some research has been done to incorporate molybdenum sulfides within various carbonaceous materials, including graphene, amorphous carbon,[67,68,177,242] carbon nanotubes,[231,243] etc. It has been shown that the textural properties of resulting composites are another critical factor that affects their overall electrochemical performance as anode materials for SIBs. To gain the maximum capacity and stability, the texture of the nanocomposites, in terms of active specific surface area, and volume and size of the pores,

should facilitate high electrode-electrolyte contact and short ion transport paths. Accordingly, constructing a porous architecture with a high active specific surface area is an efficient way to enhance electron conductivity and facilitate the interaction of active material and electrolyte.[244] A hierarchical porous structure with a wide range of pore sizes is a good example that can provide all the benefits mentioned above.[138] With this in mind, we aim to develop a simple method to prepare amorphous MoS_x anchored in a hierarchical porous carbon structure with high conductivity and high accessibility to electrolytes. Meanwhile, such a porous structure can accommodate the colossal volume change during insertion and extraction of the ions.[138,149,169] Previous studies have presented the templating synthesis of several MoS_2/hierarchical porous carbons composites with the use of hard templates like hollow carbon spheres,[138] SiO_2,[245], and NaCl.[177] However, to the best of our knowledge, there has been no report on the synthesis of amorphous MoS_x/hierarchical carbon composites for sodium ion storage.

Herein, we report a facile, scalable, one-pot method for the synthesis of amorphous MoS_x embedded within a hierarchical porous carbon (MoS_x@HPC) with a high surface area and a unique structure facilitating the electrochemistry of SIBs. This method combines simultaneously the pyrolysis of Mo and S sources for the formation of MoS_x, carbonization of starch, and KOH-assisted activation all together in a single step. The structural features of MoS_x@HPC have been examined with the use of various characterization techniques. Systematic electrochemical tests have been undertaken to reveal its performance for sodium ion storage as the anode material for SIBs, with remarkable specific capacity and high stability demonstrated. Compared with the previous reports of MoS_x/carbon anode synthesis, this method is facile, low-cost, and scalable. Additionally, the final structure of nanocomposite synthesized with this method consists of a wide range of pore sizes, enhancing the reaction kinetics and providing high cycling stability by buffering the volume changes during sodiation/desodiation.

3.2 Experimental

3.2.1 Chemicals and Materials

Chemicals and materials, including ammonium molybdate tetrahydrate ($(NH_4)_6Mo_7O_{24}.4H_2O$, 99%, Alfa Aesar), thioacetamide (C_2H_5NS, 98%, Alfa Aesar), potassium hydroxide (KOH, 90%, Aldrich), poly(vinylidene fluoride) (PVDF, Mw ≈534,000 g mol^{-1}, Aldrich), 1-methyl-2-pyrrolidone (NMP, reagent Plus 99%, Sigama-Aldrich),

hydrochloric acid (HCL, 36%, Caledon Laboratory Chemicals), and diethylene glycol dimethyl ether (Diglyme, 99+% extra dry over molecular sieve, Acroseal®, Acros Organics) were used as received without further purification. Sodium trifluoromethanesulfonate salt (CF_3SO_3Na, 98%, Aldrich) was dried under vacuum for 12 h at 80 °C before use.

3.2.2 Synthesis of MoS_x@HPC and MoS_2@HPC Composites

In the typical synthesis, 551 mg of $(NH_4)_6Mo_7O_{24}.4H_2O$ and 939 mg of C_2H_5NS were dissolved in 45 mL of deionized water in a flask under magnetic stirring. Then the solution was heated at 80 °C with an oil bath for 1 h to obtain a dark red solution. Afterward, 800 mg of potassium hydroxide (KOH) was added, followed by the gradual addition of 800 mg of corn starch under vigorous stirring. Then, the temperature was raised to 95 °C and the stirring continued until a homogeneous red gel formed. After evaporation of the majority of water, the gel was dried overnight at 95 °C in a vacuum oven. Then, the obtained solid was grinded, transferred to a ceramic boat, and placed inside a tube furnace.

For pyrolysis of the sample under a nitrogen atmosphere, the temperature was increased to 100 °C in 30 min and was kept for 2 h. Then the temperature was raised to 700 °C at 3 °C/min and was maintained at this temperature for 2 h. Then the sample was naturally cooled down to room temperature. Next, the product was washed with a 2% (w/w) HCL solution for 30 min under stirring, followed by wash with excessive water and finally with ethanol. The final product, denoted as MoS_x@HPC1, was obtained after overnight drying at 60 °C in a vacuum oven. Composite samples with different carbon contents, MoS_x@HPC2 and MoS_x@HPC3, were prepared by the same method but with different starch/KOH amounts of 400/400 mg and 1200/1200 mg, respectively. Subsequent annealing of MoS_x@HPC1 was performed by heating to 700 °C in a nitrogen atmosphere at a heating rate of 3 °C min^{-1} with a dwelling time of 2 h, which led to the pyrolysis of MoS_x into crystalline MoS_2 to render MoS_2@HPC1. The pure MoS_2 was synthesized with the same method except without the addition of starch/KOH content or the second annealing step. In addition, a porous carbon was also synthesized by pyrolysis of starch/KOH at a mass ratio of 1:1 without the addition of molybdenum or sulfur sources.

3.2.3 Materials Characterizations

The crystal structure of the samples was investigated with XRD on a Rigaku SmartLab SE X-ray diffractometer with Cu Kα radiation. A Fergie Raman spectrometer by Princeton

Instrument, equipped with a 532 nm laser, was used to obtain Raman spectra of the samples. Thermogravimetric analysis (TGA) was performed on a TA instruments Q50 TGA in an air atmosphere in a temperature range of 25–700 °C at a heating rate of 10 °C min-1. XPS were carried out on a Thermo Scientific Theta Probe XPS spectrometer with a monochromatic Al K X-ray source and a spot area of 400 m. Transmission electron microscopy (TEM) images were acquired on a JEOL 2010F field emission electron microscope operating at 200 keV. To quantify the Brunauer-Emmert-Teller (BET) specific surface area, pore volume, and pore size distribution, N_2 sorption measurements were performed at 77 K on a Micromeritics ASAP2020 physisorption analyzer.

3.2.4 Electrochemical Measurements

To fabricate the working electrodes, slurries were prepared by mixing each composite sample with Super-P, conducting carbon and PVDF at the weight ratio of 7:2:1 in NMP. Then the slurry was coated on copper foil disks followed by drying overnight at 70 °C. The mass loading of active materials on the copper foil was controlled at about 1–1.2 mg cm^{-2}. CR2032 coin cells were assembled in an argon-filled glove box ($O_2 < 0.1$ ppm & $H_2O < 0.5$ ppm) using each as-prepared electrode as the working electrode, a sodium metal disk as the counter/reference electrode, and a glass fiber membrane (Whatman GF/D) as the separator. 1 M CF_3SO_3Na in Diglyme was used as the electrolyte. A battery testing system (Land, CT2001A, China) was utilized to perform the GCD tests. CV) and EIS were performed on a Metrohm Autolab PGSTAT128N electrochemical workstation. EIS was carried out at the open circuit voltage with an oscillatory amplitude of 5 mV in the frequency range of 100 kHz to 0.01 Hz.

3.3 Results and Discussion

As shown schematically in Fig. 3.1, a simple template-free pyrolysis process is employed herein to fabricate MoS_x@HPC nanocomposites, with amorphous MoS_x clusters embedded within the hierarchal porous carbon matrix. In this approach, $(NH_4)_6Mo_7O_{24}.4H_2O$ and C_2H_5NS at a fixed molar ratio of 1:28 are used as the precursors for molybdenum sulfide, and corn starch as the carbon source with KOH as the activation agent. In the first step, the mixture of $(NH_4)_6Mo_7O_{24}.4H_2O$ and C_2H_5NS in water is heated, leading to the formation of $(NH_4)_2MoS_4$ as a dark red solution. The subsequent addition of corn starch and KOH (with a starch/KOH mass ratio of 1:1) to this solution yields a thick and homogeneous gel containing

K_2MoS_4. Pyrolysis of the dried gel at 700 °C in a nitrogen atmosphere 2% (w/w) HCL solution gives rise to MoS_x@HPC. The presence of KOH can enhance the gelation process and lead to granular swelling. In addition to the activation effect, KOH can also act as a template for the formation of porosity.[246] This method provides the construction of a hierarchical porous carbon structure and the synthesis of a-MoS_x through a one-pot process. Subsequent annealing of MoS_x@HPC results in the formation of MoS_2@HPC, with amorphous MoS_x turned into crystalline MoS_2 as verified below. In the absence of KOH/starch, pyrolysis of $(NH_4)_2MoS_4$ at 700 °C yields instead pure MoS_2. With this method, three MoS_x@HPC composites (MoS_x@HPC1, MoS_x@HPC2, and MoS_x@HPC3) of different carbon contents have been synthesized by tuning the mass of starch relative to $(NH_4)_6Mo_7O_{24}.4H_2O/C_2H_5NS$ so as to investigate the effect of carbon content on the structure and electrochemical performance of the composites. Their subsequent annealing under a N_2 atmosphere at 700 °C renders MoS_2@HPC1, MoS_2@HPC2, and MoS_2@HPC3, respectively.

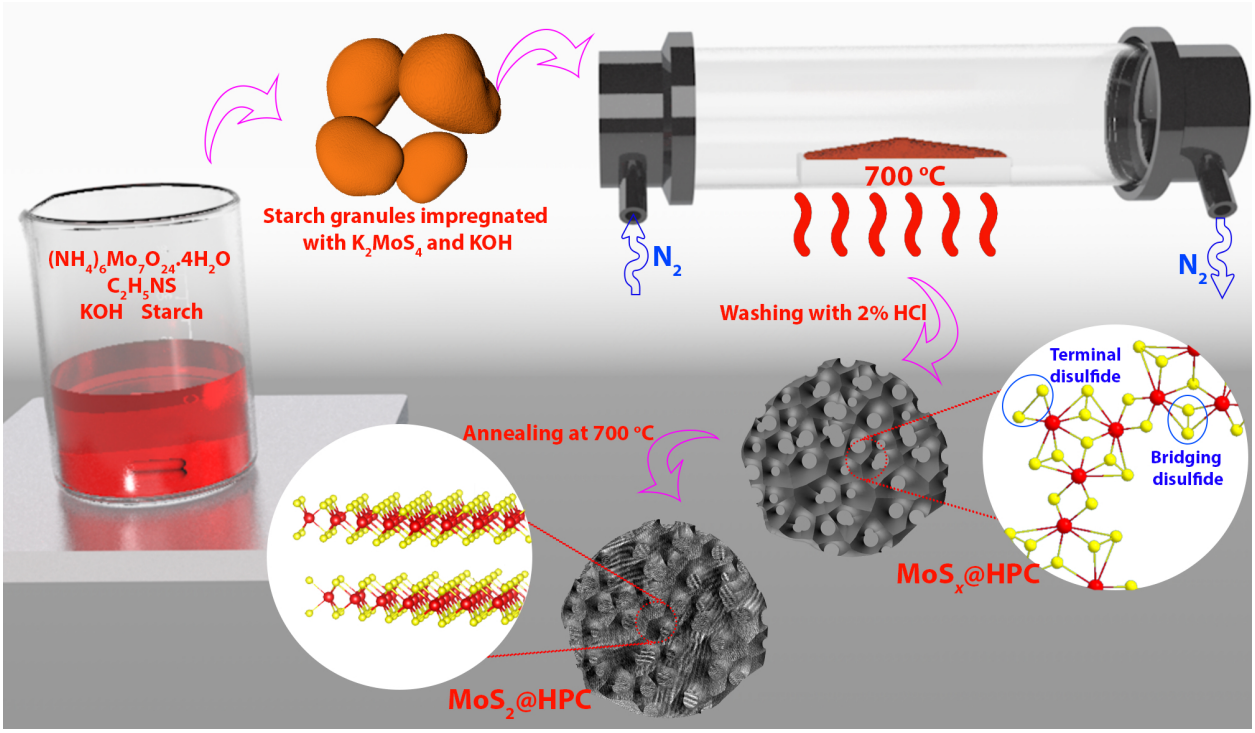

Figure 3.1: Schematic illustration of MoS_x@HPC and MoS_2@HPC synthesis method.

Transmission electron microscopy (TEM) and HRTEM have been used to investigate the morphology and structure of the MoS_x@HPC1 and MoS_2@HPC1 nanocomposites (Fig. 3.2). The TEM image of MoS_x@HPC1 (Fig. 3.2a) illustrates aggregated particles with sizes below 200 nm. The HRTEM image (Fig. 3.2b) reveals its amorphous structure without any trace

of crystalline or 2D layered structures. However, energy dispersive X-ray (EDX) elemental mapping of the sample (Fig. 3.2c) indicates the uniform distribution of molybdenum, sulfur, and carbon elements. On the other hand, according to Fig. 3.2d, the particles in MoS_2@HPC1 are somewhat smaller compared to those in MoS_x@HPC1. Meanwhile, crystalline and layered structures of MoS_2 can be clearly seen from the HRTEM image and the selected-area electron diffraction (SAED) pattern (Fig. 3.2e). An interlayer spacing of approximately 0.63 nm is observed, corresponding to (002) plane of 2H MoS_2 phase.[149,173] This confirms the conversion from amorphous MoS_x to crystalline MoS_2 following annealing. According to the elemental mapping of this sample shown in Fig. 3.2f, molybdenum and sulfur are homogeneously distributed in the carbonaceous structure.

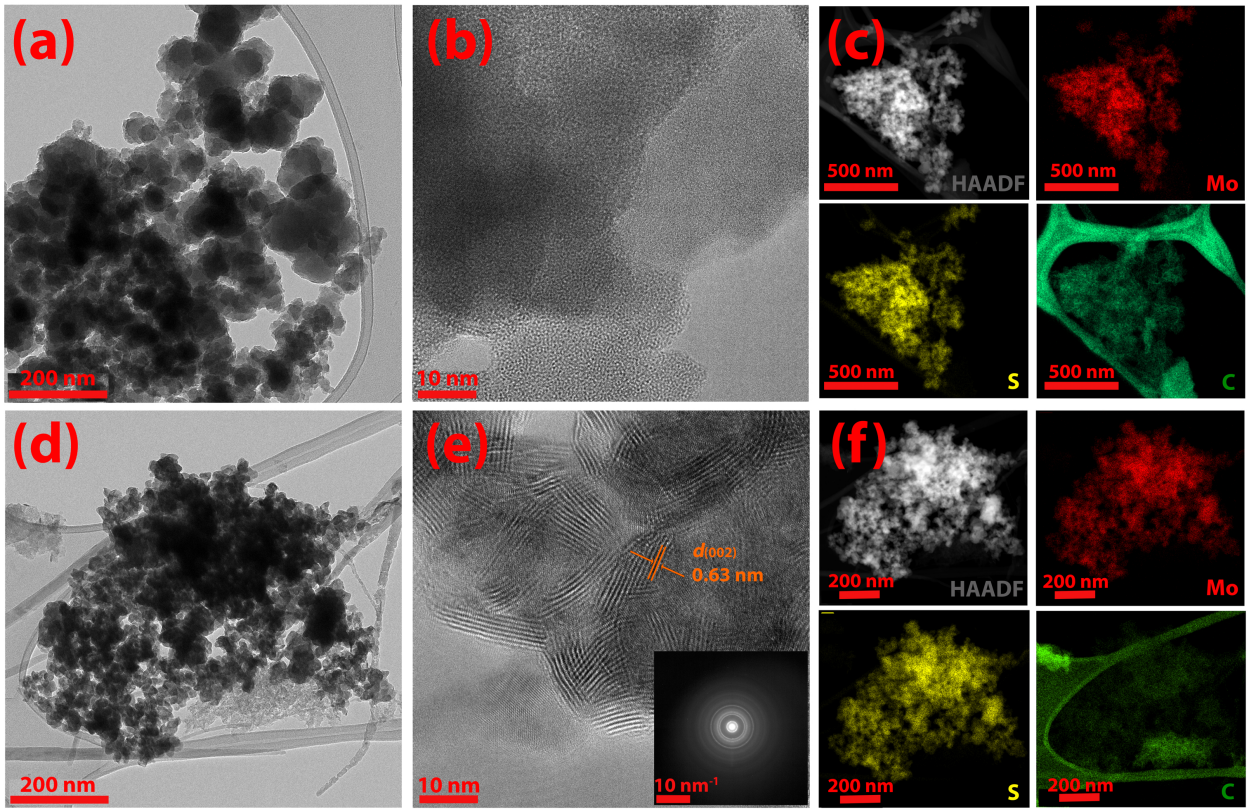

Figure 3.2: TEM (a), HRTEM (b) images, and EDX elemental mapping (c) of MoS_x@HPC1. TEM image (d), HRTEM image (e), and EDX elemental mapping (f) of MoS_2@HPC1. Inset in (e): selected-area electron diffraction of MoS_2@HPC1.

XPS survey spectra of MoS_x@HPC1 and MoS_2@HPC1 are shown in Fig. 3.S1†. In these spectra, peaks from Mo, S, C, and O are predominant, indicating the presence of

mostly molybdenum sulfide and carbon contents. Mo $3d$ spectra of both samples are depicted and compared in Fig. 3.3a. The Mo $3d$ spectrum of MoS_x@HPC1 can be deconvoluted into two doublets, one for Mo (IV) (at 229.5 eV for Mo^{4+} $3d_{5/2}$ and 232.8 eV for Mo^{4+} $3d_{3/2}$) and the other for Mo (VI) (at 232.4 eV for Mo^{6+} $3d_{5/2}$ and 235.6 for Mo^{6+} $3d_{3/2}$) that can be attributed to a small amount of MoO_3 formed during the synthesis step or afterward.[247] MoS_2@HPC1 spectrum also shows two doublets attributed to Mo (IV) and Mo (VI). The peak positions of Mo $3d$ spectra of MoS_x@HPC1 and MoS_2@HPC1 are indicated in the Table 3.S1†. a-MoS_x possesses a polymeric structure, consists of Mo^{IV} connected by bridging (S_2^{2-}), terminal (S_2^{2-}), unsaturated (S^{2-}), and apical (S^{2-}) sulfur ligands ($Mo^{IV}(S_2^{2-})(S^{2-})$).[247–250] As a result, since the oxidation state of molybdenum in both MoS_2 and a-MoS_x is +4, the spectra of both MoS_x@HPC1 and MoS_2@HPC1 show the doublet corresponding to Mo^{IV}. From the XPS data, MoS_x@HPC1 shows a S/Mo ratio of about 3, which indicates that this sample is predominantly composed of MoS_3.

S $2p$ spectra of the samples are illustrated in Fig. 3.3b. MoS_x@HPC1 has a S $2p$ spectrum similar to those of reported a-MoS_x samples.[230–232,234,247,251] In particular, the S $2p$ spectrum can be deconvoluted into two doublets. The one at lower binding energies (S $2p_{3/2}$ at 162 eV and $2p_{1/2}$ at 163.5 eV) is attributed to the terminal S_2^{2-} or unsaturated S^{2-} ligands and the other at higher binding energies (S $2p_{3/2}$ at 163.7 eV and $2p_{1/2}$ at 165 eV) is related to the bridging S_2^{2-} or apical S^{2-} ligands.[247–250] On the contrary, the S $2p$ spectrum of MoS_2@HPC (Fig. 3.3b) shows only one doublet at binding energies of about 162 eV for S $2p_{3/2}$ and 163 eV for S $2p_{1/2}$. Mo $3d$ and S $2p_{3/2}$ spectra of MoS_2@HPC1 resemble those of pure MoS_2 illustrated in Fig. 3.S2†. This confirms the conversion of a-MoS_x in MoS_x@HPC1 to MoS_2 upon annealing. The C $1s$ spectrum of MoS_x@HPC1 depicted in Fig. 3.S3† shows peaks at 284.5, 285.5, 287.0, and 289.0 eV, related to the C=C (sp^2), C−C (sp^3), C−O, and O−C=O, respectively.[177]

Powder X-ray diffraction has been used to analyze the products' crystalline structures. Fig. 3.3c shows the XRD patterns of MoS_x@HPC1 and MoS_2@HPC1, along with JCPDS No. 37-1492 reference related to hexagonal 2H-MoS_2. The XRD pattern of MoS_x@HPC1 shows only a broad peak at around 14°, revealing the amorphous nature of the sample. This is similar to the XRD patterns found with a-MoS_x samples in earlier reports.[232,234,247] All of the XRD peaks of MoS_2@HPC1 are in agreement with the crystalline structure of hexagonal 2H-MoS_2 (JCPDS No. 37-1492).

Fig. 3.3d shows the Raman spectra of MoS_x@HPC1 and MoS_2@HPC1. Distinct D-band and G-band characteristic of carbon materials are observed at about 1350 cm^{-1} and 1600

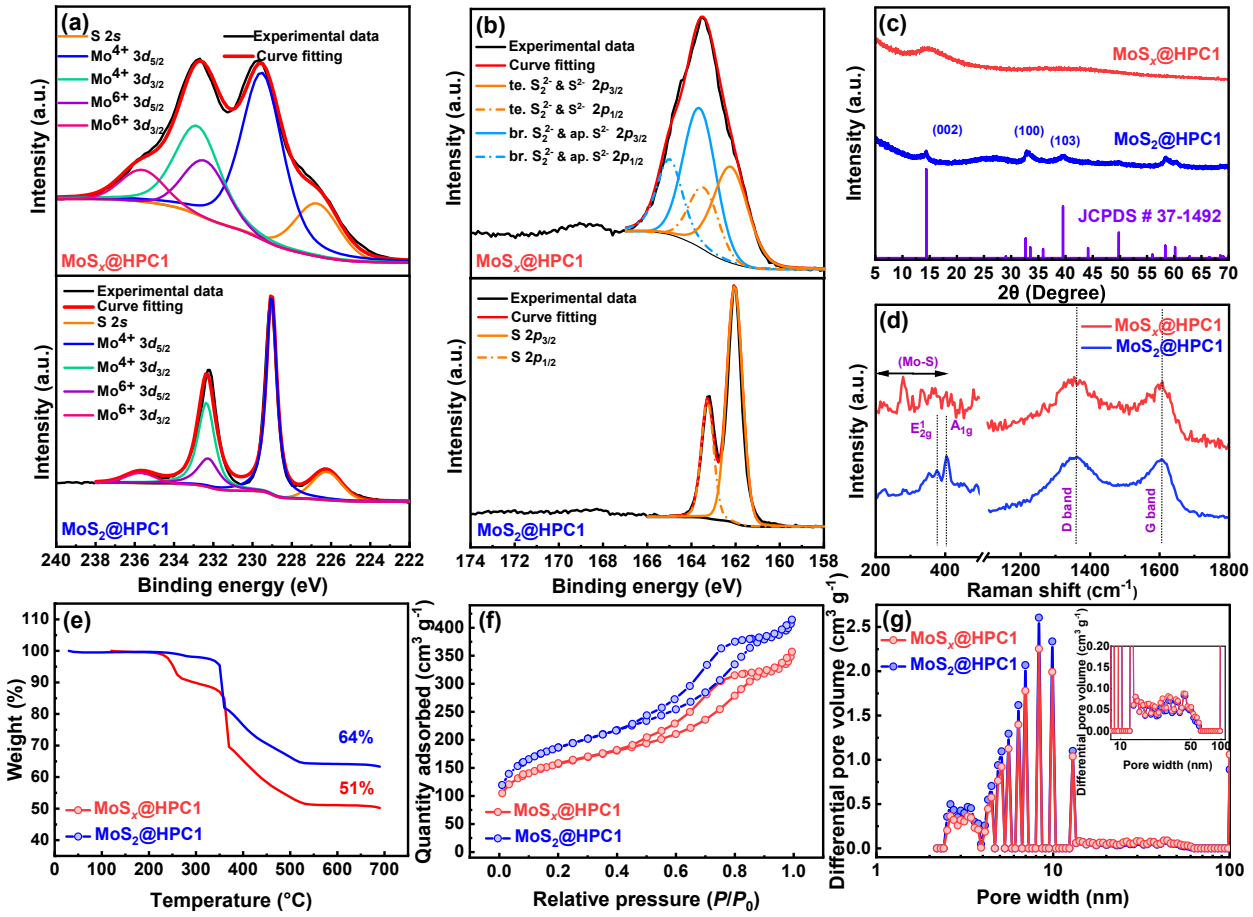

Figure 3.3: XPS spectra of (a) Mo 3*d* and (b) S 2*p*, (c) XRD patterns, (d) Raman spectra (e) TGA curves, (f) N_2 adsorption/desorption isotherms, and (g) pore size distributions of MoS_x@HPC1 and MoS_2@HPC1.

cm^{-1}, respectively, which represent discorded carbon atoms and ordered carbon atoms in 2D hexagonal lattice, respectively. The relative intensity of D-band to G-band (I_D/I_G) is a good indicator to evaluate the ratio of amorphous disordered carbon to graphitic carbon.[252,253] Both MoS_x@HPC1 and MoS_2@HPC1 have I_D/I_G of about 1. So, it can be stated that MoS_x@HPC1 and MoS_2@HPC1 consist of a significant amount of disordered amorphous carbon. In addition, characteristic Raman peaks attributable to a-MoS_x structures are also seen. In the spectrum of MoS_x@HPC1, weak peaks are observed in the range of 200 to 400 cm^{-1}, which are related to vibrations of Mo−S bonds, in agreement with the literature.[231,233,236] The spectrum of MoS_2@HPC1 shows two characteristic peaks of in-plane $E_{2g}{}^1$ mode at 376 cm^{-1} and out-of-plane mode of A_{1g} at 406 cm^{-1}, indicating 2H-MoS_2.[99]

TGA of the samples was carried out in an air atmosphere to estimate the carbon content in MoS_x@HPC1 and MoS_2@HPC1. As shown in Fig. 3.3e, MoS_x@HPC1 and MoS_2@HPC1

show a weight loss of 49% and 36%, respectively, at 550 °C, which can be attributed to the combustion of carbon and the oxidation of a-MoS_x/MoS_2 to MoO_3. As expected, the color of residues obtained after the TGA testing was yellowish-white, which matches the color of pure MoO_3. Assuming the full combustion of carbon, complete oxidation of a-MoS_x/MoS_2 into MoO_3, and the negligible presence of impurities, the carbon content is estimated to be 32 wt% in MoS_x@HPC1 and 29 wt% in MoS_2@HPC1 (see Eq. 3.S1†).

The textural properties of the nanocomposites were characterized by N_2 sorption. Fig. 3.3f illustrates the N_2 sorption isotherms of MoS_x@HPC1 and MoS_2@HPC1. Both nanocomposites show a type IV isotherm with a hysteresis loop indicating a dominantly mesoporous structure. The BET surface area is 518.4 ($S_{d<2}$ nm: 157.1 m^2 g^{-1} & $S_{d>2}$ nm: 361.3 m^2 g^{-1}) and 622.4 m^2 g^{-1} ($S_{d<2}$ nm: 160.0 m^2 g^{-1} & $S_{d>2}$ nm: 462.4 m^2 g^{-1}) for MoS_x@HPC1 and MoS_2@HPC1, respectively. From Fig. 3.3g, both samples show similar mesopore/macropore size distributions. The total pore volume is 0.55 ($V_{d<2}$ nm: 0.08 cm^3 g^{-1}; $V_{d>2}$ nm: 0.47 cm^3 g^{-1}) and 0.64 cm^3 g^{-1} ($V_{d<2}$ nm: 0.09 cm^3 g^{-1}; $V_{d>2}$ nm: 0.55 cm^3 g^{-1}) for MoS_x@HPC1 and MoS_2@HPC1, respectively. It should be noted that the control sample prepared in the absence of starch and KOH is confirmed to be pure MoS_2 (see Fig. 3.S4† for its XRD and Raman spectra) with a low specific surface area of 7.5 m^2 g^{-1} (Fig. 3.S5†). The high surface areas and predominantly mesoporous structures of MoS_x@HPC1 and MoS_2@HPC1 warrant fast sodium ion transport kinetics in addition to the improved electronic conductivity compared to pure MoS_2, which consequently improve the capacity and rate performance. Additionally, the relatively high pore volume can provide a sufficient space to buffer volume changes arising from the insertion and extraction of Na^+ ions.[138,149] Table 3.S2† summarizes the textural properties of the nanocomposites determined through N_2 sorption.

As shown in Fig. 3.S5†, MoS_x@HPC2 and MoS_x@HPC3 also have similar S 2p spectra to that of MoS_x@HPC1. According to these spectra, the sulfur content of MoS_x@HPC1, MoS_x@HPC2, and MoS_x@HPC3 consist of 63%, 53%, and 71% of bridging S_2^{2-}/apical S^{2-}, respectively (Table 3.S3†). In reference to the value of 2.9 for MoS_x@HPC1, the S/Mo ratios determined from the XPS data are 2.76 and 3.58 for MoS_x@HPC2 and MoS_x@HPC3 (synthesized with 400/400 mg and 1200/1200 mg starch/KOH, respectively, vs. 800/800 mg for MoS_x@HPC1), respectively. Accordingly, it can be stated that the more starch/KOH utilized in the synthesis step leads to a higher ratio of S/Mo in the composite. According to TGA results (Fig. 3.S7a†), the carbon content in MoS_x@HPC2 and MoS_x@HPC3 is estimated to be 14 wt% and 38 wt%, respectively, vs 32 wt% for MoS_x@HPC1. In its XRD pattern (Fig. 3.S7b†), MoS_x@HPC2, synthesized in the presence of smaller amounts of starch/KOH (400

mg/400 mg), shows some sharp peaks similar to those of 2H-MoS_2 (JCPDS No. 37-1492), indicating the presence of crystalline MoS_2 in this sample. On the contrary, MoS_x@HPC3 shows a similar XRD pattern as MoS_x@HPC1 with no distinct 2H-MoS_2 peaks, confirming its amorphous MoS_x structure. Therefore, XRD data also demonstrates a relationship between the starch/KOH amount utilized and the crystal structure of the product, with crystalline MoS_2 formed at the relatively low starch/KOH dosages.

The electrochemical performances of MoS_x@HPC1, MoS_2@HPC1, and pure MoS_2 control sample as the anode materials for sodium ion storage in SIBs have been evaluated. Half cells were assembled with each sample for the cathode and sodium metal foil as the anode and were characterized with CV, GCD, and EIS. The initial 5 CV cycles of MoS_x@HPC1 at 0.2 mV s^{-1} are illustrated in Fig. 3.4a. The sodiation of MoS_x@HPC1 is accompanied by Na^+ insertion into the structure and conversion of MoS_x into Mo and Na_2S.[229,237] The cathodic peak at 1.5 V can be related to the Na^+ insertion into a-MoS_x ($MoS_x + nNa^+ + ne^- \longrightarrow Na_nMoS_x$). The other cathodic peak located at around 0.22 V can be attributed to the conversion reactions ($MoS_x + 2xNa^+ + 2xe^- \longrightarrow Mo + xNa_2S$). In the anodic scan, there are multiple oxidation peaks in the range of 1.55 to 2.4 V that can be related to the series of oxidation reactions, including extraction of Na^+ from Na_nMoS_x ($NanMoS_x \longrightarrow MoS_x + nNa^+ + ne^-$) and oxidation of Mo to MoS_x ($Mo + xNa_2S \longrightarrow MoS_x + 2xNa + 2xe^-$).[229] These reduction/oxidation peaks are well retained in the subsequent cycles, confirming the reversible reactions. However, an irreversibility with abnormally high currents is seen in cathodic scan of the first cycle within 0–0.75 V, which can be attributed to the formation of the SEI and reaction of Na^+ with surface functional groups. CV curves in the subsequent cycles well overlap, confirming the reversibility of the charge-discharge process.

In the first CV curve of MoS_2@HPC1 (Fig. 3.4b), two reduction peaks at 0.93 and 0.08 V, respectively, can be seen. The peak at 0.93 V is attributed to the phase transition by insertion of Na^+ into MoS_2 interlayer ($MoS_2 + mNa^+ + me^- \longrightarrow Na_mMoS_2$). The other peak located at 0.08 V is related to the conversion reactions ($Na_mMoS_2 + (4 - m)Na^+ + (4 - m)e^- \longrightarrow Mo + 2Na_2S$).[107] In the anodic scan, three oxidation peaks with the main one at 1.86 V can be seen and are associated to the reverse process of phase transition ($Na_mMoS_2 \longrightarrow MoS_2 + mNa^+ + me^-$). The two reduction peaks become less obvious in further cycles that is due to the irreversible phase transitions in the first cathodic scan.[113] The CV curves practically overlap in the subsequent cycles, demonstrating high reversibility and stability of Na^+ storage in MoS_2@HPC1. The first CV curve of pure MoS_2 (Fig. 3.S8†) shows the same reduction and oxidation peaks as MoS_2@HPC1 with an additional distinctive reduction

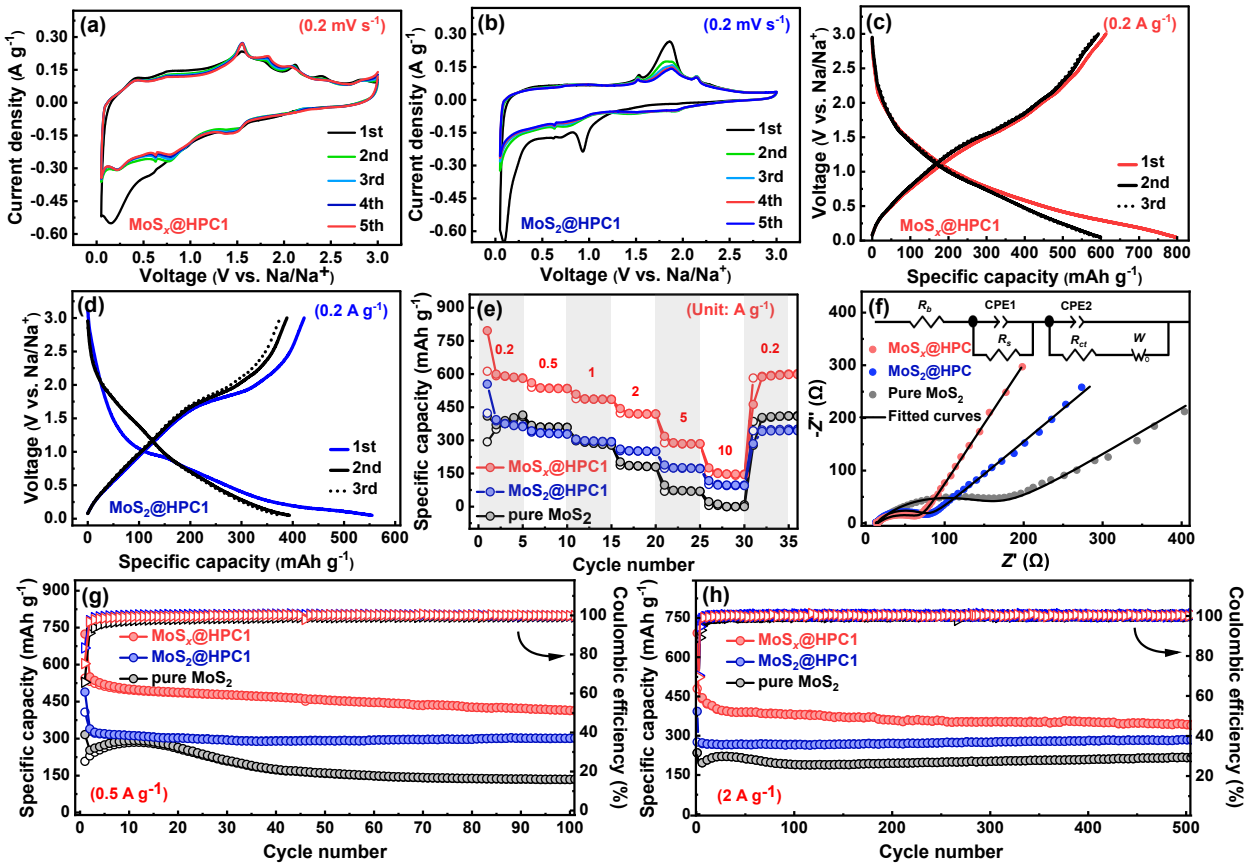

Figure 3.4: Electrochemical performances of cells assembled with MoS_x@HPC1, MoS_2@HPC1, and pure MoS_2, as the cathode and Na metal as the anode: CV curves at a scan rate of 2 mV s^{-1} of (a) MoS_x@HPC1 and (b) MoS_2@HPC1, GCD profiles at a current density of 0.2 A g^{-1} of (c) MoS_x@HPC1 and (d) MoS_2@HPC1, (e) rate performance, (f) Nyquist plots, (g) cycling at 0.5 A g^{-1}, and (h) cycling at 2 A g^{-1} of MoS_x@HPC1, MoS_2@HPC1, and pure MoS_2.

peak at 0.7 V. This additional peak comes from a multistep phase transition during Na^+ intercalation, resulting in two reduction peaks (at 0.93 V and 0.7 V). This staging process is a common phenomenon in the intercalation of large cations into transition metal sulfides and it reduces the energy required to open up the van der Waals gap between the layers. Therefore, it can be stated that in MoS_2@HPC1, the energy required to open up the van der Waals gap is much less than that of pure MoS_2.[113]

Fig. 3.4c shows the curves of the first three GCD profiles of MoS_x@HPC1 at a current density of 0.2 A g^{-1} within a potential window of 0.05–3 V. In general, slopping curves are observed with no distinct voltage plateaus. Amorphous materials possess randomly arranged atoms and a significant amount of defect sites. As a result, the Na^+ storage sites are not distinct, resulting in the absence of voltage plateaus in the charge/discharge

profile.[254] MoS_x@HPC1 exhibits the first discharge and charge capacities of 796 and 612 mAh g^{-1}, respectively. This corresponds to a low Coulombic efficiency of about 77%, which results from the formation of SEI. In the second cycle, this electrode shows a reversible capacity of 599 mAh g^{-1} with a Coulombic efficiency of almost 99%. As shown in the GCD profile of MoS_2@HPC1 (Fig. 3.4d), this electrode exhibits much lower capacities (an initial discharge capacity: 555 mAh g^{-1}) than MoS_x@HPC1 but behaves similarly with a low initial Coulombic efficiency of 76% and a reversible discharge capacity of 394 mAh g^{-1} with a Coulombic efficiency of 99% in the second discharge. The higher capacity of MoS_x@HPC1 arises from the amorphous MoS_x structure, providing more active sites for Na^+ storage compared to the crystalline structure of MoS_2.

The rate performance of the samples has been evaluated in a current density range from 0.2 to 10 A g^{-1} (Fig. 3.4e). MoS_x@HPC1 exhibits reversible specific capacities of 599, 534, 487, 421, 288, and 150 mAh g^{-1} at 0.2, 0.5, 1, 2, 5, and 10 A g^{-1}, respectively. With the current is switched back to 0.2 A g^{-1}, a reversible specific capacity of about 600 mAh g^{-1} has been retained. At all currents applied, MoS_2@HPC1 shows lower specific capacities (394, 343, 305, 260, 188, and 117 mAh g^{-1} at 0.2, 0.5, 1, 2, 5, and 10 A g^{-1}, respectively) than MoS_x@HPC1. Pure MoS_2 shows slightly higher capacities at 0.2 and 0.5 A g^{-1} than MoS_2@HPC1 (400 and 360 mAh g^{-1}, respectively). However, at higher currents, its capacities are lower than the corresponding ones of MoS_2@HPC1. The higher capacity of Pure MoS_2 at low current densities can be related to its purity (with no carbon content) with more electrochemically active sites. It should be noted that, as shown in Fig. 3.S9†, the contribution of pure carbon in the storage of sodium ions is only about 150, 90, 53, 23, 10, and 0 mAh g^{-1} at 0.2, 0.5, 1, 2, 5, and 10 A g^{-1}, respectively. However, due to the low active surface area of pure MoS_2, its Na^+ storage sites are not accessible at high currents, with the capacity of almost 0 at 10 A g^{-1}.

According to the rate performance tests, MoS_x@HPC1 shows higher capacities compared to MoS_2@HPC1 and pure MoS_2 at all applied current densities. In addition, a comparison of rate performance with reported results for other similar nanocomposites of a-MoS_x or MoS_2 with carbon reveals the remarkable performance of MoS_x@HPC1 as an anode for SIBs, particularly at lower current densities (below 1000 mA g^{-1}; see Fig. 3.S10†. This superior performance arises from the amorphous nature and unique molecular structure of a-MoS_x, leading to its smaller alkali ion diffusion energy barrier and more exposed electrochemical active sites compared to crystalline MoS_2 nanocomposites.[229,231,236]

The charge transfer kinetics of the electrodes was investigated through EIS test. Fig.

3.4f shows the Nyquist plots of MoS_x@HPC1, MoS_2@HPC1, and pure MoS_2 electrodes acquired in the charge state (≈2.8 V). The R_{ct}, determined as the diameter of the semicircle in the medium-frequency region, is 60.0, 63.9, and 148.0 Ω for MoS_x@HPC1, MoS_2@HPC1, and pure MoS_2 respectively. Accordingly, MoS_x@HPC1 has a slightly higher electron and ion conductivities compared to MoS_2@HPC1. In addition, the Warburg impedance reflected by the slope of the line in the low-frequency region, is lower with MoS_x@HPC1 than with MoS_2@HPC1, indicating the enhanced Na^+ diffusion within the former.[138] On the other hand, the electrode with pure MoS_2 shows R_{ct} of 148.0 Ω and the lowest slope in the low-frequency region of the Nyquist plot, explaining the poor electrochemical performance of pure MoS_2. The detailed results obtained from Nyquist plots including value of each component in the fitting circuit are summarized in Table 3.S4†. As shown in 3.S4†, a low R_s (≈2.0 Ω), attributed to the SEI, is found with MoS_x@HPC1, indicating the good ion transport characteristic.[255] According to the Nyquist plots obtained at different charge states, MoS_x@HPC1 shows a lower charge transfer resistance (smaller semicircle in the medium-frequency region) compared to MoS_2@HPC1 at different cell voltages of 1.5, 1, and 0.1 V, respectively (Fig. 3.S11†).

The cycling stability of the electrodes has been investigated by performing GCD at 0.5 A g^{-1} for 100 cycles (Fig. 3.4g). MoS_x@HPC1 shows a retained discharge capacity of 414 mAh g^{-1} at the 100th cycle, corresponding to a capacity retention of 75% in reference to the initial reversible discharge capacity of 550 mAh g^{-1}. Except for the first cycle, the Coulombic efficiency is maintained at about 99.7% during the entire cycling process. This high Coulombic efficiency reveals reversibility of electrochemical reactions during insertion/deinsertion of Na^+, and very low side reactions.[256] Though with a lower initial reversible capacity of 340 mAh g^{-1}, MoS_2@HPC1 shows a slightly better stability than MoS_x@HPC1 by delivering 301 mAh g^{-1} at the 100th cycle with a capacity retention of 89%. Although MoS_2@HPC1 shows a better cyclic stability, MoS_x@HPC1 delivers higher specific capacities over the entire 500 cycles, demonstrating its superior performance. On the other hand, pure MoS_2 shows an initial increase in the capacity from 253 mAh g^{-1} at the 1_{st} reversible cycle to 292 mAh g^{-1} at the 10_{th} cycle, followed by the gradual decrease in capacity to 134 mAh g^{-1} at the 100_{th} cycle (53% retention relative to 1_{st} cycle). A comparison of rate performance and stability of MoS_x@HPC1 and MoS_2@HPC1 with those of pure MoS_2 reveals the important role of the porous carbon in affecting the performance of these nanocomposites. In the absence of the carbon matrix, the low conductivity, surface area, and tolerance against volume change results in the weak electrochemical performance of pure MoS_2.[138,149]

The cycling stability is also evaluated at 2 A g^{-1} over 500 cycles (Fig. 3.4h). MoS_x@HPC1 exhibits a reversible capacity of 484, 391, and 343 mAh g^{-1} in the first, 50_{th}, and 500_{th} cycle, respectively, which conveys capacity retentions of about 71% and 88% at the 500_{th} cycle relative to the 1_{st} and 50_{th} cycles, respectively. The Coulombic efficiency of the MoS_x@HPC1 electrode is maintained at about 100% over 500 cycles. On the other hand, MoS_2@HPC1 exhibits a final capacity of 284 mAh g-1 at the 500_{th} cycle, with a retention of 98% relative to the first cycle. Relative to the 1_{st} reversible cycle, pure MoS_2 exhibit 8% of capacity increase (200 mAh g^{-1} at the first cycle and 216 mAh g^{-1} at 500_{th} cycle) at 2 A g^{-1}. The gradual capacity increase results from the electro-activation by intercalation/deintercalation of Na^+ into the interlayer lattice.[131,132]

On the basis of the above electrochemical performances, MoS_x@HPC1 shows the better performance than its annealed product MoS_2@HPC1. Therefore, the electrochemical performance of MoS_x@HPC2 and MoS_x@HPC3 have been subsequently evaluated for sodium storage (Fig. 3.S12†). Compared to MoS_x@HPC1 and MoS_x@HPC3, MoS_x@HPC2 with the lowest carbon content and S:Mo ratio shows lowest capacities at all current densities applied in the rate performance test (Fig. 3.S12a†). This electrode delivers 476 and 50 mAh g^{-1} at 0.2 and 10 A g^{-1}, respectively. By switching the current back to 0.2 A g^{-1} it shows a reversible capacity of 444 mAh g^{-1}. MoS_x@HPC3 that possess the highest carbon content and S:Mo ratio, delivers a reversible capacity of 592 mAh g^{-1} at 0.2 A g^{-1}, almost the same as the value (599 mAh g^{-1}) that MoS_x@HPC1 delivers at this current. With the increase of current, it, however, shows a faster capacity decay than MoS_x@HPC1, reaching 58 mAh g^{-1} at 10 A g^{-1}. In the cycling test at 0.5 A g^{-1} (Fig. 3.S12b†), MoS_x@HPC2 shows lower capacities but the better stability (87% capacity retention over 100 cycles) compared to its two counterparts. On the other hand, at the first reversible cycle, MoS_x@HPC3 possess the highest capacity (578 mAh g^{-1}) but it is inferior in cycling stability (61% retention over 100 cycles). The reason that MoS_x@HPC3 shows the highest initial capacity while MoS_x@HPC2 has the lowest can be associated with the types of sulfur in their structure. As shown in the XPS profiles of the samples (Fig. 3.S6) as well as in Table 3.S3†, MoS_x@HPC3 possesses the highest percentage of bridging S_2^{2-} (71%), while that of MoS_x@HPC2 is the lowest (53%). Accordingly, it can be concluded that, the sulfur species that show the doublet in the higher binding energy region of XPS S $2p$ profile have the major contribution to the charge storage process (disulfide bonds dissociation by sodium ion insertion). Similar results in previous research suggest that the higher sulfur content as well as the more sulfur in the higher

binding energy region results in the higher capacity of a-MoS_x for Na^+ storage.[237] Overall, MoS_x@HPC1 has the optimum carbon content, S:Mo ratio, and bridging S_2^{2-} content, providing it with the best electrochemical performance.

As reported in earlier studies,[62,67,257] Na^+ ion storage in the layered structure of MoS_2 takes place through two mechanisms, including intercalation at V > 0.4 and conversion reactions at V < 0.4 ($Na_mMoS_2 + (4 - m)Na^+ + (4 - m)e^- \longrightarrow Mo + 2Na_2S$). At V < 0.4, the conversion of MoS_2 to Mo nano-grains and Na_2S can adversely affect the electrochemical performance leading to the low stability of the battery, particularly at low current densities. In the case with a-MoS_x composites as an anode for alkali ion batteries, the conversion reactions ($MoS_x + 2xNa^+ + 2xe^- \longrightarrow Mo + xNa_2S$) are also expected in the low voltage range, particularly at low current densities.[231,232,234] Narrowing the potential window down to 0.4–3 V has been reported to boost the cycling stability of MoS_2 anodes but with lowered capacities.[107,147] In an attempt to improve its cyclic stability, we have also investigated the electrochemical performance of MoS_x@HPC1 in a narrowed potential window to evaluate the efficiency of this method for the a-MoS_x based anode material (Fig. 3.5). The CV curves of MoS_x@HPC1 in the voltage window of 0.4–3 (Fig. 3.5a) are similar to those acquired within 0.05–3 V, except that the peaks below 0.4 V are absent. From Fig. 3.5b, MoS_x@HPC1 shows specific capacities of 486, 406, 357, 309, 216, 139 mAh g^{-1} at the current densities of 0.2, 0.5, 1, 2, 5, and 10 A g^{-1}, respectively. Fig. 3.5c shows the cyclic stability of MoS_x@HPC1 within 0.4–3 V for 600 cycles at 0.2 A g^{-1}. With the initial value of 465 mAh g^{-1}, the specific capacity decreases to 351 mAh g^{-1} at the 50_{th} cycle and then remains rather stable with 324 mAh g^{-1} retained at the 600_{th} cycle (capacity loss of 0.05% per cycle). A further cycling test at a high current of 8 A g^{-1} shows an ultra-stable cyclability with 88% of capacity retention over 10000 cycles (Fig. 3.5d). The improved cyclic stability is ascribed to the restriction of the conversion reactions as a result of the narrowed voltage window.

To investigate the mechanism of charge and discharge reactions, CV tests were performed at five different scan rates within 0.2 to 1 mV s^{-1}. As shown in Fig. 3.6a, all CV curves show similar shapes at different scan rates but with slight shifts in reduction/oxidation peaks and enhanced current responses with the increasing scan rate. The current at any voltage follows a power-law relation with scan rate ν (Eq. 3.1).[258,259]

$$i = a\nu^b \tag{3.1}$$

The b value ranges from close to 0.5 for the diffusion-controlled battery behavior and

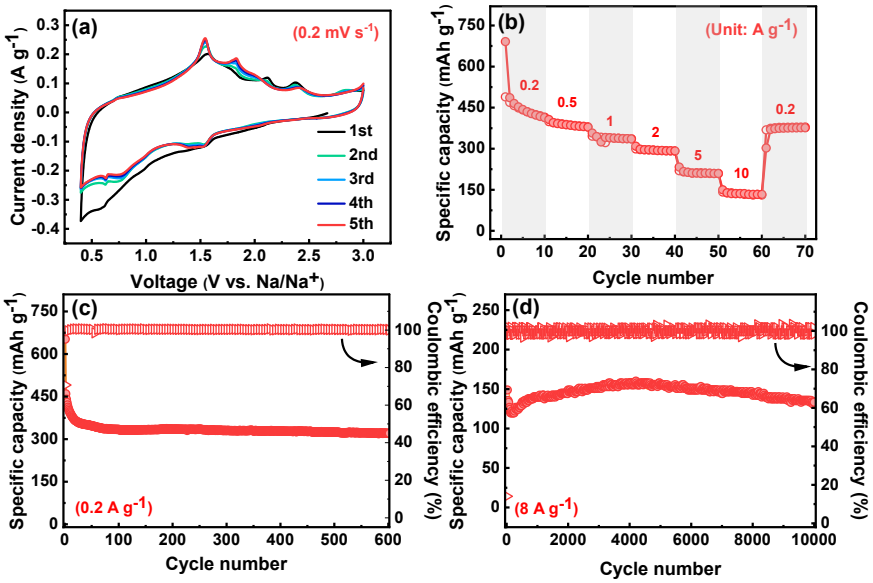

Figure 3.5: Electrochemical performance of a half cell assembled with MoS_x@HPC1 cathode and Na metal anode in the voltage window of 0.4–3 V: (a) CV curves at a scan rate of 2 mV s^{-1}, (b) rate performance with capacity at different current densities, (c) cycling at a current density of 0.2 A g^{-1}, and (d) cycling at a current density of 8 A g^{-1}.

1 for surface-induced pseudocapacitive behavior. Fig. 3.6b shows the log (i) vs. log (ν) plots for the three distinctive peaks as labelled in Fig. 3.6a. All the b values (1, 0.85, and 0.95 for Peaks 1, 2, and 3, respectively) are greater than 80%, indicating the dominant surface-induced pseudocapacitive behavior. This feature arises from the porosity of the structure and good accessibility of active sites, which is in agreement with the high rate performance of MoS_x@HPC1. The percentages of the pseudocapacitive ($k_1\nu$) and diffusion-controlled ($k_2\nu^{1/2}$) contributions to the current response at different voltage scan rates can be calculated with Eq. 3.2.[257,259]

$$i = k_1\nu + k_2\nu^{1/2} \tag{3.2}$$

where i is the current measured by CV at scan rate of ν, and k_1 and k_2 can be determined as slope and y-axis intercept point of linear fitting of $i/\nu^{1/2}$ vs. $\nu^{1/2}$ plot, respectively, at each fixed potential. By calculation of k_1 and k_2 at each fixed potential, the pseudocapacitive contribution ($k_1\nu$) can be determined for each potential in a scan (Fig. 3.6c). A peak shift as a function of scan rate can be seen in CV plots of these batteries (Fig. 3.6a, Figs. 3.S13a, and 3.S14a), which can introduce errors in the calculations. Therefore, to eliminate the effect of the peak shifts, the acquired data at 0.2 mV s^{-1} has been used to define the potentials of the peak current positions at all other scan rates.[259]

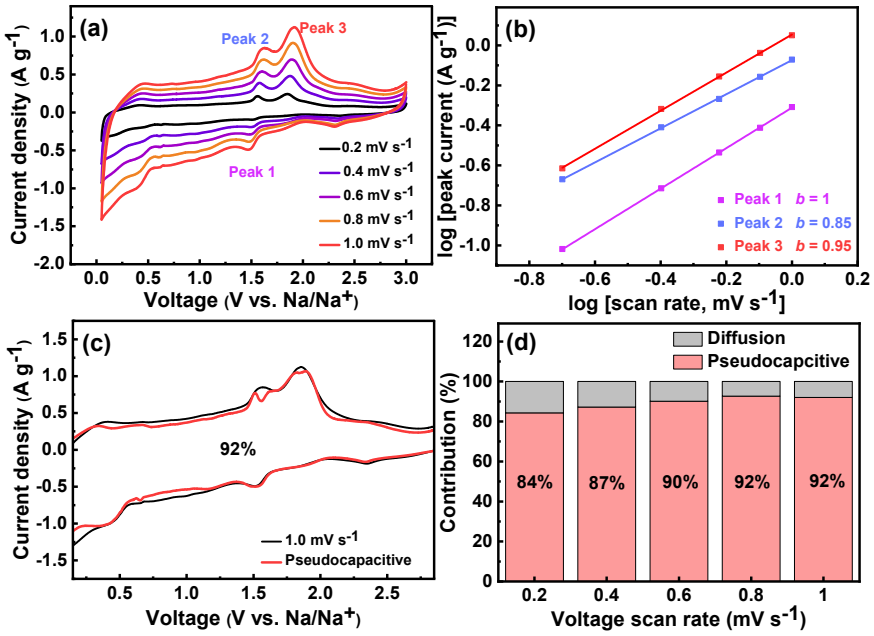

Figure 3.6: Electrochemical performance of a half cell assembled with MoS_x@HPC1 cathode and Na metal anode: (a) CV curves at different voltage scan rates, (b) log (peak current) vs. log (scan rate) plots plus the b values related to the main reduction and oxidation peaks, (c) the pseudocapacitive contribution to the current response at a voltage scan rate of 1 mV s^{-1}, and (d) comparison of capacitive and diffusion-controlled contributions to the current at different scan rates.

Accordingly, the pseudocapacitive ($k_1\nu$) and diffusion-controlled ($k_2\nu^{1/2}$) contributions to the current response at different scan rates have been quantitated. As shown in Fig. 3.6c and Fig. 3.S13†, MoS_x@HPC1 and MoS_2@HPC1 exhibit 92% and 91%, respectively, of pseudocapacitive contributions to the current response at a scan rate of 1 mV s^{-1}. As expected, with the increasing current density, the pseudocapacitive contribution increases for both electrodes (see Fig. 3.6d and Fig. 3.S13c†). Accordingly, in both MoS_x@HPC1 and MoS_2@HPC1, the pseudocapacitive behavior is predominant. At all scan rates, the pure MoS_2 control sample shows lower pseudocapacitive contributions compared to the two carbon-containing composites (Fig. 3.S14†), which is in agreement with its poor rate performance. The Na^+ storage kinetics are directly affected by the pseudocapacitive contribution.[260] With a higher pseudocapacitive contribution, the sodium ion transport is enhanced, which is clearly seen in the rate performance tests as discussed above. The kinetic test results also reveal that the MoS_x@HPC1 half cell has a remarkable performance. Nevertheless, studying anode materials in a full cell is necessary to investigate the performance for practical use and commercialization. Therefore, there is space for further investigating the performance of MoS_x@HPC1 in a full cell and making optimizations by electrode and electrolyte engineering in a further

study.[261]

3.4 Conclusions

A simple one-pot synthesis method is demonstrated to synthesize MoS_x@HPC composites with a-MoS_x embedded within a hierarchical porous carbon matrix. It has been shown that by pyrolysis of the precursors along with carbonization of the carbon source in one step, a highly porous composite of MoS_x@HPC1 with a wide range of pore size can be obtained. The subsequent annealing of MoS_x@HPC1 results in the formation of MoS_2@HPC1 consisting of crystalline MoS_2. The N2-sorption characterization reveals that both nanocomposites have a remarkable surface area of 518.4 and 622.4 $m^2\ g^{-1}$, respectively. A systematic study on the electrochemical performance of the nanocomposites as anode materials for SIBs has been undertaken. MoS_x@HPC1, with a first reversible capacity of 612 mAh g^{-1} at a current density of 0.2 A g^{-1}, possesses a higher capacity compared to the MoS_2@HPC1 and pure MoS_2. The rate capability test also reveals that MoS_x@HPC1 delivers higher capacities at all applied currents in the range of 0.2 to 10 A g^{-1}. According to the kinetic tests, MoS_x@HPC1 has a lower charge transfer resistance with improved Na^+ diffusion compared to MoS_2@HPC1. The electrochemical tests indicate the better performance of MoS_x@HPC1 than MoS_2@HPC1 for the storage of sodium ions, which is due to its unique amorphous structure with easily accessible electrochemical active sites. A comparison of these nanocomposites with pure MoS_2 electrode also reveals that the hybridization with carbon remarkably enhances the electrochemical performances of MoS_x@HPC1 and MoS_2@HPC1 in terms of capacity, rate capability, and cycling stability. The comparison of the electrochemical performance of MoS_x@HPC electrodes with different carbon contents and S:M ratios elucidated that higher S:M ratio and carbon content leads to higher capacity. However, the comparison also indicates a decrease in the cycling stability for the nanocomposite with a higher S:M ratio. As a result, MoS_x@HPC1, with S:M ratio of about 3 and carbon content of 32%, is identified as the optimal nanocomposite in terms of capacity and cycling stability.

Chapter 4

1T-2H Mixed-Phase MoS_2 Stabilized with a Hyperbranched Polyethylene Ionomer for Mg^{2+}/Li^+ Co-Intercalation Toward High-Capacity Dual-Salt Batteries[‡]

Adapted from article:

1T-2H Mixed-Phase MoS_2 Stabilized with a Hyperbranched Polyethylene Ionomer for Mg^{2+}/Li^+ Co-Intercalation Toward High-Capacity Dual-Salt Batteries

Jalal Rahmatinejad, Bahareh Raisi, Xudong Liu, Ximeng Zhang, Ahmad Sadeghi Chevinli, Liuqing Yang, Zhibin Ye

Published in: ***Small***

https://doi.org/10.1002/smll.202304878

[‡] Supplementary Information available: See Appendix B

Abstract Dual-salt magnesium/lithium-ion batteries (MLIB) benefit from fast lithium ion diffusion on the cathode side while providing safety due to the dendrite-free Mg^{2+} stripping/-plating mechanism on the anode side. Bulk MoS_2 (B-MoS_2), as a cathode for magnesium-ion batteries (MIB), suffers from low conductivity and relatively van der Waals gaps and, consequently, resists against divalent Mg^{2+} insertion due to the high Coulombic interactions. In MLIBs, it exhibits a Daniell-cell type mechanism with the sole accommodation of Li^+. In this paper, the synthesis of a 1T/2H mixed-phase MoS_2 (MP-MoS_2) modified with a hyperbranched polyethylene ionomer, I@MP-MoS_2, for high-capacity MLIBs with a distinct Mg^{2+}/Li^+ co-intercalation mechanism is reported. Benefiting from the enhanced conductivity (due to 53% metallic 1T phase), expanded van der Waals gaps (79% expansion compared to B-MoS_2, 1.11 vs. 0.62 nm), and enhanced interactions with THF-based electrolytes following the modification, I@MP-MoS_2 shows a dramatically increased Mg^{2+} storage compared to its parent analogue (144 mAh g^{-1} vs ≈2 mAh g^{-1} at 20 mA g^{-1}). In MLIBs, I@MP-MoS_2 has been demonstrated to exhibit remarkable specific capacities up to ≈270 mAh g^{-1} at 20 mA g^{-1} through a Mg^{2+}/Li^+ co-intercalation mechanism with 87% of capacity retention over 200 cycles at 100 mA g^{-1}.

4.1 Introduction

Despite its high theoretical capacity (3860 mAh g^{-1} or 2060 mAh cm^{-3}) and low negative electrochemical potential (−3.04 V vs. SHE), lithium metal as an anode for lithium-ion batteries (LIBs) is associated with serious safety issues.[30,31] The safety issues arise from dendrite growth on the surface of the lithium metal anode during the reduction of Li^+ through the electro-adsorption process, resulting in catastrophic battery failure and short-circuiting accompanied by fire.[10,11] Graphite, though with a relatively low theoretical capacity of 372 mAh g^{-1} and 735 mAh cm^{-3}, is the most common anode in today's LIBs due to the enhanced safety with the absence of dendrite formation.[2] On the other hand, MIBs with magnesium metal anodes are potential alternatives to LIBs for several reasons. Magnesium metal has a relatively low reduction potential of −2.37 versus SHE. The divalent nature of Mg^{2+} leads to its high volumetric capacity of 3833 mAh cm^{-3}, 86% more than that of lithium metal. Also, magnesium is an abundant and evenly distributed element that makes it affordable and suitable to prevent the growing depletion of lithium resources. Above all, the deposition/dissolution of Mg^{2+} on the surface of the magnesium metal is known as a dendrite-free process, providing high safety for the device. The dendrite-free charge-discharge mechanism, high melting point (660 °C), and the non-toxicity of magnesium make magnesium metal batteries safer than lithium metal batteries.[22,190,191] The main problem hindering the progress of MIBs is the lack of a suitable cathode that can overcome the sluggish solid-state kinetics of magnesium ions. This slow kinetic results from the strong Coulombic interactions induced by the divalent nature of magnesium ions.[192] One approach to bypass this issue is to fabricate hybrid MLIBs using a dual-salt electrolyte containing both magnesium and lithium salts. These batteries benefit from the kinetically efficient insertion/extraction of lithium ions in the cathode. Additionally, as the anode only experiences magnesium deposition/dissolution (due to its high redox potential), they still have the above-mentioned advantages of magnesium metal anode.[213] However, these batteries with a Daniell-type mechanism (Li^+ and Mg^{2+} are involved only in the reactions of the cathode and anode, respectively) need a large amount of electrolyte, which results in their low energy density.[?] For this purpose, a cathode material that can simultaneously accommodate both Mg^{2+} and Li^+ by co-intercalation is needed to achieve a high energy density. Bulk MoS_2, known for its 2D structure, due to its relatively small inter-layer distance of around 0.62 nm, and semiconducting nature arising from the 2H crystal phase (the most thermodynamically stable crystal phase), is generally not a suitable host for Mg^{2+}.[16] It has been proven that expanding the inter-layer spaces is a promising approach to enhance the ability of bulk MoS_2 to accommodate relatively large

ions like Na^+ and K^+ and divalent Mg^{2+} and Zn^{2+}.[16,54,62,262] In addition, the preparation of metallic 1T-rich MoS_2 through various phase engineering techniques is another promising approach to render enhanced electronic conductivity and, consequently, efficiency for storage of such ions.[93,263,264] In the past research, polymers such as PVP and PEO have been used as the guest molecules to intercalate between the layers of MoS_2, leading to its enlarged inter-layer distance and efficiency in MIBs.[16,114] In addition, the nanocomposites of MoS_2 with other highly electron-conducting compounds, such as graphene and carbon nanofibers, have been synthesized and used as cathodes for Mg^{2+}/Li^+ hybrid batteries. The co-intercalation of both ions has been shown within such nanocomposites due to their high conductivity and large inter-layer distances.[213,216] However, a synthesis technique that simultaneously provides the formation of a metallic 1T phase, increased inter-layer spacing, and enhanced electrochemistry in low-polarity THF-based electrolytes would significantly enhance Mg^{2+} storage and improve the co-intercalation of Mg^{2+} and Li^+ ions within a dual-salt battery.

Herein, a top-down method for synthesis of 1T phase-rich inter-layer expanded mixed-phase MoS_2 has been introduced, which includes the chemical exfoliation of bulk MoS_2 and the further modification with a hyperbranched polyethylene ionomer containing quaternary ammonium cations. By the exfoliation process, a few-layered 1T-2H mixed-phase product with a high content of metallic 1T phase forms and the re-stacking of the few-layered sheets is efficiently prevented by the subsequent modification/stabilization with the ionomer. The resulting product possesses high electrical conductivity and has significantly enlarged inter-layer distances, leading to more accessible active sites and accelerated Mg^{2+}/Li^+ diffusion rate. This synthesis is a facile method that revives bulk MoS_2 and turns it into an efficient material for hybrid dual-salt Mg^{2+}/Li^+ batteries.

4.2 Results and Discussion

In our strategy, a unique hyperbranched polyethylene ionomer having the hyperbranched polyethylene skeleton covalently tethered with quaternary ammonium ions is employed as the polymeric intercalant to expand the 2D MoS_2 sheets. The rationale for the selection of this ionomer includes: 1) the strong ionic interaction of its positively charged quaternary ammonium ions with the negatively charged surface of the 2D layers of MoS_2;[195] 2) its high dispersibility in nonpolar/low polarity solvents (such as THF) as a result of its nonpolar hyperbranched polyethylene skeleton. These two characteristics are expected to render the efficient intercalation of the ionomer between the 2D sheets and, meanwhile, make the resulting

nanocomposite compatible with THF-based Mg^{2+}/Li^{+} electrolyte to facilitate the facile ion transport in the liquid/solid interface. The resulting ionomer-intercalated MoS_2 nanocomposites are expected to have the advantages needed for the co-intercalation of Mg^{2+}/Li^{+} in MLIBs.

Figure 5.1 shows the schematic synthesis of the hyperbranched polyethylene ionomer and the ionomer-1T-2H mixed-phase MoS_2 (MP-MoS_2), I@MP-MoS_2. The hyperbranched polyethylene ionomer used herein is synthesized by direct catalytic copolymerization of ethylene with a quaternary ammonium-containing acrylate-type ionic liquid comonomer facilitated with a Pd-diimine catalyst.[265] It contains a quaternary ammonium content of 1.03 mol%. Hyperbranched polyethylene ionomers have been previously used for the modification of nanomaterials of negatively-surface-charged including cellulose nanocrystals[195] and gold nanorods[196] to render their stable dispersions in nonpolar or low-polarity organic solvents.

To obtain I@MP-MoS_2, B-MoS_2 is first lithiated with n-butyllithium in a mixed solvent of hexane/THF, followed by sonication in water. The n-butyllithium-assisted exfoliation is a well-known method to synthesize aqueous suspension of 1T phase-containing few-layered MP-MoS_2. During lithiation, the electron-donating nature of lithium leads to the electron transfer to the d-orbital of molybdenum to form the lithiated MoS_2 (Li_xMoS_2) and consequently induces the phase transition from 2H to 1T.[47] In the phase transition process, the initially dominant thermodynamically stable and semiconducting phase of MoS_2, characterized by hexagonal symmetry and two layers within its unit cell (referred to as 2H, with a space group of $P63/mmc$), undergoes a transformation. This transformation results in the emergence of a metastable metallic phase exhibiting trigonal symmetry, containing only one layer in its unit cell (designated as 1T, with a space group of $P3\overline{m}1$). It is important to note that the completeness of this phase transition can fall short of 100%, leading to the creation of a mixed-phased MoS_2 material, where both semiconducting and metallic phases coexist.[33,266] The subsequent hydration of Li_xMoS_2, by the reaction of lithium and water, generates LiOH and H_2 gas, pushing the MoS_2 layers apart to form exfoliated nanosheets.[46,102]

During the precipitation and drying steps, a random restacking of the exfoliated MoS_2 nanosheets often occurs, rendering the product as 1T-2H mixed-phase MoS_2 (MP-MoS_2) with a lower crystallinity and larger spaces in its structure than its bulk parent B-MoS_2.[16,113] To minimize the restacking, the aqueous dispersion of MP-MoS_2 (20 mL, 4 mg mL^{-1}) obtained following the hydration, without drying, is directly added dropwise into the solution of the ionomer (40 mL, 1.5 mg mL^{-1}) in THF under sonication to yield I@MP-MoS_2 (Step 3 in

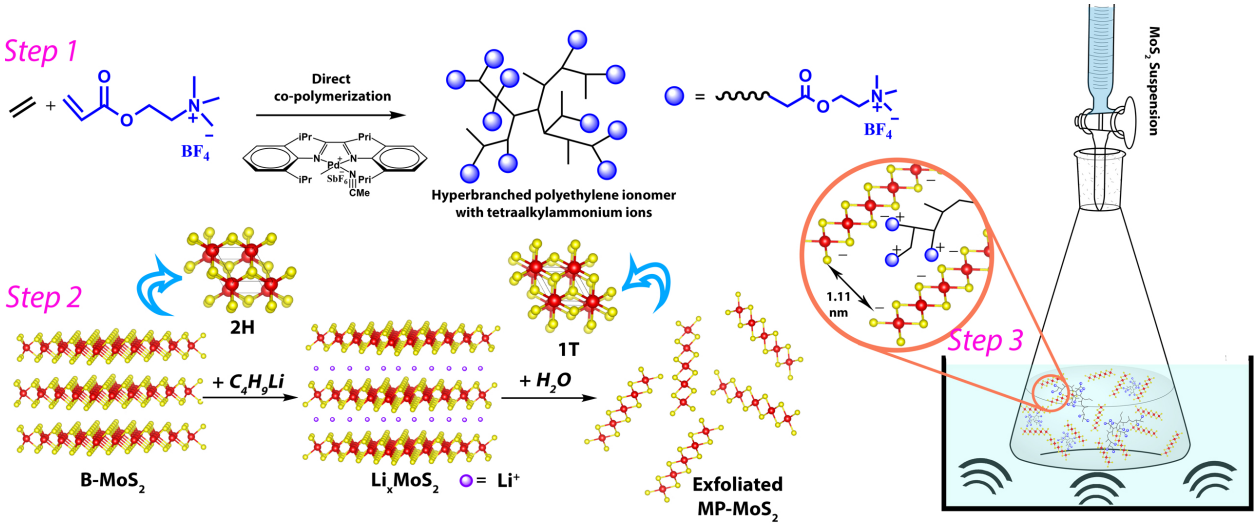

Figure 4.1: Schematic illustration of synthesis of hyperbranched polyethylene ionomer, MP-MoS_2, and I@MP-MoS_2.

Figure 5.1). A short sonication of 15 min was found sufficient to facilitate the fast intercalation of the ionomer within the few-layered MoS_2 nanosheets. Subsequently, a thorough wash with fresh THF was performed to remove excess ionomer from the product I@MP-MoS_2.

TGA was undertaken in an N_2 atmosphere to quantify the content of the ionomer in I@MP-MoS_2. Figure 4.2a shows the TGA curve of I@MP-MoS_2, along with those of the ionomer and MP-MoS_2 for comparison. As shown in Figure 4.2a, MP-MoS_2 shows a 2% weight loss in the range of 30-250 °C, which can be attributed to the removal of water and organic residues.[104] No obvious further weight loss is seen at higher temperatures up to 550 °C. The pure ionomer starts to lose weight at around 295 °C, and decomposes entirely at around 490 °C. I@MP-MoS_2 shows a weight loss of 6% at 295 °C, which increases to 15% at 550 °C. Accordingly, I@MP-MoS_2 contains the ionomer at around 9%, along with about 6% of impurities.

ζ potential of the products in each synthesis step has been measured (Figure 4.2b). Due to the possession of the quaternary ammonium ions, the ionomer as expected has a positive ζ potential of around +45.3 mV. B-MoS_2 instead possesses a negative ζ potential of -14.6 mV. Upon chemical exfoliation, MP-MoS_2 shows a more negative ζ potential of around -50.4 mV. This increase in surface charge comes from the electron transfer between the reducing agent (n-buthyllithium) and MoS_2, which is stable to some extent even after a reaction with water.[267] Also, the formation of negatively charged functional groups on the edges can also contribute to the enhanced negative charge.[268] Upon the ionomer modification, I@MP-MoS_2 show a positive ζ potential of $\approx$+27.6 mV, confirm solidly the presence of ionomer within

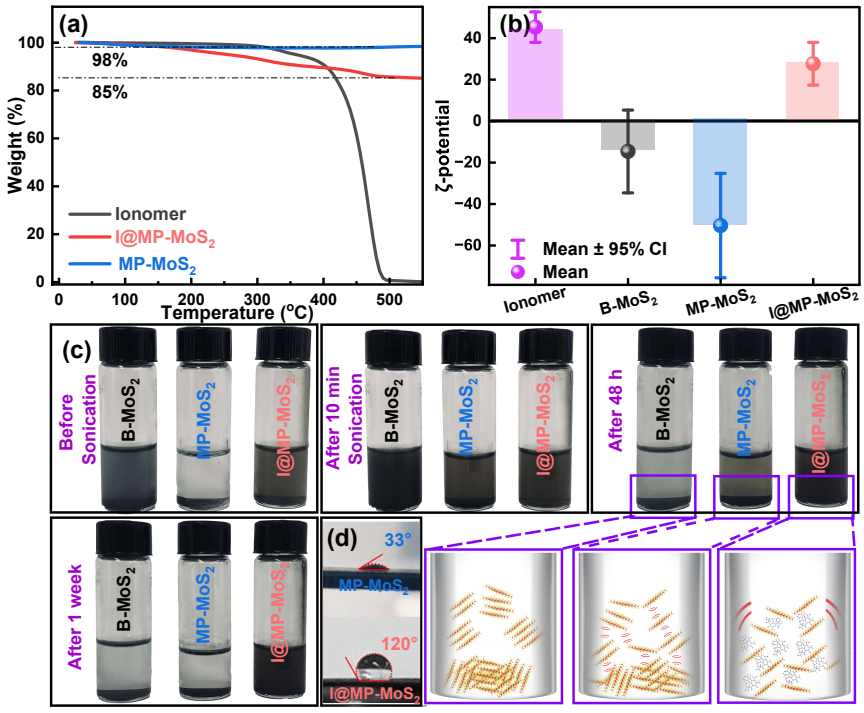

Figure 4.2: (a) TGA curves of the ionomer, MP-MoS_2, and I@MP-MoS_2, (b) ζ potentials of the suspansions of ionomer, B-MoS_2, MP-MoS_2, and I@MP-MoS_2 in THF, (c) photographs of B-MoS_2, MP-MoS_2, and I@MP-MoS_2 suspension in THF showing the sedimentation over the time, and (d) photos showing water contact angles on films of MP-MoS_2 and I@MP-MoS_2.

the structure that markedly changes the surface charge of MoS_2 nanosheets.

Hyperbranched polyethylene ionomers have a good dispersibility in non-polar and low-polarity solvents like THF due to their nonpolar hyperbranched polyethylene skeletons.[195,269,270] To investigate the impact of ionomer incorporation on the dispersibility, suspensions at 0.5 mg ml^{-1} in THF were prepared with each sample. Without sonication, a small portion of B-MoS_2 and the majority of I@MP-MoS_2 can be spontaneously dispersed, while MP-MoS_2 shows no dispersion in THF (Figure 4.2c). Following 10 min of sonication, B-MoS_2 quickly starts to settle down. The images taken after 48 h following sonication show that MP-MoS_2 also slowly settles down. After one week, both B-MoS_2 and MP-MoS_2 have almost completely settled, with a clear supernatant. The higher stability of MP-MoS_2 suspension can be explained by ζ potential test result (Figure 4.2b). A higher ζ potential results in more repulsion between particles and consequently prevents from aggregation and settling.[271] In contrast, the suspension of I@MP-MoS_2 shows the excellent stability for up to one week without obvious sedimentation. The high suspension stability of I@MP-MoS_2 should be associated with the stabilizing effect of the ionomer. The high solubility of the

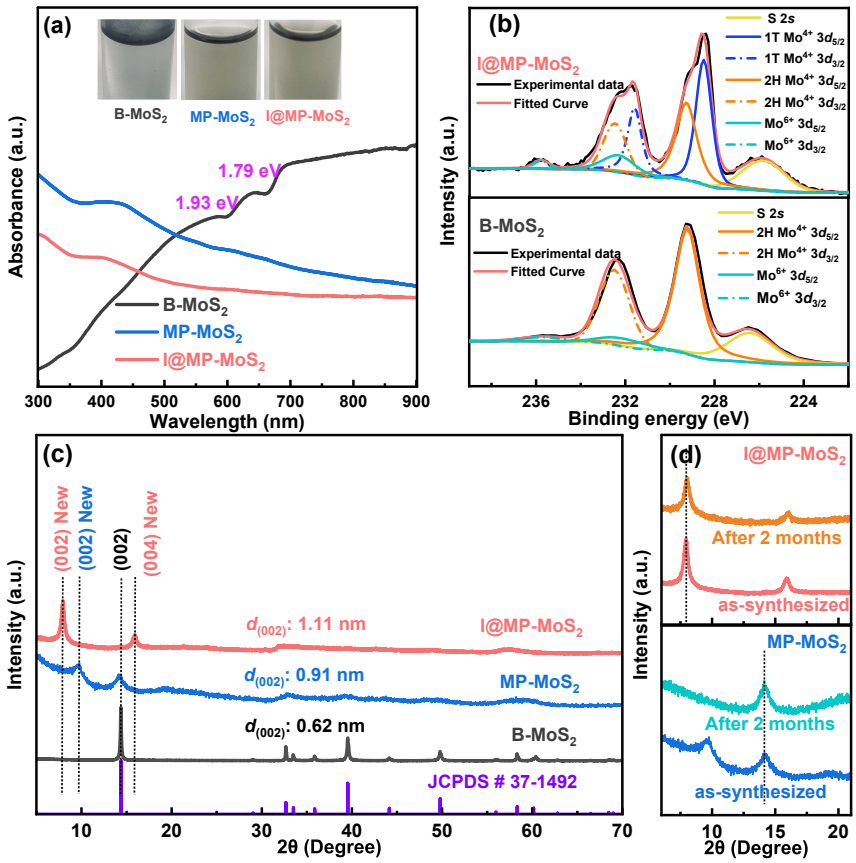

Figure 4.3: (a) UV-vis curves of B-MoS_2, MP-MoS_2, and I@MP-MoS_2 in water, (b) Mo 3d XPS spectra of B-MoS_2 and I@MP-MoS_2, (c) XRD patterns of B-MoS_2, MP-MoS_2, and I@MP-MoS_2, and (d) a comparison (zoomed in for (002) peaks) of as-synthesized samples and those following 2 months of storage after synthesis.

ionomer in THF and electrostatic connections of its positively charged ionic groups with the surface of nanosheets make the suspension stable. It is worth noting that the 1T phase-containing MoS_2 generally has high hydrophilicity and dispersibility in polar solvents such as water. However, dispersing it in non-polar and low-polarity solvents is challenging.[272] The presence of the ionomer, despite at a relatively low content, is clearly efficient in rendering I@MP-MoS_2 hydrophobic, enhancing its dispersibility and stability in THF as a low-polarity solvent. Films of B-MoS_2, MP-MoS_2, and I@MP-MoS_2 show distinctly different water contact angles (121, 33, and 120°, respectively; see Figure 4.2d; Figure 4.S1‡), further confirming the dramatic change in surface properties upon the exfoliation and ionomer incorporation. The high compatibility of I@MP-MoS_2 with THF is reasoned to render its superior wetting properties and desirable electrode/electrolyte interactions when used as an active electrode material for MIBs and MILBs with THF-based electrolytes[197], which is expected to enable

facile ion transport at the solid-electrolyte interface.

UV-vis spectroscopy was performed on aqueous suspensions of B-MoS_2, MP-MoS_2, and I@MP-MoS_2 to investigate the presence of the 1T phase.[47,273] Figure 4.3a shows their UV-vis spectra. The spectrum of B-MoS_2 exhibits two distinctive excitonic peaks at 641 (1.93 eV) and 691 nm (1.79 eV), respectively, which are related to the spin-orbit splitting of the valence band at the K point of the Brillouin zone. The positions of the peaks are consistent with those seen with bulk 2H-MoS_2 in the literature,[273,274] indicating its semiconducting nature. The UV-vis spectra of MP-MoS_2 and I@MP-MoS_2 are in good agreement with that of the previously reported 1T-MoS_2, with a monotonic decrease of the absorbance with the increasing wavelength with no distinctive peak. This is characteristic of non-plasmonic metallic nanomaterials.[47]

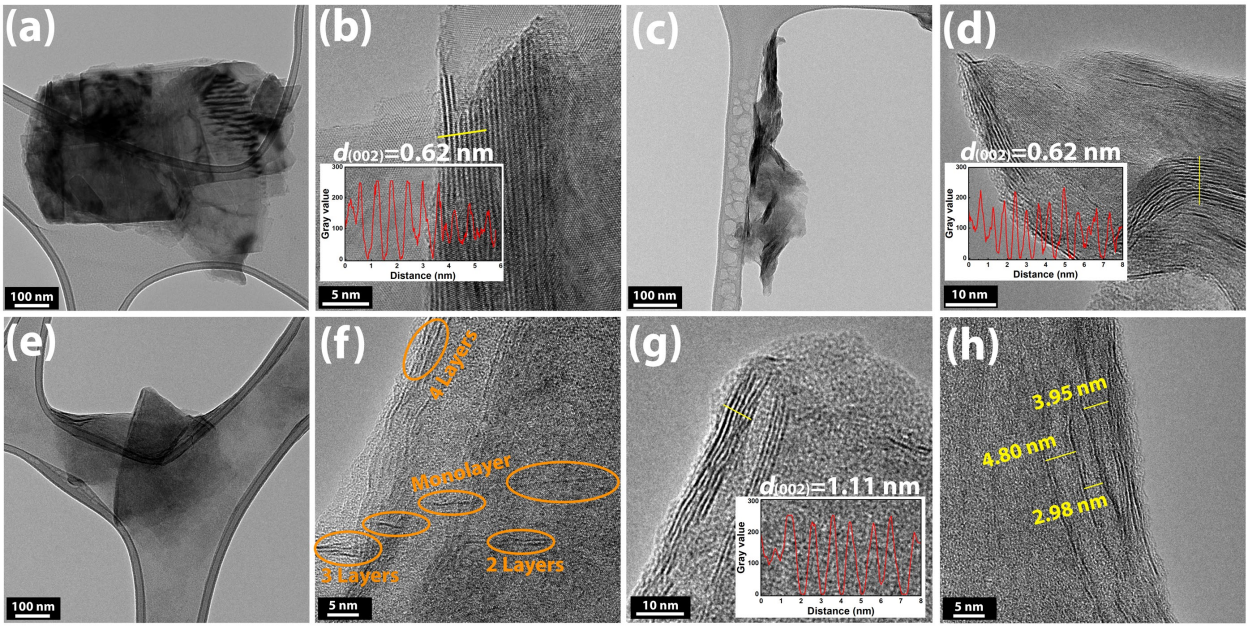

Figure 4.4: TEM and HRTEM images of (a,b) B-MoS_2, (c,d) MP-MoS_2, and (e-h) I@MP-MoS_2. The insets in (b,d,f) show the intensity profiles along with the yellow lines in corresponding HRTEM images.

XPS was carried out to further elucidate and quantify the phase structures in the three MoS_2 samples (see Figure 4.S2‡ for the XPS survey spectra). The high-resolution Mo 3d spectrum of B-MoS_2 (Figure 4.3b) exhibits two characteristic peaks at ≈229.3 and 232.5 eV, corresponding to Mo^{+4} $3d_{5/2}$ and Mo^{+4} $3d_{3/2}$, respectively.[106,107] It has been reported that, while the Mo 3d spectrum of the 2H MoS_2 phase shows only one doublet, that of mixed-phase MoS_2 typically exhibits two doublets, with the second doublet arising from the 1T phase at lower binding energies in addition to the one corresponding to the 2H

phase.[41] In consistency with the spectrum for MP-MoS_2, the Mo 3d spectrum of I@MP-MoS_2 (Figure 4.3b) shows two doublets, with one attributed to the 1T phase at lower binding energies (≈228.5 and ≈231.6 eV for Mo^{+4} $3d_{5/2}$ and Mo^{+4} $3d_{3/2}$, respectively) and the other related to the 2H phase at higher binding energies (≈229.3 and 232.5 eV for Mo^{+4} $3d_{5/2}$ and Mo^{+4} $3d_{3/2}$, respectively). Accordingly, the XPS spectra confirm the co-existence of both 1T and 2H phases in I@MP-MoS_2. Based on the deconvolution of Mo 3d spectrum, the 1T phase content for I@MP-MoS_2 is calculated to be 53 %. According to the UV-vis and XPS results, I@MP-MoS_2 contains a significant content of the 1T phase, which can render enhanced conductivity and, consequently, superior performance in electrochemical energy storage applications than B-MoS_2. In addition, the weak doublet (at ≈232.3 and 235.8 eV for Mo^{+6} $3d_{5/2}$ and Mo^{+6} $3d_{3/2}$, respectively) attributed to MoO_3 is also seen, indicating its presence as a minor impurity in B-MoS_2 and I@MP-MoS_2. According to the UV-vis and XPS results, I@MP-MoS_2 contains a significant amount of 1T phase that can render enhanced conductivity and, consequently, superior performance in electrochemical energy storage applications than B-MoS_2.

The samples have also been characterized with XRD for crystal structure. Figure 4.3c shows their XRD patterns, along with the standard JCPDS card (#37-1492) for hexagonal 2H-MoS_2. The XRD pattern of B-MoS_2 matches well with the JCPDS reference, with the (002) peak located at 14.37° with an inter-layer distance of 0.62 nm. In the pattern of MP-MoS_2, a new down-shifted (002) peak centered at 9.65° emerges, showing an increase of the inter-layer distance to about 0.92 nm. This new peak should result from the exfoliated 2D sheets following the intercalation with guest small molecules. However, the original (002) peak, although weakened and broadened, remains at the original position (14.37°), suggesting the occurrence of re-stacking of some nanosheets. A further XRD test performed on MP-MoS_2 after two months of storage at room temperature (Figure 4.3d) shows the complete disappearance of the new (002) peak, confirming that the exfoliated 2D sheets undergo complete restacking over time. Accordingly, although the n-butyllithium-assisted exfoliation is an efficient approach to produce disordered few-layered MoS_2 2D nanosheets, it is accompanied by the gradual re-stacking of the exfoliated nanosheets. Therefore, it can be stated that a significant and stable inter-layer expansion is unlikely with this exfoliation method in the absence of a stable intercalant. On the other hand, in the XRD pattern of I@MP-MoS_2 (Figure 4.3c), a new (002) peak appears at 7.93° with a large inter-layer spacing of 1.11 nm. This enlarged expansion is reasoned to result from the intercalation of the ionomer with the nanosheets by interactions of its quaternary ammonium groups with

the negatively charged surface of the MoS_2 nanosheets. Moreover, after storage for two months, its XRD patterns remains identical to that of the freshly prepared sample with the well retained new (002) peak at 7.93° (Figure 4.3d), confirming the successful prevention of the nanosheet restacking upon the stable intercalation of the ionomer.

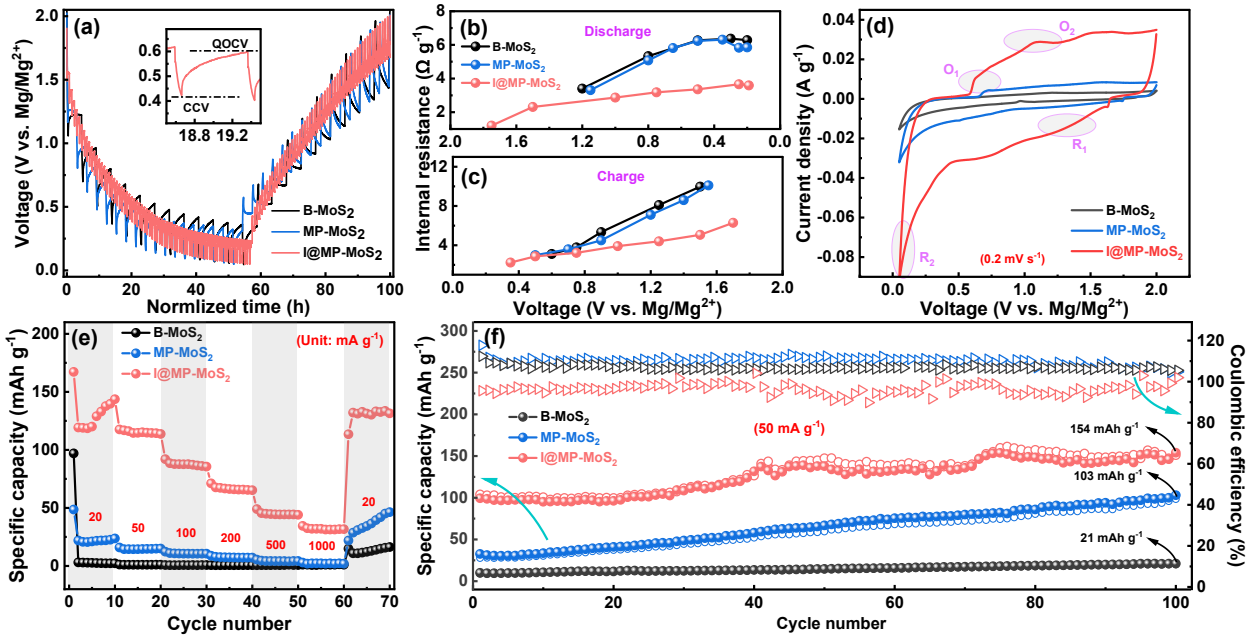

Figure 4.5: Electrochemical performances of MIBs assembled with B-MoS_2, MP-MoS_2, and I@MP-MoS_2 cathodes, respectively, and Mg metal anode: (a) GITT curves, (b) internal resistance during discharge, (c) internal resistance during charge (d) CV curves at 2 mV s^{-1}, (e) rate performance at different current densities, and (f) cycling performance at 50 mA g^{-1}.

Figure 5.2 shows the transmission electron microscopy (TEM) images of B-MoS_2, MP-MoS_2, and I@MP-MoS_2. The TEM images of B-MoS_2 (Figure 5.2a,b) show clusters of layered structures containing more than 20 layers in each cluster. As shown in its HRTEM image (Figure 5.2b) and the corresponding intensity profile for the line across the lattice fringes, the average inter-layer distance in B-MoS_2 is ≈0.62 nm, which is in good agreement with the d-spacing value (0.62 nm) determined with XRD. TEM and HRTEM images of MP-MoS_2 (Figure 5.2c,d) also show layered clusters but with decreased numbers of layers, along with some disordered exfoliated few-layered nanosheet structures. However, as seen in the inset of Figure 5.2d, the inter-layer distance in the layered clusters doesn't differ significantly from that in B-MoS_2 (≈6.2 nm). With I@MP-MoS_2, many few-layered clusters, including mono- and bi-layers, are observed in its high-resolution TEM image (Figure 5.2f). As shown in Figure 5.2g, a considerably bigger inter-layer distance of 1.11 nm is observed

with a few-layered cluster. Meanwhile, inter-layer distances as high as 4-5 nm are seen with some other few-layered clusters shown in Figure 5.2h. In line with the XRD results, these TEM images further solidly confirm the highly efficient intercalation of the ionomer within the nanosheets, which leads to the significantly enhanced inter-layer distances and even the thorough exfoliation of some of the nanosheets. The strong ionic interactions between the quaternary ammonium ions on the ionomer and the negatively charged nanosheet surface are reasoned to contribute to the high efficiency of intercalation and subsequent exfoliation of the nanosheets.

With B-MoS_2, its multi-layer structure, relatively low inter-layer distance and big particle sizes can not provide sufficient space and short transport paths for multivalent ions like Mg^{2+}. On the other hand, I@MP-MoS_2, with few-layered structures with reduced layer numbers and significantly enlarged inter-layer spaces, is expected to provide more accessible active sites and shortened pathways to accommodate Mg^{2+}.[16,114] The electrochemical performances of the samples for the storage of Mg^{2+} have been subsequently investigated. MIBs have been assembled with each sample (B-MoS_2, MP-MoS_2, and I@MP-MoS_2) as the cathode material and a magnesium disk as the anode, along with 0.4 M APC in THF as the electrolyte. Figure 4.5 summarizes the battery testing results. The battery internal resistance is a suitable indicator for the ion and electron transport rate of the active material. Figure 4.5a shows the GITT tests performed on the three MIBs, from which the values of internal resistances are calculated by Equation 4.1.[275]

$$\Delta R_{int.}(\Omega) = \mid \Delta V_{QOCV-CCV} \mid / I_{applied} \tag{4.1}$$

where $\Delta V_{QOCV-CCV}$ is the over-potential or voltage difference between quasi-open circuit voltage and closed-circuit voltage $V_{QOCV} - V_{CCV}$ (see inset in Figure 4.5a), and $I_{applied}$ represents the applied current. The GITT curves (Figure 4.5a) reveal lower over-potentials for the battery with I@MP-MoS_2 and consequently lower internal resistances (Figure 4.5b,c) than the two counterparts during both charge and discharge. The lower internal resistance suggests better charge kinetics that can facilitate the higher capacity of the electrode.[276,277] Relative to B-MoS_2, MP-MoS_2 electrode shows slightly lower internal resistance during discharge/charge.

Figure 4.S3‡ shows the first three CV cycles of the batteries at a voltage scan rate of 0.2 mV s^{-1} and Figure 4.S4‡ shows the first, second, and 10_{th} GCD curves at a current density of 20 mA g^{-1} with both tests within the potential window of 0.05–2 V. The CV and GCD curves indicate a relatively high initial discharge capacity compared to the following cycles, which

results from the formation of the SEI. Figure 4.5d compares the 2_{nd}-cycle CV curves of the MIBs. One can notice the significant differences in the capacity among the three cathodes, with the enclosed CV area of I@MP-MoS_2 cathode significantly higher than those of others, which reflects the superior Mg^{2+} storage capacity of I@MP-MoS_2. B-MoS_2 does not show any distinguishable redox peak in the CV curve, but the other two electrodes show a tail in the cathodic scan at about 0.07 V (R_2) and a step current rise at around 0.58 V (O_1) in the anodic scan. This redox pair can be related to the 2H/1T phase transitions.[130] According to the XPS test results (Figure 4.3c), I@MP-MoS_2 contains a significant content of the 2H phase despite the formation of the 1T phase during the synthesis process. In consequence, the 2H/1T phase transition can be expected upon the deep insertion of Mg^{2+}.[76] The R_1 reduction peak at around 1.2 V (also the step current drop at ≈1.6 V) and O_2 oxidation peak at ≈1.0 V are related to the insertion and extraction of the Mg^{2+} within the MoS_2 structures, respectively.[130] The overall reactions in the cathode can be described as $6MoS_2 + 4Mg \leftrightarrow Mg_4Mo_6S_{12}$.[278] The minimal Mg^{2+} insertion/extraction is the reason for the absence of any peaks in the CV curve of B-MoS_2 cathode.

The insufficient capacity of B-MoS_2 cathode is also evident in the rate performance test undertaken at different current densities increasing from 20 to 1000 mA g^{-1} (Figure 4.5e). It shows capacities less than 5 mAh g^{-1} in the entire applied current range (also see Figure 4.S5‡ for the GCD curves at different current densities). However, upon the switch of the current back to 20 mAh g^{-1}, a slight capacity increase up to 16 mAh g^{-1} can be seen in the last cycle. MP-MoS_2 shows slightly higher capacities than B-MoS_2, with 22, 14, 11, 7, 4, and 2 mAh g^{-1} at 20, 50, 100, 200, 500, and 1000 mA g^{-1}, respectively (see Figure 4.5e; Figure 4.S5‡). The slight enhancements can be attributed to the higher electrical conductivity arising from the 1T phase and the disordered structure, which can provide slightly more space and shorter paths for Mg^{2+}. Meanwhile, a gradual capacity increase is also seen in the last cycle at 20 mA g^{-1} (reaching 46 mAh g^{-1}). In sharp contrast, I@MP-MoS_2 exhibits significantly higher capacities of ≈144, 114, 86, 65, 44, 32 mAh g^{-1} at 20, 50, 100, 200, 500, and 1000 mA g^{-1}, respectively. The GCD curves and capacity retention plots of the three batteries at different currents illustrated in Figure 4.S5‡ and 4.S6‡, respectively, show the different rate performances of the cathodes. The difference in rate performance reveals the importance of the presence of the ionomer and its effect on providing sufficient spaces for Mg^{2+} storage. I@MP-MoS_2 also shows a capacity increase over cycling when applying a relatively low current (20 mA g^{-1}).

The capacity increases with the three cathodes can also be clearly seen in the cycling tests

at 50 mA g^{-1}, which were performed on the batteries already cycled in the rate performance test (Figure 4.5e). As it is shown in Figure 4.5f, MP-MoS_2, MP-MoS_2, and I@MP-MoS_2 cathodes exhibit the capacity increase from 10, 32, 101 mAh g^{-1} at the first cycle to 21, 103, 154 mAh g^{-1}, respectively, at the 100_{th} cycle. This gradual capacity increase, known as electro-activation, is a common phenomenon arising from continuous intercalation/deintercalation of the ions and consequently the increasing active surface area.[131,132] For the case of MoS_2, the intercalation of Mg^{2+} into the layered structures can lead to a certain degree of distortion and thus render the phase transition from semi-conductive 2H to metallic 1T phase. The continuous cycling increases the proportion of the 1T phase and the available active surface area. As such, more facile conditions for the accommodation of Mg^{2+} will be obtained over cycling.[76]

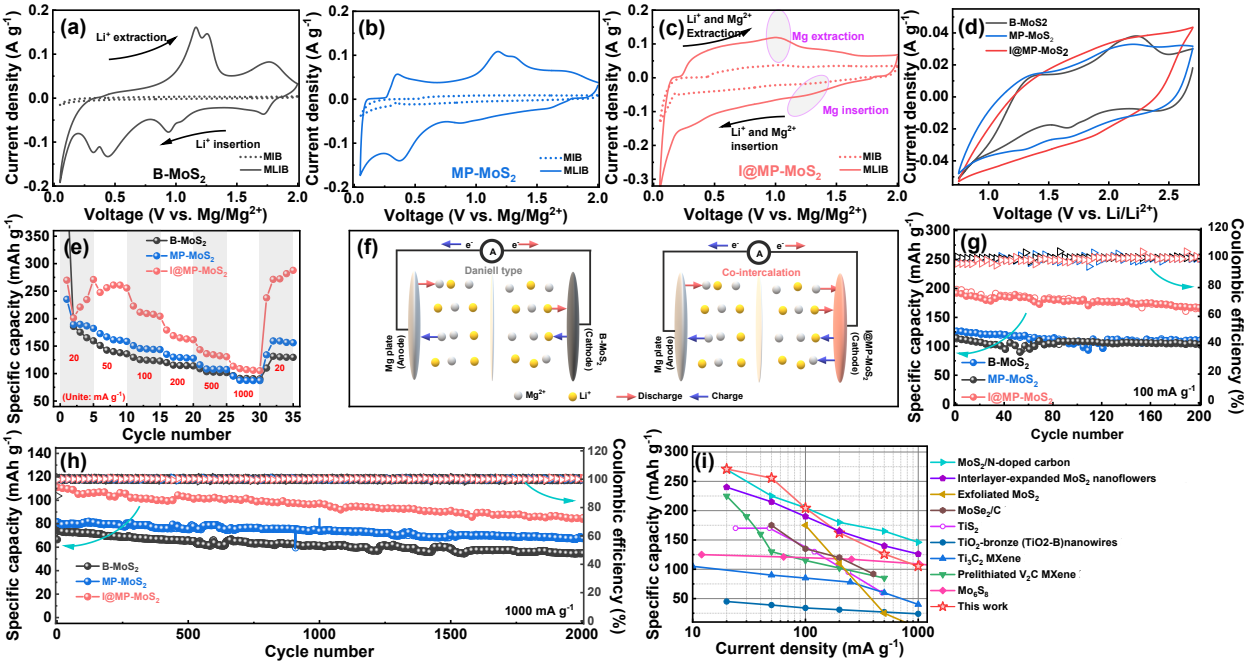

Figure 4.6: Comparison of CV curves (at 0.2 mV s^{-1}) in MLIBs and corresponding MIBs of (a) B-MoS_2, (b) MP-MoS_2, and (c) I@MP-MoS_2 cathodes; d) CV curves (at 0.2 mV s^{-1}) of LIB half-cells with B-MoS_2, MP-MoS_2, and I@MP-MoS_2 cathodes; (e) rate performances of MLIBs with B-MoS_2, MP-MoS_2, and I@MP-MoS_2 cathodes; (f) schematic illustration of Daniell type and co-intercalation mechanisms, (g) cycling test of MLIBs at 100 mA g^{-1} and (h) 1000 mA g^{-1}, and (i) comparison of the rate performance of MLIB with I@MP-MoS_2 cathode with those of previously reported Mg^{2+}/Li^+ battery cathode materials.[135,216,279–285]

We have further evaluated the performance of three cathodes in hybrid MLIBs with Mg^{2+}/Li^+ dual-salt electrolyte. For this purpose, hybrid MLIBs were assembled with B-MoS_2, MP-MoS_2, and I@MP-MoS_2 cathodes, respectively, magnesium disk anode, and 0.4

M APC/1 M LiCl electrolyte. Figure 4.S7‡ shows the first three cycles of CV curves of MLIBs at 0.2 mV s^{-1} and Figure 4.S8‡ shows their 1_{st}, 2_{nd}, and 5_{th} GCD curves at a current density of 50 mA g^{-1}, with both tests in the potential window of 0.05–2 V. Like the MIBs, the first discharge of all three MLIBs exhibits an irreversibility arising from the formation of SEI and side reactions.

In Figure 4.6a-c, CV curves of MLIBs are compared with their MIB counterparts. As shown in Figure 4.6a,b, the CV curves of B-MoS_2 and MP-MoS_2 cathodes exhibit dramatically increased areas compared to the corresponding MIBs. In addition, multiple pairs of redox peaks emerge in their MLIB CV curves, which are relatively more intense in the B-MoS_2 but almost at the same positions in both. The redox peaks are attributed to the insertion/extraction of Li^+.[213,218] In the case with I@MP-MoS_2 cathode, the CV curve of MLIB shows a bigger area compared to the MIB counterpart, but with no new peaks (Figure 4.6c). The broad redox peaks with I@MP-MoS_2 cathode are seen at the same positions as those in the corresponding MIB (Figure 4.5d) and are related to the insertion/extraction of Mg^{2+}. For the purpose of comparison, LIB half cells have also been assembled with the three cathodes and lithium metal anode, and 1M LiCl in THF electrolyte. Figure 4.6d shows the CV curves of the LIB half-cells within a potential window of 0.75-2.7 V versus Li/Li^+ (equivalent to ≈0.05-2 V vs. Mg/Mg^{2+}). As opposed to B-MoS_2 and MP-MoS_2 cathodes, I@MP-MoS_2 cathode does not show any well-defined redox peak, indicating the predominant pseudocapacitive Li^+ storage mechanism. The absence of redox peaks is attributed to the presence of the intercalated ionomer, which by keeping the layers apart from each other, minimizes the energy required to open the van der Waals gaps.[113,213] In another word, the enlarged inter-layer spaces facilitate the facile access for Li^+ to the surface active sites. Therefore, in the MLIB with I@MP-MoS_2 cathode, its CV does not show any recognizable peak related to the Li^+ insertion/extraction though the storage of Li^+ should still take place within the cathode, which enhances the capacity. Meanwhile, from Figure 4.6d, the three cathodes show similar capacities in LIBs on the basis of their similar enclosed areas of CV curves.

Figure 4.6e shows the rate performances of MLIBs. B-MoS_2 cathode delivers capacities of 174, 140, 124, 115, 103, and 91 mAh g^{-1} at 20, 20, 50, 100, 200, 500, and 1000 mA g^{-1}, respectively, which indicate a dramatic improvement compared to its MIB counterpart (Figure 4.5e). Clearly, the presence of Li^+ has significant effects on improving the capacity of the battery due to the ready insertion/extraction of small-sized Li^+ within B-MoS_2. This contrasts with the negligible capacity of B-MoS_2 for Mg^{2+} storage. However, the insertion/extraction

of Mg^{2+} cannot be completely ruled out as the insertion of Li^+ may reduce the activation energy for Mg^{2+} to some extent.[130,134] Nevertheless, due to the small inter-layer distances within B-MoS_2 (≈0.62 nm), the involvement of Mg^{2+} is less probable. Accordingly, as the insertion/extraction of Li^+ is dominant on the cathode side, the MLIB with B-MoS_2 cathode should be a Daniell-type cell (see scheme in Figure 4.6f).[216] The MLIB with MP-MoS_2 cathode also offers higher capacities (Figure 4.6e) than its corresponding MIB (Figure 4.5e) at all applied current densities (190, 161, 145, 129, 108, 87 mAh g^{-1} at 20, 50, 100, 200, 500, and 1000 mA g^{-1}, respectively). However, as in the case of MIBs, MP-MoS_2 without re-stacking prevention does not show a remarkable difference in the performance of MLIB compared to B-MoS_2, with only slightly higher capacities observed. On the contrary, I@MP-MoS_2 cathode in MLIB shows a capacity of 201 mAh g^{-1} in the first reversible discharge at 20 mA g^{-1}, with a gradual increase in the capacity to about 260 mAh g^{-1} at 50 mA g^{-1}. This capacity increase should be attributed to the reduced activation energy for Mg^{2+} storage and structural transformation toward a higher content of 1T phase following the lithiation of MoS_2.[130,134,279] The capacity increase becomes evident during the last five cycles when the current density is returned to 0.2 mA g^{-1}, suggesting that the activation process is more feasible at low currents, likely due to ions experiencing deeper insertion into the material. At the subsequent current densities, it exhibits capacities of 209, 164, 134, and 107 mAh g^{-1} at 100, 200, 500, and 1000 mA g^{-1}, respectively. At all applied currents, I@MP-MoS_2 cathode provides significantly higher capacities compared to B-MoS_2 and MP-MoS_2 cathodes in MLIB (See GCD curves and capacity retention plots of the three batteries at different currents illustrated in Figures 4.S9‡ and 4.S10‡, respectively). With the relatively high Mg^{2+} storage capacity (Figure 4.5e) and enhanced capacity in the presence of Li^+ (Figure 4.6c,e), I@MP-MoS_2 cathode exhibits a co-intercalation mechanism (Figure 4.6f). Particularly, at low currents (20-200 mA g^{-1}) where both Li^+ and Mg^{2+} can easily insert into I@MP-MoS_2 cathode, the difference in its capacity with those of the other two cathodes (B-MoS_2 and MP-MoS_2) are more pronounced. However, the difference gets smaller at higher currents due to the dominance of Li^+ insertion/extraction in the cathode. Therefore, when the insertion/extraction of Li^+ is predominant (at high currents), the capacity difference among the three cathodes in MLIBs is smaller, which can be verified in Figure 4.6e.

Figure 4.6g shows the cycling performances of the MLIBs at 100 mA g^{-1} for 200 cycles. I@MP-MoS_2 cathode shows discharge capacities of 192 and 167 mAh g^{-1} at the 1_{st} and 200_{th} cycles, respectively, corresponding to 87% of capacity retention over 200 cycles. Its average Coulombic efficiency is 99.5%, indicating the highly reversible insertion/extraction of Li^+

and Mg^{2+} over the cycling test. Though with lower initial capacities of 126 and 114 mAh g^{-1}, MP-MoS_2 and B-MoS_2 show 88% (111 mAh g^{-1}) and 90% (103 mAh g^{-1}) of capacity retention at the 200_{th} cycle, respectively. The Coulombic efficiency of MP-MoS_2 MLIB over the cycling test is also maintained high at about 99.7%. The discharge capacity values attained for B-MoS_2 surpass its charge capacity values in some cycles, signaling the presence of irreversible trapping of the ions that cannot be removed in the charge cycle and/or the occurrence of some side reactions during the discharge with B-MoS_2. A similar trend can also be seen in the long-term cycling test for 2000 cycles at 1000 mA g^{-1} (Figure 4.6h). I@MP-MoS_2 cathode shows capacities of 84 and 111 Ah g^{-1} in the first and last cycles, respectively, with a high stability of 75% over 2000 cycles. MP-MoS_2 and B-MoS_2 exhibit a slightly better stability with a capacity retention of 83%. It appears that the cycling stability may be negatively affected if more Mg^{2+} are involved in the charge storage. Nevertheless, the stability of I@MP-MoS_2 cathode is not severely affected despite the co-intercalation mechanism, with the excellent capacity retention of 75% after 2000 cycles.

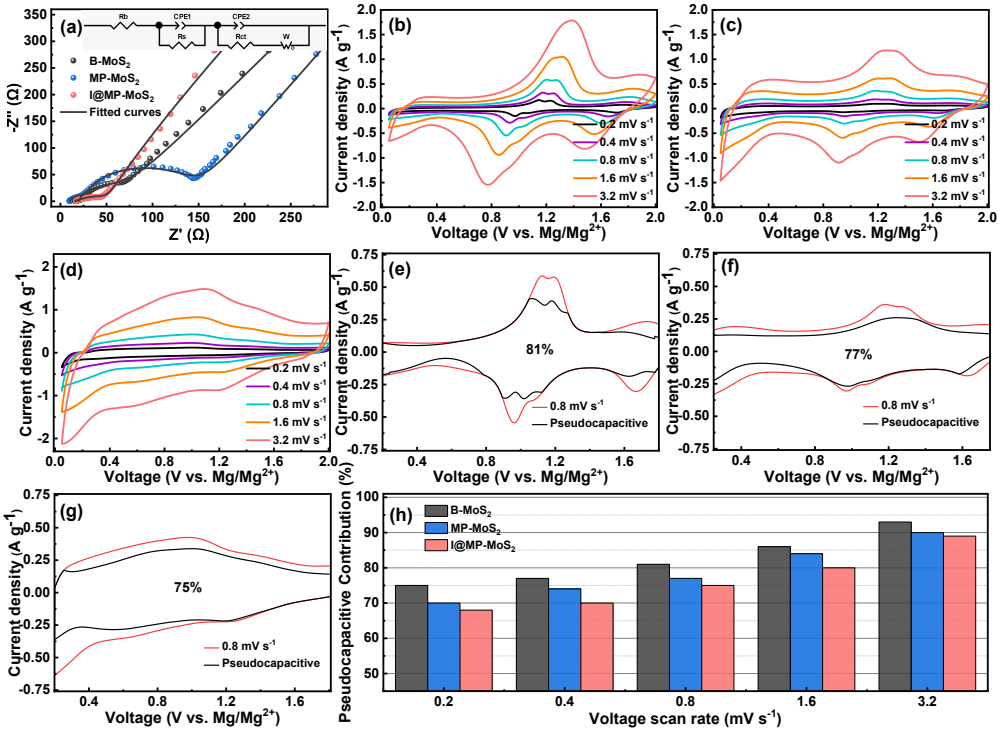

Figure 4.7: Electrochemical performance of MLIBs with B-MoS_2, MP-MoS_2, and I@MP-MoS_2 cathodes: (a) Nyquist plots of the MLIBs; CV plots at different voltage scan rates for MLIBs with (b) B-MoS_2, (c) MP-MoS_2, and (d) I@MP-MoS_2; the pseudocapacitive contribution to the current response for MLIBS with (e) B-MoS_2, (f) MP-MoS_2, and (g) I@MP-MoS_2 at a voltage scan rate of 0.8 mV s^{-1}; (h) comparison of pseudocapacitive contributions to the current in the three MLIBs at different scan rates.

Figure 4.S11‡ illustrates the ex situ XRD analysis conducted on I@MP-MoS_2 prior to any discharge, as well as at various voltage levels subsequent to the initial discharge (where the battery underwent charging/discharging at 20 mA g^{-1}). No appreciable change in the crystal structure of I@MP-MoS_2 is observed across the various voltage states. The only discernible change is a slight shift (from 7.93° to 7.81°) in the position of the (002) peak after the first discharge, reflecting a minor increase in the inter-layer distance (reaching ≈1.12 nm) due to the ions intercalation. This validates that the storage mechanism for both ions within the applied potential range (0.05-2 V vs. Mg/Mg^{2+}) is exclusively confined to intercalation/deintercalation processes and no side reactions or conversion processes take place.

XRD analysis of I@MP-MoS_2 following 50 charge/discharge cycles at 100 mA g^{-1} (Figure 4.S12‡) demonstrates its well-retained layered structure throughout the cycling process. This observation underscores the notable structural stability of the electrode material. Nevertheless, a noticeable weakening of the (002) peak is evident with cycled sample when compared with its fresh state prior to cycling, which is consistent with the electro-activation phenomenon discussed above.[216]

Overall, I@MP-MoS_2 cathode shows superior performance for both MIB and MLIB compared to B-MoS_2 and MP-MoS_2 cathodes, revealing the critical role of the intercalated ionomer in accommodating the insertion/extraction of Mg^{2+}. In Figure 4.6i, the rate performance of I@MP-MoS_2 cathode in MLIB has been compared with those of the previously reported cathode materials in MLIBs. The discharge capacity in the last cycle of each applied current has been used in the preparation of this plot. This plot reveals the remarkable capacities of I@MP-MoS_2, particularly at relatively low current densities (20-100 mA g^{-1}). This excellent performance benefits from the improved electrical conductivity arising from a high content of 1T phase formed during the exfoliation step and the presence of the intercalated ionomer, while without the use of additional conductivity enhancers. If it is further hybridized with materials with high electrical conductivity, such as graphene, its rate performance is expected to be further improved.

We have further investigated the kinetic effects and mechanism of charge and discharge reactions in the MLIBs with the three different cathodes. Figure 4.7a shows the Nyquist plots of the three MILBs after the rate performance tests (Figure 4.6e). The cell with I@MP-MoS_2 cathode shows the smallest semicircle in the middle-high frequency region, with the lowest charge transfer resistance (R_{ct}) of 36 Ω. The cell with MP-MoS_2 cathode instead shows the highest R_{ct} of 126 Ω, followed by the value of 56 Ω for that with B-MoS_2 cathode. The

high R_{ct} of the cell with MP-MoS_2 cathode indicates the inferior interface charge transfer with MP-MoS_2 active material, which arises from the highly polar surface and in turn the low wettability of MP-MoS_2 by low-polarity THF solvent. The wettability of electrodes by electrolytes is a critical factor affecting the access to electrolyte and the diffusion rate of the charge carriers in the electrodes.[198] With I@MP-MoS_2, the charge transfer resistance has been reduced favorably upon the inercalation with the ionomer in the structure. In addition, the slope of the line in the low-frequency region (Warburg resistance) is also higher with I@MP-MoS_2 cathode, indicating the enhanced ion diffusion rate within the electrode materials owing to the expanded inter-layer distances between MoS_2 sheets in the presence of the ionomer.

Figure 4.7b-d shows CV curves performed on the MLIBs at different scan rates to quantify the pseudocapacitive contributions in charge storage. Equation 5.1 is used to differentiate between the surface-controlled pseudocapacitive $(k_1\nu)$ and diffusion-controlled battery $(k_2\nu^{1/2})$ contributions to current response at various voltage scan rates.[259]

$$i = k_1\nu + k_2\nu^{1/2} \tag{4.2}$$

where i is current at a scan rate of ν at each fixed potential. k_1 and k_2 can be determined as the slope and intercept of a linear fit of $i/\nu^{1/2}$ versus $\nu^{1/2}$. As shown in Figure 4.7e-g, B-MoS_2, MP-MoS_2, and I@MP-MoS_2 cathodes show the pseudocapacitive contributions of 81, 77, and 75%, respectively, in charge storage at 0.8 mV s^{-1}. With I@MP-MoS_2, the surface-controlled pseudocapacitive contribution is the lowest among the three. As illustrated in Figure 4.7h, this trend is also observed at other applied scan rates. Therefore, the amount of pseudocapacitive behavior seems to depend on the amount of Li^+ the cathode accommodates. In this way, it can be stated that the higher the ratio of Li^+/Mg^{2+} engaged, the higher the amount of pseudocapacitive participation.

4.3 Conclusion

In this study, we have synthesized a 1T/2H mixed-phase MoS_2 with enlarged inter-layer distances, I@MP-MoS_2, by intercalation/exfoliation with a unique hyperbranched polyethylene ionomer through a convenient top-down approach. The synthesis strategy involves an initial chemical exfoliation of B-MoS_2 with n-butyllithium, followed by intercalation with the ionomer. The quaternary ammonium cations allow the ionomer to strongly bind onto the negatively charged surface of MoS_2 nanosheets, thus stably exfoliating the nanosheets at

enhanced inter-layer distances and preventing their re-stacking. With the high affinity of the hyperbranched polyethylene backbone to low-polarity THF, fast ion transport and enhanced ion access to the active sites on the nanosheets achieved with I@MP-MoS_2 in THF-based electrolytes. I@MP-MoS_2 exhibits a 79% of increase in inter-layer distances compared to B-MoS_2 and the enhanced metallic nature with a 1T phase content of 53%. In consequence, it displays exceptionally enhanced magnesium-ion storage capacities (e.g., 144 mAh g^{-1} vs. ≈2 mAh g^{-1} for B-MoS_2 at 20 mA g^{-1}). On the contrary, our findings also reveal that MP-MoS_2 without the ionomer intercalant, does not show significantly improved magnesium-ion storage performance. I@MP-MoS_2 is featured with the improved electrode/electrolyte interface charge transfer and high conductivity, which effectively overcome the sluggish solid-state kinetics of Mg^{2+} in MIBs. Moreover, compared to B-MoS_2 and MP-MoS_2, I@MP-MoS_2 also exhibits superior performance as a cathode material for hybrid dual-salt Mg^{2+}/Li^+ batteries, with co-intercalation of both Mg^{2+} and Li^+.

4.4 Experimental Section

Chemicals and materials

Chemicals and materials including 2.5 M n-butyllithium solution in hexane ($CH_3(CH_2)_3Li$, Aldrich), aluminium chloride ($AlCl_3$, 99.99%, Aldrich), 2.0 M phenylmagnesium chloride solution in THF (PhMgCl, Aldrich), anhydrous lithium chloride (LiCl, 98+%, Alfa Aesar), anhydrous tetrahydrofuran (THF, ≥ 99.9 %, Aldrich), hexane (Certified ACS, Fisher Scientific), poly(vinylidene fluoride) (PVDF, Mw ≈534,000 g mol^{-1}, Aldrich), and 1-methyl-2-pyrrolidone (NMP, reagent Plus 99%, Sigama-Aldrich), were used as received without further purification. Molybdenum(IV) sulfide (MoS_2, < 2 μm, 99%, Aldrich) was dried under vacuum for 20 h at 100 °C before use.

Synthesis of MP-MoS_2 and I@MP-MoS_2

The hyperbranched polyethylene ionomer was synthesized through direct catalytic co-polymerization of ethylene with an acrylate type ionic comonomer, [2-(acryloyloxy)ethyl]trimethylammonium tetrafluoroborate ($AETMA^+BF_4^-$) according to our previous work.[265] The reaction was conducted in a Schlenk flask with the ionic comonomers at a feed concentration of 0.3 mol L^{-1} in 10 mL of acetone under an ethylene pressure of 1 atm.

The polymerization was started by injection of a solution of the Pd-diimine catalyst (0.1 mmol) in acetone, lasted for 24 h under stirring and continuous ethylene feed, and was terminated by turning off the ethylene flow. The ionomer product was purified according to the procedure shown in our earlier paper.[265] Lithiated MoS_2 (Li_xMoS_2) was synthesized by dispersing 300 mg of B-MoS_2 in a mixture of 3 mL 2.5 M n-butyllithium in hexane and 3 mL of anhydrous THF under an argon atmosphere, followed by stirring (500 rpm) for 72 h. The product was then washed with hexane three times. By dispersing Li_xMoS_2 in 50 mL of DI water under sonication at a power of 60 W for 15 min (Fisher Scientific sonic dismembrator, FB120), a suspension of exfoliated mixed-phase MoS_2 (MP-MoS_2) was obtained. The unexfoliated particles were removed by centrifugation (Thermo Fisher Scientific, Sorvall Legend XT) at 3000 rpm for 5 min. To 40 mL of hyperbranched polyethylene ionomer dispersion in THF (1.5 mg ml^{-1}), 20 mL of MP-MoS_2 suspension in water (4 mg mL^{-1}) was added dropwise under sonication within 15 min. Then the product was washed 3 times by centrifugation in THF (12000 rpm, 15 min) and was then dried in a vacuum oven at 60 °C for 8 h to render the ionomer-intercalated mixed-phase MoS_2, I@MP-MoS_2.

Materials characterization

XRD was performed on a Rigaku SmartLab SE X-ray diffractometer with Cu Kα radiation (1200 kW>). TGA was performed in a nitrogen atmosphere on a TA instruments Q50 TGA in a temperature range of 30-600 °C at a heating rate of 10 °C min^{-1}. XPS was performed on a Thermo Scientific Theta Probe XPS spectrometer with a monochromatic Al K X-ray source and a spot area of 400 μm. Transmission electron microscopy (TEM) images were captured on a Thermo Scientific Talos 200X operating at 200 kV. ζ potential of the samples were measured by dynamic light scattering (DLS) measurements on a Brookhaven NanoBrook Omni instrument. UV-vis spectra were acquired using a Thermo Scientific Genesys 10S UV-vis spectrophotometer.

Electrochemical measurements

To make the working electrodes, homogeneous slurries were prepared by mixing each MoS_2 sample with Super-P conducting carbon and PVDF at a mass ratio of 7:2:1 in NMP. The slurry was then coated on carbon paper discs and dried overnight at 70 °C. The mass loading

of active material on the carbon paper was around 1.2-1.5 mg cm^{-2}. CR2025 coin cells were assembled in an argon filled glove box ($O_2 < 0.1$ ppm and $H_2O < 0.5$ ppm) using each as-prepared electrode as the cathode, a magnesium metal disc as the anode, and a glass fiber membrane (Whatman GF/D) as the separator. To prepare 0.4 M APC electrolyte for MIBs, 1.67 g (8 mmol) of $AlCl_3$ was added to 12 mL of anhydrous THF and was then stirred overnight. Then, 8 mL of 2M PhMgCl in THF was added dropwise to the $AlCl_3$ solution, followed by overnight stirring. The same procedure was utilized to prepare the dual-salt electrolyte for MLIBs except for adding 0.848 g LiCl in the final stage. The GCD tests were undertaken on a battery testing equipment (Land, CT2001A, China). CV and EIS measurments were performed on a Metrohm Autolab PGSTAT128N electrochemical workstation. EIS was performed at the open circuit voltage in the frequency range of 100 kHz to 0.01 Hz with an oscillatory amplitude of 50 mV. GITT was done by 5 min charge/discharge at 50 mA g^{-1} and 20 min relaxing time.

Chapter 5

Synergistic Cathode Design for High-Performance Dual-Salt Magnesium/Lithium-Ion Batteries Using 2D/2D 1T/2H-MoS_2@$Ti_3C_2T_x$ MXene Nanocomposite[§]

Adapted from article:

Synergistic Cathode Design for High-Performance Dual-Salt Magnesium/Lithium-Ion Batteries Using 2D/2D 1T/2H-MoS_2@$Ti_3C_2T_x$ MXene Nanocomposite

Jalal Rahmatinejad, Xudong Liu, Bahareh Raisi, Zhibin Ye

Published in: ***Small***

https://doi.org/10.1002/smll.202401391

[§] Supplementary Information available: See Appendix C

Abstract

Magnesium-ion batteries (MIBs) and dual-salt magnesium/lithium-ion batteries (MLIBs) have emerged as promising contenders for next-generation energy storage. In contrast to lithium metal anode in lithium metal batteries, magnesium metal anode in MIBs and MLIBs presents a safer alternative due to the limited dendrite growth and higher volumetric capacity, along with higher natural abundance. This study explores a MLIB configuration with a novel cathode design by employing a 2D/2D nanocomposite of 1T/2H mixed phase MoS_2 and delaminated $Ti_3C_2T_x$ MXene (1T/2H-MoS_2@MXene) to address challenges associated with slow kinetics of magnesium ions during cathode interactions. This cathode design takes advantage of the high electrical conductivity of $Ti_3C_2T_x$ MXene and the expanded interlayer spacing with enhanced conductivity of the 1T metallic phase in 1T/2H mixed phase MoS_2. Through a designed synthesis method, the resulting nanocomposite cathode maintains structural integrity, enabling the stable and reversible storage of dual Mg^{2+} and Li^+ ions. The nanocomposite cathode demonstrates superior performance in MLIBs compared to individual components (253 mAh g^{-1} at 50 mA g^{-1}, and 36% of capacity retention at 1,000 mA g^{-1}), showcasing short ion transport paths and fast ion storage kinetics. This work represents a significant advancement in cathode material design for cost-effective and safe MLIBs.

5.1 Introduction

The exciting potential of next-generation batteries to overcome current limitations and revolutionize energy storage has captured widespread attention, signaling a transformative phase in sustainable energy innovation.[286–289] The abundance of magnesium, coupled with the safety characteristics, positions magnesium-ion batteries (MIBs) as highly promising candidates for next-generation energy storage systems and potential alternatives to lithium metal batteries.[22,191] The lithium metal anodes for LIBs are known for serious safety concerns due to the occurrence of dendrite growth, which hamper their widespread applicability.[11,30] In contrast, magnesium metal anodes employed in MIBs offer multiple advantages. Magnesium exhibits a higher volumetric capacity than lithium metal, with values of 3833 mAh cm^{-3} and 2060 mAh cm^{-3}, respectively. Additionally, magnesium is cost-effective, and crucially, the deposition/dissolution of magnesium ions on the magnesium metal surface does not give rise to dendrite formation, thus ensuring a high level of safety. While magnesium metal has garnered attention as a promising anode, developing suitable electrolytes and active cathode materials is a key area of recent research aimed at unlocking the full potential of MIBs.[190]

A significant challenge of MIBs lies in finding suitable cathodes capable of effectively overcoming sluggish kinetics of Mg^{2+} and accommodating them properly. The slow kinetics of Mg^{2+} in traditional cathodes arises from their inherently polarizing characteristics, which promotes strong interactions between Mg^{2+} ions and the negatively charged host lattice. This phenomenon impedes the movement of Mg^{2+} ions within the cathode material. Additionally, the intense Coulombic forces between ions exacerbate this sluggishness, resulting in high energy barriers for intercalation and reduced diffusion coefficients.[15,16,22,23] One approach addressing this challenge involves the utilization of a dual-salt electrolyte to create a hybrid MLIB. In such battery configurations, the anode side (magnesium plate) experiences exclusively deposition/dissolution of Mg^{2+}. On the cathode side, either the insertion/extraction of Li^+ alone or the simultaneous insertion/extraction of both Li^+ and Mg^{2+} takes place, depending on the type of the cathode employed. Consequently, MLIBs benefit from the advantageous characteristics of Li^+ ions, including their small size and fast kinetics. This design enhances both the quantity and kinetics of ion storage on the cathode side. Simultaneously, MLIBs also possess benefits associated with a magnesium metal anode.[213,214] However, achieving a MLIB with elevated energy density necessitates the development of a cathode capable of optimally accommodating both Mg^{2+} and Li^+ throughout a co-intercalation process. Such a cathode plays a crucial role in maximizing ion storage capacity and overall battery performance.[218]

Some 2D transition metal carbides (MXenes), after some structural modification, have shown promise as active materials for storing divalent ions like Mg^{2+}, in addition to their proven performance in monovalent lithium-, sodium-, and potassium-ion batteries.[290,291] The findings in these studies underscore the significant influence of MXene's interlayer distances on their capacity for accommodating magnesium ions. According to a study by Byeon et al., $Ti_3C_2T_x$ (T_x: −OH, −O, and −F) MXenes can be used as the cathodes for MLIBs as well that function better than its MIBs in terms of capacity and rate performance.[283] Findings in another study have confirmed that the rate performance and capacity of $Ti_3C_2T_x$ MXene as a cathode for MLIBs can be substantially improved by increasing the interlayer distances through the utilization of a cationic surfactant.[292] Fan et al. employed a self-discharge mechanism for prelithiation of V_2C MXene, creating improved conductivity and open spaces that facilitate rapid ion diffusion. As a result, prelithiated V_2C MXene has demonstrated enhanced capacity as a cathode for MLIBs by enabling the co-intercalation of Mg^{2+} and Li^+ ions.[284] Nevertheless, the capacity of MIBs and MLIBs with MXene-based electrodes is underwhelming, indicating ample room for improvement in their performance. On the other hand, bulk MoS_2, a different 2D nanomaterial, exhibits limited magnesium ion storage capacity due to its semiconducting 2H crystal phase (its most thermodynamically stable phase) and its relatively small interlayer distances (≈0.62 nm).[26] Nevertheless, studies have demonstrated that the magnesium storage capability of MoS_2 can be improved through specific modifications that expand the interlayer spacing and enhance conductivity by synthesis of its metallic conductive 1T phase.[16] By implementing these changes and utilizing the modified MoS_2 as an MLIB cathode, a co-intercalation mechanism of Mg^{2+} and Li^+ can be activated, leading to the higher energy density of the battery. In contrast, an MLIB employing bulk MoS_2 as the cathode operates through a Daniell-cell type mechanism (involving the sole insertion/deinsertion of Li^+ ions in the cathode) due to its small interlayer distances and consequently provides low energy density.[135,213,216]

Accordingly, the combination of delaminated $Ti_3C_2T_x$ MXene, known for its high electrical conductivity, and interlayer expanded 1T MoS_2, featured with enhanced conductivity and short ion transport path can present a promising choice as a MLIB battery cathode. Such a nanocomposite cathode is reasoned to exhibit superior performance in MLIBs due to the synergistic effect resulting from their combined properties. The nanocomposite comprising of MoS_2 and different types of MXene have demonstrated favorable performance in the context of lithium-sulfur[176] and sodium-[293], potassium-[86], aluminium-[87] and zinc-[165,294] ion batteries. However, to the best of our knowledge, the utilization of such a nanocomposite

cathode for MLIBs remains unexplored.

In this study, we have developed a synthesis method that facilitates the formation of MoS_2 rich in the 1T metallic phase in the presence of delaminated $Ti_3C_2T_x$ MXene, ensuring the preservation of its structural integrity without oxidation. The outcome of this synthesis is a 2D/2D nanocomposite comprising of MoS_2 and MXene, harnessing the enhanced electrical conductivity from the crystal phase engineering and the $Ti_3C_2T_x$ MXene content. This nanocomposite demonstrates the capability to reversibly store ions with proper stability. With a unique structure and effective surface area, it promotes a fast kinetics of dual Mg^{2+} and Li^+ storage and provide short ion transport paths. Consequently, it exhibits superior performance as a cathode for MLIBs compared to its individual components. This research contributes to the development of safe and cost-effective hybrid Mg^{2+}/Li^+ batteries.

5.2 Results and Discussion

In our design of the 2D/2D 1T/2H-MoS_2@MXene nanocomposite, we aim to attain a 1T-rich MoS_2 to enable metallic conductivity and meanwhile to achieve favorable structural properties, such as an enhanced active surface area and expanded interlayer distance, thereby establishing short ion transport path. For the latter purpose, 2D $Ti_3C_2T_x$ MXene is employed as the substrate for the loading of 1T-rich MoS_2, resulting in nanocomposites of these two 2D materials of maximized electrical conductivity and surface area for insertion/extraction of the ions.

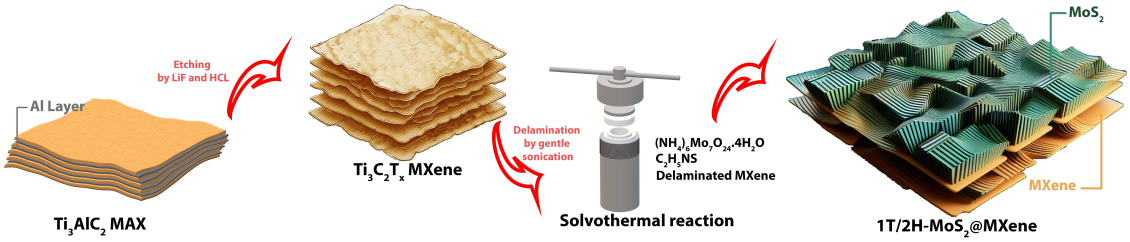

Figure 5.1: Schematic illustration of synthesis of 1T/2H-MoS_2@MXene.

Figure 5.1, shows the schematic synthesis of the nonocomposite. Delaminated $Ti_3C_2T_x$ MXene flakes are first produced by the etching of Ti_3AlC_2 (MAX phase) through the MILD method due to its demonstrated efficacy in generating high quality large flakes with fewer defects.[295–298] Herein, larger-sized MXene flakes are the preferred substrate for the loading of 1T-rich MoS_2 nano-sheets. Subsequently, the delaminated MXene flakes are dispersed in 40 mL of DMF, followed by the addition of $(NH_4)_6Mo_7O_{24}.4H_2O$ and CH_4N_2S as the respective

sources of molybdenum and sulfur for solvothermal reaction at 200 °C for 18 h. Subsequently, the resulting 2D/2D nanocomposite denoted as 1T/2H-MoS_2@MXene was vacuum-dried and collected after washing with DI water and methanol. In addition to 1T/2H-MoS_2, a second nanocomposite with a relatively higher MoS_2 content, 1T/2H-MoS_2@MXene2, and the third nanocomposite with a relatively lower MoS_2 content, 1T/2H-MoS_2@MXene3, have also been synthesized using the same method to study the effects of the nanocomposite composition on the electrochemical properties. Meanwhile, 1T/2H-MoS_2 is synthesized as the control sample with the same solvothermal method except without the addition of $Ti_3C_2T_x$ MXene.

Figure 5.2 displays transmission electron microscopy (TEM) images of delaminated $Ti_3C_2T_x$ MXene, 1T/2H-MoS_2, and 1T/2H-MoS_2@MXene. The TEM and HRTEM images of $Ti_3C_2T_x$ MXene (Figure 5.2a,b) reveal a few-layered structure, characterized by relatively large flakes. 1T/2H-MoS_2 synthesized herein through the solvothermal method shows a flower-like intertwined nano-flake structure.

A comparison of the HRTEM images of 1T/2H-MoS_2 and commercially available bulk MoS_2 featured with 2H phase reveals that the former has significantly fewer layers than the latter (Figure 5.2e vs. Figure 5.S1[§]). Moreover, the arrangement of these layers in the former appears disordered, bearing no resemblance to the well-structured layers typically observed in bulk 2H-MoS_2 (Figure 5.S1[§]).

The TEM and HRTEM images of 1T/2H-MoS_2@MXene (Figure 5.2f-h) provides evidence that the synthesis of MoS_2 in the presence of $Ti_3C_2T_x$ MXene flakes renders the MXene structure adorned with MoS_2 nanosheets. HRTEM images of this nanocomposite reveal the disordered few-layered 1T-2H-MoS_2 on the $Ti_3C_2T_x$ MXene flakes (Figure 5.2g,h). Figure 5.2i-k illustrate the HRTEM images of $Ti_3C_2T_x$ MXene, 1T/2H-MoS_2, and 1T/2H-MoS_2@MXene and the corresponding line scan profiles for the line across their lattice fringes. Based on this image analysis, interlayer distances are 1.2-1.4 nm for $Ti_3C_2T_x$ MXene, and 0.75-0.95 nm for 1T/2H-MoS_2 and 1T/2H-MoS_2@MXene (related to its MoS_2 content). These measurements serve as a cross-validation for the interlayer distances obtained based on the positions of the (002) peaks in their respective XRD spectra. The structural analysis through TEM and XRD shows that 1T/2H-MoS_2@MXene closely resembles the nanocomposite structures observed in earlier studies on MoS_2/MXene nanocomposites.[176,299] Nevertheless, a remarkable difference is evident in the interlayer spacing of MoS_2 within 1T/2H-MoS_2@MXene, which is notably larger than the interlayer spacing typically found in MoS_2 (about 0.62 nm). EDX elemental mapping images of this nanocomposite (Figure 5.2l-p) reveal a homogeneous

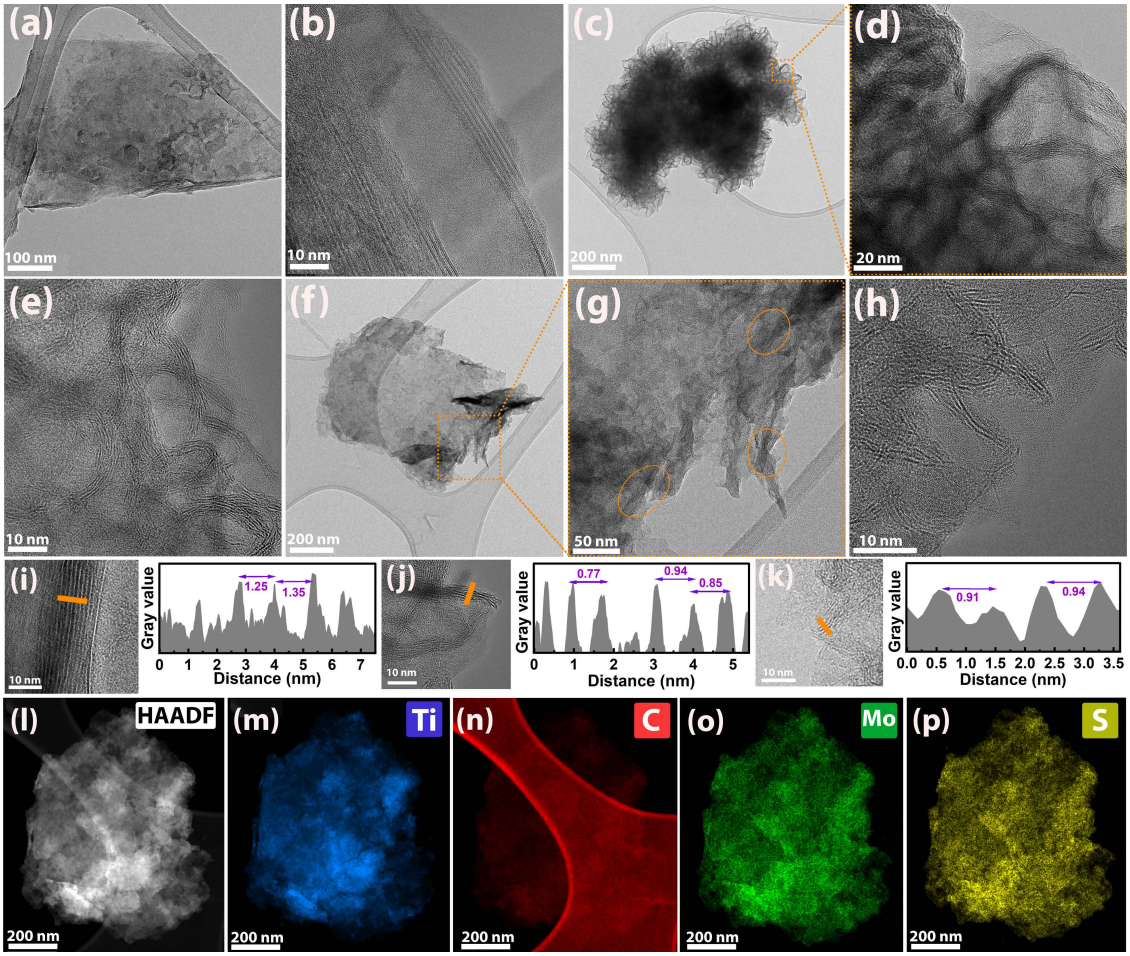

Figure 5.2: TEM (a) and HRTEM (b) images of $Ti_3C_2T_x$ MXene, TEM (c) and HRTEM (d,e) images of 1T/2H-MoS_2, and TEM (f) and HRTEM (g,h) of 1T/2H-MoS_2@MXene, HRTEM images of (i) $Ti_3C_2T_x$ MXene, (j) 1T/2H-MoS_2, and (k) 1T/2H-MoS_2@MXene and the intensity profiles along the orange lines in their corresponding HRTEM images, and EDX elemental mapping images (l-p) of 1T/2H-MoS_2@MXene.

dispersion of titanium, carbon, molybdenum, and sulfur elements throughout the nanocomposite. The even distribution of the elements suggests that the synthesis process yields a 2D/2D nanocomposite comprising of 1T/2H-MoS_2 and $Ti_3C_2T_x$ MXene.

TGA was conducted on the samples in a N_2 atmosphere within 25–700 °C to examine their thermal characteristics. As illustrated in Figure 5.S2[§], $Ti_3C_2T_x$ MXene exhibits a gradual weight loss of approximately 6% from 100 °C to 700 °C which is ascribed to the elimination of physically and chemically adsorbed water and other surface groups.[300] The total weight loss for 1T/2H-MoS_2 at 700 °C is 31%, primarily attributed to the removal of some intercalated species. The overall weight loss for 1T/2H-MoS_2@MXene at 700 °C stands at 20%, intermediate between the values of the two pristine analogues.

The crystal structure of the samples including $Ti_3C_2T_x$ MXene, 1T/2H-MoS_2, 1T/2H-MoS_2@MXene, 1T/2H-MoS_2@MXene2 and 1T/2H-MoS_2@MXene3 have been examined with XRD. **Figure 5.3**a illustrates the XRD patterns of the samples, along with the reference pattern derived from the JCPDS card (#37-1492) of the hexagonal 2H-MoS_2 phase. Bulk MoS_2 typically exhibits an interlayer spacing of approximately 0.62 nm, reflected by the (002) peak positioned at 2θ of around 14.3° as also discernible in JCPDS #37-1492 (Figure 5.S3§).[26,301] Distinctively different from the 2H phase, the XRD pattern of the synthesized 1T/2H-MoS_2 shows a broad (002) diffraction peak centered at a lowered 2θ value at 9.5° (Figure 5.3b). This shift in (002) peak position suggests an expanded interlayer spacing of about 0.93 nm (Figure 5.3b). The interlayer distance plays a significant role in determining the capacity of MoS_2 in the storage of ions with relatively larger sizes, such as Na^+ and K^+.[54,113] Furthermore, the expanded interlayer distance is particularly crucial for facilitating efficient insertion/extraction of divalent ions, including Mg^{2+} and Zn^{2+}, owing to their pronounced Coulombic interactions.[16,202] Consequently, it is anticipated that the synthesized 1T/2H-MoS_2 will exhibit enhanced performance in storing Mg^{2+} compared to typical bulk MoS_2, given its favorable interlayer characteristics. The expansion observed in the interlayer region can be attributed to the in-situ intercalation of NH_3/NH_4^+, which are generated through the decomposition of $(NH_4)_6Mo_7O_{24}.4H_2O$ and CH_4N_2S during the synthesis process.[106,119]

The delaminated $Ti_3C_2T_x$ MXene shows the characteristic diffraction pattern for this class of 2D material (Figure 5.3a). It has a distinct (002) peak at 6.19° (Figure 5.3b) highlighting the successful delamination to form an expanded interlayer spacing of 1.43 nm.[295,302] The observed interlayer distance expansion, which possesses beneficial implications for ion storage,[292] is ascribed to the removal of Al and formation of $-$F, $-$OH, and $-$O terminal groups on the surface of the nanosheets during the etching process.[303] The XRD spectra obtained from 1T/2H-MoS_2@MXene, 1T/2H-MoS_2@MXene2 and 1T/2H-MoS_2@MXene3 show distinct peaks corresponding to 1T/2H-MoS_2 and MXene phases. Specifically, the (002) peaks of $Ti_3C_2T_x$ MXene and MoS_2 appear at about 6.72° and 9.4°, with corresponding interlayer distance of 1.32 and 0.93 nm, respectively. Notably, it is evident that the interlayer distances of MXene has slightly decreased following the solvothermal reaction (1.43 nm in delaminated $Ti_3C_2T_x$ MXene vs. 1.32 nm in 1T/2H-MoS_2@MXene), likely due to the partial removal of termination groups.[303] Furthermore, a comparison of their XRD spectra reveals that, with 1T/2H-MoS_2@MXene2 and MoS_2@MXene3 with different 1T/2H-MoS_2/MXene ratios, the intensity ratio of the two (002) peaks also varies accordingly. It is important to

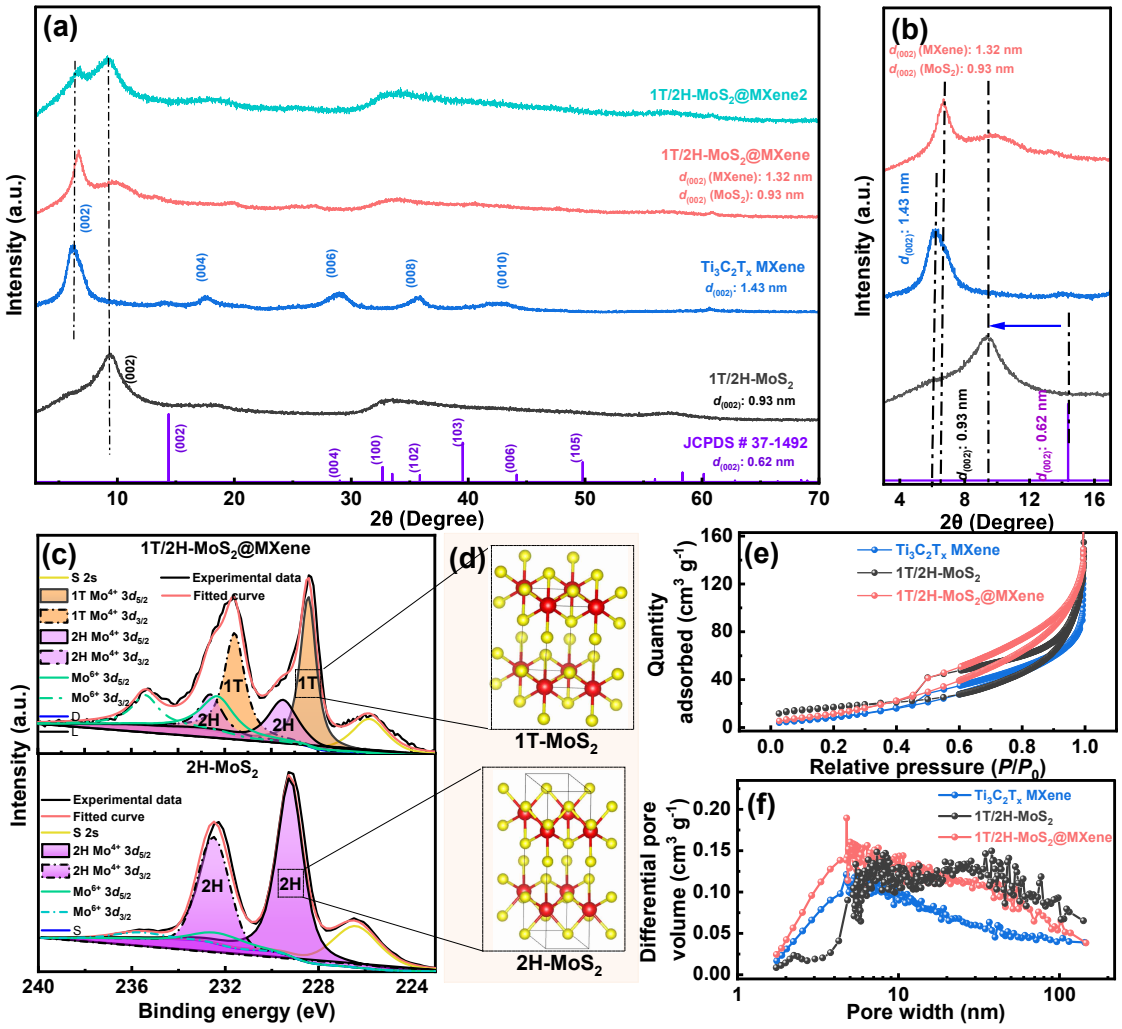

Figure 5.3: (a) XRD spectra of 1T/2H-MoS_2, $Ti_3C_2T_x$ MXene, 1T/2H-MoS_2@MXene, 1T/2H-MoS_2@MXene2, and 1T/2H-MoS_2@MXene3 and (b) the zoomed-in region of their (002) peak,(c) comparison of Mo 3d XPS spectra of 1T/2H-MoS_2@MXene and bulk MoS_2, (d) schematic illustration of 1T and 2H crystal phases of MoS_2, (e) N_2 sorption isotherms, and (f) pore size distributions of $Ti_3C_2T_x$ MXene, 1T/2H-MoS_2, and 1T/2H-MoS_2@MXene.

note that, based on weight gain following solvothermal synthesis, the estimated weight pcontent of MoS_2 in 1T/2H-MoS_2@MXene, 1T/2H-MoS_2@MXene2, and 1T/2-HMoS_2@MXene3 are approximately 51%, 78% and 22%, respectively.

The absence of any discernible peaks associated with TiO_2 in the XRD spectra of the nanocomposite samples is a noteworthy observation, indicating the absence of significant oxidation of MXene during the solvothermal reaction. It is important to highlight that a similar reaction conducted in an aqueous medium resulted in extensive oxidation of the MXene, evidenced by the prominent presence of a distinct TiO_2 peak (at about 25°) in its

XRD spectrum (Figure 5.S4[§]). Hence, the selected solvothermal technique employing DMF as the solvent seems to be a viable method for the synthesis of MoS_2-decorated MXene, effectively mitigating the risk of substantial oxidation of the MXene sheets.

XPS analysis has been conducted to gain a deeper understanding of the phase structures in 1T/2H-MoS_2 and 1T/2H-MoS_2@MXene. (See Figure 5.S5[§] for the XPS survey spectra and Figure 5.3c for Mo 3d spectra). Previous studies have shown that, while the Mo 3d spectrum of the 2H MoS_2 phase shows a single doublet (related to Mo^{+4} $3d_{5/2}$ and Mo^{+4} $3d_{3/2}$), mixed-phase 1T/2H MoS_2 typically exhibits two doublets. The second doublet originates from the 1T phase at lower binding energies, alongside the one associated with the 2H phase.[41] To clearly illustrate this distinction, Figure 5.3c compares the Mo 3d spectrum of 1T/2H-MoS_2@MXene with that of the bulk MoS_2 known for its 100% 2H phase structure. As illustrated in this figure, bulk MoS_2 exhibits a Mo 3d spectrum featuring only one distinctive doublet (with peaks located at about 229.3 and 232.5 eV, related to Mo^{+4} $3d_{5/2}$ and Mo^{+4} $3d_{3/2}$, respectively), an indicator of its exclusive 2H phase.[106,107] The 2H phase represents the most thermodynamically stable crystalline phase for MoS_2, imparting it semiconducting properties.[304] Mo 3d spectrum of 1T/2H-MoS_2@MXene shows two doublets, one attributed to the 1T phase at lower binding energies (228.4 and 231.6 eV for Mo^{+4} $3d_{5/2}$ and Mo^{+4} $3d_{3/2}$, respectively), beside the regular one for the 2H phase at higher binding energies (229.3 and 232.5 eV for Mo^{+4} $3d_{5/2}$ and Mo^{+4} $3d_{3/2}$, respectively). Thus, the XPS results confirm solidly the presence of the mixed 1T and 2H phases in 1T/2H-MoS_2@MXene.[26]

Figure 5.3d schematically illustrates the variances between the crystal structures of 2H- and 1T-MoS_2. Based on this representation, the 2H phase is characterized by hexagonal symmetry, denoted by a space group of $P63/mmc$, while the 1T phase exhibits trigonal symmetry, identified by a space group of $P3\overline{m}1$.[33,266] These structural differences yield the semiconducting nature of 2H and the electron conductivity of 1T. Notably, 1T MoS_2 demonstrates a conductivity that is seven orders of magnitude higher than that of 2H MoS_2.[41] By peak deconvolution of the Mo 3d spectrum, we have determined that the content of 1T-MoS_2 phase in 1T/2H-MoS_2@MXene amounts to approximately 66% (For comparison the content of 1T phase in 1T/2H-MoS_2 control sample is estimated to be 68%, Figure 5.S6[§]). It is worth mentioning that, compared to other reported cases involving the synthesis of metallic MoS_2, especially those by hydrothermal or solvothermal methods, our samples exhibit remarkably high contents of the 1T phase.[34] This observation strongly validates the effectiveness of the employed method in producing 1T-rich MoS_2. Given the presence of high content of 1T phase, which imparts metallic properties to MoS_2, it is anticipated that 1T/2H-MoS_2 and

1T/2H-MoS_2@MXene exhibit greater electrical conductivity compared to the conventional 2H-MoS_2. The emergence of the metallic phase at elevated content can be ascribed to two distinct factors. Primarily, NH_3 generated during the synthesis procedure not only leads to the interlayer enlargement phenomenon (by insertion into the parallel plane) but also acts as electron donors. This, in turn, contributes to increase of the surrounding electron density of the molybdenum (Mo) atoms and reduce their binding energy, ultimately leading to the formation of the metallic 1T phase.[106,119] The MoS_2 interlayer distances in 1T/2H-MoS_2 and 1T/2H-MoS_2@MXene (0.93 nm) align consistently with prior investigations, affirming the presence of an NH_3-intercalated product.[106,305] Moreover, the DMF solvent in solvothermal reactions can also infiltrate into the MoS_2, leading to interlayer expansion and facilitating a transition from the 2H to 1T phase.[306] Consequently, as elucidated earlier, the utilization of a solvothermal methodology employing DMF as the solvent not only serves to mitigate oxidation of MXene (which happens in the hydrothermal synthesis) but also induces the formation of a metallic 1T MoS_2 phase, thereby enhancing the conductivity of the final product.

In the XPS spectra of the samples, we have also observed a subtle doublet signal (at about 232.3 and 235.4 eV for Mo^{+6} $3d_{5/2}$ and Mo^{+6} $3d_{3/2}$, respectively; see Figure 5.3c), which is related to the presence of MoO_3 as a minor impurity.[26,78]

N_2 sorption analysis has been performed to characterize the textural features of the samples. Figure 5.3e displays the N_2 sorption isotherms for $Ti_3C_2T_x$ MXene, 1T/2H-MoS_2, and 1T/2H-MoS_2@MXene. The Brunauer–Emmett–Teller (BET) specific surface area of $Ti_3C_2T_x$ MXene is determined to be 40.1 m^2 g^{-1} (pore volume: 0.14 cm^3 g^{-1}), whereas 1T/2H-MoS_2 exhibits a higher surface area of 58.4 m^2 g^{-1} (pore volume: 0.19 cm^3 g^{-1}). Consequently, it appears that the MoS_2 component contributes to a greater surface area compared to the MXene alone. The pore size distribution plots presented in Figure 5.3f indicates that the pores in MoS_2 are relatively larger on average than those in $Ti_3C_2T_x$ MXene. As a result, their nanocomposite, 1T/2H-MoS_2@MXene, demonstrates a specific surface area of 56.2 m^2 g^{-1} (pore volume: 0.20 cm^3 g^{-1}), and its pore structure encompasses a broader distribution of sizes, reflecting the combined effects of both components (Figure 5.3e,f). It is noteworthy that the specific surface areas of both 1T/2H-MoS_2 and 1T/2H-MoS_2@MXene surpass the typical specific surface area observed with bulk MoS_2, which generally registers at less than 30 m^2 g^{-1}.[78,138,301] Such a hierarchical structure with a wide range of pore dimensions is expected to improve the electrode-electrolyte interactions and provide a shorter ion transport path for ion storage.[307,308]

The electronic conductivity of three samples ($Ti_3C_2T_x$ MXene, 1T/2H-MoS_2 and 1T/2H-MoS_2@MXene) has been evaluated on their thin layers with a direct current polarization method.[309] Figure 5.S7§ shows the plots of current versus voltage for the three samples, along with linear fitting. According to Ohm's Law, a higher slope of the fitting line indicates the higher conductivity. A comparison of the plots suggests that $Ti_3C_2T_x$ MXene has the highest conductivity among the three samples with a slope of 33.628 μA mV^{-1}, with the lowest slope of 0.0134 μA mV^{-1} found for 1T/2H-MoS_2. The hybridization of 1T/2H-MoS_2 with MXene clearly leads to the enhanced conductivity of 1T/2H-MoS_2@MXene, as evidenced by its slope of 0.642 μA mV^{-1}.

To investigate their electrochemical behavior, MIBs and MLIBs have been assembled with the three respective materials, including $Ti_3C_2T_x$ MXene, 1T/2H-MoS_2 and 1T/2H-MoS_2@MXene, as cathodes and a polished magnesium metal sheet as the anode. CV testing was conducted on both groups of batteries, as illustrated in **Figure 5.4**. Specifically, Figure 5.4a-c depict the CV curves for MIBs with the three cathodes at a voltage sweep rate of 0.25 mV s^{-1}. CV curves of $Ti_3C_2T_x$ MXene MIB (Figure 5.4a) reveal a relatively low current response to voltage sweeping. This observation aligns with prior findings, indicating that $Ti_3C_2T_x$ MXene, without expanded interlayer spacing by specific modifications such as cationic surfactant/ionomer intercalation, possesses limited Mg^{2+} storage capacity.[290,310] Consequently, the enclosed area in its CV curve is notably compact, with no discernible redox peaks. In contrast, the CV curves of 1T/2H-MoS_2 cathode (Figure 5.4b) exhibit an oxidation peak at 0.87 V and a reduction peak at 1.27 V, which correspond to the insertion and extraction of Mg^{2+}, respectively. The same redox peaks are also visible in the CV curves of 1T/2H-MoS_2@MXene (Figure 5.4c) with a slight shift, the oxidation peak at 0.93 V and the reduction peak at 1.22 V. Given that MXene exhibits no observable peaks associated with the insertion or extraction of magnesium ions, it can be concluded that these peaks originate from the 1T/2H-MoS_2 component within the nanocomposite.

CV curves in Figure 5.4d-f pertain to MLIBs featuring $Ti_3C_2T_x$ MXene, 1T/2H-MoS_2, and 1T/2H-MoS_2@MXene cathodes, respectively. As depicted in Figure 5.4d, it is evident that the area enclosed within the CV curve of $Ti_3C_2T_x$ MXene has significantly increased in the MLIB configuration compared to its MIB analogue (Figure 5.4d vs. Figure 5.4a). In its CV curves, two broaden peaks emerge at 1 V (reduction peak) and 1.2 V (oxidation peak), which are related to the insertion and extraction of Li^+, respectively.[283] The same observation is valid for MLIBs with 1T/2H-MoS_2 and 1T/2H-MoS_2@MXene cathodes. In comparison with their MIB counterparts, the current at a given voltage in their CV curves in the

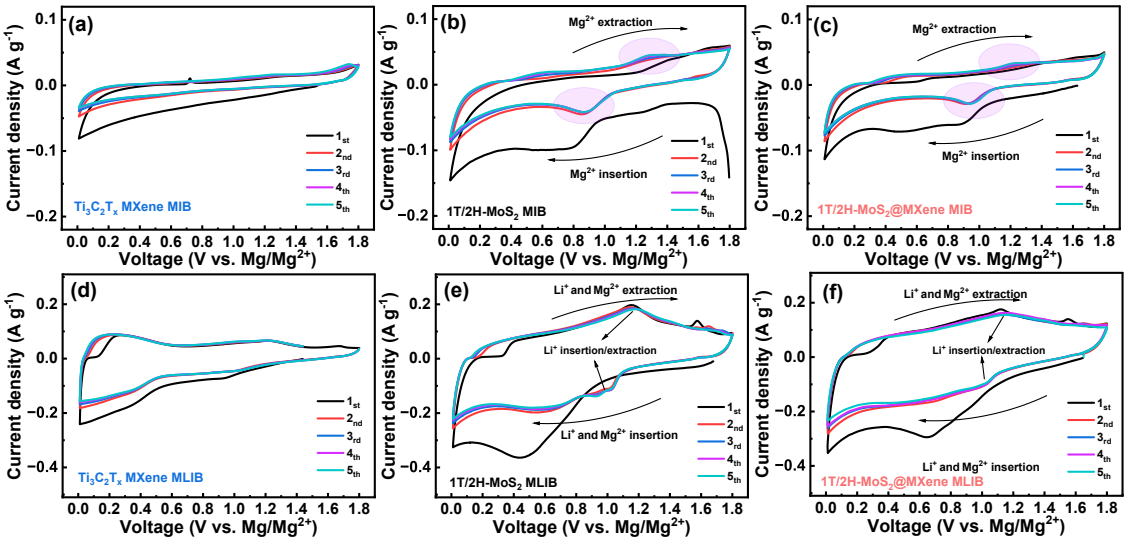

Figure 5.4: CV curves of (a-c) MIBs and (d-f) MLIBs with $Ti_3C_2T_x$ MXene, 1T/2H-MoS_2, and 1T/2H-MoS_2@MXene cathodes, respectively, acquired at 0.25 mV s^{-1}.

MLIB configuration (Figure 5.4e,f) is also significantly intensified (Figure 5.4b,c). Evidently, the presence of Li^+ has a pronounced impact on enhancing the batteries' capacity, owing to the facile insertion and extraction of small-sized monovalent Li^+ within the cathodes. With the 1T/2H-MoS_2 and 1T/2H-MoS_2@MXene cathodes, their MLIB CV curves exhibit pairs of relatively broad reduction and oxidation peaks centered at 1.00 V and 1.15 V, respectively. These peaks are attributed mainly to the insertion/extraction of Li^+ within the 2D materials, MoS_2 in the former and both MoS_2 and MXene in the latter. Nevertheless, Mg^{2+} insertion/extraction may also take place, but in a minor role on the basis of the CV curves of MIBs. It is important to mention that previous research indicates that bulk MoS_2, when used in a MLIB, experiences sole Li^+ insertion/extraction in the cathode side and exhibits only peaks associated with Li^+.[26] For a more direct comparison, **Figure 5.5**a illustrates the third-cycle CV curves of both MIB and MLIB, each with 1T/2H-MoS_2@MXene as the cathode. The juxtaposition of these curves clearly highlights the enhanced battery capacity achieved through the incorporation of the dual-salt electrolyte. As depicted schematically in Figure 5.5b, the discharge process involves the dissolution of Mg^{2+} on the anode side (magnesium plate) and a simultaneous co-intercalation process storing both Li^+ and Mg^{2+} on the cathode side. Conversely, during the charging process, Mg^{2+} is exclusively deposited on the anode side (due to its higher redox potential compared to Li/Li^+[311]), while the cathode undergoes an extraction process for both Li^+ and Mg^{2+}. This unique mechanism endows the batteries with the combined advantages of a magnesium anode (safety, oxidation resistance, and high volumetric capacity) and benefits from the fast kinetics, small size, and

low Coulombic interactions of Li^+ on the cathode.

It is noteworthy that, depending on the cathode type employed, such dual-salt batteries may exhibit either a Daniell-cell type mechanism (involving only the insertion/extraction of Li^+ in the cathode) or a co-intercalation mechanism (involving insertion/extraction of both Li^+ and Mg^{2+}).[214] The CV test conducted on the MIB with 1T/2H-MoS_2@MXene cathode (Figure 5.4c) demonstrates its ability to store Mg^{2+}, suggesting its capacity to host both ions and consequently exhibit a co-intercalation mechanism. However, it is crucial to recognize that the degree of involvement of these ions in the insertion/extraction process is tied to the applied current density. In scenarios with high current densities, a greater percentage of engaged Li^+ is observed compared to Mg^{2+}.[26]

It is also noteworthy that, the intercalated Li^+ can accelerate Mg^{2+} diffusion due to the reduced activation energy following the intercalation of the former. Intercalated Li^+ ions interact with the host lattices, thereby leading to the weakened interactions between Mg^{2+} and the host material.[133–135] The advantage of the co-intercalation mechanism over the Daniell-cell type lies in its potential to utilize less electrolyte (considering the limited solubility of lithium salts in conventional electrolytes for MLIBs), thereby achieving higher energy density.[213] This co-intercalation mechanism has also been observed in AZIBs, demonstrating the simultaneous intercalation of H^+ and Zn^{2+}.[215,312]

While Li^+ ions are stored in $Ti_3C_2T_x$ MXene through ion intercalation/deintercalation ($xLi^+ + Ti_3C_2T_x + xe^- \leftrightarrow Li_xTi_3C_2T_x$),[313] the ion storage mechanism in MoS_2 involves either an intercalation/deintercalation ($yLi^+ + MoS_2 + ye^- \leftrightarrow Li_yMoS_2$) process or conversion reactions ($Li_yMoS_2 + (4 - y)Li^+ + (4 - y)e^- \leftrightarrow 2Li_2S + Mo$). Previous studies have demonstrated that the peak associated with conversion reactions, resulting in the formation of Li_2S and Mo nanograins, typically occurs at around 0.5 V versus Li/Li^+ in CV tests. These conversion reactions are known to adversely impact the cyclic stability of the battery.[57,60,314,315] Given the applied voltage window of 0.01-1.8 V versus Mg/Mg^{2+} ($\approx$ 0.7-2.5 vs. Li/Li^+) for these MLIBs, the likelihood of conversion reactions is minimal. Consequently, the storage of lithium ions in 1T/2H-MoS_2@MXene should take place predominantly through intercalation/deintercalation reactions. According to prior theoretical calculations with density functional theory, the suggested overall reaction for the storage of Mg^{2+} is determined to be $6MoS_2 + 4Mg \leftrightarrow Mg_4Mo_6S_{12}$.[278]

To further evaluate the performance of the compounds as MLIBs cathodes, a rate performance test was conducted, subjecting them to various discharge currents of 50, 100, 250, 500, 750, and 1,000 mA g^{-1}, respectively. See Figure 5.5c for rate performance results and

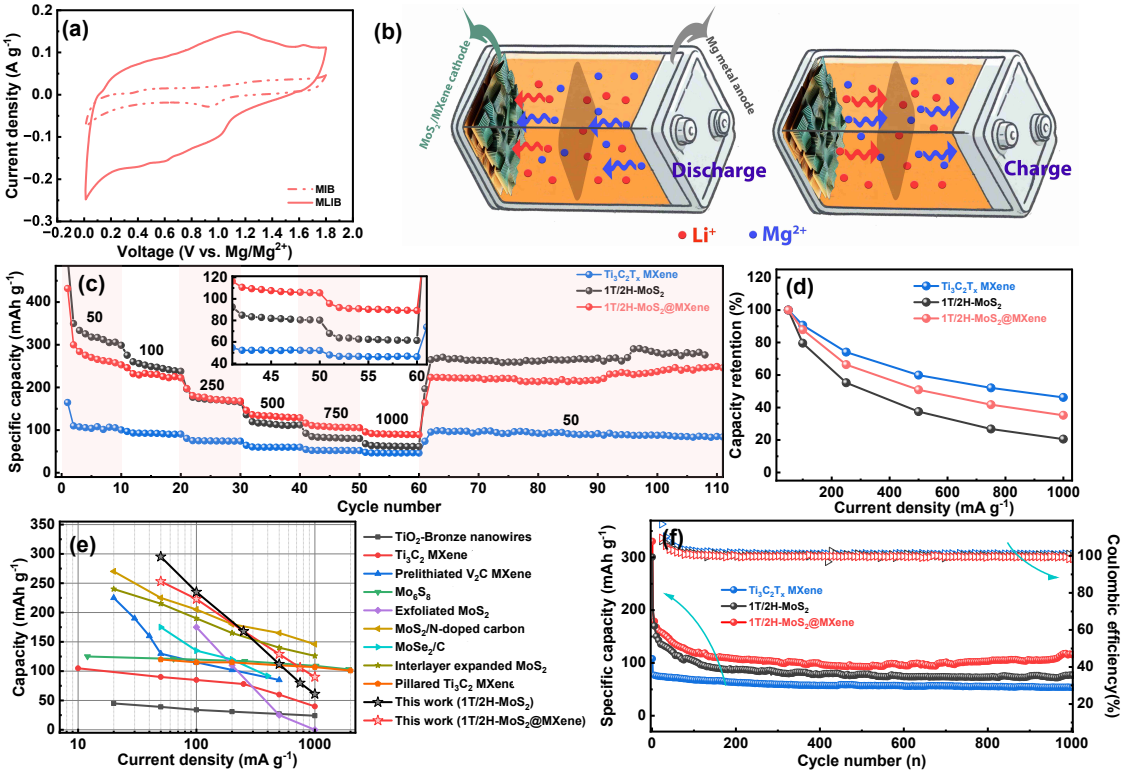

Figure 5.5: (a) Comparison of CV curves of MIB and MLIB with 1T/2H-MoS_2@MXene cathodes at 0.25 mV s^{-1}; (b) schematic illustration of 1T/2H-MoS_2@MXene MLIB charge/discharge mechanism; (c) rate performance test of MLIBs with $Ti_3C_2T_x$ MXene, 1T/2H-MoS_2 and 1T/2H-MoS_2@MXene cathodes; (d) their capacity retention at different current densities; (e) comparison of the rate performance of 1T/2H-MoS_2 and 1T/2H-MoS_2@MXene MLIBs with those of previously reported Mg^{2+}/Li^+ battery cathode materials;[135,216,279,280,282–285,292] (f) cycling performances of MLIBs with $Ti_3C_2T_x$ MXene, 1T/2H-MoS_2, and 1T/2H-MoS_2@MXene cathodes at 500 mA g^{-1} for 1,000 cycles.

Figure 5.S8[§] for first three cycles of GCD curves at 50 mA g^{-1} and GCD curves at different current densities. Notably, $Ti_3C_2T_x$ MXene consistently exhibits the lowest capacity values across all applied currents, registering ≈103 mAh g^{-1} at 50 mA g^{-1} and ≈46 mAh g^{-1} at 1,000 mA g^{-1}. 1T/2H-MoS_2, owing to its unique characteristics including disordered structure and high 1T phase content, displays notably high capacity during the rate performance test, particularly at relatively low currents. It records capacity values (in the last cycles at each applied current) of 298, 235, 168, 112, 80, and 61 mAh g^{-1} at 50, 100, 250, 500, 750, and 1,000 mA g^{-1}, respectively. Despite its impressive capacities at low current densities, 1T/2H-MoS_2 exhibits a weaker rate performance compared to MXene (Figure 5.5d). At 1,000 mA g^{-1}, this battery maintains only 20% of its capacity at 50 mA g^{-1}, whereas the MXene sample retains 46%. This remarkable rate performance of MXene is attributed to

its high conductivity, 2D nature, and delaminated structure that provides fast diffusion of Li^+.[283] In contrast, despite the various advantages offered by 1T/2H-MoS_2, such as its 1T phase, it alone is insufficient to achieve a sufficient rate performance. Remarkably, 1T/2H-MoS_2@MXene demonstrats optimal behavior in the rate performance test, achieving capacity values of 253, 223, 168, 129, 106, and 90 mAh g^{-1} at 50, 100, 250, 500, 750, and 1,000 mA g^{-1}, respectively. Although it exhibits a slight capacity deficit compared to 1T/2H-MoS_2 at low currents, it showcases superior performance at high currents, retaining 36% of its initial capacity at 1,000 mA g^{-1} (Figure 5.5d).

The electrochemical performances of 1T/2H-MoS_2@MXene2 and 1T/2H-MoS_2@MXene3 are also presented in Figure 5.S9[§]. An analysis of the GCD curves and rate performance curve of 1T/2H-MoS_2@MXene2 (Figure 5.S9a,c,e[§]) reveals that increasing the MoS_2/MXene ratio in the nanocomposite results in capacity values comparable to those of 1T/2H-MoS_2 at low current densities (295 mAh g^{-1} in the last discharge at 50 mA g^{-1}) and slightly improved rate performance relative to 1T/2H-MoS_2, with 26% of the initial capacity retained at 1,000 mA g^{-1} (Figure 5.S9f[§]). However, this increase in MoS_2/MXene ratio compromises the rate performance compared to 1T/2H-MoS_2@MXene (26% vs. 36% of capacity retention at 1,000 mA g^{-1}). An examination of the GCD curves and rate performance results of 1T/2H-MoS_2@MXene3 with a lower 1T/2H-MoS_2 content (Figure 5.S9b,d,f[§]) indicates lower capacities compared to two other nanocomposites (207 mAh g^{-1} at 50 mA g^{-1} and 70 mAh g^{-1} at 1000 mA g^{-1}). However, in terms of capacity retention, 1T/2H-MoS_2@MXene3 is superior to 1T/2H-MoS_2@MXene2 and closely resembles 1T/2H-MoS_2@MXene, exhibiting 34% of capacity retention at 1,000 mA g^{-1}. This shows the significant impact of $Ti_3C_2T_x$ MXene content on capacity retention at high current densities and verifies that 1T/2H-MoS_2@MXene has the optimum nanocomposite composition.

Notably, at relatively high current densities (> 500 mA g^{-1}), 1T/2H-MoS_2@MXene exhibits greater capacities than the other cathodes (see the inset in Figure 5.5c). When compared to prior research on MLIBs featuring cathodes based on different types of MXene, MoS_2, or other inorganic compounds, 1T/2H-MoS_2, operating independently without hybridizing with other materials, outperforms them at low currents (Figure 5.5e). Comparing the rate performance of 1T/2H-MoS_2@MXene to that of 1T/2H-MoS_2 (Figure 5.5d), as well as considering the values documented in prior research (Figure 5.5e), it is evident that 1T/2H-MoS_2@MXene exhibits optimum behavior and demonstrates a relative advantage compared to previously reported cathodes for MLIBs.

Upon completion of the rate performance test, the current was switched back to a 50 mA

g^{-1} and the MLIBs were subjected to 50 additional charge-discharge cycles (Figure 5.5c). Over the additional cycling, $Ti_3C_2T_x$ MXene retains 89% of its capacity (95 and 85 mAh g^{-1} at 1_{st} and 50_{th} cycle, respectively), indicating its relative stability over the cycling at low currents. Nevertheless, both 1T/2H-MoS_2 and 1T/2H-MoS_2@MXene exhibit remarkably stable cycling performance with slight capacity increases from 261 to 276 mAh g^{-1} for 1T/2H-MoS_2 and from 223 to 249 mAh g^{-1} for 1T/2H-MoS_2@MXene. The electro-activation process, a gradual enhancement in capacity, is a commonly observed phenomenon in MoS_2-based electrodes, arising from the continual insertion/extraction of the ions. This dynamic process leads to an enhanced active surface area, as discussed in previous studies.[131,132] On the other hand, when ions insert into the layered structures of MoS_2, they induce specific distortions, triggering a transition from the semi-conductive 2H phase to the metallic 1T phase. With repeated cycling, both the proportion of the 1T phase and the accessible active surface area undergo a progressive increase. This cyclic evolution creates more accessible active sites and conductivity for the effective storage of the ions.[76]

The results from cycling tests of MLIBs at a current of 500 mA g^{-1} for 1,000 charge/discharge are illustrated in Figure 5.5f, including their respective Coulombic efficiencies. The data reveals a noteworthy 67% of capacity retention for $Ti_3C_2T_x$ MXene, with initial reversible and final discharge values of 80 and 54 mAh g^{-1}, respectively. In contrast, 1T/2H-MoS_2 exhibits a capacity retention of 45% in the final cycle, while 1T/2H-MoS_2@MXene demonstrates a retention of 65%, with initial reversible and final discharge values of 177 and 115 mAh g^{-1}, respectively. The results suggest that $Ti_3C_2T_x$ MXene exhibits superior stability during the intricate charge/discharge process in such a dual-salt battery, potentially contributing to the overall stability of the 1T/2H-MoS_2@MXene. Throughout the entire 1,000 cycles, 1T/2H-MoS_2 maintains an average Coulombic efficiency of 99.6%, highlighting its efficacy in storing and delivering ions with minimal charge loss.

On the anode side, only deposition/dissolution of Mg^{2+} is expected due to a dynamic redox potential that is approximately 0.67 V lower than that of Li/Li^+.[311] To verify this, XRD analysis has been conducted on both fresh Mg anode and the cycled one in 1T/2H-MoS_2@MXene MLIB subjected to the rate performance test (Figure 5.5c). As depicted in Figure 5.S10[§], the XRD patterns of both anodes are nearly identical, suggesting the absence of newly emerged phases associated with lithium/lithium oxide. This provides the evidence excluding the deposition/dissolution of Li^+ on the Mg anode in MLIBs.

The battery performance tests indicate that 1T/2H-MoS_2@MXene stands out as the optimal cathode, showcasing superior rate performance and decent cyclability. Its superior

rate performance, compared to 1T/2H-MoS_2, can be attributed to the inclusion of MXene that enhances electrical conductivity and imparts unique structural characteristics resulting from the hybridization of two 2D materials. This hybrid structure contributes to improved surface properties and better interactions with the electrolyte, collectively enhancing the overall performance of the nanocomposite material. To delve deeper into this from a kinetic perspective, EIS tests have been conducted on MLIB cells following the rate performance tests, with their Nyquist plots depicted in **Figure 5.6**a,b.

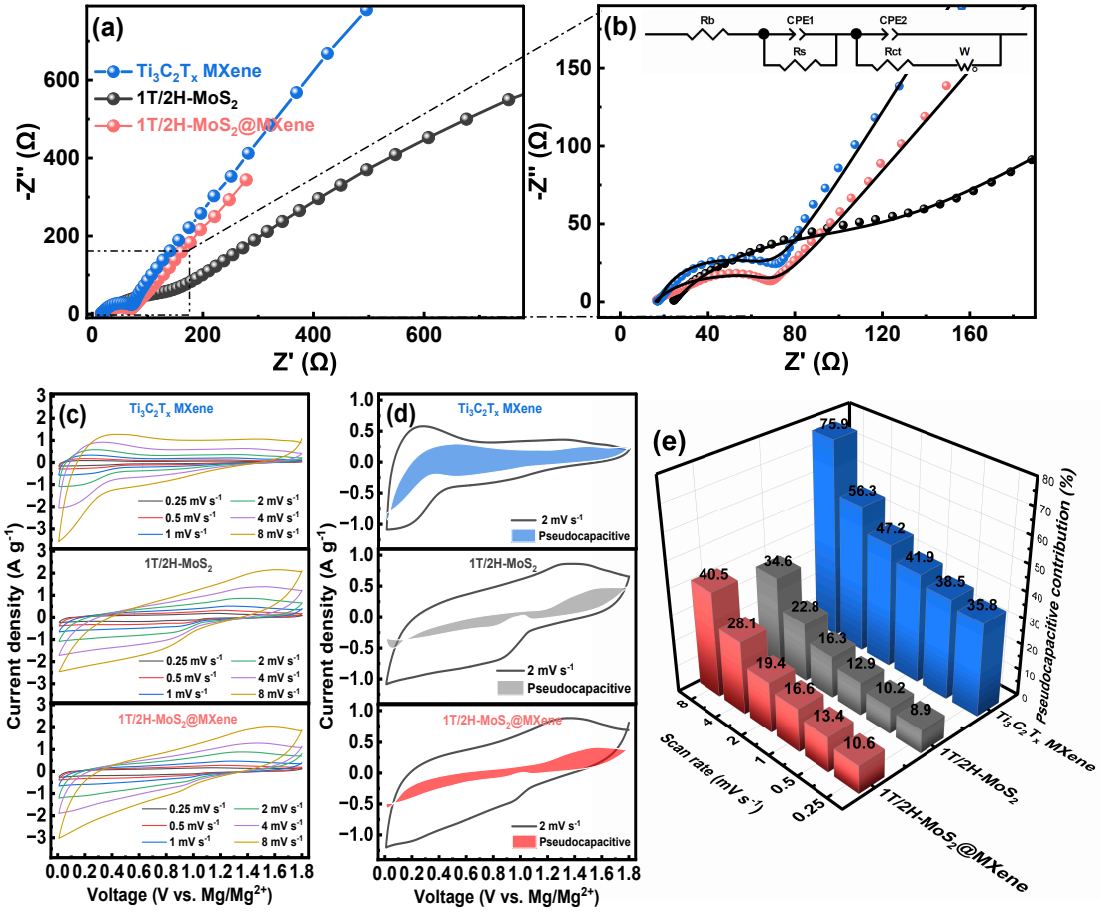

Figure 5.6: (a) Nyquist plots of the MLIBs with $Ti_3C_2T_x$ MXene, 1T/2H-MoS_2, and 1T/2H-MoS_2@MXene cathodes; (b) a closer look at the Nyquist plots, in the high-frequency region; (c) CV plots at different voltage scan rates for MLIBs with $Ti_3C_2T_x$ MXene, 1T/2H-MoS_2, and 1T/2H-MoS_2@MXene cathodes; (d) their pseudocapacitive contribution in charge storage at 2 mV s^{-1}; (e) comparison of their pseudocapacitive contributions at different voltage scan rates.

Significantly, from the Nyquist plots, it is evident that $Ti_3C_2T_x$ MXene has the smallest semicircle in the middle-high frequency region, i.e., the smallest R_{ct} of 49 Ω. Consequently,

$Ti_3C_2T_x$ MXene emerges as the superior material with respect to both electron and ion conductivity. Following closely, 1T/2H-MoS_2@MXene shows R_{ct} of 53 Ω. In contrast, 1T/2H-MoS_2 exhibits the largest R_{ct} of 88 Ω compared to the other two samples. The EIS test results corroborate the significant impact of hybridizing MXene and MoS_2 on reducing R_{ct}, which can be a reason for the enhanced rate performance of 1T/2H-MoS_2@MXene. This trend of change in R_{ct} results is in good agreement with the conductivity results measured above. Moreover, the elevated slope observed in the low-frequency range (Warburg resistance) for $Ti_3C_2T_x$ MXene suggests superior ion diffusion rates in this electrode material. This can be attributed to relatively more expanded interlayer distances and exceptionally high conductivity associated with $Ti_3C_2T_x$. Moreover, the observed slope is at its minimum for 1T/2H-MoS_2 but undergoes a significant increase upon hybridization with $Ti_3C_2T_x$ (1T/2H-MoS_2@Mxene). It implies that, while 1T/2H-MoS_2 possesses high capacity as an electrode material for storing Li^+ and Mg^{2+} in a MLIB due to its inherent characteristics, there is still room for improvement in its charge transfer kinetics. This improvement is realized in our study through the incorporation of $Ti_3C_2T_x$ MXene, contributing to an enhanced charge transfer process.

For a more thorough exploration of the charge storage mechanism in the three electrodes, CV curves of their MLIBs were acquired at varying scan rates (Figure 5.6c). Then equation (5.1) is employed to quantitatively distinguish the current response contributions between surface-controlled pseudocapacitive ($k_1\nu$) and diffusion-controlled battery type ($k_2\nu^{1/2}$) contributions to the current response at different voltage scan rates.[78,259]

$$i = k_1\nu + k_2\nu^{1/2} \tag{5.1}$$

where, at each fixed potential, i is the measured current at a scan rate of ν, and k_1 and k_2 are calculated as the slope and intercept of linear fitting of $i/\nu^{1/2}$ versus $\nu^{1/2}$.

Based on these calculations, we have determined the pseudocapacitive contributions at various scan rates (0.25, 0.5, 1, 2, 4, and 8 mV s^{-1}), as illustrated in Figure 5.6e. Figure 5.6d provides a comparison of the pseudocapacitive contributions of the three MLIBs at 2 mV s^{-1}. In Figure 5.6e, it is evident that at lower scan rates, $Ti_3C_2T_x$ MXene exhibits battery-like behavior, with a pseudocapacitive contribution of 35.8% at 0.25 mV s^{-1} (see Figure 5.6e). However, with increasing scan rates, its pseudocapacitive behavior becomes dominant, reaching 75.9% at 8 mV s^{-1} (Figure 5.6e). In contrast, 1T/2H-MoS_2 primarily demonstrates battery-like behavior, showing a maximum pseudocapacitive contribution of 34.6% at 8 mV s^{-1}.

With 1T/2H-MoS_2@MXene the pseudocapacitive contribution increases Upon hybridization with $Ti_3C_2T_x$ MXene. Specifically, 1T/2H-MoS_2@MXene exhibits 10.6% and 40.5% of pseudocapacitive behavior at 0.25 and 8 mV s^{-1}, respectively. The heightened pseudocapacitive contribution, which accelerates ion storage kinetics, is attributed to the enhanced conductivity and unique structure of the 2D/2D nanocomposite. Based on the findings from the kinetics analysis of the batteries, it appears that the combination of fast kinetics and pseudocapacitive behavior from $Ti_3C_2T_x$ MXene and the substantial capacity derived from the 1T/2H-MoS_2 component has rendered the nanocomposite exhibiting significant potential as a MLIB cathode.

5.3 Conclusion

In conclusion, this study has addressed key challenges in advancing MIBs and MLIBs by introducing a distinctive cathode design. The synthesis of a 2D/2D nanocomposite, incorporating delaminated $Ti_3C_2T_x$ MXene and MoS_2, strategically enhances the synergistic effects arising from their combined properties, thereby overcoming limitations associated with individual components. The nanocomposite material, 1T/2H-MoS_2@MXene, exhibits significantly higher capacities compared to the pure MXene, while simultaneously demonstrating superior kinetics and rate performance compared to the pure 1T/2H-MoS_2. This underscores the improved kinetics arising from the inherent conductivity of $Ti_3C_2T_x$ MXene, alongside the substantial capacity offered by 1T/2H-MoS_2. Notably, the enlarged interlayer distances in both materials play a critical role in ensuring sufficient ion storage within the 2D structure. Our findings underscore the importance of a tailored cathode design to unlock the full potential of MLIBs. The demonstrated ability of the nanocomposite cathode to co-intercalate Mg^{2+} and Li^+ ions, along with its superior safety features, represents a substantial leap toward realizing safe, economical, and high energy density dual-salt Mg^{2+}/Li^+ batteries. This research not only provides crucial insights for optimizing energy storage technologies but also paves the way for the development of high-performance MIBs with practical applications in the realm of sustainable energy solutions.

5.4 Experimental Section

Chemicals and materials

Chemicals and materials, including , aluminium chloride ($AlCl_3$, 99.99 %, Aldrich), 2.0 M phenylmagnesium chloride solution in THF (PhMgCl, Aldrich), anhydrous lithium chloride (LiCl, 98+ %, Alfa Aesar), ammonium molybdate tetrahydrate $(NH_4)_6Mo_7O_{24}.4H_2O$, 99%, Alfa Aesar), thioacetamide (C_2H_5NS, 98%, Alfa Aesar), lithium fluoride (LiF, Aldrich), hydrochloric acid (HCl, 36%, Caledon Laboratory Chemicals), poly(vinylidene fluoride) (PVDF, Mw ≈534,000 g mol^{-1}, Aldrich), and 1-methyl-2-pyrrolidone (NMP, reagent plus 99%, Sigama-Aldrich), were used as received without further purification. Ternary titanium aluminum carbide (Ti_3AlC_2 MAX phase) powders with a size <40 μm was supplied by Y-Carbon Ltd., Ukraine. Commercial bulk molybdenum (IV) sulfide (MoS_2, < 2 μm, 99%) was purchased from Aldrich.

Synthesis of $Ti_3C_2T_x$ MXene and 1T/2H-MoS_2@MXene

Delaminated $Ti_3C_2T_x$ was synthesized according to the minimally intensive layer delamination (MILD) method with slight modification.[295–298] The etching process involved the gradual addition of 500 mg of Ti_3AlC_2 over a 10-min period to an etchant solution containing 0.8 g of LiF in 10 mL of 9 M HCL, followed by stirring for 24 h at 35 °C. Subsequently, the solution underwent multiple cycles of washing with DI water through centrifugation (3500 rpm for 3 min). After each cycle, the acidic supernatant was decanted, followed by the addition of DI water before initiating another centrifugation cycle. The washing cycles were repeated until a pH of 5 was achieved. To remove unexfoliated components, a 3-min sonication was applied, followed by centrifugation (3500 rpm for 5 min), and the settled part was removed. Subsequently, the dispersed part (delaminated MXene) was collected through centrifugation at 15000 rpm and dried over night under vacuum at 80 °C.

1T/2H mixed-phase MoS_2 embedded in $Ti_3C_2T_x$ MXene (1T/2H-MoS_2@MXene) was synthesized by a solvo-thermal reaction conducted in the presence of the MXene. In a typical synthesis, 120 mg of the as-synthesized MXene was dispersed in 40 mL of DMF. Subsequently, 330 mg $(NH_4)_6Mo_7O_{24}.4H_2O$ and 285 mg CH_4N_2S were introduced as the sources of molybdenum and sulfur, respectively. After 10 min stirring at room temperature, the resulting dispersion was transferred to a Teflon-lined autoclave, where a solvothermal reaction was conducted at a temperature of 200 °C for 18 h. Afterward,

the resulting product underwent thorough washing, rinsing, and drying, ultimately serving as the active material, 1T/2H-MoS_2@MXene, for the electrodes. Pure 1T/2H-MoS_2 was synthesized following the same procedure except for the addition of MXene. In addition to 1T/2H-MoS_2@MXene, two additional nanocomposite samples were synthesized, denoted as 1T/2H-MoS_2/MXene2 and 1T/2H-MoS_2/MXene3, with a higher and lower 1T/2H-MoS_2/MXene ratio, respectively. These were synthesized by using the same procedure, with the only modification of MXene dosage (60 mg for the former and 180 mg for the latter).

Materials Characterization

Crystal structures were examined using XRD on a Rigaku SmartLab SE X-ray diffractometer with Cu Kα radiation. XPS measurements were carried out on a Thermo Scientific Theta Probe XPS spectrometer equipped with a monochromatic Al K X-ray source and a spot area of 400 μm. Transmission electron microscopy (TEM) images were captured by using a Thermo Fisher Scientific Spectra Ultra, double-corrected HRTEM/STEM instrument operated at 300 kV. N_2 sorption measurements were performed at 77 K on a Micromeritics ASAP2020 physisorption analyzer to quantify the BET specific surface area, pore volume, and pore size distribution. TGA was performed on a TA instruments Q50 TGA in an N_2 atmosphere. The conductivity of the nanocomposites was evaluated by using the direct current polarization method. For the measurement, dry powders of each sample (thickness of about 0.4 mm and diameter of about 17 mm) were compacted and sandwiched between two circular stainless steel electrodes. Various voltages were applied between the two electrodes with a Metrohm Autolab PGSTAT128N electrochemical workstation and the resulting currents were measured to construct the current-voltage plot.

Electrochemical Measurements

To fabricate the working electrodes, each sample was compounded with PVDF and Super-P conducting carbon at a ratio of 7:2:1 in NMP. Then, the resulting dispersion was deposited on copper foil discs as current collectors and was dried overnight at 60 °C. The electrodes had an active material mass loading of 1 to 1.2 mg cm^{-2}. CR2032 coin cells were fabricated in an argon-filled glove box ($O_2 < 0.1$ ppm and $H_2O < 0.5$ ppm), with a polished magnesium metal disc as the anode, and a Whatman GF/D glass fiber membrane as the separator. For the MIBs, a 0.4 M APC electrolyte was prepared by stirring 1.67 g (8 mmol) of $AlCl_3$ in 12 mL

of anhydrous THF overnight, followed by the addition of 8 mL of 2M PhMgCl and further stirring overnight. The same procedure was followed to prepare the dual-salt electrolyte for MLIBs, with the addition of 0.848 g of LiCl in the final stage. GCD tests were conducted on a battery testing equipment from Land (CT2001A, China). CV and EIS were performed on a Metrohm Autolab PGSTAT128N electrochemical workstation. EIS measurements were carried out in the frequency range of 100 kHz to 0.01 Hz with an oscillatory amplitude of 50 mV.

Chapter 6

Contributions and Significance of Thesis Research, and Suggestions for Future Work

6.1 Contributions and Significance of Thesis Research

This thesis makes several significant contributions to the field of electrochemical energy storage by advancing the understanding and application of MoS_2-based nanocomposite electrodes for post-LIBs. The research addresses critical challenges in the design and performance of MoS_2-based materials for alkali and multivalent ion storage, paving the way for next-generation energy storage technologies. The key contributions are as follows:

Comprehensive Review of MoS_2 Nanocomposite Architectures for Post-LIBs:

The thesis provides an exhaustive review of MoS_2-based materials tailored for post-LIBs, detailing various structural modifications such as interlayer engineering, defect engineering, crystal phase engineering, heteroatom doping, hybridization, and morphology design. This review synthesizes findings from both theoretical and experimental studies, offering valuable insights into the design principles necessary to enhance the electrochemical performance of MoS_2.

Synthesis of Innovative MoS_2-Based Nanocomposites:

This thesis focuses on the design and synthesis of advanced MoS_2-based nanocomposites to address key challenges in energy storage technologies. By employing novel strategies and innovative material combinations, the research highlights the potential of MoS_2 as a versatile electrode material, offering solutions for enhancing conductivity, stability, and ion

transport. These advancements contribute to the development of next-generation energy storage systems, emphasizing the significance of material engineering in achieving superior electrochemical performance.

In this thesis, four types of nanocomposites were synthesized. Chapter 3 introduces the synthesis method for crystalline MoS_2 and amorphous MoS_x embedded in a hierarchically porous carbon matrix. The novelty of the synthesis methods for these two nanocomposites lies in the following aspects: firstly, it is a facile, scalable, and straightforward process; secondly, its parameters can be adjusted to enable the formation of either the amorphous or crystalline phase of molybdenum sulfide; and thirdly, the carbon matrix is derived from a bio-based and abundant source, starch, making the method both cost-effective and environmentally friendly. The synthesized composites exhibit synergistic properties, including high conductivity from the carbon content and optimal porosity, which contribute to their excellent electrochemical performance as anode materials for SIBs.

In Chapter 4, the synthesis of a novel composite of MoS_2 and a hyperbranched polyethylene ionomer using a top-down methodology is described. This innovative hybridization resulted in a composite that addresses several challenges associated with MoS_2 for multivalent ion storage. Specifically, the composite demonstrated excellent performance in MIBs and MLIBs. The incorporation of the hyperbranched polyethylene ionomer is responsible for the enlarged interlayer spaces in the MoS_2 structure, which improves ion diffusion. Additionally, phase engineering of MoS_2 enhances its conductivity, facilitating better charge transfer. These combined modifications effectively address the limitations of MoS_2 as a cathode material for multivalent ion storage. The resulting nanocomposite demonstrates significant potential as a solution to the lack of suitable cathodes for storing multivalent ions, such as Mg^{2+}.

In Chapter 5, the synthesis of a 2D/2D nanocomposite of MoS_2 and $Ti_3C_2T_x$ MXene through a bottom-up synthesis approach is described. This method is facile, scalable, and straightforward, ensuring simplicity and efficiency in the synthesis process. The combination of two highly electrochemically active 2D nanomaterials in this composite results in a synergistic effect, including enhanced conductivity, improved stability, and a unique structure that facilitates efficient ion transport. These features collectively address key challenges in electrode design and contribute to the composite's excellent performance as a cathode material for hybrid MLIBs. The interplay of MoS_2 and MXene in the nanocomposite not only optimizes electrochemical properties but also provides structural integrity, making it a promising candidate for advanced energy storage systems.

New Insights into Amorphous Molybdenum Sulfide (MoS_x) for Na^{2+} Storage:

In this thesis, Chapter 3 presents a detailed investigation comparing the amorphous and crystalline phases of molybdenum disulfide for Na^{2+} storage. Specifically, amorphous MoS_x embedded in a hierarchically porous carbon matrix was compared with crystalline MoS_2 in a similar matrix. Such studies on amorphous materials are relatively rare in recent research, with many of their properties and potential applications yet to be fully explored. This investigation evaluated key parameters, including capacity, stability, and charge transfer resistance, revealing that in certain aspects, the amorphous phase can demonstrate superior electrochemical performance. This research provides valuable insights and paves the way for future studies to unlock the potential of amorphous materials as active components in battery technologies.

Exploring Phase Engineering of MoS_2 for Multivalent Ion Storage:

Phase engineering is a crucial aspect of MoS_2 research, particularly in electrochemical applications, as the electronic properties of MoS_2 are highly dependent on its crystalline phase. These properties can be tuned between semiconducting and electron-conducting states. Theoretically, the 1T metallic phase of MoS_2, with its conductive behavior, is better suited for battery applications. However, understanding how critical phase engineering is, how effective it can be, and whether it remains impactful without other ion-storage-enhancing modifications are significant challenges, particularly for multivalent ion storage, which is inherently more difficult than monovalent ion storage. In this thesis, Chapter 4 presents a detailed study on the 1T phase of MoS_2 synthesized through alkali-ion intercalation and its interlayer-expanded version stabilized by a cationic ionomer. This research examines how phase engineering, both with and without enhancements such as ionomer-assissted modofication, influences the multivalent ion storage capabilities of MoS_2. The findings provide critical insights into the role of the crystalline phase in multivalent ion storage and emphasize the importance of additional modifications to achieve significant performance improvements. Such an investigation into MoS_2 as an active cathode material for multivalent-ion batteries is rare, offering valuable guidance for future research in this domain.

Advancing the Understanding of Hybrid Dual-Salt Batteries:

In Chapters 4 and 5, a recently discovered type of battery, hybrid dual-salt batteries, was studied. These batteries combine the safety and accessibility of multivalent metal anodes with the enhanced storage capabilities of swift monovalent Li^+ storage in the cathode. The findings of this research contribute to advancing the scientific understanding of dual-salt batteries and provide valuable insights to guide future research and development in this

emerging field.

6.2 Suggestions for Future Work

While the research presented in this thesis makes substantial advancements in the field of Post-LIBs, several areas warrant further investigation to continue the development and optimization of MoS_2-based battery materials:

Exploration of Additional Nanocomposites: Future research should focus on the design of MoS_2 nanocomposites in combination with other metal oxides, metal sulfides, TMDs, various carbon-based materials, and transition metal carbides with diverse properties such as different crystal phases and porosity. These efforts could further enhance the electrochemical properties of battery electrodes. Additionally, exploring various combinations of TMDs and conductive matrices may lead to the development of new materials with superior performance characteristics.

In-Depth In-Situ Studies: Conducting detailed studies using advanced characterization techniques such as in-situ XRD and Raman spectroscopy can provide deeper insights into the structural and phase transformations occurring during battery cycling. Gaining an atomic-level understanding of these changes will aid in the design of more robust and efficient electrode materials.

Scalability and Commercialization: Addressing the scalability of the synthesis methods and the potential for commercialization is crucial. Future work should focus on optimizing the production processes to ensure they are cost-effective and scalable for industrial applications. Additionally, collaborations with industry partners could facilitate the translation of lab-scale discoveries to commercial products.

Integration with Advanced Battery Systems: Investigating the integration of MoS_2-based electrodes with other advanced battery systems, such as solid-state batteries and flexible batteries, could open up new applications and improve the overall performance of energy storage devices. Research into the compatibility and performance of MoS_2 electrodes in these systems would be valuable.

Environmental Impact and Sustainability: Assessing the environmental impact and sustainability of the materials and synthesis processes used in the production of MoS_2 nanocomposites is essential. Future studies should aim to develop eco-friendly synthesis methods and evaluate the life cycle of the materials to ensure they contribute to sustainable energy storage solutions.

By addressing these areas, future research can build on the foundations laid by this thesis, further advancing the development of high-performance, sustainable, and efficient energy storage systems based on MoS_2 nanocomposites.

The following section outlines, case by case, how the projects presented in chapters 3 to 5 can be further developed.

Chapter 3: In this chapter, the crystalline MoS_2@HPC sample demonstrated excellent cyclic stability as a sodium battery anode. However, optimizing the ratio of HPC to MoS_2 could further increase capacity while maintaining this stability.

Additionally, the MoS_x@HPC sample exhibited a high capacity for Na^+ storage, but its stability was lower than that of the crystalline form. Future improvements could focus on enhancing the stability of this electrode by optimizing the carbon content or exploring alternative binders.

Furthermore, constructing a sodium ion full-cell battery would allow for evaluating the efficiency of both electrodes in a full-cell battery system, providing insight into their advantages and limitations.

Chapter 4: Modifications of MoS_2 through crystal phase engineering, exfoliation, and ionomer incorporation yielded significant results for Mg^{2+} storage. These composites could be applied in future projects to store other multivalent ions, such as Zn^{2+} and Al^{3+}, with further investigations into their performance. The I@MP-MoS_2 composite, with its favorable interlayer spaces, electrical conductivity, and disordered structure, also shows potential for storing larger alkali ions, such as Na^+ and K^+. Exploring this composite for these applications would be a promising direction for future research.

Since I@MP-MoS_2 exhibits excellent performance as a cathode in dual-salt Mg^{2+}/Li^+ batteries, it can be used in future projects as a cathode for more advanced dual systems that do not contain lithium, such as Mg^{2+}/Na^+ or Mg^{2+}/K^+ batteries.

Chapter 5: The use of 1T/2H-MoS_2@MXene for the development of lithium-free dual-salt batteries is recommended for future research.

Additionally, 1T/2H-MoS_2@MXene exhibits enlarged interlayer spacing, good electrical conductivity, and relatively high hydrophilicity due to the presence of MXene and 1T phases, making it well-suited for aqueous energy storage systems. Therefore, the investigation on its performance as cathode material for aqueous ZIBs and MIBs is suggested for future projects.

References

[1] B. Liu, J.-G. Zhang, W. Xu, Joule **2018**, 2, 833.

[2] J. Qian, W. A. Henderson, W. Xu, P. Bhattacharya, M. Engelhard, O. Borodin, J.-G. Zhang, Nat. Commun. **2015**, 6, 6362.

[3] A. Yaroshevsky, Geochem. Int. **2006**, 44, 48.

[4] M. Li, Z. Du, M. A. Khaleel, I. Belharouak, Energy Storage Mater. **2020**, 25, 520.

[5] C. Yang, S. Xin, L. Mai, Y. You, Adv. Energy Mater. **2021**, 11, 2000974.

[6] X. Yang, A. L. Rogach, Adv. Energy Mater. **2020**, 10, 2000288.

[7] R. Rajagopalan, Y. Tang, X. Ji, C. Jia, H. Wang, Adv. Funct. Mater. **2020**, 30, 1909486.

[8] P. K. Nayak, L. Yang, W. Brehm, P. Adelhelm, Angew. Chem. Int. Ed. **2018**, 57, 102.

[9] K. Kubota, M. Dahbi, T. Hosaka, S. Kumakura, S. Komaba, Chem. Rec. **2018**, 18, 459.

[10] J. Xiao, Science **2019**, 366, 426.

[11] A. Hagopian, M.-L. Doublet, J.-S. Filhol, Energy Environ. Sci. **2020**, 13, 5186.

[12] A. Ponrouch, J. Bitenc, R. Dominko, N. Lindahl, P. Johansson, M. R. Palacín, Energy Storage Mater. **2019**, 20, 253.

[13] X. Zhang, R. Lv, W. Tang, G. Li, A. Wang, A. Dong, X. Liu, J. Luo, Adv. Funct. Mater. **2020**, 30, 2004187.

[14] Y. Liang, H. Dong, D. Aurbach, Y. Yao, Nat. Energy **2020**, 5, 646.

[15] B. T. McAllister, L. T. Kyne, T. B. Schon, D. S. Seferos, Joule **2019**, 3, 620.

[16] Y. Liang, H. D. Yoo, Y. Li, J. Shuai, H. A. Calderon, F. C. Robles Hernandez, L. C. Grabow, Y. Yao, Nano Lett. **2015**, 15, 2194.

[17] L. E. Blanc, D. Kundu, L. F. Nazar, Joule **2020**, 4, 771.

[18] D. Sun, D. Ye, P. Liu, Y. Tang, J. Guo, L. Wang, H. Wang, Adv. Energy Mater. **2018**, 8, 1702383.

[19] W. Ren, H. Zhang, C. Guan, C. Cheng, Adv. Funct. Mater. **2017**, 27, 1702116.

[20] K. Ma, Y. Liu, H. Jiang, Y. Hu, R. Si, H. Liu, C. Li, CCS Chem. **2021**, 3, 1472.

[21] B. Jia, Q. Yu, Y. Zhao, M. Qin, W. Wang, Z. Liu, C.-Y. Lao, Y. Liu, H. Wu, Z. Zhang, X. Qu, Adv. Funct. Mater. **2018**, 28, 1803409.

[22] H. D. Yoo, I. Shterenberg, Y. Gofer, G. Gershinsky, N. Pour, D. Aurbach, Energy Environ. Sci. **2013**, 6, 2265.

[23] Y. Zhang, H. Geng, W. Wei, J. Ma, L. Chen, C. C. Li, Energy Storage Mater. **2019**, 20, 118.

[24] W. Liu, J. Hao, C. Xu, J. Mou, L. Dong, F. Jiang, Z. Kang, J. Wu, B. Jiang, F. Kang, Chem. Comm. **2017**, 53, 6872.

[25] R. D. Shannon, Acta Crystallogr. Sect. A **1976**, 32, 751.

[26] J. Rahmatinejad, B. Raisi, X. Liu, X. Zhang, A. Sadeghi Chevinli, L. Yang, Z. Ye, Small **2024**, 20, 2304878.

[27] N. Zhang, X. Chen, M. Yu, Z. Niu, F. Cheng, J. Chen, Chem. Soc. Rev. **2020**, 49, 4203.

[28] F. Wu, H. Yang, Y. Bai, C. Wu, Adv. Mater. **2019**, 31, 1806510.

[29] T. Leisegang, F. Meutzner, M. Zschornak, W. Münchgesang, R. Schmid, T. Nestler, R. A. Eremin, A. A. Kabanov, V. A. Blatov, D. C. Meyer, Front. Chem. **2019**, 7, 268.

[30] W. Li, H. Yao, K. Yan, G. Zheng, Z. Liang, Y.-M. Chiang, Y. Cui, Nat. Commun. **2015**, 6, 7436.

[31] J. Park, J. Jeong, Y. Lee, M. Oh, M.-H. Ryou, Y. M. Lee, Adv. Mater. Interfaces **2016**, 3, 1600140.

[32] Y. Zhang, S. Liu, Y. Ji, J. Ma, H. Yu, Adv. Mater. **2018**, 30, 1706310.

[33] M. Chhowalla, H. S. Shin, G. Eda, L.-J. Li, K. P. Loh, H. Zhang, Nat. Chem. **2013**, 5, 263.

[34] S. Shi, Z. Sun, Y. H. Hu, J. Mater. Chem. A **2018**, 6, 23932.

[35] Z. Wang, B. Mi, Environ. Sci. Technol. **2017**, 51, 8229.

[36] R. J. Toh, Z. Sofer, J. Luxa, D. Sedmidubskỳ, M. Pumera, Chem. Comm. **2017**, 53, 3054.

[37] A. Splendiani, L. Sun, Y. Zhang, T. Li, J. Kim, C.-Y. Chim, G. Galli, F. Wang, Nano Lett. **2010**, 10, 1271.

[38] G. Gao, Y. Jiao, F. Ma, Y. Jiao, E. Waclawik, A. Du, J. Phys. Chem. C **2015**, 119, 13124.

[39] D. Voiry, A. Mohite, M. Chhowalla, Chem. Soc. Rev. **2015**, 44, 2702.

[40] K. F. Mak, C. Lee, J. Hone, J. Shan, T. F. Heinz, Phys. Rev. Lett. **2010**, 105, 136805.

[41] M. Acerce, D. Voiry, M. Chhowalla, Nat. Nanotechnol. **2015**, 10, 313.

[42] X. Zhang, L. Hou, A. Ciesielski, P. Samorì, Adv. Energy Mater. **2016**, 6, 1600671.

[43] J. N. Coleman, M. Lotya, A. O'Neill, S. D. Bergin, P. J. King, U. Khan, K. Young, A. Gaucher, S. De, R. J. Smith, I. V. Shvets, S. K. Arora, G. Stanton, H.-Y. Kim, K. Lee, G. T. Kim, G. S. Duesberg, T. Hallam, J. J. Boland, J. J. Wang, J. F. Donegan, J. C. Grunlan, G. Moriarty, A. Shmeliov, R. J. Nicholls, J. M. Perkins, E. M. Grieveson, K. Theuwissen, D. W. McComb, P. D. Nellist, V. Nicolosi, Science **2011**, 331, 568.

[44] P. May, U. Khan, J. M. Hughes, J. N. Coleman, J. Phys. Chem. C **2012**, 116, 11393.

[45] R. J. Smith, P. J. King, M. Lotya, C. Wirtz, U. Khan, S. De, A. O'Neill, G. S. Duesberg, J. C. Grunlan, G. Moriarty, J. Chen, J. Wang, A. I. Minett, V. Nicolosi, J. N. Coleman, Adv. Mater. **2011**, 23, 3944.

[46] J. Zheng, H. Zhang, S. Dong, Y. Liu, C. Tai Nai, H. Suk Shin, H. Young Jeong, B. Liu, K. Ping Loh, Nat. Commun. **2014**, 5, 2995.

[47] K. Chang, X. Hai, H. Pang, H. Zhang, L. Shi, G. Liu, H. Liu, G. Zhao, M. Li, J. Ye, Adv. Mater. **2016**, 28, 10033.

[48] J. Feng, X. Sun, C. Wu, L. Peng, C. Lin, S. Hu, J. Yang, Y. Xie, J. Am. Chem. Soc. **2011**, 133, 17832.

[49] Y. Li, H. Wang, L. Xie, Y. Liang, G. Hong, H. Dai, J. Am. Chem. Soc. **2011**, 133, 7296.

[50] C. Nagaraju, C. V. M. Gopi, J.-W. Ahn, H.-J. Kim, New J. Chem. **2018**, 42, 12357.

[51] Y.-H. Lee, X.-Q. Zhang, W. Zhang, M.-T. Chang, C.-T. Lin, K.-D. Chang, Y.-C. Yu, J. T.-W. Wang, C.-S. Chang, L.-J. Li, T.-W. Lin, Adv. Mater. **2012**, 24, 2320.

[52] S. Murugesan, A. Akkineni, B. P. Chou, M. S. Glaz, D. A. Vanden Bout, K. J. Stevenson, ACS Nano **2013**, 7, 8199.

[53] G. Wang, J. Zhang, S. Yang, F. Wang, X. Zhuang, K. Müllen, X. Feng, Adv. Energy Mater. **2018**, 8, 1702254.

[54] K. Xie, K. Yuan, X. Li, W. Lu, C. Shen, C. Liang, R. Vajtai, P. Ajayan, B. Wei, Small **2017**, 13, 1701471.

[55] Y. Dong, Z. Zhu, Y. Hu, G. He, Y. Sun, Q. Cheng, I. P. Parkin, H. Jiang, Nano Res. **2021**, 14, 74.

[56] B. Chen, H. Lu, J. Zhou, C. Ye, C. Shi, N. Zhao, S.-Z. Qiao, Adv. Energy Mater. **2018**, 8, 1702909.

[57] G. Wang, Y. Zhang, H. S. Cho, X. Zhao, F. Kim, J. Zou, ACS Appl. Energy Mater. **2021**, 4, 14180.

[58] S. Sui, H. Xie, B. Chen, T. Wang, Z. Qi, J. Wang, J. Sha, E. Liu, S. Zhu, K. Lei, S. Zheng, G. Zhou, C. He, W. Hu, F. He, N. Zhao, Angew. Chem. Int. Ed. **2024**, page e202411255.

[59] H. Zhang, S. Zhang, B. Guo, L.-j. Yu, L. Ma, B. Hou, H. Liu, S. Zhang, J. Wang, J. Song, Y. Tang, X. Zhao, Angew. Chem. **2024**, 136, e202400285.

[60] L. Zhang, D. Sun, J. Kang, J. Feng, H. A. Bechtel, L.-W. Wang, E. J. Cairns, J. Guo, Nano Lett. **2018**, 18, 1466.

[61] S. Hao, X. Shen, M. Tian, R. Yu, Z. Wang, L. Chen, Nano Energy **2017**, 41, 217.

[62] Z. Hu, L. Wang, K. Zhang, J. Wang, F. Cheng, Z. Tao, J. Chen, Angew. Chem. Int. Ed. **2014**, 53, 12794.

[63] X. Fang, X. Guo, Y. Mao, C. Hua, L. Shen, Y. Hu, Z. Wang, F. Wu, L. Chen, Chem. Asian J. **2012**, 7, 1013.

[64] L. Wang, Q. Zhang, J. Zhu, X. Duan, Z. Xu, Y. Liu, H. Yang, B. Lu, Energy Storage Mater. **2019**, 16, 37.

[65] G. Li, D. Luo, X. Wang, M. H. Seo, S. Hemmati, A. Yu, Z. Chen, Adv. Funct. Mater. **2017**, 27, 1702562.

[66] S. Zhang, X. Yu, H. Yu, Y. Chen, P. Gao, C. Li, C. Zhu, ACS Appl. Mater. Interfaces **2014**, 6, 21880.

[67] J. Wang, C. Luo, T. Gao, A. Langrock, A. C. Mignerey, C. Wang, Small **2015**, 11, 473.

[68] C. Zhu, X. Mu, P. A. van Aken, Y. Yu, J. Maier, Angew. Chem. **2014**, 126, 2184.

[69] C. Zhu, X. Mu, P. A. van Aken, J. Maier, Y. Yu, Adv. Energy Mater. **2015**, 5, 1401170.

[70] R. Wang, S. Wang, Y. Zhang, D. Jin, X. Tao, L. Zhang, Nanoscale **2018**, 10, 11165.

[71] E. Pomerantseva, Y. Gogotsi, Nat. Energy **2017**, 2, 1.

[72] L. David, R. Bhandavat, G. Singh, ACS Nano **2014**, 8, 1759.

[73] X. Xie, Z. Ao, D. Su, J. Zhang, G. Wang, Adv. Funct. Mater. **2015**, 25, 1393.

[74] K. Yao, Z. Xu, M. Ma, J. Li, F. Lu, J. Huang, Adv. Funct. Mater. **2020**, 30, 2001484.

[75] B. Tan, S. Han, W. Luo, Z. Chao, J. Fan, M. Wang, J. Alloys Compd. **2020**, 841, 155732.

[76] S. Zhuo, G. Huang, R. Sougrat, J. Guo, N. Wei, L. Shi, R. Li, H. Liang, Y. Shi, Q. Zhang, P. Wang, H. N. Alshareef, ACS Nano **2022**, 16, 3955.

[77] J. Xu, Q. Liu, Z. Dong, L. Wang, X. Xie, Y. Jiang, Z. Wei, Y. Gao, Y. Zhang, K. Huang, ACS Appl. Mater. Interfaces **2021**, 13, 54974.

[78] J. Rahmatinejad, X. Liu, X. Zhang, B. Raisi, Z. Ye, J. Energy Chem. **2022**, 75, 240.

[79] M. Huang, Y. Mai, L. Zhao, X. Liang, Z. Fang, X. Jie, ChemElectroChem **2020**, 7, 4218.

[80] X. Xie, T. Makaryan, M. Zhao, K. L. Van Aken, Y. Gogotsi, G. Wang, Adv. Energy Mater. **2016**, 6, 1502161.

[81] W. Ren, W. Zhou, H. Zhang, C. Cheng, ACS Appl. Mater. Interfaces **2017**, 9, 487.

[82] J. Wu, Z. Lu, K. Li, J. Cui, S. Yao, M. I.-u. Haq, B. Li, Q.-H. Yang, F. Kang, F. Ciucci, J.-K. Kim, J. Mater. Chem. A **2018**, 6, 5668.

[83] S. Li, Y. Liu, X. Zhao, Q. Shen, W. Zhao, Q. Tan, N. Zhang, P. Li, L. Jiao, X. Qu, Adv. Mater. **2021**, 33, 2007480.

[84] W. Yang, H. Lu, Y. Cao, B. Xu, Y. Deng, W. Cai, ACS Sustain. Chem. Eng. **2019**, 7, 4861.

[85] Q. Deng, F. Chen, S. Liu, A. Bayaguud, Y. Feng, Z. Zhang, Y. Fu, Y. Yu, C. Zhu, Adv. Funct. Mater. **2020**, 30, 1908665.

[86] J. Li, B. Rui, W. Wei, P. Nie, L. Chang, Z. Le, M. Liu, H. Wang, L. Wang, X. Zhang, J. Power Sources **2020**, 449, 227481.

[87] B. Tan, T. Lu, W. Luo, Z. Chao, R. Dong, J. Fan, Energy Fuels **2021**, 35, 12666.

[88] Y. Wu, P. Nie, J. Jiang, B. Ding, H. Dou, X. Zhang, ChemElectroChem **2017**, 4, 1560.

[89] H. Wang, H. Jiang, Y. Hu, N. Li, X. Zhao, C. Li, J. Mater. Chem. A **2017**, 5, 5383.

[90] M. Huang, Y. Mai, L. Zhao, X. Liang, Z. Fang, X. Jie, Electrochim. Acta **2021**, 388, 138624.

[91] G. Wang, X. Bi, H. Yue, R. Jin, Q. Wang, S. Gao, J. Lu, Nano Energy **2019**, 60, 362.

[92] B. Lu, J. Liu, R. Hu, H. Wang, J. Liu, M. Zhu, Energy Storage Mater. **2018**, 14, 118.

[93] X. Geng, Y. Jiao, Y. Han, A. Mukhopadhyay, L. Yang, H. Zhu, Adv. Funct. Mater. **2017**, 27, 1702998.

[94] J. Li, W. Qin, J. Xie, R. Lin, Z. Wang, L. Pan, W. Mai, Chem. Eng. J. **2018**, 332, 260.

[95] D. Sun, D. Huang, H. Wang, G.-L. Xu, X. Zhang, R. Zhang, Y. Tang, D. Abd EI-Hady, W. Alshitari, A. S. AL-Bogami, K. Amine, M. Shao, Nano Energy **2019**, 61, 361.

[96] J. Liu, P. Xu, J. Liang, H. Liu, W. Peng, Y. Li, F. Zhang, X. Fan, Chem. Eng. J. **2020**, 389, 124405.

[97] J. Yang, J. Wang, L. Zhu, X. Wang, X. Dong, W. Zeng, J. Wang, F. Pan, Sustain. Energ. Fuels **2021**, 5, 5471.

[98] N. Panjulingam, S. Lakshmipathi, Ionics **2023**, 29, 4751.

[99] H. Li, Q. Zhang, C. C. R. Yap, B. K. Tay, T. H. T. Edwin, A. Olivier, D. Baillargeat, Adv. Funct. Mater. **2012**, 22, 1385.

[100] X. Fan, P. Xu, D. Zhou, Y. Sun, Y. C. Li, M. A. T. Nguyen, M. Terrones, T. E. Mallouk, Nano Lett. **2015**, 15, 5956.

[101] Y. Fang, J. Pan, J. He, R. Luo, D. Wang, X. Che, K. Bu, W. Zhao, P. Liu, G. Mu, H. Zhang, T. Lin, F. Huang, Angew. Chem. **2018**, 130, 1246.

[102] G. Eda, T. Fujita, H. Yamaguchi, D. Voiry, M. Chen, M. Chhowalla, ACS Nano **2012**, 6, 7311.

[103] Z. Xia, Y. Tao, Z. Pan, X. Shen, Results Phys. **2019**, 12, 2218.

[104] G. Eda, H. Yamaguchi, D. Voiry, T. Fujita, M. Chen, M. Chhowalla, Nano Lett. **2011**, 11, 5111.

[105] Q. Ke, X. Zhang, W. Zang, A. M. Elshahawy, Y. Hu, Q. He, S. J. Pennycook, Y. Cai, J. Wang, Small **2019**, 15, 1900131.

[106] Q. Liu, X. Li, Q. He, A. Khalil, D. Liu, T. Xiang, X. Wu, L. Song, Small **2015**, 11, 5556.

[107] J. Wu, J. Liu, J. Cui, S. Yao, M. Ihsan-Ul-Haq, N. Mubarak, E. Quattrocchi, F. Ciucci, J.-K. Kim, J. Mater. Chem. A **2020**, 8, 2114.

[108] F. Niu, Z. Bai, J. Chen, Q. Gu, X. Wang, J. Wei, Y. Mao, S. X. Dou, N. Wang, ACS Nano **2024**, 18, 6487.

[109] Y. Zhang, J. Wang, L. Shan, B. Han, Q. Gao, Z. Cai, C. Zhou, X. Tian, R. Sun, L. Mai, Adv. Energy Mater. **2024**, 14, 2303464.

[110] C. Wu, G. Zhao, X. Yu, C. Liu, P. Lyu, G. Maurin, S. Le, K. Sun, N. Zhang, Chem. Eng. J. **2021**, 412, 128736.

[111] J. Shuai, H. D. Yoo, Y. Liang, Y. Li, Y. Yao, L. C. Grabow, Mater. Res. Express **2016**, 3, 064001.

[112] H. Liang, Z. Cao, F. Ming, W. Zhang, D. H. Anjum, Y. Cui, L. Cavallo, H. N. Alshareef, Nano Lett. **2019**, 19, 3199.

[113] Y. Li, Y. Liang, F. C. R. Hernandez, H. D. Yoo, Q. An, Y. Yao, Nano Energy **2015**, 15, 453.

[114] C. Wu, G. Zhao, S. Gong, N. Zhang, K. Sun, J. Mater. Chem. A **2019**, 7, 4426.

[115] Y. Liu, L.-Z. Fan, L. Jiao, J. Power Sources **2017**, 340, 104.

[116] C. Wu, L. Zhang, G. Zhao, X. Yu, C. Liu, J. He, K. Sun, N. Zhang, ChemElectroChem **2021**, 8, 4559.

[117] F. Li, H. Ma, H. Sheng, Z. Wang, Y. Qi, D. Wan, M. Shao, J. Yuan, W. Li, K. Wang, E. Xie, W. Lan, Small **2024**, 20, 2306276.

[118] Z. Yao, W. Zhang, X. Ren, Y. Yin, Y. Zhao, Z. Ren, Y. Sun, Q. Lei, J. Wang, L. Wang, T. Ji, P. Huai, W. Wen, X. Li, D. Zhu, R. Tai, ACS Nano **2022**, 16, 12095.

[119] M. A. R. Anjum, H. Y. Jeong, M. H. Lee, H. S. Shin, J. S. Lee, Adv. Mater. **2018**, 30, 1707105.

[120] P. Tao, J. He, T. Shen, Y. Hao, J. Yan, Z. Huang, X. Xu, M. Li, Y. Chen, Adv. Mater. Interfaces **2019**, 6, 1900460.

[121] H.-P. Komsa, A. V. Krasheninnikov, Phys. Rev. B **2015**, 91, 125304.

[122] J.-Y. Noh, H. Kim, Y.-S. Kim, Phys. Rev. B **2014**, 89, 205417.

[123] G. Barik, S. Pal, J. Phys. Chem. C **2019**, 123, 21852.

[124] W. Xu, C. Sun, K. Zhao, X. Cheng, S. Rawal, Y. Xu, Y. Wang, Energy Storage Mater. **2019**, 16, 527.

[125] Y. Li, R. Zhang, W. Zhou, X. Wu, H. Zhang, J. Zhang, ACS Nano **2019**, 13, 5533.

[126] Z. Yang, L. Zhu, C. Lv, R. Zhang, H. Wang, J. Wang, Q. Zhang, Mater. Chem. Front. **2021**, 5, 5880.

[127] Y. Xu, F. Bahmani, M. Zhou, Y. Li, C. Zhang, F. Liang, S. H. Kazemi, U. Kaiser, G. Meng, Y. Lei, Nanoscale Horiz. **2019**, 4, 202.

[128] K. Yao, Z. Xu, J. Huang, M. Ma, L. Fu, X. Shen, J. Li, M. Fu, Small **2019**, 15, 1805405.

[129] S. Li, Y. Liu, X. Zhao, K. Cui, Q. Shen, P. Li, X. Qu, L. Jiao, Angew. Chem. **2021**, 133, 20448.

[130] Z. Li, X. Mu, Z. Zhao-Karger, T. Diemant, R. J. Behm, C. Kübel, M. Fichtner, Nat. Commun. **2018**, 9, 5115.

[131] P. S. Toth, M. Velickỳ, M. A. Bissett, T. J. Slater, N. Savjani, A. K. Rabiu, A. M. Rakowski, J. R. Brent, S. J. Haigh, P. O'Brien, R. A. W. Dryfe, Adv. Mater. **2016**, 28, 8256.

[132] S. Liu, Y. Yin, M. Wu, K. S. Hui, K. N. Hui, C.-Y. Ouyang, S. C. Jun, Small **2019**, 15, 1803984.

[133] H. Li, N. L. Okamoto, T. Hatakeyama, Y. Kumagai, F. Oba, T. Ichitsubo, Adv. Energy Mater. **2018**, 8, 1801475.

[134] H. Li, T. Ichitsubo, S. Yagi, E. Matsubara, J. Mater. Chem. A **2017**, 5, 3534.

[135] X. Yu, G. Zhao, H. Huang, C. Liu, P. Lyu, N. Zhang, Chem. Eng. J. **2022**, 428, 131214.

[136] Q. Pan, Q. Zhang, F. Zheng, Y. Liu, Y. Li, X. Ou, X. Xiong, C. Yang, M. Liu, ACS Nano **2018**, 12, 12578.

[137] S. H. Choi, Y. N. Ko, J.-K. Lee, Y. C. Kang, Adv. Funct. Mater. **2015**, 25, 1780.

[138] X. Hu, Y. Li, G. Zeng, J. Jia, H. Zhan, Z. Wen, ACS Nano **2018**, 12, 1592.

[139] W. Zhan, M. Zhu, J. Lan, H. Yuan, H. Wang, X. Yang, G. Sui, ACS Appl. Mater. Interfaces **2020**, 12, 51488.

[140] B. Chen, T. Wang, S. Zhao, J. Tan, N. Zhao, S. P. Jiang, Q. Zhang, G. Zhou, H.-M. Cheng, Adv. Mater. **2021**, 33, 2007090.

[141] G. Zhou, S. Zhao, T. Wang, S.-Z. Yang, B. Johannessen, H. Chen, C. Liu, Y. Ye, Y. Wu, Y. Peng, C. Liu, S. P. Jiang, Q. Zhang, Y. Cui, Nano Lett. **2019**, 20, 1252.

[142] B.-W. Zhang, T. Sheng, Y.-D. Liu, Y.-X. Wang, L. Zhang, W.-H. Lai, L. Wang, J. Yang, Q.-F. Gu, S.-L. Chou, H.-K. Liu, S.-X. Dou, Nat. Commun. **2018**, 9, 4082.

[143] H. Xie, B. Chen, C. Liu, G. Wu, S. Sui, E. Liu, G. Zhou, C. He, W. Hu, N. Zhao, Energy Storage Mater. **2023**, 60, 102830.

[144] H. Zhang, Y. Wang, S. Guo, Y. Hui, H. Wei, J. Song, X. Zhao, Batteries Supercaps **2023**, 6, e202200482.

[145] T. Yang, Y. Chen, B. Qu, L. Mei, D. Lei, H. Zhang, Q. Li, T. Wang, Electrochim. Acta **2014**, 115, 165.

[146] X. Wu, X. Xie, H. Zhang, K.-J. Huang, J. Colloid Interface Sci. **2021**, 595, 43.

[147] W. Ye, F. Wu, N. Shi, H. Zhou, Q. Chi, W. Chen, S. Du, P. Gao, H. Li, S. Xiong, Small **2020**, 16, 1906607.

[148] S. Wang, F. Cao, Y. Li, Z. Zhang, D. Zhou, Y. Yang, Z. Tang, Adv. Sci. **2019**, 6, 1900028.

[149] H. Wang, T. Yao, C. Li, L. Meng, Y. Cheng, Chem. Eng. J. **2020**, 397, 125385.

[150] N. Shi, B. Xi, M. Huang, X. Ma, H. Li, J. Feng, S. Xiong, Small **2020**, 16, 2000952.

[151] Y. Fang, D. Luan, Y. Chen, S. Gao, X. W. Lou, Angew. Chem. **2020**, 132, 7245.

[152] X. Lin, J. Liu, H. Zhang, Y. Zhong, M. Zhu, T. Zhou, X. Qiao, H. Zhang, T. Han, J. Li, Adv. Sci. **2021**, 8, 2002298.

[153] H. Zhu, F. Zhang, J. Li, Y. Tang, Small **2018**, 14, 1703951.

[154] J. Hu, Y. Xie, X. Zhou, Z. Zhang, ACS Appl. Mater. Interfaces **2019**, 12, 1232.

[155] L. Han, S. Wu, Z. Hu, M. Chen, J. Ding, S. Wang, Y. Zhang, D. Guo, L. Zhang, S. Cao, S. Chou, ACS Appl. Mater. Interfaces **2020**, 12, 10402.

[156] Q. Sun, H. Wu, H. Ming, L. Sun, L. Zhou, C. Wang, X. Wang, L. Wang, J. Ming, J. Mater. Chem. A **2019**, 7, 5677.

[157] J. Qi, Q. Li, M. Huang, J. Ni, Y. Sui, Q. Meng, F. Wei, L. Zhu, W. Wei, Colloids Surf. A: Physicochem. Eng. Asp. **2024**, 683, 132998.

[158] F. Liu, L. Li, S. Xu, J. Guo, Y. Ling, Y. Zhang, W. Gong, L. Wei, C. Wang, Q. Zhang, Q. Li, Energy Storage Mater. **2023**, 55, 1.

[159] J. Kang, Y. Peng, L. Zhu, Y. Tang, F. Teng, G. Guo, Y. Xiang, Y. Huang, X. Wu, X. Wu, Small **2024**, 20, 2309112.

[160] P. Zhang, X. Wang, Y. Yang, H. Yang, C. Lu, M. Su, Y. Zhou, A. Dou, X. Li, X. Hou, Y. Liu, J. Colloid Interface Sci. **2024**, 655, 383.

[161] L. Zeng, F. Luo, X. Xia, M.-Q. Yang, L. Xu, J. Wang, X. Feng, Q. Qian, M. Wei, Q. Chen, Chem. Comm. **2019**, 55, 3614.

[162] P. Li, Y. Yang, S. Gong, F. Lv, W. Wang, Y. Li, M. Luo, Y. Xing, Q. Wang, S. Guo, Nano Res. **2019**, 12, 2218.

[163] Z. Sheng, P. Qi, Y. Lu, G. Liu, M. Chen, X. Gan, Y. Qin, K. Hao, Y. Tang, ACS Appl. Mater. Interfaces **2021**, 13, 34495.

[164] Q. Liu, X. Weijun, Z. Wu, J. Huo, D. Liu, Q. Wang, S. Wang, Nanotechnology **2016**, 27, 175402.

[165] W. Yang, L. Mou, B. Xiao, J. Chen, D. Wang, S. Peng, J. Huang, ACS Appl. Mater. Interfaces **2023**, 15, 51231.

[166] Y. Wang, Q. Qu, G. Li, T. Gao, F. Qian, J. Shao, W. Liu, Q. Shi, H. Zheng, Small **2016**, 12, 6033.

[167] Z. Li, M. Han, Y. Zhang, F. Yuan, Y. Fu, J. Yu, Adv. Sci. **2023**, 10, 2207234.

[168] S. Zhou, S. Liu, W. Chen, Y. Cheng, J. Fan, L. Zhao, X. Xiao, Y.-H. Chen, C.-X. Luo, M.-S. Wang, T. Mei, X. Wang, H.-G. Liao, Y. Zhou, L. Huang, S.-G. Sun, ACS Nano **2021**, 15, 13814.

[169] C. Zhao, C. Yu, B. Qiu, S. Zhou, M. Zhang, H. Huang, B. Wang, J. Zhao, X. Sun, J. Qiu, Adv. Mater. **2018**, 30, 1702486.

[170] Z. Chen, D. Yin, M. Zhang, Small **2018**, 14, 1703818.

[171] Z. Yuan, L. Wang, D. Li, J. Cao, W. Han, ACS Nano **2021**, 15, 7439.

[172] H. Lim, S. Yu, W. Choi, S.-O. Kim, ACS Nano **2021**, 15, 7409.

[173] C. Zhang, F. Han, F. Wang, Q. Liu, D. Zhou, F. Zhang, S. Xu, C. Fan, X. Li, J. Liu, Energy Storage Mater. **2020**, 24, 208.

[174] S. Di, P. Ding, Y. Wang, Y. Wu, J. Deng, L. Jia, Y. Li, Nano Res. **2020**, 13, 225.

[175] W. Ding, L. Hu, J. Dai, X. Tang, R. Wei, Z. Sheng, C. Liang, D. Shao, W. Song, Q. Liu, M. Chen, X. Zhu, S. Chou, X. Zhu, Q. Chen, Y. Sun, S. X. Dou, ACS Nano **2019**, 13, 1694.

[176] Y. Zhang, Z. Mu, C. Yang, Z. Xu, S. Zhang, X. Zhang, Y. Li, J. Lai, Z. Sun, Y. Yang, Y. Chao, C. Li, X. Ge, W. Yang, S. Guo, Adv. Funct. Mater. **2018**, 28, 1707578.

[177] J. K. Kim, S.-K. Park, J.-S. Park, Y. C. Kang, J. Mater. Chem. A **2019**, 7, 2636.

[178] L. Cao, X. Liang, X. Ou, X. Yang, Y. Li, C. Yang, Z. Lin, M. Liu, Adv. Funct. Mater. **2020**, 30, 1910732.

[179] Y. Wang, W. Kang, D. Cao, M. Zhang, Z. Kang, Z. Xiao, R. Wang, D. Sun, J. Mater. Chem. A **2018**, 6, 4776.

[180] T. Han, Z. He, W. Kuang, J. Zhou, Y.-y. Li, Nano Energy **2024**, 128, 109953.

[181] Y. Zhou, M. Zhang, Q. Han, Y. Liu, Y. Wang, X. Sun, X. Zhang, C. Dong, F. Jiang, Chem. Eng. J. **2022**, 428, 131113.

[182] J. Zhan, K. Wu, X. Yu, M. Yang, X. Cao, B. Lei, D. Pan, H. Jiang, M. Wu, Small **2019**, 15, 1901083.

[183] H. Wu, Z. Xiong, Y. Mao, H. Zhang, Y. Hu, J. Shen, B. Wang, X. Yu, J. Mater. Sci. Technol. **2023**, 143, 43.

[184] Y. Tang, G. Li, S. Cui, W. Cui, H. Chong, L. Han, H. Pang, Adv. Funct. Mater. **2024**, page 2403351.

[185] L. Yu, X. Tao, D. Sun, L. Zhang, C. Wei, L. Han, Z. Sun, Q. Zhao, H. Jin, G. Zhu, Adv. Funct. Mater. **2024**, page 2311471.

[186] Y. Wu, W. Zhong, Q. Yang, C. Hao, Q. Li, M. Xu, S.-j. Bao, Chem. Eng. J. **2022**, 427, 130960.

[187] X. Zhang, H. Shi, L. Liu, C. Min, S. Liang, Z. Xu, Y. Xue, C. Hong, Z. Cai, J. Colloid Interface Sci. **2022**, 605, 472.

[188] K. Ma, Y. Dong, H. Jiang, Y. Hu, P. Saha, C. Li, Chem. Eng. J. **2021**, 413, 127479.

[189] H. Huang, J. Cui, G. Liu, R. Bi, L. Zhang, ACS Nano **2019**, 13, 3448.

[190] R. Attias, M. Salama, B. Hirsch, Y. Goffer, D. Aurbach, Joule **2019**, 3, 27.

[191] M. Rashad, M. Asif, Y. Wang, Z. He, I. Ahmed, Energy Storage Mater. **2020**, 25, 342.

[192] Y. Shen, Y. Wang, Y. Miao, M. Yang, X. Zhao, X. Shen, Adv. Mater. **2020**, 32, 1905524.

[193] J. Liu, Y. Zhong, X. Li, T. Ying, T. Han, J. Li, Nanoscale Adv. **2021**, 3, 5576.

[194] M. Xu, N. Bai, H.-X. Li, C. Hu, J. Qi, X.-B. Yan, Chinese Chem. Lett. **2018**, 29, 1313.

[195] L. Huang, Z. Ye, R. Berry, ACS Sustain. Chem. Eng. **2016**, 4, 4937.

[196] Z. Dong, P. Xiang, L. Huang, Z. Ye, RSC Adv. **2016**, 6, 43574.

[197] O. Mizrahi, N. Amir, E. Pollak, O. Chusid, V. Marks, H. Gottlieb, L. Larush, E. Zinigrad, D. Aurbach, J. Electrochem. Soc. **2007**, 155, A103.

[198] Y. Zhang, W. Sun, Z.-Z. Luo, Y. Zheng, Z. Yu, D. Zhang, J. Yang, H. T. Tan, J. Zhu, X. Wang, Q. Yan, S. X. Dou, Nano Energy **2017**, 40, 576.

[199] H. Yu, D. Chen, T. Zhang, M. Fu, J. Cai, W. Wei, X. Ji, Y. Chen, L. Chen, Small Struct. **2022**, 3, 2200143.

[200] W. S. V. Lee, T. Xiong, X. Wang, J. Xue, Small Methods **2021**, 5, 2000815.

[201] J. Xu, Z. Dong, K. Huang, L. Wang, Z. Wei, L. Yu, X. Wu, Scr. Mater. **2022**, 209, 114368.

[202] C. Li, C. Liu, Y. Wang, Y. Lu, L. Zhu, T. Sun, Energy Storage Mater. **2022**, 49, 144.

[203] H. Liu, J.-G. Wang, W. Hua, Z. You, Z. Hou, J. Yang, C. Wei, F. Kang, Energy Storage Mater. **2021**, 35, 731.

[204] J. Liu, N. Gong, W. Peng, Y. Li, F. Zhang, X. Fan, Chem. Eng. J. **2022**, 428, 130981.

[205] H. Zhai, H. Liu, Y. Zhang, J. Wen, W. Yang, H. Xu, X. Yan, W. Peng, J. Liu, J. Mater. Sci. Technol. **2024**.

[206] F. Niu, Y. Mao, N. Wang, Z. Feng, J. Chen, L. Ye, S. Zhang, Z. Bai, S. Dou, J. Colloid Interface Sci. **2024**, 655, 760.

[207] C. W. Kang, J. Park, G. H. Kim, K. C. Ko, S. U. Son, ACS Appl. Mater. Interfaces **2023**, 15, 7887.

[208] Y. Gogotsi, B. Anasori, ACS Nano **2019**, 13, 8491.

[209] B. Zhang, R. Kang, W. Zhou, Y. Du, H. Wang, J. Wan, J. Zhang, ACS Appl. Energy Mater. **2023**, 6, 3366.

[210] Z. Li, B. Niu, J. Liu, J. Li, F. Kang, ACS Appl. Mater. Interfaces **2018**, 10, 9451.

[211] S. Guo, H. Yang, M. Liu, X. Feng, H. Xu, Y. Bai, C. Wu, ACS Appl. Energy Mater. **2021**, 4, 7064.

[212] J. Tu, X. Xiao, M. Wang, S. Jiao, J. Phys. Chem. C **2019**, 123, 26794.

[213] X. Yu, G. Zhao, C. Liu, C. Wu, H. Huang, J. He, N. Zhang, Adv. Funct. Mater. **2021**, 31, 2103214.

[214] P. Wang, X. Yan, Energy Storage Mater. **2022**, 45, 142.

[215] S. Li, C. Huang, L. Gao, Q. Shen, P. Li, X. Qu, L. Jiao, Y. Liu, Angew. Chem. Int. Ed. **2022**, 61, e202211478.

[216] X. Yu, G. Zhao, C. Liu, H. Huang, X. Shen, N. Zhang, J. Mater. Chem. A **2021**, 9, 11545.

[217] C.-J. Hsu, C.-Y. Chou, C.-H. Yang, T.-C. Lee, J.-K. Chang, Chem. Comm. **2016**, 52, 1701.

[218] X. Fan, R. R. Gaddam, N. A. Kumar, X. S. Zhao, Adv. Energy Mater. **2017**, 7, 1700317.

[219] Y.-H. Tan, F. Zhou, Z.-H. Huang, W.-T. Yao, T.-W. Zhang, H.-B. Yao, L.-L. Lu, S.-H. Yu, ChemElectroChem **2018**, 5, 996.

[220] X. Hou, H. Shi, T. Chang, K. Hou, L. Feng, G. Suo, X. Ye, L. Zhang, Y. Yang, W. A. Wang, Chem. Eng. J. **2021**, 409, 128271.

[221] J. Rahmatinejad, X. Liu, B. Raisi, Z. Ye, Small **2024**, 20, 2401391.

[222] Q. Shu, X. Hou, K. Hou, X. Ye, Q. Cao, D. Li, G. Suo, J. Alloys Compd. **2023**, 966, 171584.

[223] Z. Xiong, G. Zhu, H. Wu, G. Shi, P. Xu, H. Yi, Y. Mao, B. Wang, X. Yu, ACS Appl. Energy Mater. **2022**, 5, 6274.

[224] M. J. Park, H. Yaghoobnejad Asl, A. Manthiram, ACS Energy Lett. **2020**, 5, 2367.

[225] H. Y. Asl, S. Sharma, A. Manthiram, J. Mater. Chem. A **2020**, 8, 8262.

[226] M. J. Park, A. Manthiram, ACS Appl. Energy Mater. **2020**, 3, 5015.

[227] J. M. Lee, G. Singh, W. Cha, S. Kim, J. Yi, S.-J. Hwang, A. Vinu, ACS Energy Lett. **2020**, 5, 1939.

[228] T. Perveen, M. Siddiq, N. Shahzad, R. Ihsan, A. Ahmad, M. I. Shahzad, Renew. Sustain. Energy Rev. **2020**, 119, 109549.

[229] Y. Shi, Y. Wang, J. I. Wong, A. Y. S. Tan, C.-L. Hsu, L.-J. Li, Y.-C. Lu, H. Y. Yang, Scientific reports **2013**, 3, 1.

[230] H. Ye, L. Ma, Y. Zhou, L. Wang, N. Han, F. Zhao, J. Deng, T. Wu, Y. Li, J. Lu, PNAS **2017**, 114, 13091.

[231] H. Ye, L. Wang, S. Deng, X. Zeng, K. Nie, P. N. Duchesne, B. Wang, S. Liu, J. Zhou, F. Zhao, N. Han, P. Zhang, J. Zhong, X. Sun, Y. Li, Y. Li, J. Lu, Adv. Energy Mater. **2017**, 7, 1601602.

[232] U. Chang, J. T. Lee, J.-M. Yun, B. Lee, S. W. Lee, H.-I. Joh, K. Eom, T. F. Fuller, ACS Nano **2018**, 13, 1490.

[233] J. Yu, J. Xiao, A. Li, Z. Yang, L. Zeng, Q. Zhang, Y. Zhu, L. Guo, Angew. Chem. Int. Ed. **2020**, 59, 13071.

[234] H. Chen, G. Ke, X. Wu, W. Li, Y. Li, H. Mi, L. Sun, Q. Zhang, C. He, X. Ren, Chem. Eng. J. **2021**, 406, 126775.

[235] G. Shirota, A. Nasu, M. Deguchi, A. Sakuda, M. Tatsumisago, A. Hayashi, J. Power Sources Adv. **2021**, 10, 100061.

[236] M. Huang, B. Xi, L. Mi, Z. Zhang, W. Chen, J. Feng, S. Xiong, Small **2022**, 18, 2107819.

[237] G. Shirota, A. Nasu, M. Deguchi, A. Sakuda, M. Tatsumisago, A. Hayashi, Solid State Ion. **2022**, 376, 115848.

[238] J. H. Ku, J. H. Ryu, S. H. Kim, O. H. Han, S. M. Oh, Adv. Funct. Mater. **2012**, 22, 3658.

[239] Y. Liu, Y. Xu, X. Han, C. Pellegrinelli, Y. Zhu, H. Zhu, J. Wan, A. C. Chung, O. Vaaland, C. Wang, L. Hu, Nano Lett. **2012**, 12, 5664.

[240] M. Ma, S. Zhang, L. Wang, Y. Yao, R. Shao, L. Shen, L. Yu, J. Dai, Y. Jiang, X. Cheng, Y. Wu, X. Wu, X. Yao, Q. Zhang, Y. Yu, Adv. Mater. **2021**, 33, 2106232.

[241] Y. Zhou, Y. Li, Q. Wang, Q. Wang, R. Du, M. Zhang, X. Sun, X. Zhang, L. Kang, F. Jiang, ChemElectroChem **2019**, 6, 3113.

[242] Y.-L. Ding, P. Kopold, K. Hahn, P. A. van Aken, J. Maier, Y. Yu, Adv. Mater. **2016**, 28, 7774.

[243] T. S. Sahu, Q. Li, J. Wu, V. P. Dravid, S. Mitra, J. Mater. Chem. A **2017**, 5, 355.

[244] Z. Deng, H. Jiang, C. Li, Small **2018**, 14, 1800148.

[245] S.-K. Park, J. Lee, S. Bong, B. Jang, K.-d. Seong, Y. Piao, ACS Appl. Mater. Interfaces **2016**, 8, 19456.

[246] X. Wu, L. Jiang, C. Long, Z. Fan, Nano Energy **2015**, 13, 527.

[247] B. Li, L. Jiang, X. Li, Z. Cheng, P. Ran, P. Zuo, L. Qu, J. Zhang, Y. Lu, Adv. Funct. Mater. **2019**, 29, 1806229.

[248] L. R. L. Ting, Y. Deng, L. Ma, Y.-J. Zhang, A. A. Peterson, B. S. Yeo, ACS Catal. **2016**, 6, 861.

[249] Y. Deng, L. R. L. Ting, P. H. L. Neo, Y.-J. Zhang, A. A. Peterson, B. S. Yeo, ACS Catal. **2016**, 6, 7790.

[250] T. Weber, J. Muijsers, J. Niemantsverdriet, J. Phys. Chem. **1995**, 99, 9194.

[251] Z. Ye, J. Yang, B. Li, L. Shi, H. Ji, L. Song, H. Xu, Small **2017**, 13, 1700111.

[252] Z. Wan, J. Shao, J. Yun, H. Zheng, T. Gao, M. Shen, Q. Qu, H. Zheng, Small **2014**, 10, 4975.

[253] Z.-T. Shi, W. Kang, J. Xu, Y.-W. Sun, M. Jiang, T.-W. Ng, H.-T. Xue, Y. Denis, W. Zhang, C.-S. Lee, Nano Energy **2016**, 22, 27.

[254] T.-H. Kim, J. Shin, K.-S. Lee, E. Cho, ACS Appl. Mater. Interfaces **2020**, 12, 22721.

[255] J. Zhang, Z. Meng, D. Yang, K. Song, L. Mi, Y. Zhai, X. Guan, W. Chen, J. Energy Chem. **2022**, 68, 27.

[256] Y. Wan, K. Song, W. Chen, C. Qin, X. Zhang, J. Zhang, H. Dai, Z. Hu, P. Yan, C. Liu, S. Sun, S.-L. Chou, C. Shen, Angew. Chem. **2021**, 133, 11582.

[257] X. Xu, R. Zhao, W. Ai, B. Chen, H. Du, L. Wu, H. Zhang, W. Huang, T. Yu, Adv. Mater. **2018**, 30, 1800658.

[258] H.-S. Kim, J. B. Cook, H. Lin, J. S. Ko, S. H. Tolbert, V. Ozolins, B. Dunn, Nat. Mater **2017**, 16, 454.

[259] J. Wang, J. Polleux, J. Lim, B. Dunn, J. Phys. Chem. C **2007**, 111, 14925.

[260] K. Ma, H. Jiang, Y. Hu, C. Li, Adv. Funct. Mater. **2018**, 28, 1804306.

[261] J. Zhang, J. Gai, K. Song, W. Chen, Cell Rep. Phys. Sci. **2022**, page 100868.

[262] H. Li, Q. Yang, F. Mo, G. Liang, Z. Liu, Z. Tang, L. Ma, J. Liu, Z. Shi, C. Zhi, Energy Storage Mater. **2019**, 19, 94.

[263] K. Wu, X. Cao, M. Li, B. Lei, J. Zhan, M. Wu, Small **2020**, 16, 2004178.

[264] F. Long, Q. Zhang, J. Shi, L. Wen, Y. Wu, Z. Ren, Z. Liu, Y. Hou, K. Mao, K. Niu, N. Liu, Z. Zhang, L. Li, J. Su, F. Long, Y. Gao, Chem. Eng. J. **2022**, 455, 140539.

[265] P. Xiang, Z. Ye, Macromolecules **2015**, 48, 6096.

[266] Q. Tang, D.-e. Jiang, Chem. Mater. **2015**, 27, 3743.

[267] D. Voiry, M. Salehi, R. Silva, T. Fujita, M. Chen, T. Asefa, V. B. Shenoy, G. Eda, M. Chhowalla, Nano Lett. **2013**, 13, 6222.

[268] W. Divigalpitiya, R. Frindt, S. R. Morrison, Science **1989**, 246, 369.

[269] L. Xu, Z. Ye, Q. Cui, Z. Gu, Macromol. Chem. Phys. **2009**, 210, 2194.

[270] L. Xu, Z. Ye, S. Siemann, Z. Gu, Polymer **2014**, 55, 3120.

[271] D. M. Sim, H. J. Han, S. Yim, M.-J. Choi, J. Jeon, Y. S. Jung, ACS Omega **2017**, 2, 4678.

[272] B. Vedhanarayanan, J. Shi, J.-Y. Lin, S. Yun, T.-W. Lin, Chem. Eng. J. **2021**, 403, 126318.

[273] A. Ejigu, I. A. Kinloch, E. Prestat, R. A. Dryfe, J. Mater. Chem. A **2017**, 5, 11316.

[274] T. P. Nguyen, W. Sohn, J. H. Oh, H. W. Jang, S. Y. Kim, J. Phys. Chem. C **2016**, 120, 10078.

[275] J. Kim, S. Park, S. Hwang, W.-S. Yoon, J. Electrochem. Sci. Technol. **2022**, 13, 19.

[276] Y. Cui, W. Liu, W. Feng, Y. Zhang, Y. Du, S. Liu, H. Wang, M. Chen, J. Zhou, Adv. Funct. Mater. **2020**, 30, 1908755.

[277] S. Ding, X. Dai, Z. Li, C. Wang, A. Meng, L. Wang, G. Li, J. Huang, S. Li, Energy Storage Mater. **2022**, 47, 211.

[278] Y. Liang, R. Feng, S. Yang, H. Ma, J. Liang, J. Chen, Adv. Mater. **2011**, 23, 640.

[279] B. Li, Z. Li, H. Chen, X. Zhang, S. Wu, H. Xu, Y. Yao, Y. Li, X. Li, Z. Hu, R. M. Laine, J. Zou, K. Zhang, Mater. Today Energy **2022**, 27, 101047.

[280] J.-J. Fan, S.-Y. Shen, Y. Chen, L.-N. Wu, J. Peng, X.-X. Peng, C.-G. Shi, L. Huang, W.-F. Lin, S.-G. Sun, Electrochem. Commun. **2018**, 90, 16.

[281] T. Gao, F. Han, Y. Zhu, L. Suo, C. Luo, K. Xu, C. Wang, Adv. Energy Mater. **2015**, 5, 1401507.

[282] Y. Meng, D. Wang, Y. Wei, K. Zhu, Y. Zhao, X. Bian, F. Du, B. Liu, Y. Gao, G. Chen, J. Power Sources **2017**, 346, 134.

[283] A. Byeon, M.-Q. Zhao, C. E. Ren, J. Halim, S. Kota, P. Urbankowski, B. Anasori, M. W. Barsoum, Y. Gogotsi, ACS Appl. Mater. Interfaces **2017**, 9, 4296.

[284] F. Liu, Y. Liu, X. Zhao, K. Liu, H. Yin, L.-Z. Fan, Small **2020**, 16, 1906076.

[285] Y. Cheng, Y. Shao, J.-G. Zhang, V. L. Sprenkle, J. Liu, G. Li, Chem. Comm. **2014**, 50, 9644.

[286] M. M. Huie, D. C. Bock, E. S. Takeuchi, A. C. Marschilok, K. J. Takeuchi, Coord. Chem. Rev. **2015**, 287, 15.

[287] T. Zhang, Y. Tang, S. Guo, X. Cao, A. Pan, G. Fang, J. Zhou, S. Liang, Energy Environ. Sci. **2020**, 13, 4625.

[288] J. Wang, H. Jia, Z. Liu, J. Yu, L. Cheng, H.-G. Wang, F. Cui, G. Zhu, Adv. Mater. **2024**, 36, 2305605.

[289] L. Cheng, J. Yu, L. Chen, J. Chu, J. Wang, H.-G. Wang, D. Feng, F. Cui, G. Zhu, Small **2023**, 19, 2301578.

[290] M. Xu, S. Lei, J. Qi, Q. Dou, L. Liu, Y. Lu, Q. Huang, S. Shi, X. Yan, ACS Nano **2018**, 12, 3733.

[291] M.-Q. Zhao, C. E. Ren, M. Alhabeb, B. Anasori, M. W. Barsoum, Y. Gogotsi, ACS Appl. Energy Mater. **2019**, 2, 1572.

[292] X. Li, Y. Tang, L. Liu, Y. Zhang, R. Sheng, Y. NuLi, J. Colloid Interface Sci. **2022**, 608, 2455.

[293] T. Wang, K. Yao, Y. Hua, E. G. Shankar, R. Shanthappa, J. S. Yu, J. Chem. Eng. **2023**, 457, 141363.

[294] F. Long, Q. Zhang, J. Shi, L. Wen, Y. Wu, Z. Ren, Z. Liu, Y. Hou, K. Mao, K. Niu, N. Liu, Z. Zhang, L. Li, J. Su, F. Long, Y. Gao, Chem. Eng. J. **2023**, 455, 140539.

[295] M. Alhabeb, K. Maleski, B. Anasori, P. Lelyukh, L. Clark, S. Sin, Y. Gogotsi, Chem. Mater. **2017**, 29, 7633.

[296] X. Sang, Y. Xie, M.-W. Lin, M. Alhabeb, K. L. Van Aken, Y. Gogotsi, P. R. Kent, K. Xiao, R. R. Unocic, ACS Nano **2016**, 10, 9193.

[297] A. Lipatov, M. Alhabeb, M. R. Lukatskaya, A. Boson, Y. Gogotsi, A. Sinitskii, Adv. Electron. Mater. **2016**, 2, 1600255.

[298] M. Ghidiu, M. R. Lukatskaya, M.-Q. Zhao, Y. Gogotsi, M. W. Barsoum, Nature **2014**, 516, 78.

[299] C. Chen, X. Xie, B. Anasori, A. Sarycheva, T. Makaryan, M. Zhao, P. Urbankowski, L. Miao, J. Jiang, Y. Gogotsi, Angew. Chem. Int. Ed. **2018**, 57, 1846.

[300] Z. Li, L. Wang, D. Sun, Y. Zhang, B. Liu, Q. Hu, A. Zhou, Mater. Sci. Eng. B. **2015**, 191, 33.

[301] H. Liu, D. Su, R. Zhou, B. Sun, G. Wang, S. Z. Qiao, Adv. Energy Mater. **2012**, 2, 970.

[302] M. Naguib, M. Kurtoglu, V. Presser, J. Lu, J. Niu, M. Heon, L. Hultman, Y. Gogotsi, M. W. Barsoum, Adv. mater. **2011**, 23, 4248.

[303] L. Wang, X. Zhang, Y. Xu, C. Li, W. Liu, S. Yi, K. Wang, X. Sun, Z.-S. Wu, Y. Ma, Adv. Funct. Mater. **2021**, 31, 2104286.

[304] Y. Guo, D. Sun, B. Ouyang, A. Raja, J. Song, T. F. Heinz, L. E. Brus, Nano Lett. **2015**, 15, 5081.

[305] F. Wang, M. Zheng, B. Zhang, C. Zhu, Q. Li, L. Ma, W. Shen, Sci. Rep. **2016**, 6, 31092.

[306] S. Venkateshwaran, S. M. Senthil Kumar, ACS Sustain. Chem. Eng. **2022**, 10, 5258.

[307] M. Chandran, A. Thomas, A. Raveendran, M. Vinoba, M. Bhagiyalakshmi, J. Energy Storage **2020**, 30, 101446.

[308] K. She, Y. Huang, W. Fan, M. Yu, J. Zhang, C. Chen, J. Colloid Interface Sci. **2024**, 656, 270.

[309] Z. Yang, F. Wang, Z. Hu, J. Chu, H. Zhan, X. Ai, Z. Song, Adv. Energy Mater. **2021**, 11, 2102962.

[310] B. Raisi, X. Liu, J. Rahmatinejad, Z. Ye, Small Methods **2024**, page 2400004.

[311] H. D. Yoo, Y. Liang, Y. Li, Y. Yao, ACS Appl. Mater. Interfaces. **2015**, 7, 7001.

[312] J. Chu, Z. Liu, J. Yu, L. Cheng, H.-G. Wang, F. Cui, G. Zhu, Angew. Chem. **2024**, 136, e202314411.

[313] H. Zhang, X. Xin, H. Liu, H. Huang, N. Chen, Y. Xie, W. Deng, C. Guo, W. Yang, J. Phys. Chem. C **2019**, 123, 2792.

[314] X. Du, J. Huang, X. Guo, X. Lin, J.-Q. Huang, H. Tan, Y. Zhu, B. Zhang, Chem. Mater. **2019**, 31, 8801.

[315] X. Du, X. Guo, J. Huang, Z. Lu, H. Tan, J.-Q. Huang, Y. Zhu, B. Zhang, Nanoscale Horiz. **2020**, 5, 1618.

Appendix A

Supplementary Information

for

Embedding Amorphous MoS_x Within Hierarchical Porous Carbon by Facile One-Pot Synthesis for Superior Sodium Ion Storage

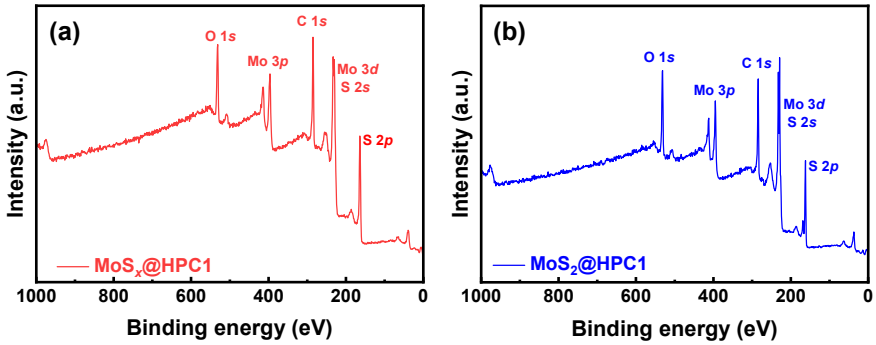

Figure 3.S1: XPS survey spectra of (a) MoS_x@HPC1 and (b) MoS_2@HPC1.

Table 3.S1: The peak positions of Mo $3d$ spectra of MoS_x@HPC1 and MoS_2@HPC1.

Sample	Peak positio (eV)			
	Mo^{4+} $3d_{5/2}$	Mo^{4+} $3d_{3/2}$	Mo^{6+} $3d_{5/2}$	Mo^{6+} $3d_{3/2}$
MoS_x@HPC1	229.5	232.8	232.4	235.6
MoS_2@HPC1	229.0	232.4	232.3	235.7

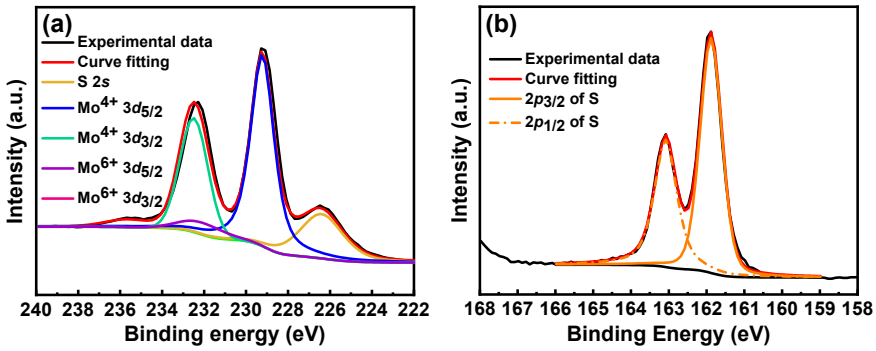

Figure 3.S2: XPS spectra of (a) Mo $3d$ and (b) S $2p$ regions of pure MoS_2.

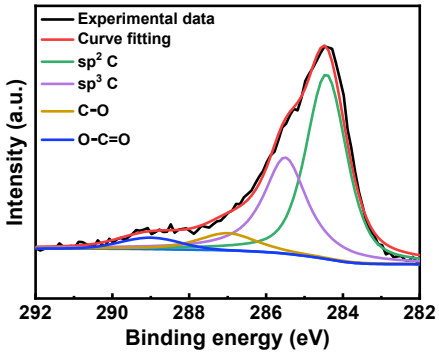

Figure 3.S3: XPS spectra of C 1s region for MoS_x@HPC1.

Equation 3.S1 has been used to calculate the carbon content of the samples:

$$Carbon(\%) = 100 - remainingmass(\%)\frac{M_{MoS_x}}{M_{MoO_3}} \tag{3.S1}$$

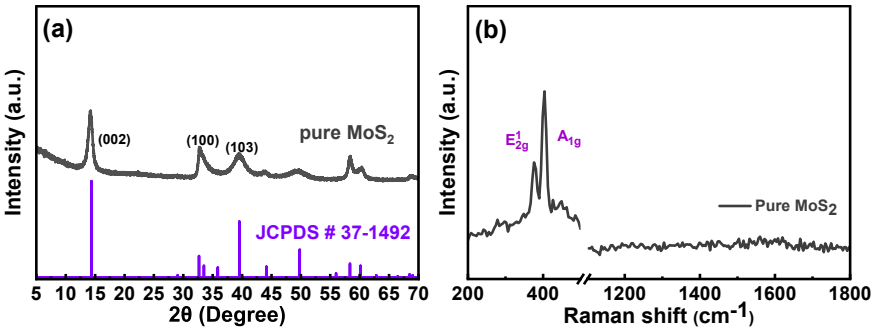

Figure 3.S4: (a) XRD and (b) Raman Spectra of pure MoS_2@HPC1.

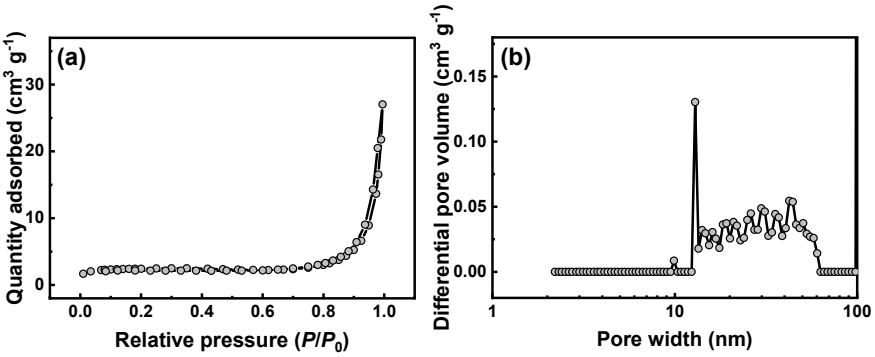

Figure 3.S5: N_2 adsorption/desorption isotherms (a) and pore size distribution (b) of pure MoS_2.

Table 3.S2: BET surface area, pore volume, and average pore width of MoS_x@HPC1, MoS_2@HPC1, and pure MoS_2.

Sample	Surface Area (m^2 g^{-1})			Pore Volume (cm^3 g^{-1})			Average pore width (Å)
	S_{BET}	$S_{d<2}$ nm	$S_{d>2}$ nm	V_{Total}	$V_{d<2}$ nm	$V_{d>2}$ nm	
MoS_x@HPC1	518.4	157.1	361.3	0.55	0.08	0.47	42.63
MoS_2@HPC1	622.4	160.0	462.4	0.64	0.09	0.55	41.19
pure MoS_2	7.5	4.8	2.7	0.04	≈0.00	≈0.04	222.27

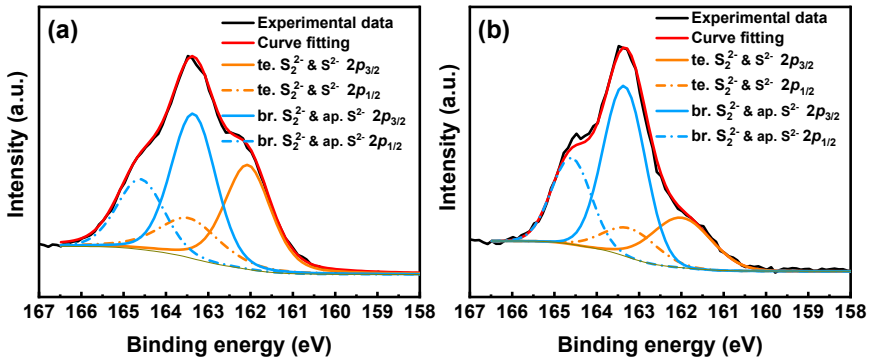

Figure 3.S6: XPS spectra of S $2p$ regions for (a) MoS_x@HPC2 and (b) MoS_x@HPC3.

Table 3.S3: S/Mo ratio and $S_{bridging-apical}$ content of MoS_x@HPC1, MoS_x@HPC2, and MoS_x@HPC3.

Sample	S/Mo (Atomic ratio)	$S_{bridging-apical}$ (%)
MoS_x@HPC1	2.90	63%
MoS_x@HPC2	2.76	53%
MoS_x@HPC3	3.58	71%

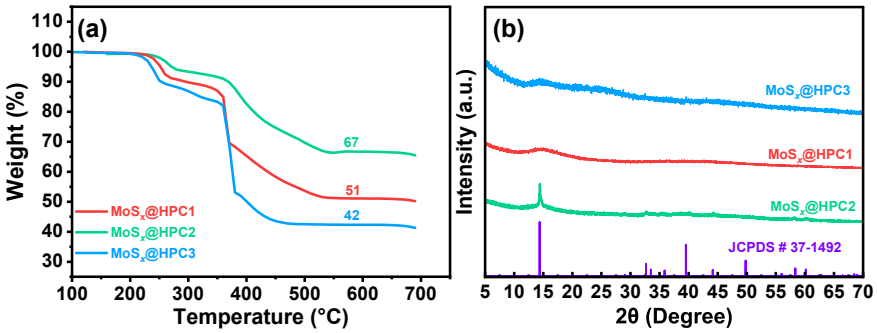

Figure 3.S7: (a) TGA curves and (b) XRD spectra of MoS_x@HPC1, MoS_x@HPC2, and MoS_x@HPC3.

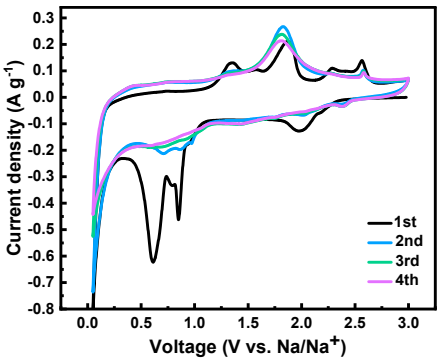

Figure 3.S8: CV curves at 0.2 mV s^{-1} for a half cell with pure MoS_2 as the cathode vs. sodium metal foil anode.

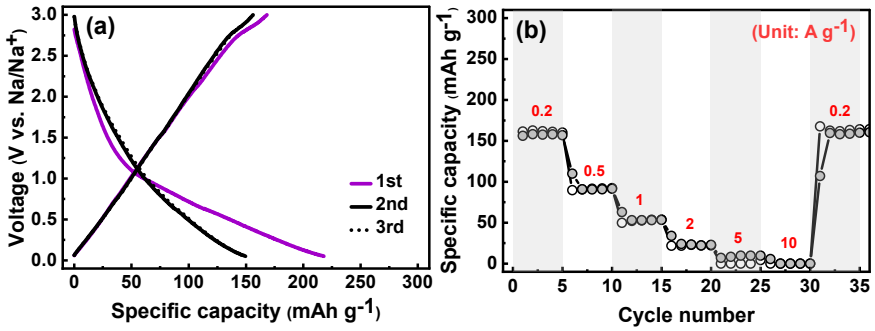

Figure 3.S9: Electrochemical performance of a half cell assembled with porous carbon cathode and Na metal anode: (a) GCD profiles at 0.2 A g^{-1} and (b) rate performance of a half cell with porous carbon as the cathode vs. sodium metal foil anode.

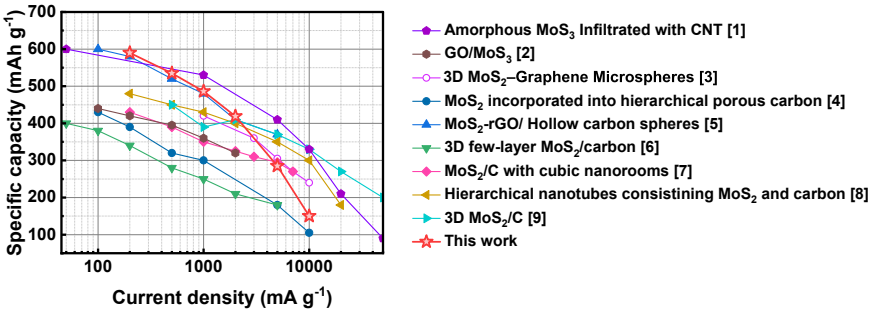

Figure 3.S10: Comparison of rate performance of various a-MoS_x and MoS_2 nanocomposites as anode material for SIBs.

Table 3.S4: The component values in the fitting circuit of Nyquist plots of MoS_x@HPC1, MoS_2@HPC1, and pure MoS_2.

Sample	MoS_x@HPC1	MoS_2@HPC1	pure MoS_2
$R_b\Omega$	14.00	12.89	15.32
CPE1-T	1×10^{-5}	1×10^{-5}	1×10^{-5}
CPE1-P	1.00	1.00	1.00
$R_s\Omega$	2.00	2.19	0.51
CPE2-T	1.3×10^{-3}	2.7×10^{-4}	2.7×10^{-4}
CPE2-P	5.8×10^{-1}	7.8×10^{-1}	6.8×10^{-1}
$R_{ct}\Omega$	60.0	63.9	148.0
W-R	3×10^{-3}	2.9×10^{-3}	9×10^{-3}
W-T	2.75×10^{-6}	2.1×10^{-8}	2.25×10^{-9}
W-P	3.75×10^{-1}	2.85×10^{-1}	2.32×10^{-1}

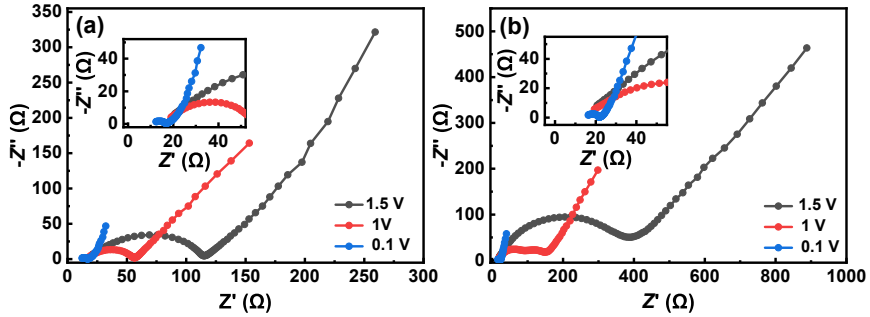

Figure 3.S11: Nyquist plots of (a) MoS_x@HPC1 and (b) MoS_2@HPC1 at different voltages.

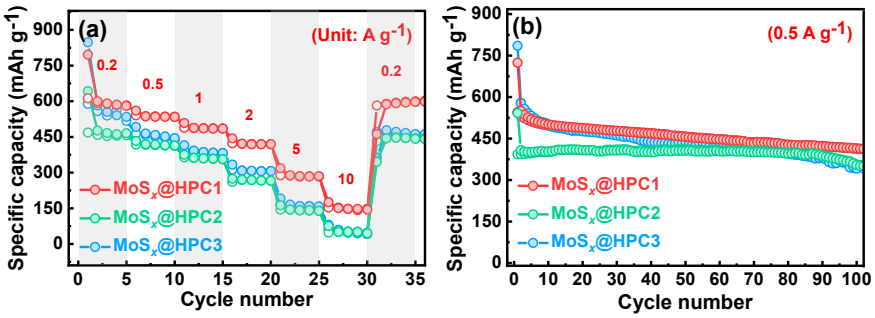

Figure 3.S12: Electrochemical performance of a half cell assembled with MoS_x@HPC1, MoS_x@HPC2, and MoS_x@HPC3 cathodes and Na metal anode: (a) The rate capability and (b) cyclic stability at 0.5 A g^{-1}.

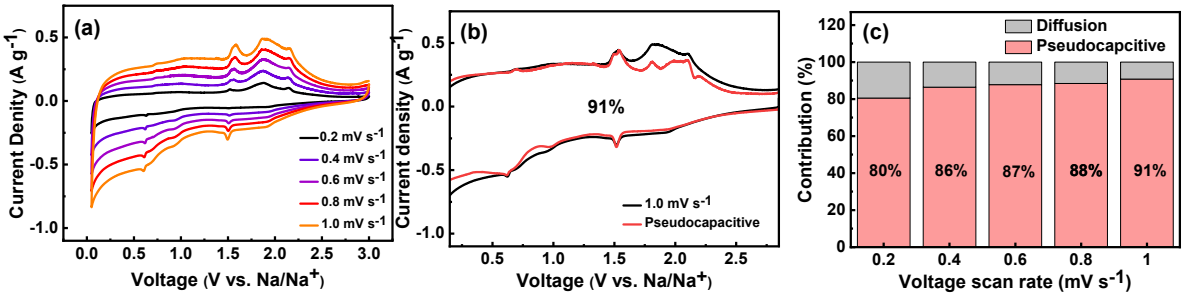

Figure 3.S13: Electrochemical performance of a half cell assembled with MoS_2@HPC1 cathode and Na metal anode: (a) CV curves with different voltage scan rates, (b) the pseudocapacitive contribution to the current response at a voltage scan rate of 1 mV s^{-1}, and (c) comparison of capacitive and diffusion-controlled contributions to the current at different scan rate.

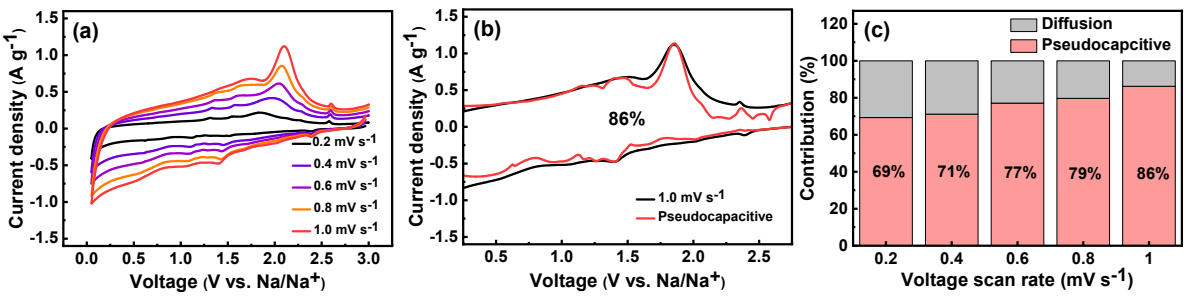

Figure 3.S14: Electrochemical performance of a half cell assembled with pure MoS_2 cathode and Na metal anode: (a) CV curves with different voltage scan rates, (b) the pseudocapacitive contribution to the current response at a voltage scan rate of 1 mV s^{-1}, and (c) comparison of capacitive and diffusion-controlled contributions to the current at different scan rates.

References for Figure 3.S10

[1] H. Ye, L. Wang, S. Deng, X. Zeng, K. Nie, P.N. Duchesne, B. Wang, S. Liu, J. Zhou, F. Zhao, Amorphous MoS_3 infiltrated with carbon nanotubes as an advanced anode material of sodium-ion batteries with large gravimetric, areal, and volumetric capacities, Adv. Energy Mater. 7 (2017) 1601602.

[2] Y. Zhou, Y. Li, Q. Wang, Q. Wang, R. Du, M. Zhang, X. Sun, X. Zhang, L. Kang, F. Jiang, Ultrasmall MoS_3 loaded GO nanocomposites as high-rate and long-cycle-life anode materials for lithium-and sodium-ion batteries, ChemElectroChem 6 (2019) 3113-3119.

[3] S.H. Choi, Y.N. Ko, J.K. Lee, Y.C. Kang, 3D MoS_2–graphene microspheres consisting of multiple nanospheres with superior sodium ion storage properties, Adv. Funct. Mater. 25 (2015) 1780-1788.

[4] S.-K. Park, J. Lee, S. Bong, B. Jang, K.-d. Seong, Y. Piao, Scalable synthesis of few-layer MoS_2 incorporated into hierarchical porous carbon nanosheets for high-performance Li-and Na-ion battery anodes, ACS Appl. Mater. Interfaces 8 (2016) 19456-19465.

[5] X. Hu, Y. Li, G. Zeng, J. Jia, H. Zhan, Z. Wen, Three-dimensional network architecture with hybrid nanocarbon composites supporting few-layer MoS_2 for lithium and sodium storage, Acs Nano 12 (2018) 1592-1602.

[6] Z.-H. Zhao, X.-D. Hu, H. Wang, M.-Y. Ye, Z.-Y. Sang, H.-M. Ji, X.-L. Li, Y. Dai, Superelastic 3D few-layer MoS_2/carbon framework heterogeneous electrodes for highly reversible sodium-ion batteries, Nano Energy 48 (2018) 526-535.

[7] J.K. Kim, S.-K. Park, J.-S. Park, Y.C. Kang, Uniquely structured composite microspheres of metal sulfides and carbon with cubic nanorooms for highly efficient anode materials for sodium-ion batteries, J. Mater. Chem. A 7 (2019) 2636-2645.

[8] Z.-T. Shi, W. Kang, J. Xu, Y.-W. Sun, M. Jiang, T.-W. Ng, H.-T. Xue, Y. Denis, W. Zhang, C.-S. Lee, Hierarchical nanotubes assembled from MoS_2-carbon monolayer sandwiched superstructure nanosheets for high-performance sodium ion batteries, Nano Energy 22 (2016) 27-37.

[9] H. Wang, T. Yao, C. Li, L. Meng, Y. Cheng, Constructing three-dimensional ordered porous MoS_2/C hierarchies for excellent high-rate long-life pseudocapacitive sodium storage, Chem. Eng. J. 397 (2020) 125385.

Appendix B

Supplementary Information

for

1T-2H Mixed-Phase MoS_2 Stabilized with a Hyperbranched Polyethylene Ionomer for Mg^{2+}/Li^{+} Co-Intercalation Toward High-Capacity Dual-Salt Batteries

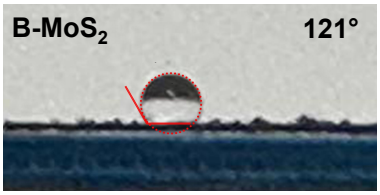

Figure 4.S1: Water contact angle on film of B-MoS_2.

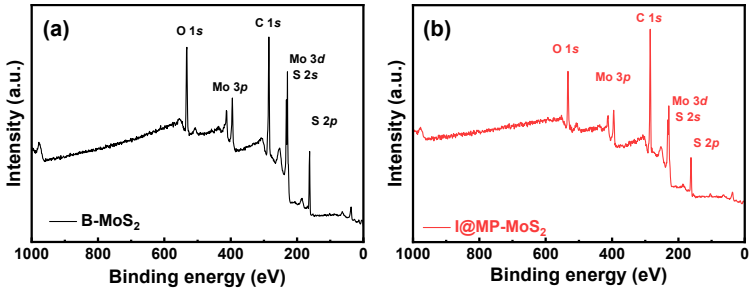

Figure 4.S2: XPS survey spectra of (a) B-MoS_2 and (b) I@MP-MoS_2.

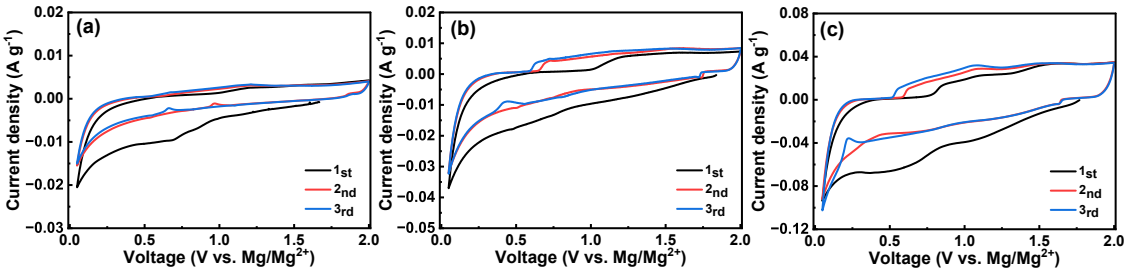

Figure 4.S3: CV curves of MIBs with (a) B-MoS_2, (b) MP-MoS_2, and (c) I@MP-MoS_2 cathodes at 0.2 mV s^{-1}.

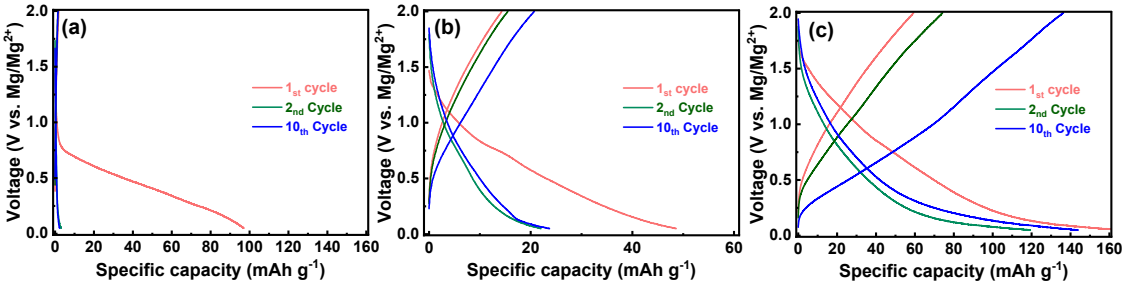

Figure 4.S4: GCD curves of MIBs with (a) B-MoS_2, (b) MP-MoS_2, and (c) I@MP-MoS_2 cathodes at 20 mA g^{-1}.

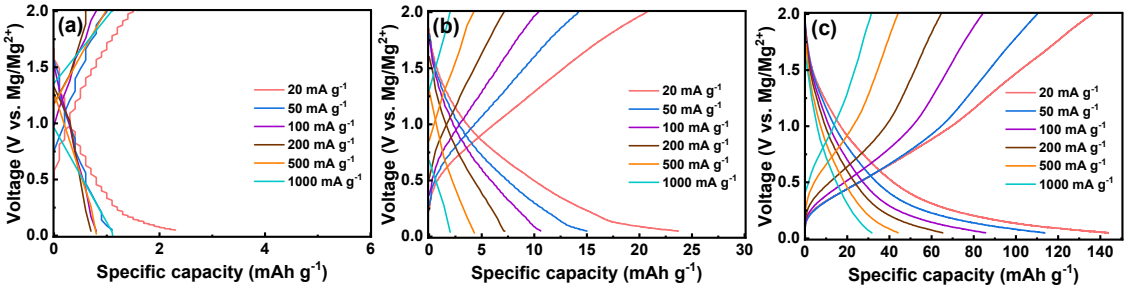

Figure 4.S5: GCD curves of MIBs with (a) B-MoS_2, (b) MP-MoS_2, and (c) I@MP-MoS_2 cathodes at different current densities.

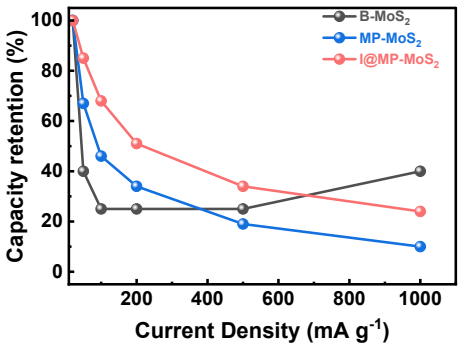

Figure 4.S6: Capacity retention of MIBs with B-MoS_2, MP-MoS_2, and I@MP-MoS_2 cathodes at different current densities.

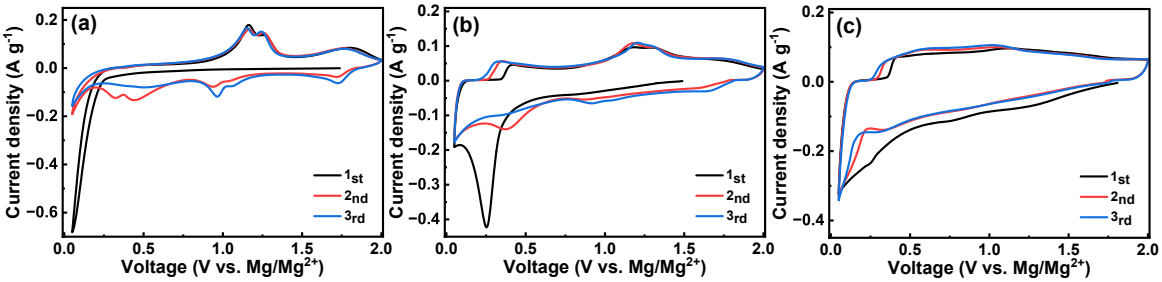

Figure 4.S7: CV curves of MLIBs with (a) B-MoS_2, (b) MP-MoS_2, and (c) I@MP-MoS_2 cathodes at 0.2 mV s^{-1}.

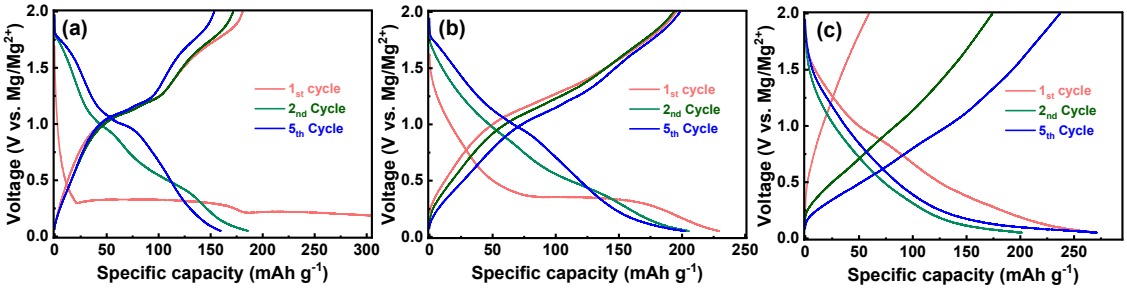

Figure 4.S8: GCD curves of MLIBs with (a) B-MoS_2, (b) MP-MoS_2, and (c) I@MP-MoS_2 cathodes at 20 mA g^{-1}.

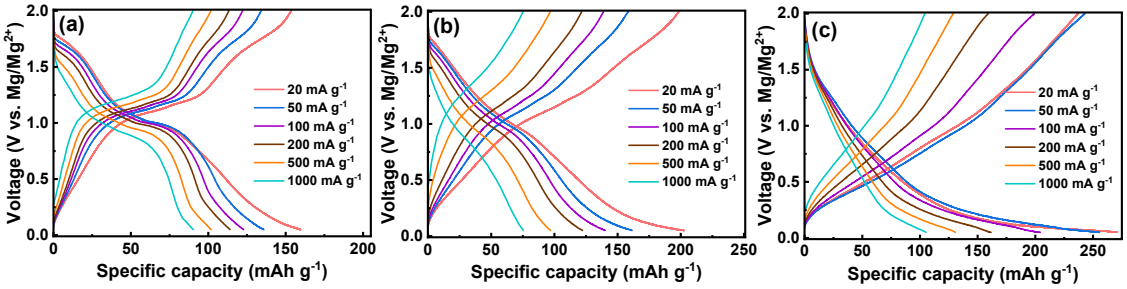

Figure 4.S9: GCD curves of MIBs with (a) B-MoS_2, (b) MP-MoS_2, and (c) I@MP-MoS_2 cathodes at different current densities.

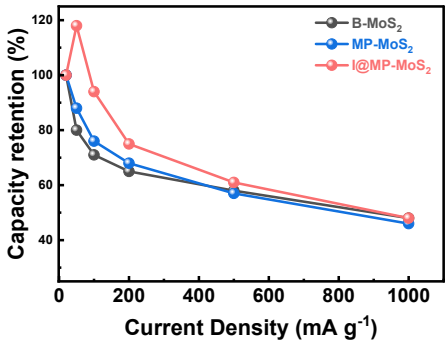

Figure 4.S10: Capacity retention of MLIBs with B-MoS_2, MP-MoS_2, and I@MP-MoS_2 cathodes at different current densities.

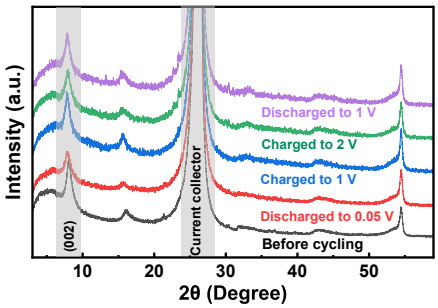

Figure 4.S11: Ex-situ XRD results of I@MP-MoS_2 electrode before cycling and at various voltage states during a discharge/charge cycle at 20 mA g^{-1}.

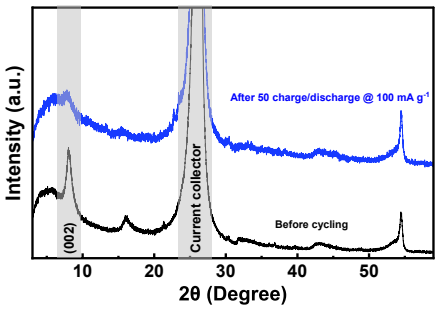

Figure 4.S12: Ex-situ XRD results of I@MP-MoS_2 electrode before cycling and after 50 charge/discharge cycles at 100 mA g^{-1}.

Appendix C

Supplementary Information

for

Synergistic Cathode Design for High-Performance Dual-Salt Magnesium/Lithium-Ion Batteries Using 2D/2D 1T/2H-MoS_2@$Ti_3C_2T_x$ MXene Nanocomposite

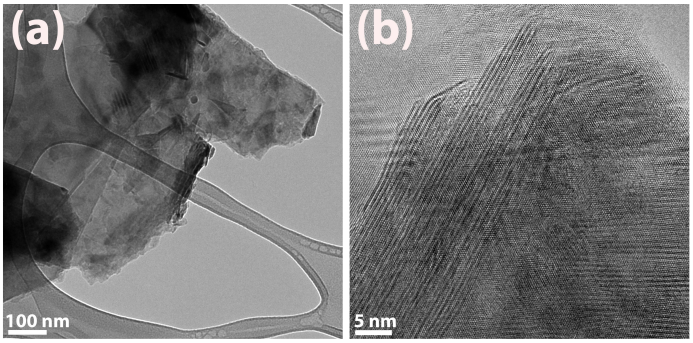

Figure 5.S1: (a)TEM and (b) HRTEM image of commercial bulk 2H-MoS_2.

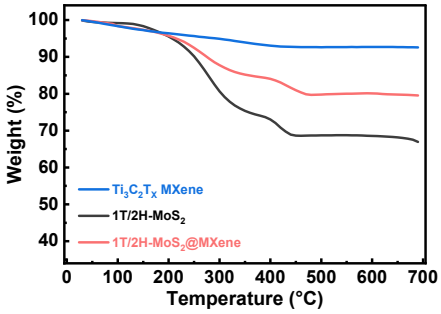

Figure 5.S2: TGA curves of $Ti_3C_2T_x$ MXene, 1T/2H-MoS_2, and 1T/2H-MoS_2@MXene in a N_2 atmosphere.

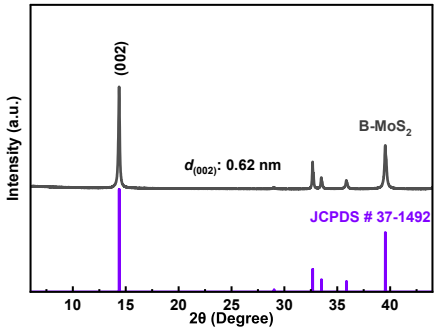

Figure 5.S3: XRD spectra of commercially available bulk MoS_2 and #37-1492 JCPDS reference pattern for 2H-MoS_2.

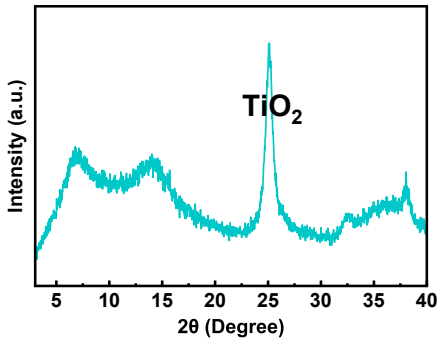

Figure 5.S4: XRD spectrum of hydrothermally synthesized 1T/2H-MoS_2@MXene.

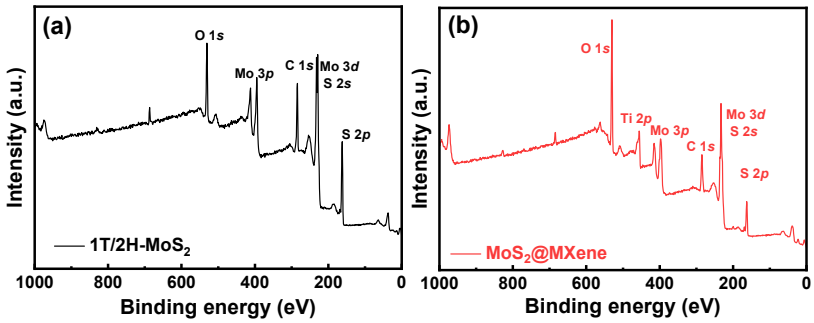

Figure 5.S5: XPS survey spectra of (a) 1T/2H-MoS_2 and (b) MoS_2@MXene.

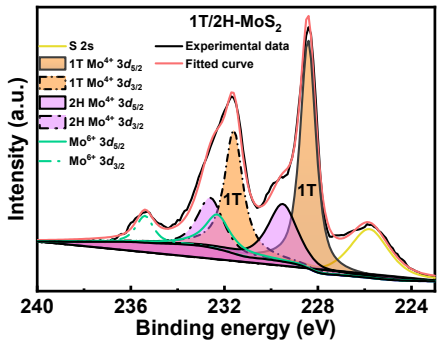

Figure 5.S6: Mo 3d XPS spectra of 1T/2H-MoS_2.

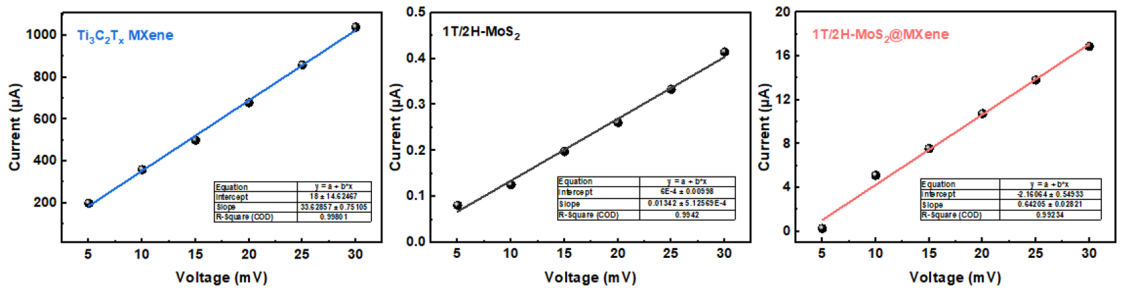

Figure 5.S7: Electronic conductivity measurements of $Ti_3C_2T_x$ MXene, 1T/2H-MoS_2, and 1T/2H-MoS_2@MXene by a direct current method.

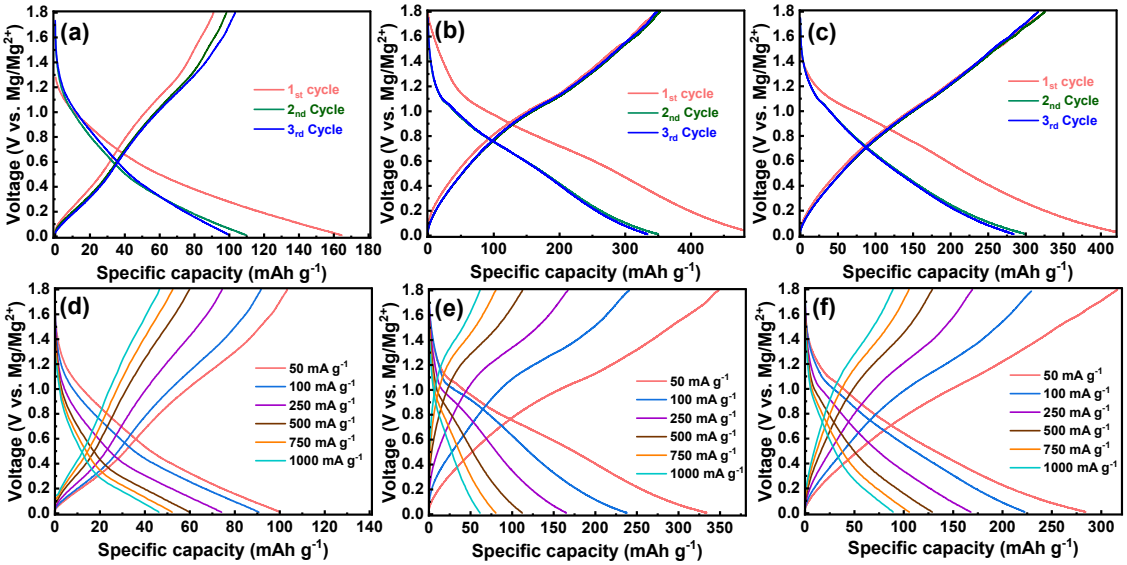

Figure 5.S8: The GCD curves in the first three cycles at 50 mA g^{-1} and GCD curves at different current densities of MLIBs with (a,d) $Ti_3C_2T_x$ MXene, (b,e) 1T/2H-MoS_2, and (c,f) 1T/2H-MoS_2@MXene cathodes.

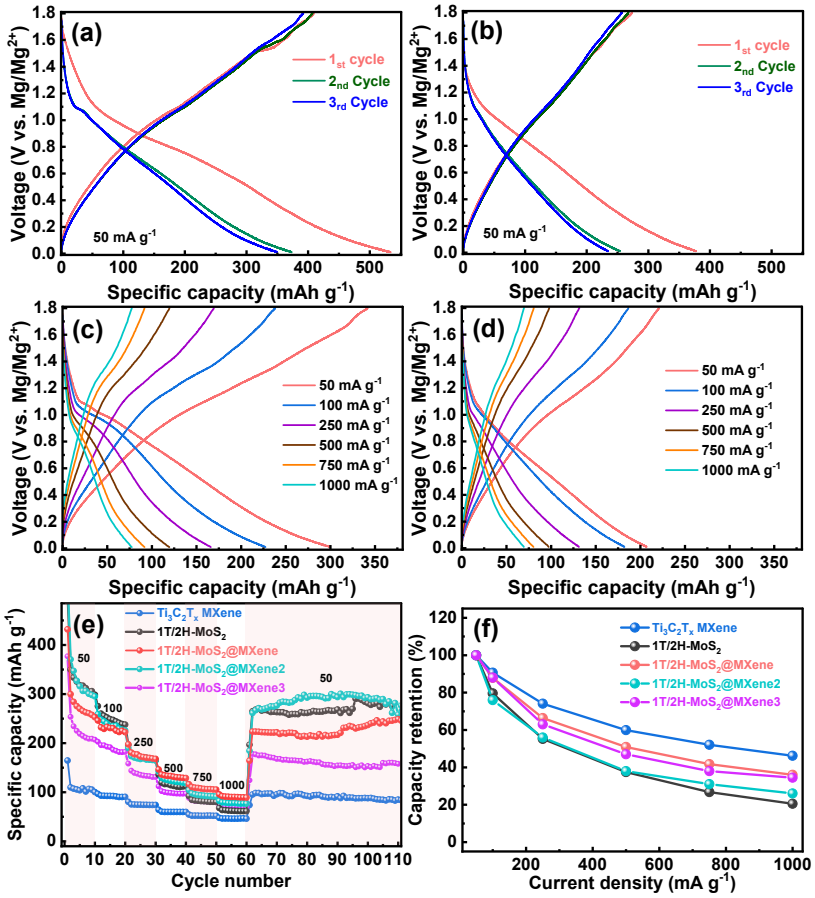

Figure 5.S9: The GCD curves of MLIBs with (a) 1T/2H-MoS_2@MXene2 and (b) 1T/2H-MoS_2@MXene3 cathodes in the first 3 cycles at 50 mA g^{-1}, GCD curves at different current densities of MLIBs with (c) 1T/2H-MoS_2@MXene2 and (d) MoS_2@MXene3 cathodes, and comparison of (e) rate performance and (f) capacity retention of the cathodes at different current densities.

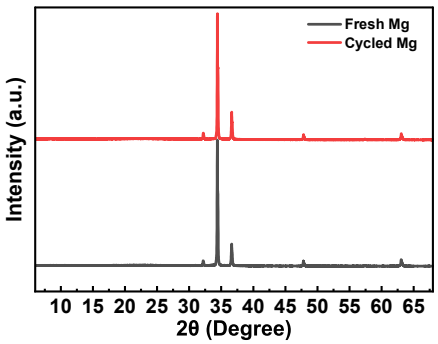

Figure 5.S10: XRD spectra of the fresh Mg plate and cycled Mg plate anode within 1T/2H-MoS_2@MXene MLIB following the rate performance test.